INSTITUTE OF PHYSICS, POLISH ACADEMY OF SCIENCES

DOCTORAL DISSERTATION

SARS-CoV-2: Antibodies and effect of non-structural proteins on protein synthesis in human ribosomes

Author: **Hung Van Nguyen**

Supervisor: Prof. dr hab. **Mai Suan Li**

A thesis submitted in partial fulfilment of the requirements
for the degree of Doctor of Philosophy
in the Division of Theoretical Physics

Warsaw, September 2024

Declaration

I, Hung Van Nguyen, declare that this thesis titled "SARS-CoV-2: Antibodies and effect of non-structural proteins on protein synthesis in human ribosomes" and the work presented within it are my own. I would like to confirm that:

- This work was carried out entirely during the period of pursuing a research degree at the Institute of Physics, Polish Academy of Sciences, Poland.
- Where any part of this thesis has been previously presented for a degree or any other credential at this institute or any other educational institution, it has been explicitly indicated.
- Where I have consulted the published work of others, I always consistently provide clear attributions.
- Where I have quoted from the work of others, the source is always given or cited. Aside from these quotations, this thesis solely represents my own work.
- I have acknowledged all primary sources of help.
- Where the thesis is based on work done by myself jointly with others, I have distinctly delineated between the contributions of others and my own input.

Warsaw, September 2024

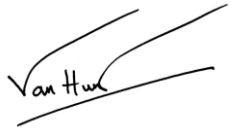

Hung Van Nguyen

Abstract

Severe acute respiratory syndrome coronavirus 2 (SARS-CoV-2) is the causal agent responsible for the formidable global COVID-19 pandemic, officially declared by the World Health Organization in March 2020. Notably, the relentless pursuit of scientific endeavors has led to the development of numerous vaccines, pharmaceuticals, and immunotherapies, which have undoubtedly played an instrumental role in saving countless human lives. However, the fight against the COVID-19 pathogen continues, marked by the emergence of immune-evading variants of concern, such as the Delta and Omicron strains.

In an effort to develop more effective treatments and to understand the intricacies of adverse effects caused by vaccines and therapeutic agents, it is imperative to gain a deep understanding of the molecular interactions of SARS-CoV-2 with these interventions and the cellular constituents of the human body. Computational methods play a crucial role in improving the design of antiviral drugs, vaccines, and antibodies/nanobodies (Abs/Nbs) for the treatment of COVID-19. They are also essential for understanding complex processes such as membrane fusion, RNA splicing, messenger RNA (mRNA) translation, and protein trafficking, especially when SARS-CoV-2 non-structural proteins (NSPs) are involved in the ribosome. Computational approaches span the spectrum from all-atom to coarse-grained models, enabling a deeper understanding of these complex phenomena.

In this dissertation, three computational studies focus on SARS-CoV-2, pursuing two main objectives. First, we delve into the interactions of Abs and Nbs with the SARS-CoV-2 spike (S) protein. Second, we shed light on the impact of SARS-CoV-2 non-structural protein 1 (NSP1) on the protein synthesis process in the human ribosome. The dissertation consists of five chapters detailing these research endeavors.

Chapter 1 provides an introductory section covering key aspects, including the COVID-19 pandemic, the structure of SARS-CoV-2 and its variants, the life cycle of SARS-CoV-2, an overview of the interaction of Abs and Nbs with the S protein, and the interaction of NSP1 with the human ribosome.

Chapter 2 provides an overview of the computational methodologies used in the research presented in this dissertation. It includes a brief summary of the molecular dynamics simulations used to estimate the binding affinity of various SARS-CoV-2 biomolecular complexes, such as steered molecular dynamics (SMD), umbrella sampling (US), and alchemical simulations.

Chapter 3 is dedicated to the interaction of Abs and Nbs with the receptor binding domain (RBD) of the SARS-CoV-2 S protein, where their binding affinity is assessed through all-atom SMD and coarse-grained US simulations. This chapter encompasses two separate research publications: In the first publication, the study revolves around the binding of REGN10933 Ab, REGN10987 Ab, and their combination to RBD. It is observed that REGN10933 exhibits a stronger binding affinity to RBD than REGN10987. Interestingly, the combination of REGN10933 and REGN10987 displays even stronger binding to RBD. The stability of REGN10933-RBD and REGN10933+REGN10987-RBD complexes is primarily governed by electrostatic interactions, whereas the stability of REGN10987-RBD depends on

van der Walls (vdW) interactions. In particular, REGN10933 and REGN10933+REGN10987 show similar potency against the Delta variant and the wild type. However, they are less effective against the Omicron variant, confirming recent experimental results. The second publication examines the concurrent binding of H11-H4 Nb and CR3022 Ab to RBD, revealing a markedly increased binding affinity compared to their individual associations with RBD. The combination of H11-H4 and CR3022 increases the ability to neutralize SARS-CoV-2. The stability of the H11-H4-RBD complex is mainly driven by vdW interactions, while electrostatic interactions play a more significant role in the stability of CR3022-RBD and H11-H4+CR3022-RBD complexes. CR3022 is a promising candidate for the treatment of COVID-19, especially against the wild type strain. In addition, it is noteworthy that H11-H4 exhibits strong neutralizing capabilities against Alpha, Kappa, and the highly concerning Delta variants, consistent with recent experimental data.

Chapter 4 focuses on the interaction between mRNA and the 40S ribosome in the presence and absence of NSP1. Using all-atom SMD and coarse-grained alchemical simulations, our analysis revealed that mRNA exhibits significantly stronger binding affinity for the 40S-NSP1 complex compared to the 40S ribosome alone. These results are in close agreement with experimental observations. Furthermore, our studies showed that the electrostatic interaction between mRNA and the 40S ribosome plays a key role in driving the mRNA translation process. Upon entry into host cells, NSP1 can bind to the 40S ribosome, thereby interfering with the translation process.

Finally, Chapter 5 provides a summary of the findings presented in this thesis and outlines potential directions for future research.

Streszczenie

Ciężki ostry zespół oddechowy koronawirus 2 (SARS-CoV-2) odpowiedzialny jest za wybuch pandemii COVID-19, ogłoszonej przez Światową Organizację Zdrowia w marcu 2020 roku. W celu przeciwdziałania skutkom koronawirusa prowadzone są liczne badania naukowe. Doprowadziły one do opracowania wielu szczepionek, leków i terapii immunologicznych, które odegrały kluczową rolę w ratowaniu niezliczonych ludzkich istnień. Jednak przeciwdziałanie COVID-19 ciągle trwa, co jest szczególnie istotne ze względu na pojawienie się nowych wariantów koronawirusa, takich jak Delta i Omikron, które potrafią unikać odpowiedzi immunologicznej organizmu.

W dążeniu do opracowania bardziej skutecznych terapii i zrozumienia złożoności skutków ubocznych wywołanych przez szczepionki i środki terapeutyczne, konieczne jest dogłębne zrozumienie ich oddziaływań z molekułami koronawirusa oraz składnikami komórkowymi ludzkiego ciała. Metody obliczeniowe odgrywają kluczową rolę w udoskonalaniu metod projektowania leków przeciwwirusowych, szczepionek oraz przeciwciał/nanocząsteczek (Abs/Nbs) do leczenia COVID-19. Są one również niezbędne do zrozumienia złożonych procesów, takich jak fuzja błon, składanie RNA, translacja mRNA i transportu białek. Jest to szczególnie istotne, ponieważ niestrukturalne białka koronawirusa (NSP) biorą udział w funkcjonowaniu rybosomu. Podejścia obliczeniowe obejmują szerokie spektrum od modeli na pełnoatomowych do modeli zgrubnych (gruboziarnistych), umożliwiając pełne zrozumienie tych skomplikowanych zjawisk.

W niniejszej dysertacji przedstawione są trzy badania obliczeniowe, które koncentrują się na SARS-CoV-2, realizując dwa główne cele badawcze. Po pierwsze, zbadałem oddziaływania Abs i Nbs z białkiem kolca (S) SARS-CoV-2. Po drugie, dostarczam wskazówek molekularnych dotyczących wpływu niestrukturalnego białka 1 (NSP1) SARS-CoV-2 na proces syntezy białek w ludzkim rybosomie. Dysertacja składa się z pięciu rozdziałów opisujących te badania.

Rozdział 1 zawiera wstępną sekcję, obejmującą kluczowe aspekty, w tym pandemię COVID-19, strukturę SARS-CoV-2 i jego wariantów, cykl życia koronawirusa, opis oddziaływania Abs i Nbs z białkiem S oraz NSP1 z ludzkim rybosomem.

Rozdział 2 przedstawia przegląd metod obliczeniowych użytych w badaniach przedstawionych w tej dysertacji. Obejmuje on także krótki opis symulacji dynamiki molekularnej użytych do oszacowania siły wiązania różnych kompleksów biomolekularnych SARS-CoV-2, takich jak sterowane dynamiki molekularne (SMD), próbkowanie typu „parasola” (US) i symulacje alchemiczne.

Rozdział 3 poświęcony jest oddziaływaniu Abs i Nbs z domeną wiążącą receptor (RBD) białka S SARS-CoV-2, gdzie oceniana jest ich siła wiązania przy użyciu symulacji SMD na poziomie pełnoatomowym i gruboziarnistym. Rrozdział ten obejmuje dwie oddzielne publikacje badawcze: W pierwszej publikacji badania koncentrują się na wiązaniu przeciwciała REGN10933, REGN10987 i ich kombinacji z RBD. Obserwuje się, że REGN10933 wykazuje większą siłę wiązania z RBD niż REGN10987. Co ciekawe, kombinacja REGN10933 i REGN10987 wykazuje jeszcze silniejsze wiązanie z RBD, a

stabilność kompleksów REGN10933-RBD i REGN10933+REGN10987-RBD jest głównie determinowana przez oddziaływania elektrostatyczne, podczas gdy stabilność kompleksu REGN10987-RBD zależy głównie od oddziaływań van der Waalsa (vdW). W szczególności, REGN10933 i REGN10933+REGN10987 wykazują podobną skuteczność przeciwko wariantowi Delta i dzikiemu typowi, są jednak mniej skuteczne przeciwko wariantowi Omikron, co potwierdza niedawne wyniki eksperymentalne. Druga publikacja bada jednoczesne wiązanie nanocząsteczki H11-H4 i przeciwciała CR3022 z RBD, wykazując znacznie większą siłę wiązania w porównaniu do ich indywidualnych oddziaływań z RBD, a kombinacja H11-H4 i CR3022 zwiększa zdolność do neutralizacji SARS-CoV-2. Stabilność kompleksu H11-H4-RBD jest głównie wynikiem oddziaływań vdW, podczas gdy oddziaływania elektrostatyczne odgrywają większą rolę w stabilności kompleksów CR3022-RBD i H11-H4+CR3022-RBD. CR3022 wydaje się być obiecującym kandydatem do leczenia COVID-19, zwłaszcza przeciwko standardowemu typowi. Ponadto warto zauważyć, że H11-H4 wykazuje silne zdolności neutralizujące przeciwko wariantom Alpha, Kappa i wariantowi Delta, co jest zgodne z najnowszymi danymi eksperymentalnymi.

Rozdział 4 koncentruje się na oddziaływaniach między mRNA a rybosomem 40S w obecności i nieobecności NSP1. Korzystając z pełnoatomowych symulacji SMD i gruboziarnistych symulacji alchemicznych wykazałem, że mRNA charakteryzuje się znacznie większą siłę wiązania z kompleksem 40S-NSP1 w porównaniu do samego rybosomu 40S – wyniki te są zgodne z obserwacjami eksperymentalnymi. Ponadto nasze badania wykazały, że oddziaływania elektrostatyczne między mRNA a rybosomem 40S odgrywają kluczową rolę w napędzaniu procesu translacji mRNA. Po wniknięciu do komórek gospodarza, NSP1 może wiązać się z rybosomem 40S, zakłócając w ten sposób proces translacji.

Rozdział 5 zawiera podsumowanie wyników przedstawionych w tej dysertacji oraz przedstawia potencjalne kierunki przyszłych badań.

Publications

- **Publications presented in this thesis**:

1. **Nguyen, H.**; Pham, D. L.; Nissley, D. A.; O'Brien, E. P.; Li, M. S. Cocktail of REGN antibodies binds more strongly to SARS-CoV-2 than its components, but the Omicron variant reduces its neutralizing ability. *J. Phys. Chem. B*. 2022, 126(15), 2812-2823.
2. **Nguyen, H.**; Li, M. S. Antibody-nanobody combination increases their neutralizing activity against SARS-CoV-2 and nanobody H11-H4 is effective against Alpha, Kappa and Delta variants. *Sci. Rep*. 2022, 12 (9701).
3. **Nguyen, H.**; Nguyen, H. L; Li, M. S. Binding of SARS-CoV-2 non-structural protein 1 to 40S ribosome inhibits mRNA translation. *J. Phys. Chem. B*. 2024, 128(29), 7033-7042.

- **Other publications during my doctoral program**:

1. **Nguyen, H.**; Pham, D. L.; Nissley, D. A.; O'Brien, E. P.; Li, M. S. Electrostatic interactions explain the higher binding affinity of the CR3022 antibody for SARS-CoV-2 than the 4A8 antibody. *J. Phys. Chem. B.* 2021, 125(27), 7368-7379.
2. **Nguyen, H.**; Nguyen, H. L.; Lan, P. D.; Thai, N. Q.; Mateusz, S.; Li, M. S. Interaction of SARS-CoV-2 with host cells and antibodies: Experiment and simulation. *Chem. Soc. Rev.* 2023, 52(18), 6497-6553.

- **Other publications**:

1. **Nguyen, H.**; Le, L.; Ho, T. B. Computational study on ice growth inhibition of Antarctic bacterium antifreeze protein using coarse grained simulation. *J. Chem. Phys.* 2014, 140(22), 225101.
2. **Nguyen, H.**; Le, L. Steered molecular dynamics approach for promising drugs for influenza A virus targeting M2 channel protein. *Eur. Biophys. J.* 2015, 44(6), 447-455.
3. **Nguyen, H.**; Tran, T.; Fukunishi, Y.; Higo, J.; Nakamura, H.; Le, L. Computational study of drug binding affinity to Influenza A neuraminidase using smooth reaction path generation (SRPG) method. *J. Chem. Inf. Model.* 2015, 55(9), 1936-1943.
4. **Nguyen, H.**; Van, T. D.; Le, L. Coarse grained simulation reveals antifreeze properties of hyperactive antifreeze protein from Antarctic bacterium Colwellia sp. *Chem. Phys. Lett.* 2015, 638, 137-143.
5. **Nguyen, H.**; Nguyen, H. T.; Le, L. Investigation of free energy profiles of amantadine and rimantadine in the AM2 binding pocket. *Eur. Biophys. J.* 2015, 45(1), 63-70.
6. **Nguyen, H.**; Van, T. D.; Tran, N.; Le, L. Exploring the effects of subfreezing temperature and salt concentration on ice growth inhibition of Antarctic Gram-negative bacterium Marinomonas Primoryensis using coarse grained simulation. *Appl. Biochem. Biotechnol.* 2016, 178(8), 1534-1545.

7. **Nguyen, H.**; Nguyen, T.; Le, L. Computational study of Glucose 6 phosphate dehydrogenase deficiencies using molecular dynamics simulation. *S. Asian J. Life Sci*. 2016, 4(1), 32-39.
8. **Nguyen, H.**; Le, L. Investigation of changes in structure and thermodynamics of Spruce Budworm antifreeze protein under subfreezing temperature. *Sci. Rep.* 2017, 7, 40032.
9. **Nguyen, H.**; Do, N.; Phan, T.; Pham, T. Steered molecular dynamics for investigating the interaction between Insulin Receptor Tyrosine Kinase (IRK) and variants of Protein Tyrosine Phosphatase 1B (PTP1B). *Appl. Biochem. Biotechnol.* 2018, 184(2), 401-413.
10. **Nguyen, H.**; Nguyen, H. L.; Linh, H. Q.; Nguyen, M. T. Binding affinity of the L-742,001 inhibitor on endonuclease domain of A/H1N1/PA influenza virus variants: Molecular simulation approaches. *Chem. Phys.* 2018, 500, 26-36.
11. **Nguyen, H.**; Pham, T.; Nguyen, H. L.; Phan, T. Investigation of binding affinity of Prokaryotic proteins (AHU-IHF) and DNAs: Steered molecular dynamics approach. *Appl. Biochem. Biotechnol.* 2018, 186(4), 834-846.
12. Pham, T.; Nguyen, H. L.; Phan-Toai, T.; **Nguyen, H**. Investigation of binding affinity between potential antiviral agents and PB2 protein of influenza A: Non-equilibrium molecular dynamics simulations approach. *Int. J. Med. Sci.* 2020, 17(13), 2031-2039.

Reuse and permissions license

In this thesis, I have included my three first-author articles: Two published in The Journal of Physical Chemistry B and one in Scientific Reports. I have meticulously listed the permissions from the respective journals below.

- The Journal of Physical Chemistry B: These publications are licensed under CC-BY 4.0.
- Scientific Reports: This publication is licensed under a Creative Commons Attribution 4.0 International License.

Acknowledgments

First and foremost, I would like to express my profound gratitude to Prof. Mai Suan Li, whose unwavering guidance has been instrumental throughout my journey in pursuit of a Ph.D. On the scientific front, he consistently shared his invaluable insights, empowering me to conquer challenges and explore new scientific horizons. Additionally, his willingness to respect my ideas bolstered my confidence in executing my research efforts. Also, I extend my heartfelt thanks to Li's wife, Mrs. Nguyen Thi Ngoc Tam, for her unwavering support. She cared for me like a mother figure, making sure that I felt welcome and at ease at her home while assisting me with various practical issues.

I would like to express my special appreciation to my collaborators: Prof. Edward P. O'Brien from Penn State University, Dr. Daniel A. Nissley from the University of Oxford, Dr. Hoang Linh Nguyen from Duy Tan University, and Mr. Pham Dang Lan from the Institute for Computational Science and Technology at Ho Chi Minh City for the great collaboration.

I wish to present my special thanks to Prof. Łukasz Cywiński, Prof. Emilia Witkowska, Prof. Piotr Deuar, Prof. Bartosz Różycki, Prof. Niedźwiecka Anna, Dr. Paweł Krupa, Miss. Pamela Smardz, and together with all members of my research group, ON5, and IFPAN for their contributions to fostering a friendly and intellectually stimulating work environment. Their efforts greatly enhanced my experience at IFPAN, making my time there enjoyable and fruitful.

I am deeply grateful to my extended family for their profound significance in my life. I would like to express my deepest appreciation to my wife - Nguyen Thi Bich Lieu, and my daughter - Nguyen Ngoc Minh Han, who have been with me throughout this journey.

Lastly, I would like to express my gratitude to the Narodowe Centrum Nauki in Poland (Grant 2019/35/B/ST4/02086) for the support of this work.

Table of contents

List of figures

Figure 3.1: REGN10933 and REGN10987 in complex with RBD of A) wild type, B) Delta variant, and C) Omicron variant. Notably, mutations in the Omicron variant RBD are located in the binding regions for both components of REGN-COV2 cocktail. Mutations in the Delta variant RBD specifically affect REGN10933 binding site. Residues that carry a charge in the wild type RBD are shown in blue, while those that gain a charge after mutation are highlighted in red.

Figure 3.2: 3D structures of A) H11-H4 Nb and CR3022 Ab bound to RBD, and B) RBD mutations of variants Alpha, Beta, Gamma, Kappa, Delta, Lambda and Mu. They have contact with H11-H4, but not with CR3022.

Figure 4.1: The 3D structure of the mRNA-40S-NSP1 complex, including 40S ribosome (ribosomal proteins: green-cyan, ribosomal RNA: wheat), mRNA (red), NSP1 (blue), and Mg^{2+} and Zn^{2+} ions (dark-salmon).

List of tables

Abbreviation

COVID-19	**CO**rona**VI**rus **D**isease of 20**19**
SARS-CoV-2	**S**evere **A**cute **R**espiratory **S**yndrome **Co**rona**V**irus **2**
SARS-CoV	**S**evere **A**cute **R**espiratory **S**yndrome **Co**rona**V**irus
MERS-CoV	**M**iddle **E**ast **R**espiratory **S**yndrome **Co**rona**V**irus
WHO	**W**orld **H**ealth **O**rganization
ORF	**O**pen **R**eading **F**rame
S	**S**pike
RBD	**R**eceptor **B**inding **D**omain
RBM	**R**eceptor **B**inding **M**otif
NTD	**N-T**erminal **D**omain
FP	**F**usion **P**eptide
HR1	**H**eptad **R**epeat **1**
HR2	**H**eptad **R**epeat **2**
TMH1-TMH3	**T**rans**M**embrane **H**elices (**1-3**)
ACE2	**R**eceptor **A**ngiotensin **C**onverting **E**nzyme **2**
Mpro	**M**ain **pro**tease
3CLpro	**3C-L**ike **pro**tease
RdRp	**R**NA-**d**ependent **R**NA **p**olymerase
SAM	**S-A**denosyl **M**ethionine
VOCs	**V**ariants **O**f **C**oncern**s**
ER	**E**ndoplasmic **R**eticulum
FDA	**F**ood and **D**rug **A**dministration
Ab	**A**nti**b**ody
mAb	**m**onoclonal **A**nti**b**ody
Nb	**N**ano**b**ody
mRNA	**m**essenger **RNA**
rRNA	**r**ibosomal **RNA**
rprotein	**r**ibosomal **protein**
NSP	**N**on-**S**tructural **P**rotein
MD	**M**olecular **D**ynamics

SMD	**S**teered **M**olecular **D**ynamics
TI	**T**hermodynamics **I**ntegration
FEP	**F**ree **E**nergy **P**erturbation
LJ	**L**ennard-**J**ones
US	**U**mbrella **S**ampling
vdW	**v**an **d**er **W**alls
AFM	**A**tomic **F**orce **M**icroscopy
SPR	**S**urface **P**lasmon **R**esonance
BLI	**B**io**L**ayer **I**nterferometry
DFS	**D**ynamic **F**orce **S**pectroscopy
FFC	**F**luorescence **F**low **C**ytometry
1D-PMF	**One**-**D**imensional **P**otential of **M**ean **F**orce
CoM	**C**enter **o**f **M**ass
SRP	**S**ignal **R**ecognition **P**article

Chapter 1: Introduction

1.1 COVID-19 pandemic

The first case of coronavirus disease 2019 (COVID-19) was detected in Wuhan, China, at the end of 2019 [1-2]. The disease rapidly spread throughout the world, prompting the World Health Organization (WHO) to declare it a pandemic in March 2020 due to a substantial surge in both the number of cases and fatalities. The total cumulative number of confirmed cases has far surpassed those observed during the severe acute respiratory syndrome coronavirus (SARS-CoV) period during 2003 [3]. Following the emergence of SARS-CoV in 2003 and the Middle East respiratory syndrome coronavirus (MERS-CoV) in 2012, the severe acute respiratory syndrome coronavirus 2 (SARS-CoV-2) constitutes the third zoonotic human coronavirus of the twenty-first century [4].

The number of cases and the death toll from COVID-19 classify it as one of the most catastrophic infectious diseases in human history. Although several years have passed since the onset of the pandemic, the origin of SARS-CoV-2 remains enigmatic. One hypothesis posits a zoonotic origin for SARS-CoV-2, wherein the virus is transmitted to humans from wildlife, such as bats [3, 5-6]. A meta-analysis indicates that the probability of a natural disaster that causes millions of deaths, similar to COVID-19, is extremely small. In contrast, the probability of a virus leaking from a laboratory accident is higher [7], thereby supporting the hypothesis that the virus may be the product of genetic research. Another plausible scenario is the emergence of the virus through an evolutionary and selective process, involving a human-transmitted variant of the coronavirus that circulates within the population, culminating in a pandemic [8].

Since the onset of the pandemic, the research community has exerted tremendous effort to identify effective treatments for COVID-19. Despite the notable success of current vaccines, particularly messenger RNA (mRNA) vaccines [9], antibodies (Abs) [10-11], and pharmaceuticals such as Remdesivir, Molnupiravir [12-14], and Paxlovid [15], the battle against SARS-CoV-2 continues, with the emergence of an increasing number of variants of concerns, such as Delta and Omicron. The pandemic has progressed through multiple waves [16-17], including the initial, second, and third waves, attributed to the ancestral Wuhan strain, Beta and Delta variants [18], respectively. Subsequently, the fourth and fifth waves have been ignited by the Omicron variant and its sub-lineages [17, 19], which are competing among themselves to establish dominance within the viral lineage [20]. Even individuals who have received the original mRNA vaccine and a bivalent BA.5 booster have displayed limited neutralization efficacy against Omicron subvariants, including BA.2.75.2, BQ.1.1, XBB.1, *etc*. [21], posing fresh challenges to public health [22-23]. Such observations underscore the imperative for researchers to gain a deeper understanding of the interaction between novel variants and human cells. This understanding must encompass immune evasion and intricate details of viral replication mechanisms to facilitate the development of more potent Abs and vaccines [24]. These circumstances emphasize the enduring commitment to COVID-19 research within the scientific community.

1.2 SARS-CoV-2 structure

SARS-CoV-2 belongs to the beta-coronavirus within the Coronaviridae family, which comprises four genera: Alpha, Beta, Gamma, and Delta coronaviruses. It is spherical in shape and has a size of about 100 nm. SARS-CoV-2 genome is a single-strand positive-sense RNA, which distinguishes it as larger than most other RNA viruses [25]. This molecule possesses a 5′-cap and a 3′-poly(A) tail, enabling it to function as functional mRNA for the translational synthesis of replicase polyproteins [26]. Approximately two-thirds of the viral genomic region is occupied by the replicase gene, referred to as open reading frames (ORFs), which have the potential to encode non-structural proteins (NSPs) known as pp1a and pp1ab polyproteins, respectively (Figure 1.1).

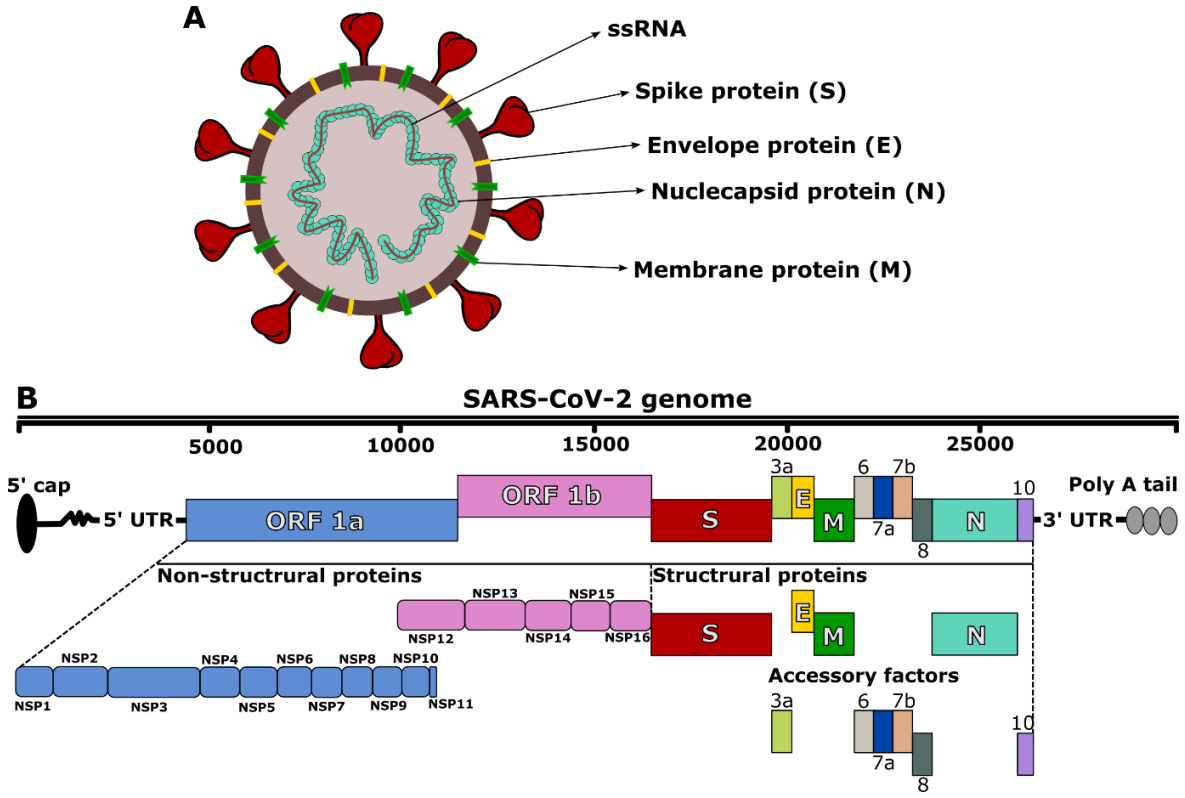

Figure 1.1: Illustration shows A) SARS-CoV-2 structure and B) a schematic of SARS-CoV-2 components.

The pp1a encompasses NSP1 to NSP11, while the pp1ab consists of NSP12 to NSP16. The remaining region preceding the 3′-end encodes various structural proteins, including spike (S), envelope (E), membrane (M), and nucleocapsid (N) proteins [27] (Figure 1.1). Here, structural genes also encode accessory proteins, such as ORF3a, ORF6, ORF7a, ORF7b, ORF8, ORF10, and others [28]. Moreover, the genomic region immediately preceding the 5′-end contains two distinct domains: The leader sequence and the untranslated region. These domains are capable of forming a multitude of stem-loop structures that are essential for the replication and transcription of the viral genome [26].

1.2.1 Structural proteins

Structural proteins are essential components that living organisms employ to maintain their shape and structural integrity. These proteins are composed of amino acids, which serve as their fundamental building blocks or monomers. Amino acids are analogous to beads on a pearl necklace, binding together to form proteins. Each amino acid consists of a carbon alpha (C_α) linked to an amino group (NH2), a carboxyl group (COOH), hydrogen (H), and a variable side chain denoted as (R), which confers different chemical properties on the amino acid. The complement of amino acids comprises twenty canonical types, each possessing unique chemical characteristics. These canonical amino acids are further categorized into groups based on the chemical properties of their side chains, which include positively charged amino acids, negatively charged amino acids, uncharged polar amino acids, and nonpolar amino acids. Proteins exhibit four hierarchical levels of structural organization. The primary structure refers to the linear sequence of amino acids in a polypeptide chain that extends from the N-terminus (NH2) to the C-terminus (COOH). The secondary structure in proteins is defined by the localized spatial arrangement of the polypeptide chain, which is stabilized through hydrogen bonds within the peptide backbone. Common secondary structures include the α-helix and β-strand. The three-dimensional conformation of a single polypeptide chain, shaped by interactions between its side chains, is referred to as the tertiary structure. When a protein is composed of multiple polypeptide chains, its overall structure is referred to as the quaternary structure.

The SARS-CoV-2 genome encodes four structural proteins - S, E, N, and M - using genes located near the 3′ end. The S protein plays a crucial role in binding to and neutralizing the host cell membrane. The M protein, the most abundant structural protein in the viral structure, plays a key role in protecting the virus. The M protein aids in the formation of the virus and reinforces the curvature of the viral membrane by interacting with the N protein. Within the virus, the E protein plays a role by harboring a small quantity of a transient membrane protein, often referred to as the coat protein. The E protein is instrumental in the processes of assembly, release, and pathogenicity of the virus. The N protein is another crucial viral component that tightly binds to the RNA genome and forms a symmetrical helical nucleocapsid structure. The N protein comprises two domains that facilitate their attachment to the RNA genome through various mechanisms [29]. Detailed information on the structural proteins of SARS-CoV-2 is provided in the following.

a) S protein: The entry of SARS-CoV-2 into host cells is facilitated by the S glycoprotein [30-32]. This transmembrane S glycoprotein assembles into homotrimers (Figure 1.2A) that protrude from the viral surface (Figure 1.1). Due to its crucial role in facilitating the entry of coronaviruses into host cells, the S protein is an attractive target for antiviral intervention. The S protein consists of two functional subunits: S1 and S2. The S1 subunit binds primarily to host cell receptors, whereas the S2 subunit facilitates the fusion of viral and host cell membranes. At the junction between the S1 and S2 subunits, there is a cleavage site known as the S1/S2 protease cleavage site (Figure 1.2A). Host proteases are responsible for cleaving the S protein at the S2 cleavage site in all coronaviruses. This cleavage event activates the

protein and is essential for triggering irreversible conformational changes necessary for the fusion of viral and host cell membranes [33-34].

In the prefusion conformation, the S1 and S2 subunits remain associated via non-covalent bonds. Various coronaviruses employ specific domains within the S1 subunit to interact with distinct entry receptors. To enter into host cells, SARS-CoV-2 relies on the recognition of the receptor angiotensin-converting enzyme 2 (ACE2) on the surface of host cells, a process primarily mediated by the receptor binding domain (RBD) within the S1 subunit (Figure 1.2A). The S protein can adopt two distinct structural forms: The "closed" and "open" states. In the "closed" state, the three receptor recognition motifs do not extend beyond the interface formed by the three S protein protomers. The "open" state exhibits an upward orientation of RBD, which is essential for the fusion of SARS-CoV-2 with the host cell membranes, thereby enabling the virus to enter host cells efficiently [33].

The formation of the six-helical bundle is based on the interaction between heptad repeat 1 (HR1) and heptad repeat 2 (HR2) (Figure 1.2A), and this structural motif plays a crucial role in membrane fusion, mediated primarily by the S protein. Consequently, HR1 and HR2 have become attractive targets for drug development [35-36]. Three HR1 domains converge to create a spiral coil trimer oriented in a parallel configuration. At the same time, three HR2 domains intertwined around the center antiparallelly, primarily driven by hydrophobic forces. Hydrophobic residues located on the HR2 domain form interactions with the hydrophobic grooves formed by every pair of neighboring HR1 helices [37].

Because RBD specifically binds to the ACE2 receptor, it is a crucial target for antiviral drugs and Abs [38]. RBD consists of two structural domains: The core and the external subdomains. The core subdomain exhibits a high degree of conservation and is composed of five β strands arranged in an antiparallel fashion, featuring a disulfide bond bridging two of these β strands. Conversely, the external subdomain is predominantly defined by a loop region that is stabilized through another disulfide bond [39]. The core of RBD consists of five antiparallel β sheets connected by loops and short helices. Situated between the antiparallel β4 and β7 strands is the receptor binding motif (RBM), characterized by loops, α helices, and short β5 and β6 strands. The RBM contains the majority of the binding sites for both SARS-CoV-2 and ACE2. Within RBD, eight out of the nine Cysteine residues engage in the formation of four pairs of disulfide bonds. Three of these disulfide bonds are located within RBD's core, enhancing the stability of the β sheet structure. The remaining disulfide bond’s role is to facilitate connections between the loops within the RBM. The N-terminal peptidase domain of ACE2 encompasses the binding site, formed by two lobes involving the RBM and ACE2. Specifically, the RBM binds to the smaller lobe of ACE2 on its lower side. The surface of the RBM exhibits a slight inward curvature to accommodate the presence of ACE2 [33]. RBD undergoes conformational changes reminiscent of a hinge, leading to the exposure or concealment of S protein elements that engage with host cell receptors. These conformational shifts manifest as two distinct states: the "up" and "down" conformations. Here, only the "up" conformation of SARS-CoV-2 is capable of binding to ACE2; the "down" conformation of SARS-CoV-2 cannot recognize ACE2 on host cells.

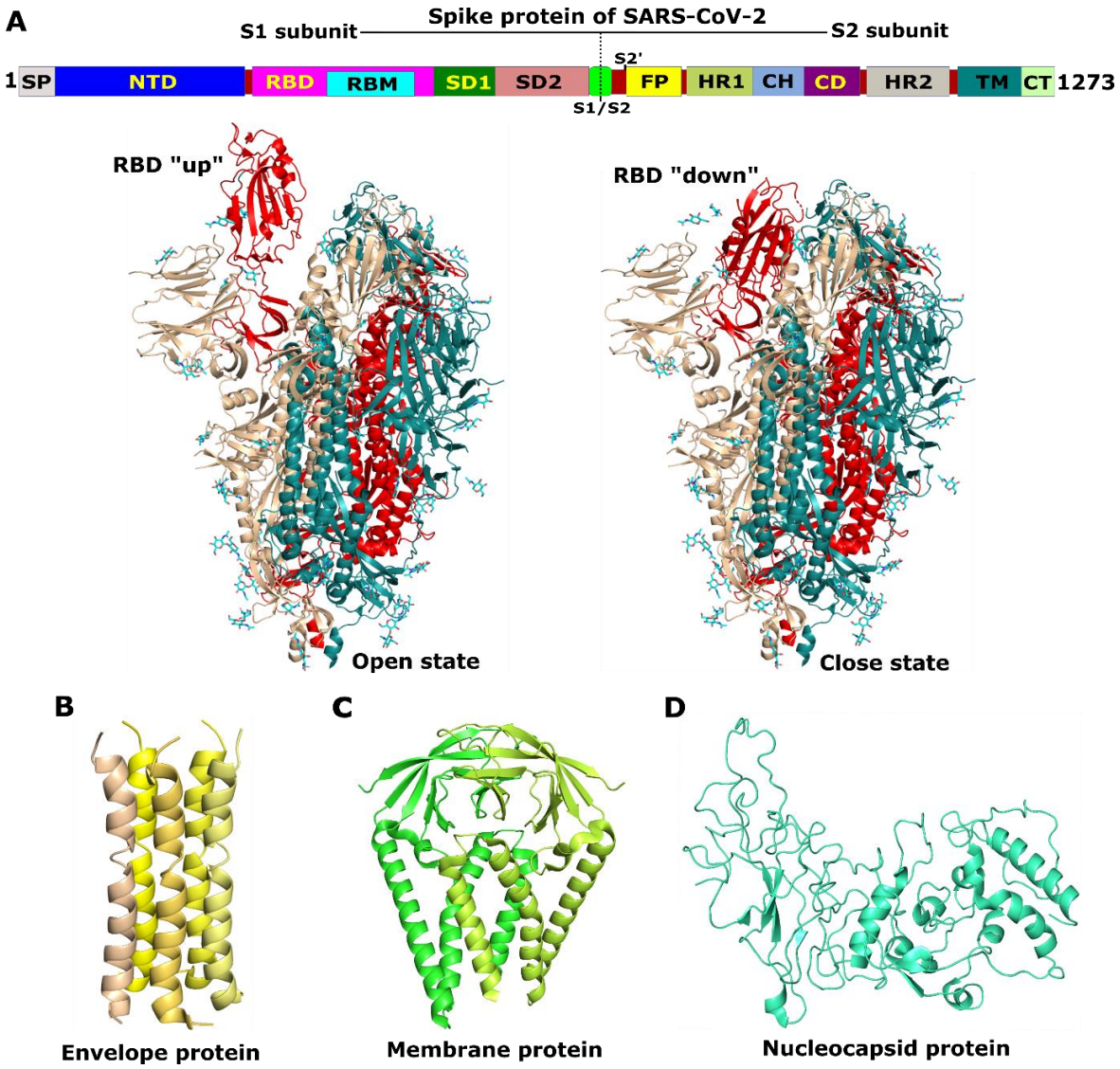

Figure 1.2: SARS-CoV-2 structural proteins include A) S protein structures in open (PDB ID: 6VYB) and closed (6VXX) states, B) E protein transmembrane domain (7K3G), C) M protein (8CTK), and D) N monomer protein (8FD5).

b) E protein: The E protein in SARS-CoV-2 is the smallest among all the structural proteins but plays a significant role in pathogenesis, virus assembly, and release [40]. The E protein is characterized by a five-helix bundle surrounding a narrow, dehydrated pore that contains a bipartite channel (Figure 1.2B). Although the amino acid compositions of the E protein vary considerably, their structural features remain conserved across different genera of β coronaviruses. Typically, this protein displays a short hydrophilic N-terminus, a sizable hydrophobic region, and a hydrophilic C-terminal tail [41].

c) M protein: The M protein is the most abundant structural protein and features three distinct transmembrane domains [42]. These domains include an ectodomain at the N-terminus, three transmembrane helices (TMH1-TMH3), and an endo-domain at the C-terminus [43] (Figure 1.2C). Specifically, the TMH1-TMH2 intersegment is located in the interior, while the

TMH2-TMH3 intersegment is on the exterior. The C-terminal region is predicted to contain at least two casein kinase II phosphorylation sites, which are relevant to interactions with S, E, and N proteins [44]. These interactions play a vital role in inducing membrane bending and act as a checkpoint for new virion formation [45]. The M protein is associated with other viral structural proteins, including the N protein, thereby facilitating the molecular assembly of virus particles and potentially contributing to pathogenesis [46]. Although the amino acid composition of the M protein varies, its structural features are conserved in different genera [47]. In particular, O-linked glycosylation is observed in β and δ coronaviruses, while other coronavirus M proteins undergo N-linked glycosylation [48-49]. This glycosylation plays a crucial role in organ tropism and interferon signaling [50].

d) N protein: The N protein plays a vital role exclusively in structural organization. It is characterized by three highly conserved domains: an N-terminal domain, an RNA-binding domain (or linker region), and a C-terminal domain [51] (Figure 1.2D). These domains are believed to collectively regulate RNA binding [52], with the phosphorylation status of the N protein being a critical factor that induces structural changes, thereby enhancing its affinity for viral RNA over non-viral RNA [53]. The N protein is actively involved in the RNA packaging, adopting a "beads-on-a-string" conformation. Beyond its role in organizing the viral genome, the N protein also contributes to virion assembly and improves virus transcription efficiency, among other functions [52].

1.2.2 Non-structural proteins

A non-structural protein (NSP) is a protein encoded by a virus but not part of the viral particle and arises during viral replication. SARS-CoV-2 contains sixteen NSPs, designated as NSP1 to NSP16 (Figure 1.3). Below is a description of the NSPs of SARS-CoV-2.

a) NSP1: NSP1 is composed of three domains: an N-terminal domain, a linker domain, and a C-terminal domain. The C-terminal domain can bind to the 40S subunit of the human ribosome, resulting in inhibition of mRNA translation [54]. The N-terminal and linker domains of NSP1 do not bind directly to the 40S mRNA entry channel; instead, they play a role in stabilizing its association with the ribosome and mRNA [55].

b) NSP2: NSP2 consists of the N-terminal and C-terminal domains. Although NSP2 is involved in viral processes, its precise functions and structural basis remain unknown [29]. Notably, a highly conserved cysteine residue that coordinates a zinc ion within a zinc ribbon-like motif exhibits significant structural similarity to RNA-binding proteins. This motif plays a crucial role in NSP2's interactions with nucleic acids [56].

c) NSP3: NSP3 is the largest membrane-bound protein, encompassing several domains [57]. NSP3 functions as a membrane-anchored scaffold that associates with host proteins and other NSPs to form the viral replication-transcription complex [58].

d) NSP4: NSP4 consists of four transmembrane domains: N-terminal, lumenal, TM3 and C-terminal [59]. Transmembrane domains 1 to 3 (the N-terminal, lumenal, TM3), along with a specifically charged residue, play a crucial role in facilitating productive virus infection, while the C-terminal domain is exposed on the cytoplasmic side of the membrane [60]. NSP4 plays a role in anchoring the viral replication-transcription complex, in conjunction with other integral viral membrane proteins such as NSP3 and NSP6 [61]. The co-expression of NSP4 and NSP3 leads to the induction of concentrated foci in the perinuclear region and the redistribution of proteins from the endoplasmic reticulum (ER) to the foci [58].

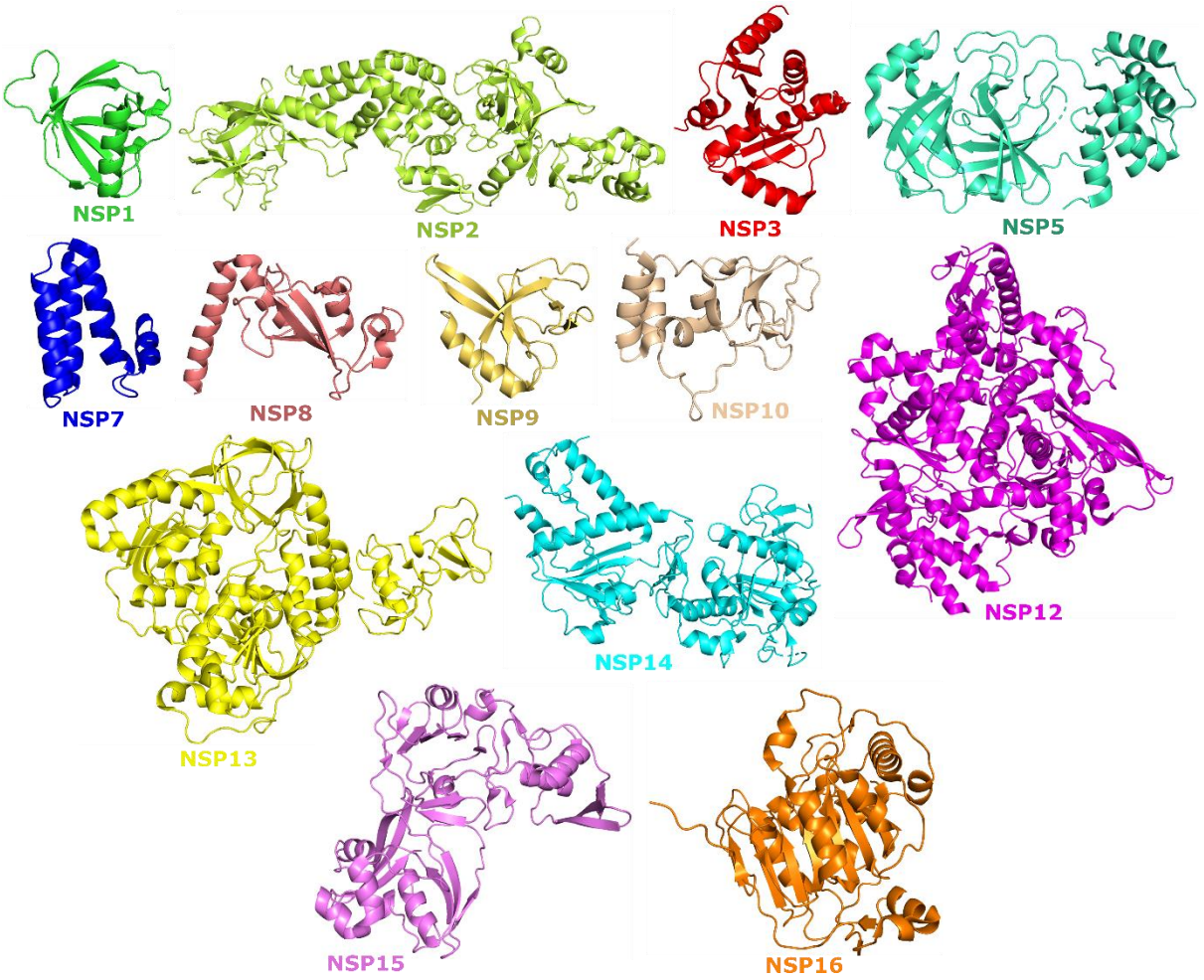

Figure 1.3: Illustration is NSPs of SARS-CoV-2, including NSP1 (7K7P), NSP2 (7MSW), NSP3 (6YWL), NSP5 (7QBB), NSP7 and NSP8 (7DCD), NSP9 (7BWQ), NSP10 (7ORR), NSP12 (6NUR), NSP13 (6ZSL), NSP14 (7R2V), NSP15 (7KOR) and NSP16 (6WVN).

e) NSP5: NSP5, known as the main protease (Mpro) or 3C-like protease (3CLpro), is comprised of monomers with N-terminal domains (domain I and domain-II) and a C-terminal domain (domain-III) [62]. Its primary function is to catalyze the processing of viral polyproteins, making it a promising target for antiviral therapy with SARS-CoV-2 [63].

f) NSP6: NSP6 is a multi-spanning transmembrane protein consisting of six transmembrane domains [64], which are located in the ER [65]. It plays a role in facilitating the generation of autophagosomes, which are responsible for releasing viral components to lysosomes for degradation [66].

g) NSP7, NSP8, and NSP12: NSP7 consists of an α-helical structure with three helical bundle folds, while NSP8 is comprised of two subdomains: an N-terminal "shaft" domain and a C-terminal "head" domain [67]. The crystal structure of the NSP7-NSP8 complex forms a hollow cylindrical hexadecameric structure with a dimer conformation. This complex has a negatively charged outer surface and a positively charged inner core [68], facilitating the passage of the nucleic acid phosphate backbone through the cylindrical channel without electrostatic repulsion. The cylindrical NSP7-NSP8 complex is stabilized by a salt bridge [69].

NSP12 functions as a multi-subunit RNA-dependent RNA polymerase (RdRp) [70], including two main functional domains: an N-terminal domain and a polymerase domain [71]. The polymerase domain is at the C-terminus, and it adopts a "right hand" cupped-shaped conformation, comprising finger, palm, and thumb subdomains [72]. The N-terminus contains a nidovirus RdRp-associated nucleotidyl transferase (NiRAN) domain linked to the C-terminus of the RdRp, along with an extended N-terminal β-hairpin domain [71]. The NiRAN domain is followed by an interface domain, and the β-hairpin domain inserts into a groove formed by the palm domain and NiRAN domain [73]. The active site of RdRp is located at the interface between the finger and thumb subdomains, which is the center of the substrate domain where RNA synthesis occurs [74]. RdRp is known to be an important target for drug development to combat coronavirus infections, including COVID-19 [75-76].

NSP12 forms a complex with NSP7 and NSP8, connected by two salt bridges to NSP7 and NSP8. The binding of the NSP7-NSP8 heterodimer to the finger loop stabilizes the polymerase domain, enhancing its affinity for the template RNA. The second subunit of NSP8 is believed to play a crucial role in polymerase activity, possibly by binding to template RNA and providing an expanded interaction surface, helping anchor the RNA strand. In the presence of both NSP7 and NSP8, NSP12's binding affinity to template primer RNA is significantly enhanced, leading to increased polymerase activity [73].

h) NSP9: NSP9 is composed of a central core featuring a six-stranded barrel, which is flanked by a C-terminal helix and an N-terminal extension. NSP9 serves as a single-stranded RNA binding protein, facilitated primarily by its β-barrel loop structure. Dimerization and interactions with other proteins are likely facilitated by the C-terminal β-hairpin and helix, and these structural elements are conserved across various coronaviruses [77]. NSP9 has a role in the synthesis of viral RNA. It exists in a dimeric form, and forms a unique structure, providing a nucleic acid binding site crucial for efficient virus replication [78].

i) NSP10, NSP14, and NSP16: NSP10 is a single-domain protein that binds two zinc ions. It plays a pivotal role in SARS-CoV-2 viral transcription by stimulating both the 3'-5'-exoribonuclease activity of NSP14 and the 2'-O-methyltransferase activity of NSP16.

Therefore, NSP10 is essential for the methylation of the viral mRNA cap. It can bind to single- and double-stranded RNA and DNA and has an allosteric effect on the activity of NSP14 3'-5'-exoribonuclease, allowing the formation of the substrate binding pocket [79-80]. Similarly, the allosteric interaction of NSP10 with NSP16 improves mRNA binding to the 2'-O-methyltransferase activity of NSP16 [81].

NSP14 is a multidomain protein that acts as an enzyme with two distinct activities: an exoribonuclease activity that acts on single- and double-stranded RNA and an N7-guanine methyltransferase activity [82]. The exoribonuclease domain of NSP14 features a DEEDh motif similar to the DEDD motif found in other exoribonuclease enzymes. This domain, the zinc-binding sites, is necessary for exoribonuclease activity [79, 83]. NSP10 interacts with NSP14, leading to an allosteric effect on its exoribonuclease activity [80, 84]. The Guanine-N7-methyltransferase domain of NSP14 lacks the Rossmann fold typically observed in methyltransferase enzymes. This Guanine-N7-methyltransferase domain is responsible for the initial 5’ methylation of the GpppA cap, enabling efficient RNA translation and protection from the host's innate immune system [85].

NSP16 is a ribose 2’-O-methyltransferase that forms a heterodimer with its allosteric activator, NSP10 [86-87]. Its role in the virus’s life cycle is to perform the final step of RNA cap synthesis. Capping the 5’-end of the mRNA stabilizes it, preventing degradation by the host cell and reducing the innate immune response [88-89]. The NSP10-NSP16 complex modifies the cap-0 structure of mRNA, previously methylated by NSP14, another S-adenosyl methionine (SAM)-dependent methyltransferase. NSP16 converts cap-0 (m7GpppN-RNA) to a cap-1 structure (m7GpppNm-RNA) by adding a methyl group at the ribose 2’-O position of the first nucleotide, using SAM as a methyl donor. Here, NSP10 acts as a cofactor for NSP16, stabilizing the SAM-binding pocket and significantly improving the enzymatic activity [86, 90].

j) NSP11: NSP11 is a short peptide formed through the cleavage of the pp1a polyprotein by the 3CLpro/Mpro proteinase at the NSP10/NSP11 junction. NSP11 is encoded in the genomic RNA region where the translational reading frame shift takes place, transitioning from ORF1a to ORF1b. This frameshift leads to the generation of NSP12 to NSP16 proteins from the pp1ab polyprotein [91].

k) NSP13: NSP13 plays a pivotal role in viral replication and exhibits the highest degree of sequence conservation among its counterparts [92]. Its primary function is to safeguard the virus from degradation. NSP13 performs the conversion of double-stranded DNA into two single-stranded RNAs, making them suitable for replication [93-94]. The terminal portion of NSP13 is predicted to form a cluster of zinc, which provides resistance against coronaviruses and nidoviruses [95]. NSP13 has NTPase activity, using the energy derived from ATP hydrolysis to facilitate the unwinding of base pairs. This activity is believed to be crucial for RNA-related processes, including transcription and translation [96].

l) NSP15: NSP15 is a nidoviral RNA uridylate-specific endoribonuclease, its C-terminal catalytic domain belongs to the EndoU family, involving various critical biological functions

associated with RNA processing. It produces 2'-3' cyclic phosphodiester and 5'-hydroxy termini following RNA endonuclease activity on single- and double-stranded RNA, specifically targeting uridine. The precise functional significance of NSP15 remains elusive. Coronaviruses lacking NSP15 are viable and capable of replication. Nevertheless, conflicting research findings exist regarding NSP15's impact on impeding the innate immune response. Some suggest that NSP15 may degrade viral RNA as a strategy to conceal it from host defenses [97-98].

1.2.3 Accessory proteins

Accessory proteins are essential virulence factors involved in various pathogenesis pathways during SARS-CoV-2 infection. Most of these proteins are believed to contribute to immune evasion strategies. Below is information about several types of SARS-CoV-2 accessory proteins.

a) ORF3a: ORF3a, situated between the S and E proteins**,** is the largest accessory protein in SARS-CoV-2. The ORF3a is O-linked glycosylated and features three transmembrane domains. ORF3a forms dimers and its six transmembrane helices collectively create an ion channel in the host cell membrane that exhibits higher permeability to Ca^{2+}/K^{+} cations than Na^{+} ions. Additionally, the ORF3a is involved in virus release, apoptosis, and pathogenesis [99-100].

b) ORF6: ORF6 is a membrane-associated protein. ORF6 expression has been confirmed in virus-infected Vero E6 cells, as well as in the lung and intestinal tissues of patients. In expressing cells and virus-infected cells, it is primarily located in the ER and Golgi compartments [101].

c) ORF7a: ORF7a is a type I transmembrane protein that includes a signal peptide sequence, a luminal domain, a transmembrane domain, and a short C-terminal tail. Conversely, the ORF7b is an integral membrane protein expressed in SARS-CoV-2 infected cells, where it remains localized in the Golgi compartment. ORF7b has been found to be closely associated with intracellular virus particles, further underscoring its significance and importance [102-103].

d) ORF8: ORF8 exhibits low homology to SARS-CoV-2 due to a deletion. Its structure resembles an immunoglobulin (Ig)-like fold, primarily due to the β-strand core. ORF8 has been observed to interact with the major histocompatibility complex I, thus facilitating their degradation in cell culture and potentially contributing to immune evasion [104].

e) ORF10: ORF10 is predicted to be located downstream of the N gene. Although its corresponding single guide RNA is rarely detected, the ORF10 has been found in infected cells [105].

1.3 SARS-CoV-2 life cycle

SARS-CoV-2 interacts with cellular receptors such as human ACE2 and host proteases, which activate the S protein. Below are seven stages describing SARS-CoV-2 life cycle (Figure 1.4).

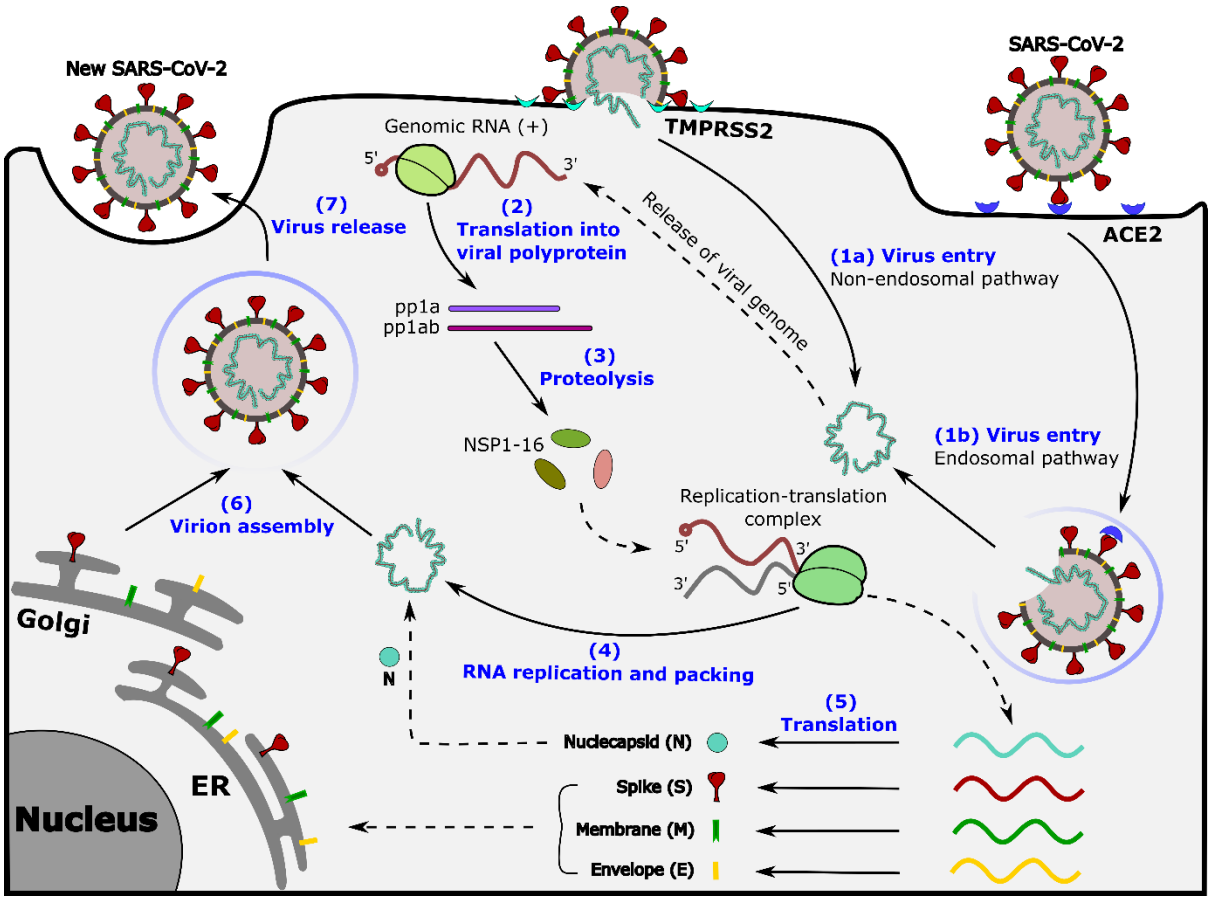

Figure 1.4: SARS-CoV-2 life cycle encompasses seven stages required for the creation of new SARS-CoV-2 particles and their release from human cells [106].

Stage (1): SARS-CoV-2 can enter the cell cytoplasm through two mechanisms: (1a) The viral particle is endocytosed before fusing with the endosomal membrane. (1b) The viral membrane fuses directly with the cell membrane at the cell surface [107].

Stage (2): Once inside the host cell and after releasing its RNA, translation begins immediately using the host cell ribosomes. Translation results in the formation of two large polypeptide chains: pp1a and pp1ab.

Stage (3): These polypeptide chains undergo proteolysis to produce individual NSPs, which then assemble to form the viral replication and transcription complex [108-109].

Stages (4 and 5): This complex transcribes a series of subgenomic mRNAs through a process of discontinuous transcription. Subsequently, these subgenomic mRNAs are translated into viral structural proteins. The N protein forms a complex with genomic RNA,

while the S, E, and M proteins are inserted into the viral envelope of the intermediate compartments within the intermediate compartments of the ER and Golgi.

Stages (6 and 7): Newly assembled viral particles are formed and released from infected cells through exocytosis [110].

1.4 SARS-CoV-2 variants

Since the outbreak of SARS-CoV-2, the virus has undergone mutations in its genes, some of which have been found to change its virulence and transmissibility. As a result, multiple variants have emerged, each with distinct characteristics compared to the original strain. According to the WHO, there have been five variants of concerns (VOCs) of COVID-19: Alpha (B.1.1.7), Beta (B.1.351), Gamma (P.1), Delta (B.1.617.2), and Omicron (B.1.1.529) [111-112] (Figure 1.5), as well as two variants of interest: Lambda and Mu [113]. VOCs are known to exhibit increased transmissibility and resistance to therapeutic agents, resulting in high rates of hospitalization and mortality [114-115]. Each variant can be further classified into several sublineages. For instance, Omicron has been identified to have many sublineages: BA.1, BA.2, BA.3, BA.4, BA.5 and others [116]. Below is information on SARS-CoV-2 variants of concerns.

1.4.1 Alpha variant

The Alpha variant (B.1.1.7) is one of the first mutated strains derived from the original SARS-CoV-2. It was initially identified in the United Kingdom in November 2020, and infections surged in December 2020 [117]. This VOC has acquired key mutations, including several S protein mutations located on RBD at N501Y, and specific deletions in N-terminal domain of S protein (NTD) at positions 69-70 and 144. Additionally, some non-S mutations were associated with this variant [118-119].

1.4.2 Beta variant

The Beta variant (B.1.351) was initially identified in South Africa at the end of 2020 and spread to other countries. This VOC has nine S protein mutations located on RBD with some key mutations at positions K417N, E484K, and N501Y, and specific deletions in NTD at positions 242-244 [120].

1.4.3 Gamma variant

The Gamma variant (P.1) was initially identified in Brazil in November 2020 [121]. Genetic sequencing of numerous virus samples from infected individuals revealed that the Gamma variant has accumulated over 22 mutations, including approximately 12 mutations in the S protein, without deletions. This variant has been associated with a significantly higher rate of hospitalization and morbidity, exceeding that of previously discovered variants by 3 to 4 times [122].

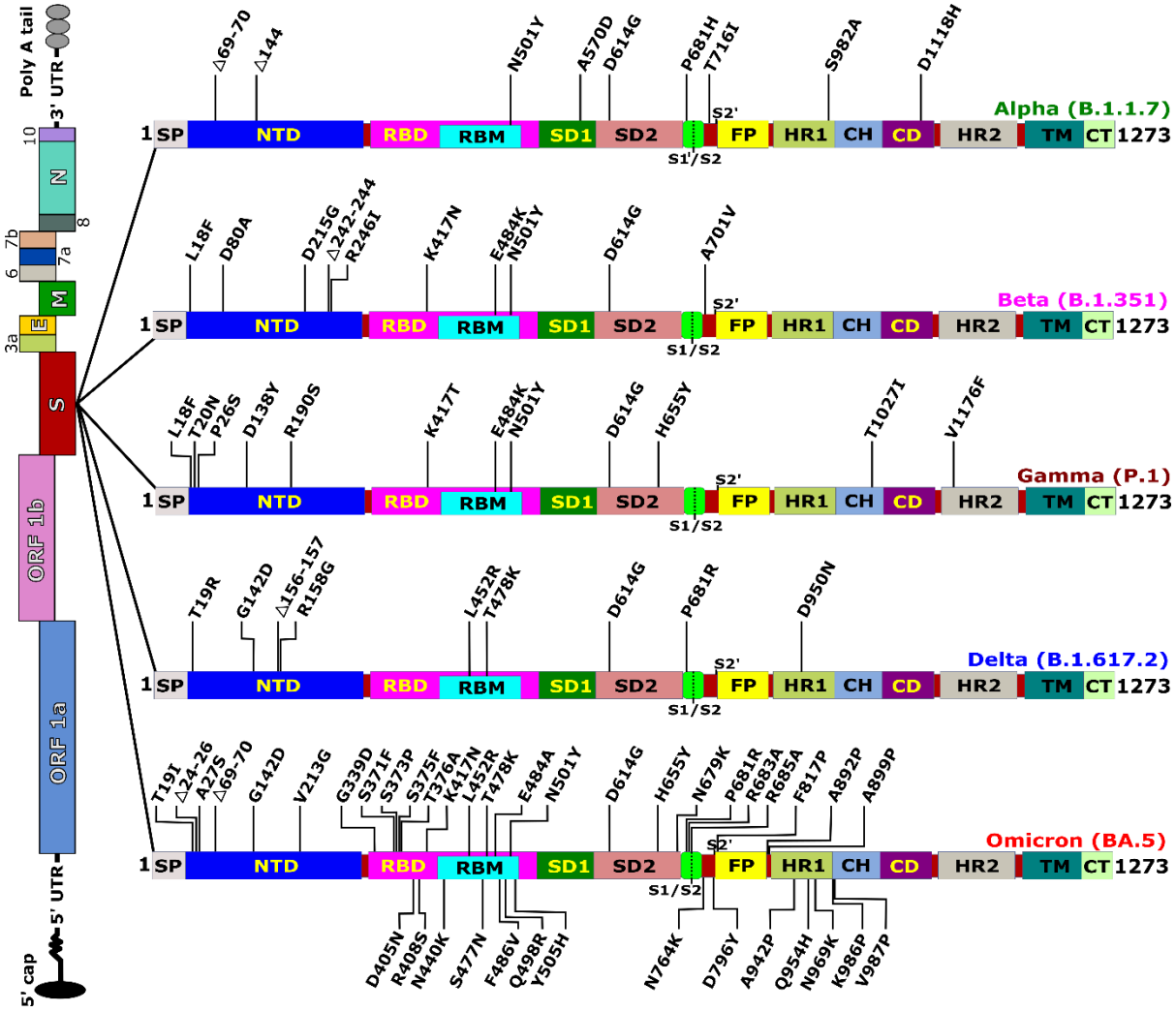

Figure 1.5: The key mutations and deletions on SARS-CoV-2 S protein of the five variants of concern: Alpha, Beta, Gamma, Delta, and Omicron (BA.5).

1.4.4 Delta variant

The Delta variant (B.1.617.2) was initially identified in India in late 2020 and rapidly became the dominant strain in many countries. It possesses 23 mutations, including approximately 9 mutations and deletions in the S protein. Key mutations of this variant include L452R and T478K mutations on RBD and P681R mutations on the cleavage site. This variant exhibits higher transmission and infection rates compared to other variants [123-124].

1.4.5 Omicron variant and its sublineages

The Omicron variant (B.1.1.529) was first identified in Botswana in southern Africa in late November 2021, and cases rapidly began to appear and spread in other countries. It was classified as a variant of concern due to several worrisome characteristics. This variant harbors an extensive number of mutations exceeding 50 points, many of which contribute to immune evasion and enhanced transmissibility. In particular, the S protein alone has accumulated at least 32 genetic changes, with no apparent connection to previous variants [125-

[127]. The emergence of the Omicron variant led to a rapid surge in the number of daily cases in the United States, exceeding one million cases. In 2022, it gave rise to several subvariants, including BA.5, BQ.1, BQ.1.1, and others [116, 128]. By 2023, new Omicron subvariants known as XBB.1.5, JN.1, and others had become the predominant cause of infection [129].

1.5 COVID-19 antiviral medicines

COVID-19 medication helps manage symptoms, prevents the virus from spreading in the body, and regulates the body's immune response. There are several antiviral drugs for COVID-19, such as nirmatrelvir-ritonavir (Paxlovid), remdesivir (Veklury), molnupiravir (Lagevrio), and others.

1.5.1 Nirmatrelvir-ritonavir (Paxlovid)

Nirmatrelvir is a protease inhibitor that treats COVID-19 by blocking a specific protease, the Mpro, which the virus needs to replicate and continue infecting. Ritonavir is also a protease inhibitor, and low-dose ritonavir is used to slow the breakdown of nirmatrelvir. This allows nirmatrelvir to remain in your body longer, enhancing its effectiveness against COVID-19. Nirmatrelvir-ritonavir is approved to treat mild to moderate COVID-19 in people aged 12 and older who are at increased risk of serious illness. Nirmatrelvir-ritonavir was first authorized for use in December 2021 and became fully food and drug administration (FDA) -approved for adults in May 2023 [15].

1.5.2 Remdesivir (Veklury)

Remdesivir is an RNA polymerase inhibitor that acts as a nucleotide analog against SARS-CoV-2. It blocks the activity of RdRp in SARS-CoV-2, which is required for the virus to replicate and grow. Specifically, remdesivir resembles one of the building blocks of RNA in SARS-CoV-2. When remdesivir is present, it can be incorporated into the virus’s RNA during replication, preventing the virus from spreading by using the incorrect building material. Remdesivir was first authorized for use in May 2020 for inpatient use. It became fully FDA-approved in October 2020 for people aged 12 and older. In January 2022, its use was expanded to outpatient treatment for all ages. In April 2022, it became fully approved for certain children aged 28 days and older [130].

1.5.3 Molnupiravir (Lagevrio)

Molnupiravir is a nucleoside analog that treats COVID-19 by targeting the RdRp in SARS-CoV-2. It disrupts the process the virus uses to replicate, preventing it from making additional copies and spreading the infection. Molnupiravir was first authorized by the FDA in December 2021 [131].

1.6 Antibodies and nanobodies: Pioneering in SARS-CoV-2 treatment

1.6.1 Therapeutic antibodies targeting SARS-CoV-2

Ab is a component of the immune system, produced and secreted primarily by differentiated B cells, which include plasma cells and memory B cells. Ab is structured as a pair of polypeptide chains that form a flexible Y-shape. The stem of the Y is composed of the ends of two identical heavy chains, while each arm consists of the remainder of the heavy chain and a smaller protein known as a light chain. In specific Ab classes, the stem and the lower portions of the arms exhibit significant similarity and are collectively referred to as the constant region. In contrast, the tips of the arms exhibit significant sequence diversity, allowing them to bind to a wide range of antigens [132-133]. In essence, each Ab comprises two fragments: one fragment is the antigen binding site (Fab), located at the end of each arm, allowing the immune system to recognize a diverse range of antigens, and the other fragment is the crystallizable region (Fc), formed by two heavy chains [134] (Figure 1.6A).

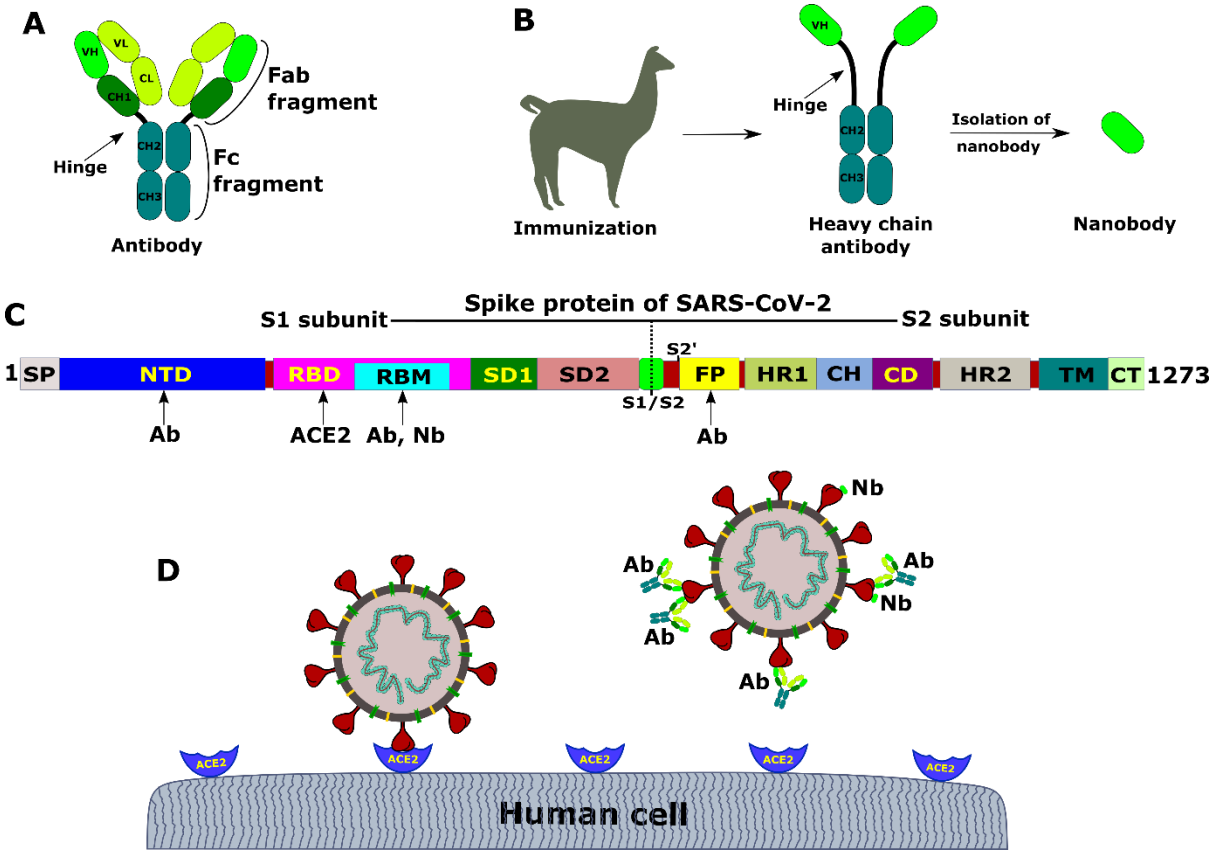

Figure 1.6: A) Ab structure contains antigen binding sites (Fab) and crystallization region fragments (Fc), which include VH (heavy chain variable domain), VL (light chain variable domain), CH (heavy chain constant region), and CL (light chain constant region). B) Nb isolated from the heavy chain of Ab that is extracted from the Camelidae members. C) The S protein structure; ACE2, Ab and Nb bind to RBD while Ab also binds to NTD and FP. D) SARS-CoV-2 binds to ACE2 to infect a human cell; Ab and Nb bind to the S protein to prevent SARS-CoV-2 from entering the human cell.

A monoclonal antibody (mAb) is a laboratory-produced protein designed to specifically bind to particular targets within the body, such as antigens present on the surface of cancer cells. It has been developed using hybridoma technology, recognized as the initial reliable source of Ab therapy [135-136]. The therapeutic and preventive potential of mAb against various conditions, including cancer, neurological disorders, and infectious viruses (such as HIV, Ebola, MERS-CoV, SARS-CoV, SARS-CoV-2, *etc*.) has already been well-established [137-140]. However, they can lead to certain side effects, mainly associated with immunomodulation and therapeutic Ab. These side effects may include phenomena such as Ab-dependent enhancement and cytokine storms, which could be linked to infection [141-143].

As mentioned in the preceding section, the S protein comprises two functional subunits: S1, responsible for the attachment to host cells, and S2, which facilitates the fusion of the virus with host cell membranes [144-145]. Although Ab targets both S1 (specifically RBD and NTD) and S2 (more specifically fusion peptide (FP)), it is noteworthy that most Ab is found to primarily target RBD [145-147] (Figure 1.6C). Note that Ab can bind to RBD in closed and open states, but SARS-CoV-2 cannot interact with host cell ACE2 when in the down state [106]. Therefore, Ab binding to the inactive RBD conformation is not relevant for further discussion.

Ab has proven to be a promising class of therapeutics against SARS-CoV-2 infection [148-152]. While convalescent plasma from recovered patients contains Ab generated by the adaptive immune response, its impact on improving survival rates remains a topic of ongoing debate [153-154]. Moreover, the large-scale production of plasma-based therapies poses substantial challenges, primarily due to high costs. Therefore, the search for potent Ab on an industrial scale is emerging as one of the most viable strategies to combat COVID-19. In particular, the combination of Ab with another (either Ab or a nanobody (Nb)) can enhance neutralizing activity, providing a more effective approach to SARS-CoV-2 therapy [155].

Numerous Abs targeting RBD, such as REGN-CoV (REGN10933 + REGN10987), S309, LY-CoV555, LY-CoV016, AZD7442 (AZD8895 + AZD1061), CT-P59, LYCoV1404, P2C-1F11, *et al*. have received emergency use authorization as therapeutic agents. These Abs have demonstrated potential for treating SARS-CoV-2, effective against the wild type and various variants, including Alpha, Beta, Gamma, Delta, Omicron, and others. For example, REGEN-CoV, a mAb cocktail composed of REGN10933 and REGN10987, effectively reduces viral load and the number of COVID-19 patients. REGN10933 binds to the top of RBD, while REGN10987 attaches to the side. The binding domain of REGN10933 significantly overlaps with the ACE2 binding site on RBD, whereas the binding region of REGN10987 has a slight overlap with the RBD-ACE2 interface. Consequently, when these Abs bind to the S protein, they occupy the RBD-ACE2 interaction interface, fully blocking ACE2-S interaction. These Abs have demonstrated *in vitro* activity against various variants of SARS-CoV-2. The Beta and Gamma variants are fully resistant to REGN10933 and weakly resistant to REGN10987 in neutralization, whereas the Alpha and Omicron variants are not resistant to the neutralizing activity of REGN-CoV. The combination of REGN10933 and REGN10987 demonstrates both prophylactic and therapeutic efficacy against SARS-CoV-2 variants, including Alpha, Beta, and Gamma, but not against Omicron. Although

REGN10987 shows reduced neutralizing ability against the Delta variant, REGN10933 alone and in combination with REGN10987 can still effectively block the S protein from entering host cells [156-158].

Various Abs targeting NTD have been identified, such as 4A8, FC05, DH1050.1, DH1052, and others. Some of these Abs can block SARS-CoV-2 infection, while others may unintentionally increase viral infectivity and are associated with severe cases of COVID-19. Although NTD-targeting Abs do not prevent the virus from binding to ACE2, they are of significant interest due to their potential to neutralize SARS-CoV-2. These Abs induce conformational changes in the S protein that hinder the transition of RBD from its "down" to "up" position, thereby reducing the virus's ability to infect cells, even without directly blocking ACE2 binding. This underscores the S protein as a critical focus for vaccine and drug development [159-161].

For Abs targeting FP, the S2 subunit is more conserved among coronaviruses compared to S1, resulting in greater cross-reactivity. However, Abs targeting S2 exhibits weaker neutralizing activity than those targeting S1. Abs COV91-27, COV44-62, VN01H1, C13B8, and others can neutralize wild type and multiple variants, including Alpha, Beta, Gamma, Delta, and Omicron (BA.2 and BA.4/5), though their neutralizing activity is limited compared to Abs targeting RBD and NTD. Abs targeting S2 offers insights into immune defenses and potential targets for vaccine development based on the conserved S2 subunit. S2-specific Abs may inhibit the conformational changes necessary for membrane fusion. FP is also considered a candidate epitope for next-generation coronavirus vaccines [162-164].

Numerous experimental studies have examined the binding of Abs to the S protein, but computational studies using molecular dynamics (MD) simulations remain limited. Nguyen *et al*. [165] recently employed MD simulations to estimate the binding affinities of Abs CR3022 and 4A8 to RBD and NTD, respectively. Their findings indicated that CR3022 has a stronger affinity for RBD compared to 4A8 for NTD, suggesting that CR3022 may be a more effective candidate for COVID-19 therapy. In a separate study, Gigon *et al*. [166] used a combination of constant-pH Monte Carlo simulations and the PROCEEDpKa method to map electrostatic epitopes for certain mAbs and ACE2 on RBDs of both SARS-CoV-1 and SARS-CoV-2. They proposed structural modifications to CR3022 that could enhance its binding affinity for SARS-CoV-2. Beshnova *et al*. [167] developed a computational method named SARS-AB for predicting the binding interactions between the S protein and mAbs. They validated this approach using existing structures from the protein data bank (PDB) and demonstrated its effectiveness in predicting Abs-S protein interactions. It was shown that SARS-AB can be used to design potent Abs against emerging SARS-CoV-2 variants that may evade current Ab protections. SARS-AB could greatly speed up the discovery of neutralizing Abs against SARS-CoV-2 and its variants. Although several studies have highlighted the role of Abs in treating SARS-CoV-2, a comprehensive understanding of how a combination of Abs can prevent SARS-CoV-2 infection is still required. An experimental study recently showed that combining REGN10933 Ab with REGN10987 Ab significantly enhances neutralizing capacity [156, 168]. However, the investigation of the exact mechanisms underlying

this synergistic effect still needs to be completed. This thesis filled this gap by testing the phenomenon using full-atom and coarse-grained MD simulations [169].

1.6.2 Therapeutic nanobodies targeting SARS-CoV-2

Nb is a recombinantly produced, antigen-specific, single-domain Ab segment derived from camelid heavy chain Ab. Nb is a relatively recent addition to recombinant Ab and is derived from animals such as camels, llamas, and alpacas [170-171] (Figure 1.6B). While Nb lacks a light chain, which can be seen as a disadvantage in terms of antigen binding, they possess intriguing properties. These properties include higher solubility, smaller size, greater resistance to denaturation under certain conditions, and increased thermal and chemical stability compared to conventional Ab. Nb can be administered directly into the respiratory tract, the most common site of SARS-CoV-2 infection, using an inhaler [172-173]. For example, camelid Nb composed solely of heavy chains, known as VHH, could provide a cost-effective and straightforward method for producing antiviral agents for passive immunization. Furthermore, Nb exhibits better tissue penetration and extravasation compared to classical Ab, enhancing its therapeutic potential [174]. Nb is classified as naïve or synthetic. Naïve Nb is extracted from camelids, including llamas, alpacas, camels, and dromedaries [175]. Synthetic Nbs are produced through various methods and are available in different libraries, such as the humanized synthetic Nb library and the display of synthetic Nb on the yeast surface [176-177].

Nb therapy has emerged as a promising approach for treating COVID-19 [173]. Nb targets RBD, disrupting the interaction between the S protein and ACE2, and thus inhibiting the virus's entry into host cells [178-180] (Figure 1.6D). Nb exhibits a high-affinity neutralization of SARS-CoV-2, making RBD an attractive target for vaccine development [181]. Although synthetic Nb shows a high affinity for the prefusion S glycoprotein and exhibits strong neutralizing activities [182], it has certain limitations that can hinder its ability to meet therapeutic requirements. Nb can bind to two RBD domains: one with a binding epitope that overlaps with ACE2 binding region and another with a non-overlapping binding epitope that does not intersect with ACE2 binding region. Like Abs, Nbs also targets both open and closed RBDs. Additionally, Nb provides a rapid avenue for exploiting avidity, thus enhancing affinity and efficacy in the treatment of COVID-19 [183-184]. Given that SARS-CoV-2 is prone to rapid mutations that can evade most potential Abs, Nb stands out as a promising candidate to address dangerous variants, such as Alpha, Beta, Gamma, Delta, and others [185-187]. When combined with Nb or Ab, Nb can significantly enhance neutralizing activity, offering a more effective approach to the treatment of SARS-CoV-2 [176].

Many Nbs have been identified, but only a few, such as HH1-H4, H11-D4, and Ty1 have demonstrated significant potential for COVID-19 treatment. These Nbs target RBD and disrupt its interaction with ACE2. Through experimental studies, Huo *et al*. [176] disclosed that Nbs H11-D4 and H11-H4, bind to RBD with high affinity, preventing the S protein from attaching to ACE2. In another study, Hanke *et al*.[188] found Ty1, RBD-specific Nb that effectively neutralizes SARS-CoV-2. Ty1 offers several practical advantages, including high-yield bacterial production, low cost, and scalability. Ty1 blocks the binding of RBD to ACE2 through steric exclusion by overlapping with the ACE2 binding site, while H11-H4 and H11-

D4 attach to different regions of RBD and do not overlap with the ACE2 site. Using MD simulation, Golcuk *et al.* [189] showed that H11-H4 can displace ACE2 from RBD due to repulsive electrostatic interactions, as both H11-H4 and ACE2 have similarly charged residues in close proximity when bound to RBD. H11-D4 also inhibits ACE2 binding, although to a lesser extent. Thus, H11-H4 and Ty1 disrupt ACE2 binding through different mechanisms, while H11-D4 is the least effective inhibitor among them. For SARS-CoV-2 variants, the ability of H11-H4 to disrupt ACE2 binding was diminished by the N501Y/E484K/K417N mutations in the Beta variant RBD, while H11-D4 was much less effective in preventing ACE2 binding to RBD with these triple mutations. In contrast, Ty1 binds to the Beta variant with twice the strength of ACE2, allowing it to neutralize this variant by sterically blocking ACE2 binding. For the Delta variant, the L452R mutation at H11-H4, H11-D4, and Ty1 binding interface may not affect their binding affinity [188, 190-191]. While the impact of H11-H4 on RBD has been observed, theoretical studies have yet to explore the combination of H11-H4 with CR3022 Ab for treating SARS-CoV-2. To address this, we hypothesized that combining H11-H4 with CR3022 Ab could enhance the neutralizing ability against SARS-CoV-2, potentially leading to a new treatment for COVID-19. This hypothesis was validated through all-atom and coarse-grained MD simulations [192].

1.7 Impact of SARS-CoV-2 on protein synthesis process

Upon entering host cells, ORF1a and ORF1b undergo translation and subsequent proteolytic processing mediated by virus-encoded proteinases. This process yields a functional NSP, which plays a pivotal role in viral infection and replication of the RNA genome [193]. NSP encompasses numerous indispensable enzymes involved in RNA processing and viral replication [194-195].

40S ribosome is responsible for mediating the interaction between mRNA codons and transfer RNA anti-codons, which facilitate the transfer of amino acids to form polypeptides [196]. In the absence of NSP1, mRNA translation proceeds normally, leading to protein synthesis. In the presence of NSP1, it binds to the mRNA entry channel, folds into two helices, and interacts with the 18S ribosomal RNA (rRNA) at h18 as well as with the 40S ribosomal protein (rprotein) uS3 in the head and uS5 and eS30 in the body, where SARS-CoV-2 NSP1 would partially overlap with fully accommodated mRNA [197]. Here, only the C-terminal domain binds to the 40S subunit of the human ribosome, leading to inhibition of mRNA translation [54] (Figure 1.7). Although this finding provides valuable information on the role of SARS-CoV-2 in invading and subverting human cells, the precise impact of binding of NSP1 to the 40S ribosome on mRNA translation remains unclear.

Some studies reported that several mutations in NSP1 can alter its structural and functional characteristics concerning SARS-CoV-2. The double mutation K164A/H165A within the C-terminal domain eliminates its ability to bind to the 40S ribosome [198-199]. Mutations such as Y154A/F157A and R171E/R175E also result in the loss of ribosome binding capability. In the linker domain, mutations R124A/K124A impair mRNA endonucleolytic cleavage guided by NSP1. The R99A mutation, located in the N-terminal domain, not only abolishes NSP1 evasion but also hinders NSP1-guided mRNA cleavage [55].

Even a minor deletion of essential amino acids within NSP1 is sufficient to nullify its evasion function [200-201]. In addition, some drugs targeting NSP1 were found and have shown promise as potential candidates for antiviral therapy against SARS-CoV-2. For example, montelukast sodium hydrate, an FDA-approved drug, binds to the C-terminal of NSP1, reducing its inhibitory effect on host protein synthesis [202-203].

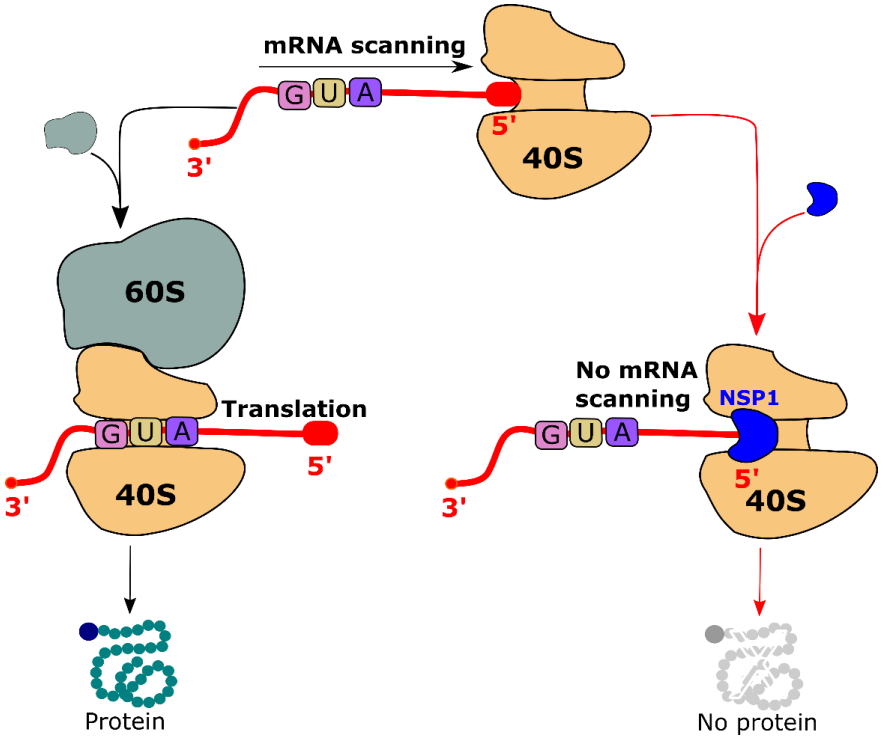

Figure 1.7: A schematic depicting (left) an mRNA translation process occurring in normal human ribosomes to synthesize protein, and (right) NSP1 action to suppress mRNA translation.

Recently, Borišek *et al.* [197] used MD simulation to investigate the interaction of SARS-CoV-2 NSP1 and SARS-CoV NSP1 with the 40S subunit of the ribosome. They found that binding of SARS-CoV-2 NSP1 and SARS-CoV NSP1 to the 40S subunit causes a critical switch in the residues Gln158/Glu158 and Glu159/Gln159. This switch remodels the pattern of interaction between NSP1 and neighboring rproteins (uS3 and uS5), as well as rRNA (h18) that surrounds the mRNA entry tunnel. This finding provides a clear picture of how SARS-CoV-2 invades human cells. However, the effect of SARS-CoV-2 NSP1 binding to the 40S ribosome on mRNA translation has not been theoretically studied, which prompted us to investigate this issue [204]. We hypothesized that NSP1 binding increases the binding affinity of mRNA to its entry channel, leading to the arrest of its translation and hence protein synthesis. This hypothesis was confirmed by our all-atom and coarse-grained MD simulations [204].

Chapter 2: Computational methods

2.1 A general introduction to molecular dynamics simulation

Computer simulations serve as a bridge between microscopic length and time scales and the macroscopic world. Currently, two primary families of simulation techniques are prevalent: MD and Monte Carlo simulations. MD simulations play a crucial role as a tool for studying biomolecules and biomaterials. In the following sections, we characterize the classical MD simulation by describing its two main components: (1) Numerical schemes for integrating equations of motion are used to obtain the classical trajectories of the studied system in phase space, and (2) force fields are simplified energy expressions that enable the rapid evaluation of forces acting within the system during the simulation.

2.1.1 Dynamics of a molecular system

MD simulation is a computational method for studying molecular systems using computers. In MD simulation, trajectories of atoms are obtained using the Langevin equation along with numerical methods to simulate mainly many body systems. These simulations are of particular interest to chemists and biologists [205].

The stochastic differential Langevin equation is similar to Newton's equation, but the fiction and noise terms are added as follows.

$$m\frac{d^2\vec{r}}{dt^2} = \overrightarrow{F_c} - \gamma\frac{d\vec{r}}{dt} + \vec{\Gamma} \equiv \vec{F} \tag{1}$$

m is mass of atom, γ is the friction coefficient, and $\overrightarrow{F_c} = \nabla V$, here V is potential of a biomolecular system. Random force $\vec{\Gamma}$ related to random interactions between atoms of the system and environment is noise, which is described as below.

$$\langle \Gamma(t) \rangle = 0$$

$$\langle \Gamma(t)\Gamma(t') \rangle = 2\gamma k_B T\delta(t - t') \tag{2}$$

where k_B is a Boltzmann's constant, T is absolute temperature, and $\delta(t - t')$ is the Dirac delta function.

The motion Eq. (1) can be solved by using the leap-frog algorithm, or the original Verlet, or the velocity Verlet algorithms [206-208]. During MD simulation, the length of all bonds associated with hydrogen atoms can be constrained by the SHAKE or the LINCS (or P-LINCS) algorithms [209-211]. The temperature is maintained through the Langevin thermostat [212] with a collision frequency (often 2 ps^{-1}). A cutoff point is chosen to calculate van der Walls (vdW) and electrostatic interactions, in which the particle mesh Ewald method is applied for electrostatic interaction [213]. The simulation box is chosen large enough to avoid interaction with the periodic images, and size effects are minimized by applying periodic boundary conditions. Counterions are added to neutralize the system.

2.1.2 Force fields for all-atom and coarse-grained models

In this thesis, both all-atom and coarse-grained models are utilized to explore the kinetics and thermodynamics of biomolecular systems.

a) All-atom model: The all-atom model is used to investigate the structures and properties of biomolecules at the atomistic level (Figure 2.1A). This approach allows for direct exploration of time scales ranging from tens to thousands of nanoseconds and length scales of up to tens of nanometers. In all-atom MD simulations, interactions between particles are calculated using an energy function known as a force field, which encompasses bonded and non-bonded interactions [214]. Some force fields commonly used in all-atom MD simulations of biomolecules include OPLS, AMBER, CHARMM, and GROMOS [215]. The general form of the force field for MD simulation is as follows [211, 216].

$$V = \sum_{bonds} k_b(r - r_0)^2 + \sum_{angles} k_\theta(\theta - \theta_0)^2 + \sum_{n=1,dihedrals}^{3} k_n[1 + cos(n\omega - \gamma_n)] + \sum_{i,j}\left[\left(\frac{A_{ij}}{r_{ij}^{12}}\right) - \left(\frac{B_{ij}}{r_{ij}^{6}}\right)\right] + \sum_{i,j}\frac{q_i q_j}{4\pi\varepsilon_0 r_{ij}} \quad (3)$$

Here the first two terms of the Eq. (3) describe the bonded potential between two and three particles, which are modeled using harmonic functions with force constants k_b, k_θ and equilibrium values of r_0, θ_0, respectively. The third term represents the dihedral potential between four points, where k_n is the dihedral force constant, n is dihedral periodicity and γ_n is a phase of the dihedral angle. The last two terms describe the non-bonded potentials, including the vdW interaction represented by the 6-12 Lennard-Jones (LJ) function and the electrostatic interactions modeled by Coulombic interactions. The choice of different parameters in Eq. (3) depends on the force fields developed by different groups.

b) Coarse-grained models: Coarse-grained models have been developed to address certain challenges of larger biomolecular systems. They consolidate multiple atoms into a single interaction center, which not only saves computational time and resources but also often produces results that agree well with all-atom MD simulations and experimental data [217]. Several common models, such as multiscale [218-219], C_α-based [220-221], Martini [219, 222-223], UNRES coarse-graining [224-225], and others are widely employed to investigate the dynamical properties of biomolecular systems.

- *C_α coarse-grained model:* In this model, each residue is presented by one interaction site centered on the C_α atom (Figure 2.1B). There are many coarse-grained models, but in this dissertation, we used a Go-like model in which the potential energy for a given configuration is given by the following expression [220-221].

$$
\begin{aligned}
V = & \sum_i k_b\,(r_i - r_0)^2 \\
& + \sum_i -\frac{1}{\gamma} ln\left\{exp[-\gamma(k_\alpha(\theta_i - \theta_\alpha)^2 + \varepsilon_\alpha)] + exp\left[-\gamma k_\beta\left(\theta_i - \theta_\beta\right)^2\right]\right\} \\
& + \sum_i \sum_j^4 k_{D_j}\left(1 + cos\left[j\varphi_i - \delta_j\right]\right) + \sum_{ij} \frac{q_i q_j e^2}{4\pi\varepsilon_0\varepsilon_r r_{ij}} exp\left[-\frac{r_{ij}}{l_D}\right] \\
& + \sum_{ij\in\{NC\}} \epsilon_{ij}^{NC}\left[13\left(\frac{\sigma_{ij}}{r_{ij}}\right)^{12} - 18\left(\frac{\sigma_{ij}}{r_{ij}}\right)^{10} + 4\left(\frac{\sigma_{ij}}{r_{ij}}\right)^{6}\right] \\
& + \sum_{ij\notin\{NC\}} \epsilon_{ij}^{NN}\left[13\left(\frac{\sigma_{ij}}{r_{ij}}\right)^{12} - 18\left(\frac{\sigma_{ij}}{r_{ij}}\right)^{10} + 4\left(\frac{\sigma_{ij}}{r_{ij}}\right)^{6}\right]
\end{aligned} \tag{4}
$$

These terms correspond to the energy contributions of C_α - C_α bonds, bond angles, dihedral angles, electrostatic interactions, and LJ like attractive and repulsive interactions for both native and non-native contacts. Specifically, the bond potential between two adjacent interaction sites is described by a harmonic potential with a bond force constant k_b, an equilibrium bond length r_0, and a pseudo bond length r_i for the i^{th} bond. The angle potential is modeled by a double-well potential, which describes the bond angle associated with bond α-helix and β-sheet conformations [226]. The constants of the double-well angle potential include γ, k_α, θ_α, ε_α, k_β, and θ_β. The k_{Dj} and δ_j are the dihedral force constant and the phase at periodicity j, respectively. The φ_i is the i^{th} pseudo dihedral angle. Electrostatics are treated using the Debye-Hückel theory with a Debye length l_D and a dielectric constant of 78.5. Lysine and arginine C_α sites are assigned q = +e, glutamic acid and aspartic acid are assigned q = -e, and all other interaction sites are uncharged [227]. The contribution from native interactions is computed using the 12-10-6 potential of Karanicolas and Brooks [228], with the depth of the energy minimum for a native contact $\epsilon_{ij}^{NC} = n_{ij}\epsilon_{HB} + \eta\epsilon_{ij}$, where ϵ_{HB} and ϵ_{ij} represent energic contributions arising from hydrogen bonding and vdW contacts between residues i and j identified from the crystal structure of the protein, respectively. n_{ij} is the number of hydrogen bonds formed between residues i and j. The value of ϵ_{ij} is set based on the Betancourt-Thirumalai pairwise potential [229], while the scaling factor η is determined for each protein based on a previously published training set to reproduce realistic protein stabilities for different structural classes. In this work, the values of η for intra-protein interactions in Abs (REGN10933 and REGN10987) and RBD domain (Table 2.1), were obtained using a procedure described in a previously published training set [230]. Collision diameters σ_{ij} between C_α interaction sites involved in native contacts are set equal to the distance between the C_α of the corresponding residues in the crystal structure divided by $2^{\frac{1}{6}}$. For non-native interactions, ϵ_{ij}^{NN}, and σ_{ij} are set to the average of the radii of the residues involved [228]. NC and NN stand for native contact and non-native contact, respectively [220].

Table 2.1: The η values determined for the stability of protein domains and interfaces, as well as for interactions between Abs and RBD in C_α coarse-grained simulations.

	REGN10933	**REGN10987**	**RBD**	**REGN10933-RBD**	**REGN10987-RBD**
η	Chain L: 2.480 Chain H: 2.480 Interface: 2.124	Chain L: 2.480 Chain H: 2.480 Interface: 2.124	1.916	1.9	1.9

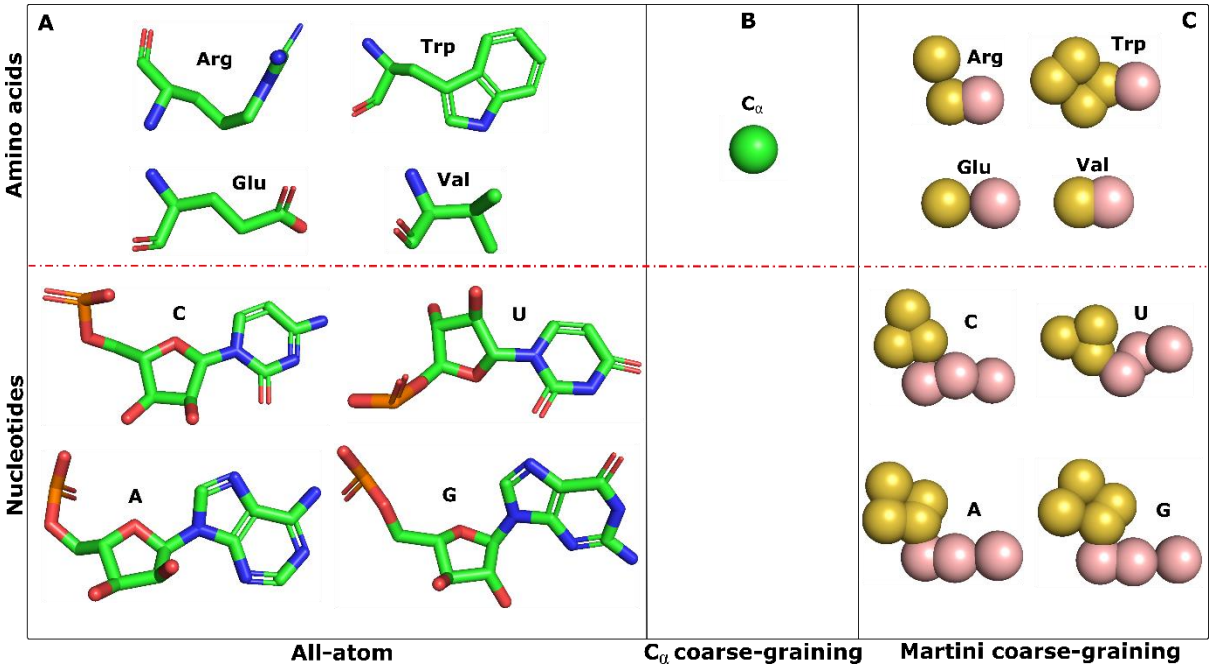

Figure 2.1: 3D structures of several amino acids (Trp, Arg, Glu, and Val) and nucleotides (C, U, A, and G). A) All-atom model with N atoms in blue, O atoms in red, C atoms in green, and P atoms in orange; B) C_α coarse-grained model for only amino acids, highlighting the C_α atom in green; and C) Martini coarse-grained model with backbone beads in light pink and side chain beads in wheat. The number of side chain beads varies depending on the type of amino acid and nucleotide.

- *Martini coarse-grained model:* The Martini model uses a four-to-one mapping, where, on average, four heavy atoms are represented by a single interaction center, except in the case of ring-like molecules. The general four-to-one mapping rule is insufficient for capturing the geometric specificity of small ring-like fragments or molecules. Therefore, ring-like molecules are mapped with a higher resolution. The model accounts for four primary types of interaction sites: polar (P), nonpolar (N), apolar (C), and charged (Q). Subtypes within a primary type are differentiated either by a letter indicating hydrogen-bonding capabilities or by a number representing the level of polarity [231-232].

In the coarse-grained model for proteins, most amino acids are mapped to specific bead types. Apolar amino acids (Leu, Pro, Ile, Val, Cys, and Met) are represented by C-type

beads, while polar uncharged amino acids (Thr, Ser, Asn, and Gln) are mapped to P-type beads. Amino acids with small negatively charged side chains, such as Glu and Asp, are modeled as Q-type beads. Positively charged amino acids, Arg and Lys, are represented by a combination of a Q-type bead and an uncharged bead. Larger, ring-based side chains (His, Phe, and Tyr) are depicted using three ring-class beads, and Trp is represented by four. Gly and Ala residues are only represented by the backbone bead. The type of backbone varies depending on the secondary structure of the protein: in solution, or in a coil or bend, the backbone is strongly polar (P-type), whereas in a helix or β-strand, the inter-backbone hydrogen bonds greatly reduce its polarity (N-type) (Figure 2.1C) [231].

Concerning the coarse-grained model for RNA, the RNA parameters were developed following the Martini parameterization strategy, which integrates top-down and bottom-up approaches [232]. Each nucleotide is represented by six or seven coarse-grained beads. The backbone is modeled using three beads, with the phosphate mapped to one bead and the sugar mapped to two beads. The pyrimidines (cytosine and uracil) are represented as three-bead rings, and the purines (adenine and guanine) as four-bead rings. For each nucleotide, the beads are divided into backbone beads (BB1, BB2, and BB3) and side chain beads (SC1, SC2, SC3, and SC4 for the purines). The first backbone bead (BB1) is the phosphate, and the last one (BB3) is the 3′ end of the sugar. For the side chains, the beads are defined in cyclical order so that SC1 is attached to the backbone, and in dsRNA, the SC2 and SC3 beads would be base pairs with the opposing strand (Figure 2.1C) [232-233].

The energy of the Martini model is given by the following formula [219, 222-223].

$$V = \frac{1}{2}\sum_{ij} k_b\left(r_{ij} - r_b\right)^2 + \frac{1}{2}\sum_{ijk} k_a\left(\cos\left(\theta_{ijk}\right) - \cos\left(\theta_a\right)\right)^2 + \sum_{ijkl} k_d\left[1 + cos\left(n\varphi_{ijkl} - \varphi_d\right)\right] + \sum_{ijkl} k_{id}\left(\varphi_{ijkl} - \varphi_{id}\right)^2 + \sum_{ij} 4\varepsilon_{ij}\left[\left(\frac{\sigma_{ij}}{r_{ij}}\right)^{12} - \left(\frac{\sigma_{ij}}{r_{ij}}\right)^{6}\right] + \sum_{ij} \frac{q_i q_j}{4\pi\varepsilon_0\varepsilon_r r_{ij}} \quad (5)$$

It includes the two-body harmonic, three-body angular, and four-body dihedral angle potentials. The non-bonded interactions in the Martini force field are based on the shifted and truncated 12-6 LJ and Coulomb potentials. For bonded interactions, the forces act between bonded sites i, j, k, l with equilibrium distance r_b, angle θ_a, and dihedral angles φ_d and φ_{id}. The force constants k_b, k_a, k_d and k_{id} are generally weak, including molecular flexibility at the coarse-grained level as a result of collective motions at the fine-grained level. The bonded potential is used for chemically bonded sites, and the angle potential represents the stiffness of the chain. Proper dihedral angle potential is currently used only to impose the secondary structure of the peptide backbone, while improper dihedral angle potential is used to prevent out-of-plane distortions of planar groups. For non-bonded interactions, the strength of LJ interactions of all particle pairs i and j at distance r_{ij} determines by the well-depth ε_{ij}, depending on the interacting particle types. The effective size of the particles is governed by the LJ parameter σ_{ij}. In addition to the LJ interaction, charged groups (type Q) bearing a

charge q_i and q_j interact via a Coulombic energy function with a relative dielectric constant ε_r for explicit screening [223, 231-232].

The Martini model enables long simulations of large systems by reducing the number of degrees of freedom compared to all-atom models. However, one limitation of the Martini model is its use of an elastic network model for keeping the tertiary structure of protein/RNA, which is incapable of folding protein/RNA, which may introduce artificial stiffness that could affect free energy calculations. This issue requires further study, but despite this limitation, the free energy estimates obtained with the coarse-grained Martini model generally agree well with experimental results [234-235].

2.2 Experimental and computational methods for estimation of binding affinity

The determination of binding affinity in biomolecular systems is of great interest, primarily because it can be used to characterize the stability of biomolecular complexes [236]. Currently, several experimental methods have been developed to investigate the binding affinity of two interacting molecules, including atomic force microscopy (AFM) [237], surface plasmon resonance (SPR) [238], biolayer interferometry (BLI) [239], fluorescence flow cytometry (FFC) [240], dynamic force spectroscopy (DFS) [241], *et al*. In parallel, various computational methods have been developed to evaluate the binding affinity, such as thermodynamic integration (TI) [242], free energy perturbation (FEP) [243], molecular mechanics with Poisson-Boltzmann or generalized born and surface area (MM-PBSA and MM-GBSA) [244], linear interaction energy (LIE) [245], steered molecular dynamics (SMD) [246], umbrella sampling (US) [247], and others.

2.2.1 Experimental methods for estimating binding affinity

a) AFM: AFM is extensively utilized to study the structure and function of biomolecules and their interactions in response to external forces. AFM is particularly effective for examining the binding properties of protein-ligand and protein-protein complexes, as the mechanical force required for their dissociation is approximately 100 pN. When an external force is applied to the target protein through the cantilever, the force experienced by the protein is calculated as kδx, where k represents the stiffness of the cantilever, and δx is the bending of the cantilever detected by the laser. The stability of the complex is characterized by the rupture force (F_{max}), observed in the force-extension/time profile obtained with a constant pulling speed. A higher F_{max} indicates greater binding affinity [237].

b) Other experimental methods: Several experimental techniques, such as SPR [238], BLI [239], FFC [240], and DFS [241], have been employed to examine the stability of protein-protein complexes. These methods are used to determine dissociation constant (K_D), where a lower K_D indicates a higher binding affinity and greater stability of the complex. Both SPR and BLI methods are commonly used to estimate the K_D.

- *SPR*: SPR is an optical technique used to measure molecular interactions in real-time. It occurs when plane-polarized light hits a metal film under conditions of total internal reflection. The SPR signal depends directly on the refractive index of the medium on the

sensor chip. The binding of biomolecules alters the refractive index on the sensor surface. In an SPR experiment, one molecule (protein or ligand) is immobilized on a sensor chip, and binding to a second molecule (analyte) is measured under flow conditions. The response is measured in resonance units and is proportional to the mass on the surface; for any given interactant, the response is proportional to the number of molecules bound to the surface. This response is recorded and displayed as a sensorgram in real-time. SPR experiments can be used to measure kinetic binding constants [238].

- *BLI*: BLI is an optical method used to measure macromolecular interactions by examining the interference patterns of white light reflected from the surface of a biosensor tip. BLI experiments are used to determine the kinetics and affinity of molecular interactions. In a BLI experiment, one molecule is immobilized on a dip and read biosensor, and binding to a second molecule is measured. A change in the number of molecules bound to the end of the biosensor tip causes a shift in the interference pattern, which is measured in real-time [239].

2.2.2 Computational methods for estimating binding affinity

a) SMD simulation: SMD [246] was designed to capture single-molecule force spectroscopy experiments, including AFM [248], laser optical tweezers [249], and magnetic tweezers [250]. In SMD simulations, an external force is applied to a dummy moving with constant speed v in the pulling direction (Figure 2.2). This dummy atom is connected with the pulled atom of the studied system through a spring with a spring constant k. If we define Δz as the displacement of the pulled atoms from its initial position, then the external force experienced by the system F is.

$$F = k(\Delta z - vt) \tag{6}$$

A typical force-displacement or force-time profile has the $F_{\max}$ (Figure 2.2), which can be used to characterize the mechanical stability of the biomolecular complex. It has been shown [251] that the non-equilibrium work (W) performed by an extended chain characterizes the mechanical stability better than $F_{\max}$. Using the force-displacement profile obtained from the SMD simulations, W is estimated using the trapezoidal rule.

$$W = \int F dz = \sum_{i=1}^{N} \frac{F_{i+1}+F_i}{2}(z_{i+1} - z_i) \tag{7}$$

where N is the number of simulation steps, F_i and z_i are the force experienced by the target and position at step i, respectively.

To estimate the non-equilibrium binding free energy (ΔG), we can use Jarzynski's equality [252] extended to the case of when the applied external force grows at a constant speed v [253].

$$exp\left(\frac{-\Delta G}{k_B T}\right) = \left\langle exp\left(\frac{W_t - \frac{1}{2}k(z_t - vt)^2}{k_B T}\right)\right\rangle_N \tag{8}$$

here $\langle ... \rangle_N$ is the average over N trajectories, z_t is the time-dependent displacement, and W_t is the non-equilibrium work at time t determined by the Eq. (7).

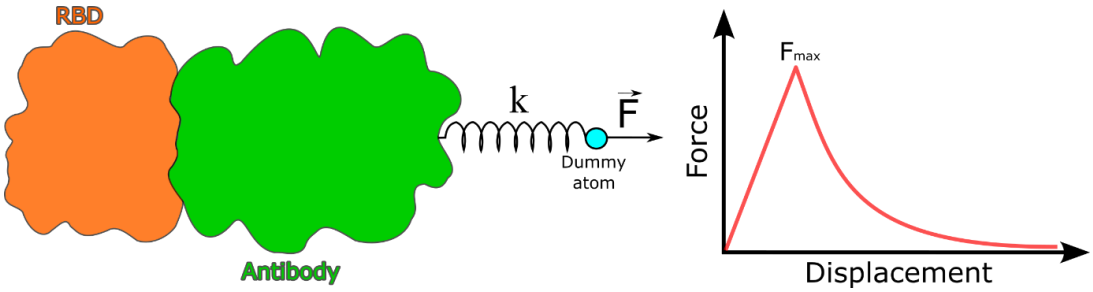

Figure 2.2: (Left) Schematic of SMD simulations of pulling Ab from RBD. (Right) Force-displacement profile from SMD simulations.

From the Eq. (8), we can extract the equilibrium free energy provided that the number of SMD trajectories is sufficiently large and the pulling is conducted at a slow enough rate. This approach proves to be feasible for small systems [254] but not for larger ones. Nevertheless, we can estimate the non-equilibrium binding and unbinding barriers that delineate the transition state (TS) from the bound state at $t = 0$ and the unbound state at t_{end} [255]. This estimation enables us to distinguish between weak binding and strong binding.

b) US simulation: US is a technique employed to compute the potential of mean force along a predefined reaction coordinate ξ. The primary objective of the US is to surmount the limitations commonly encountered in conventional MD simulations, which are often constrained by limited simulation time and face challenges in exploring infrequent events due to elevated energy barriers. The US method involves the introduction of a harmonic biasing potential that generates a series of configurations along the reaction coordinate. Some of these configurations serve as initial states for different US windows, each executed through independent simulations (Figure 2.3). In this work, we utilized coarse-grained US simulations to estimate the binding affinities of biomolecular systems.

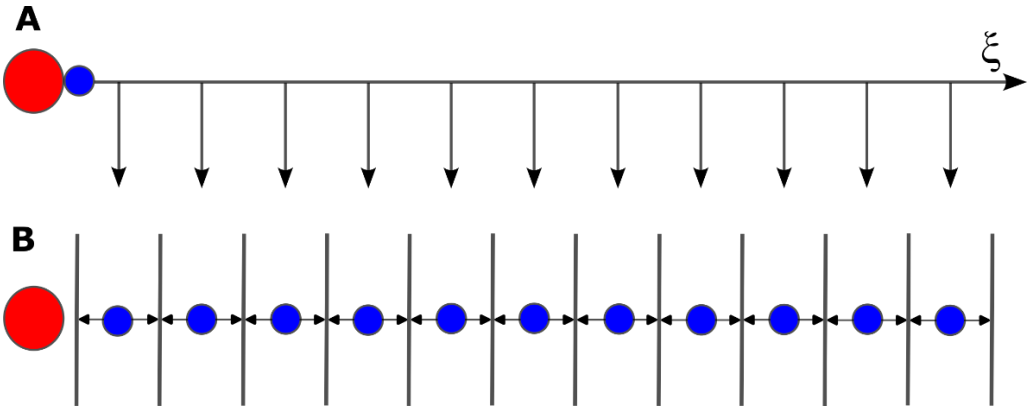

Figure 2.3: Schematic of US simulations to calculate the potential of mean force along the reaction coordinate. The first molecule (red) is kept fixed. A) The reaction coordinate is divided into small regions, and B) each region is sampled independently. To keep the second molecule (blue) to move within a spatial window, a harmonic potential is applied.

Subsequently, the weighted histogram analysis method procedure [256] is used to obtain the one-dimensional potential of mean force (1D-PMF) as a function of the reaction coordinate. Standard error calculations and auto-correlations in the sampled time series are also taken into account.

- *Estimation of K_D value from US simulations:* K_D is calculated as [165, 257].

$$K_D = \frac{P_u}{P_b}[A] \tag{9}$$

$[A]$ represents the concentration of the free cofactor, in unbound state. It is defined as.

$$[A] = \frac{P_u}{V(r^*)}C_0 \tag{10}$$

where C_0 = 1660 is standard concentration used to normalize $[A]$ to the units of molarity, $V(r^*) = (4/3)\pi {r^*}^3$ is the simulation volume in which we found free monomers in the unbound state. P_u is the probability of the system being in the unbound state, $P_u = 1 - P_b$. The bound state probability P_b is calculated from numerical integration of the 1D-PMF profile as.

$$P_b = \frac{\int_0^{r_b} 4\pi r^2 e^{-\beta G_{1D}(r)} dr}{\int_0^{r^*} 4\pi r^2 e^{-\beta G_{1D}(r)} dr} \tag{11}$$

here $G_{1D}(r)$ is the 1D-PMF, r_b is the distance threshold separating bound and unbound states, $\beta = 1/k_B\,T$, and r^* is the maximum distance between unbound cofactors found during the simulation process.

- *Estimation of binding free energy (ΔG_{bind}) from US simulations:* ΔG_{bind} is defined as the difference between the free energies in the bound and unbound states [258].

$$\Delta G_{bind} = \left(-k_B T ln \int^{bound} e^{\frac{-G_{1D}(r)}{k_B T}}\right) - \left(-k_B T ln \int^{unbound} e^{\frac{-G_{1D}(r)}{k_B T}}\right) \tag{12}$$

here $G_{1D}(r)$ is the 1D-PMF as a function of r, k_B is the Boltzmann constant, and T is the absolute temperature. The symbols $\int^{bound}$ and $\int^{unbound}$ refer to summation over the bound and unbound regions, respectively.

c) Alchemical free energy calculations: Alchemical free energy calculations represent typical approaches that operate at the highest level of theoretical rigor and are also feasible with current computational capabilities. The alchemical method, known as the TI or FEP, relies on a derived nonphysical thermodynamic cycle. This cycle involves the calculation of the binding free energy as the sum of multiple steps during which the ligand/protein/DNA/RNA is "inserted" or "removed" from different environments, such as transitioning from the bound to the unbound state or vice versa [259-260].

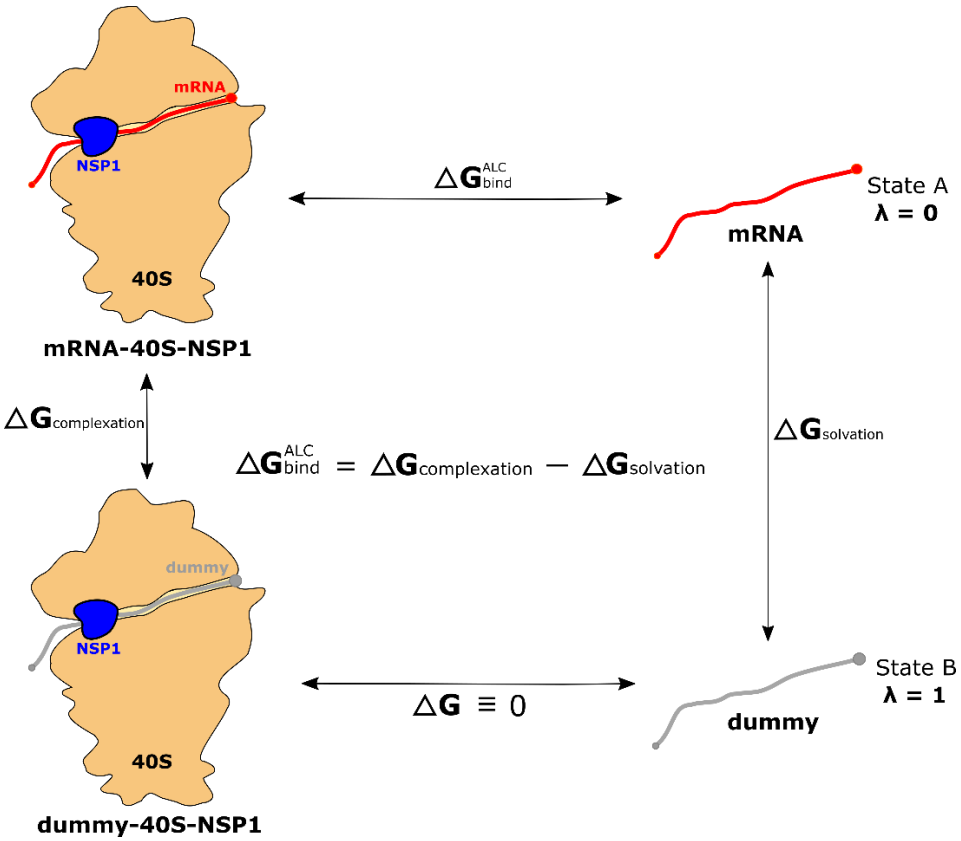

Figure 2.4: Thermodynamic cycle to calculate the binding free energy of mRNA to 40S-NSP1. State A (λ = 0) describes the full interaction between mRNA and 40S-NSP1, while state B (λ = 1) presents mRNA (dummy) without interaction with 40S-NSP1. Alchemical simulations are used in the Martini coarse-grained model.

The utilization of alchemical simulations has streamlined the process of conducting free energy calculations, making them more accessible than manually setting them up within MD simulations. Furthermore, this approach has demonstrated success in determining free energy differences in various scenarios: (1) Estimating the partition of a compound between different environments; (2) Assessing binding affinities of various biomolecular complexes (protein-ligand, protein-protein, protein-DNA/RNA) while modifying or mutating the protein or DNA/RNA; (3) Investigating how one or more mutations at the interface impact the binding of protein-protein or protein-DNA/RNA interactions [261]. In summary, alchemical methods allow for the computation of free energy differences, either in terms of relative free energies of binding or absolute free energies of binding [262].

In this thesis, to evaluate the free energy associated with the binding of mRNA to the 40S ribosome both with and without NSP1, we formulate the thermodynamic cycle illustrated in Figure 2.4. Through this thermodynamic cycle, we can obtain the binding free energy $\Delta G_{\text{bind}}^{\text{ALC}}$ (the superscript ALC refers to alchemical simulation).

$$\Delta G_{\text{bind}}^{\text{ALC}} - \Delta G = \Delta G_{\text{complexation}} - \Delta G_{\text{solvation}} \quad (13)$$

where $\Delta G \equiv 0$ as is related to non-interacting (λ=1) mRNA being dummy and dummy-40S-NSP1. Then, the binding free energy has the following form.

$$\Delta G_{bind}^{ALC} = \Delta G_{complexation} - \Delta G_{solvation} \quad (14)$$

For alchemical transformations, we used a set of λ-values ranging from $\lambda = 0$ to $\lambda = 1$, where $\lambda = 0$ and $\lambda = 1$ correspond to a system with and without full interaction, respectively.

2.3 Analysis tools

We used Inkscape [263] and Grace [264] to plot figures from the data. PYMOL [265] and VMD [266] were utilized to visualize the biomolecular complexes. Modeller [267] was used to add missing residues for protein and missing nucleic acids for RNA. SwissPDB Viewer [268] and PDB Tools [269] were used to add missing atoms for protein and RNA.

Chapter 3: Antibodies and nanobodies bind to SARS-CoV-2 spike protein, preventing SARS-CoV-2 from entering human cells

3.1 Cocktail of REGN antibodies binds more strongly to SARS-CoV-2 than its components, but the Omicron variant reduces its neutralizing ability

3.1.1 Introduction

mAb therapies for the treatment of COVID-19 have been shown to be highly effective in reducing virus load and alleviating symptoms when administered shortly after diagnosis [270-271]. mAbs bind to the virus by targeting the S protein, which comprises the S1 and S2 subunits, thereby preventing SARS-CoV-2 from binding to the ACE2 receptor and inhibiting infection [34]. The S1 subunit is often the primary target for the binding of mAb to both RBD and NTD [272]. RBD-specific mAbs can be classified into four main classes, while NTD-specific mAbs typically focus on regions distant from RBD. It should be noted that ongoing research is actively exploring the discovery of mAbs that target the S2 subunit [146, 273].

Ab cocktails consisting of combinations of mAbs have shown promise in preventing viruses from evading neutralization *in vitro* [138, 274]. One such example is a dual Ab cocktail called REGN-COV2, developed to combat SARS-CoV-2. This cocktail consists of two mAbs, REGN10933 and REGN10987, and has advanced to phase 2/3 clinical trials. REGN-COV2 is a therapeutic approach developed by Regeneron Pharmaceuticals, where both mAbs target RBD (Figure 3.1A) [156, 158]. REGN10933 binds to the upper region of RBD, significantly overlapping with ACE2 binding site. In contrast, REGN10987 binds to a lateral region of RBD, distinct from REGN10933 epitope, and has no significant effect on ACE2 binding site [156]. *In vitro* studies have shown that combining these two non-competing Abs provides protection against the rapid viral escape observed with either Ab alone [158]. Subsequent studies have confirmed the efficacy of the combination-based approach, highlighting that REGN-COV2 retains its neutralization potency against SARS-CoV-2 [156, 158].

Numerous experimental studies on SARS-CoV-2 variants, such as Alpha, Beta, Gamma, Delta, Lambda, Omicron, *etc.*, have demonstrated their increased ability to infect host cells and evade host immunity. This increased infectivity is often associated with enhanced binding affinity to ACE2 and reduced neutralizing capacity against most SARS-CoV-2's Abs [114, 125, 275-281]. There are specific Abs capable of recognizing and binding to the S protein of these variants, thereby preventing the virus from entering human cells. One such promising approach involves the use of a mAb cocktail comprising REGN10933 and REGN10987, which has shown potential in neutralizing various variants of SARS-CoV-2, including Alpha, Gamma, Delta, and others [282-283]. However, the emergence of the Omicron variant in November 2021 has raised concerns about the effectiveness of mAb cocktails in treating COVID-19 [125, 280]. Therefore, gaining a comprehensive understanding of the molecular mechanisms underlying the activity of SARS-CoV-2 variants remains imperative for identifying appropriate and timely therapies for COVID-19.

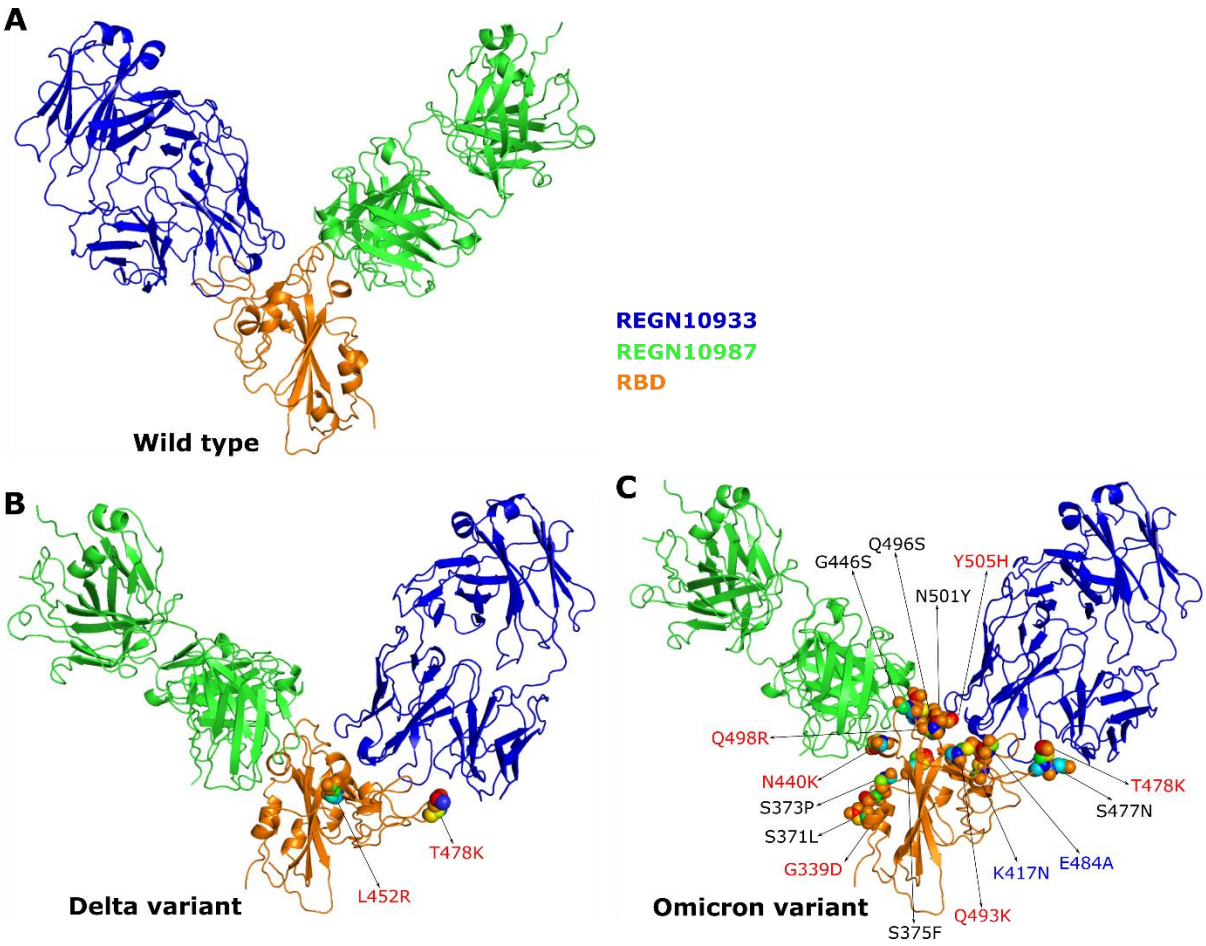

Figure 3.1: REGN10933 and REGN10987 in complex with RBD of A) wild type, B) Delta variant, and C) Omicron variant. Notably, mutations in the Omicron variant RBD are located in the binding regions for both components of REGN-COV2 cocktail. Mutations in the Delta variant RBD specifically affect REGN10933 binding site. Residues that carry a charge in the wild type RBD are shown in blue, while those that gain a charge after mutation are highlighted in red.

Despite the recognized importance of REGN-COV2 cocktail in the treatment of COVID-19, there is a noticeable lack of atomic-level studies on the structure and binding mechanisms of REGN-COV2 cocktail to RBD. In this work, we applied all-atom SMD and C_α coarse-grained US simulations to assess the binding affinity of REGN10933, REGN10987, and REGN10933+REGN10987 combination to RBD.

For SMD simulations, a pulling speed v = 0.5 nm/ns is used to complete the dissociation of REGN10933 or REGN10987 or RBD from the binding region. We considered only this pulling speed because the relative binding affinity of the complexes does not change between the different pulling speeds, as demonstrated by Nguyen *et al.* [165]. The pulling direction of three systems is determined as follows: For REGN10933-RBD and REGN10987-RBD cases, an external force is applied to a dummy atom connected to the C_α atom closest to the Ab center of mass (CoM). The pulling direction is parallel to the vector connecting the CoMs of RBD and Ab. For the REGN10933+REGN10987-RBD complex, the pulling

direction is along the line connecting the CoM of RBD perpendicular to the line connecting the CoMs of REGN10933 and REGN10987. These complexes were then rotated to align the unbinding pathway of REGN10933-RBD, REGN10987-RBD, or REGN10933+REGN10987-RBD along the z-axis [169]. We obtained F_{max} = 411.0 and 318.3 pN for REGN10933-RBD and REGN10987-RBD, which are lower than that of REGN10933+REGN10987-RBD (F_{max} = 511.3 pN). This results in a ranking of the binding affinities of REGN-COV2 Abs to RBD as follows: REGN10987 < REGN10933 < REGN10933+REGN10987. The association of REGN10987 with RBD was shown to be driven by vdW interactions, while electrostatic interactions dominate in the cases of REGN10933 and REGN10933+REGN10987.

For C_α coarse-grained US simulations, a total of 200 umbrella windows were generated by translating Ab in increments of 0.05 nm away from RBD along the vector connecting their two interface CoMs. A harmonic restraint was applied to maintain the Ab and RBD domain at target distances. The K_D values estimated from this approach for REGN10933 and REGN10987 binding to the RBD domain were 1.73 and 16.38 nM, respectively. This confirms that the binding affinity of REGN10933 is stronger than that of REGN10987, consistent with the all-atom SMD results.

Given the essential role of Delta and Omicron variants (Figure 3.1B&C) in viral infection, we further examined their interaction with REGN-COV2. Our all-atom SMD studies revealed that the binding affinity of REGN10933, REGN10987, and REGN10933+REGN10987 to the Delta variant remained nearly unchanged compared to the wild type. However, a significant decrease in interaction with the REGN-COV2 cocktail was observed for the Omicron variant, consistent with experimental observations [125, 280]. This comprehensive analysis provides important mechanistic insights into the stability of these complexes, which may be instrumental in the development of Ab cocktail therapies for COVID-19.

3.1.2 Publication

a) Abstract: A promising approach to combat COVID-19 infections is the development of effective antiviral antibodies that target SARS-CoV-2 spike protein. Understanding the structures and molecular mechanisms underlying the binding of antibodies to SARS-CoV-2 can contribute to quickly achieving this goal. Recently, a cocktail of REGN10987 and REGN10933 antibodies was shown to be an excellent candidate for the treatment of COVID-19. Here, using all-atom steered molecular dynamics and coarse-grained umbrella sampling, we examine the interactions of the receptor-binding domain (RBD) of SARS-CoV-2 spike protein with REGN10987 and REGN10933 separately as well as together. Both computational methods show that REGN10933 binds to RBD more strongly than REGN10987. Importantly, the cocktail binds to RBD (simultaneous binding) more strongly than its components. The dissociation constants of REGN10987-RBD and REGN10933-RBD complexes calculated from the coarse-grained simulations are in good agreement with the experimental data. Thus, REGN10933 is probably a better candidate for treating COVID-19 than REGN10987, although the cocktail appears to neutralize the virus more efficiently than

REGN10933 or REGN10987 alone. The association of REGN10987 with RBD is driven by van der Waals interactions, while electrostatic interactions dominate in the case of REGN10933 and the cocktail. We also studied the effectiveness of these antibodies on the two most dangerous variants Delta and Omicron. Consistent with recent experimental reports, our results confirmed that the Omicron variant reduces the neutralizing activity of REGN10933, REGN10987, and REGN10933+REGN10987 with the K417N, N440K, L484A, and Q498R mutations playing a decisive role, while the Delta variant slightly changes their activity.

- DOI: 10.1021/acs.jpcb.2c00708
- Publication source: https://pubs.acs.org/doi/10.1021/acs.jpcb.2c00708

b) Author contribution statements:

Hung Van Nguyen
Division of Theoretical Physics
Institute of Physics, Polish Academy of Sciences
Al. Lotnikow 32/46
02-668 Warsaw, Poland

INSTYTUT FIZYKI
POLSKIEJ AKADEMII NAUK

STATEMENT

I declare that I am the co-author of the publication:

- Nguyen, H.; Pham, D. L.; Nissley, D. A.; O'Brien, E. P.; Li, M. S. **Cocktail of REGN antibodies binds more strongly to SARS-CoV-2 than its components, but the Omicron variant reduces its neutralizing ability**. J. Phys. Chem. B. **2022**, *126*(15), 2812-2823.

My contribution consisted of designing the research, performing all-atom simulations, analyzing the results, preparing figures, and writing the manuscript.

Warsaw, August 2024

Hung Van Nguyen

Pham Dang Lan
Life Sciences Lab
Institute for Computational Science and Technology
SBI Building, Quang Trung Software City, Tan Chanh
Hiep Ward, District 12, Ho Chi Minh City, Vietnam

STATEMENT

I declare that I am the co-author of the publication:

- Nguyen, H.; Pham, D. L.; Nissley, D. A.; O'Brien, E. P.; Li, M. S. **Cocktail of REGN antibodies binds more strongly to SARS-CoV-2 than its components, but the Omicron variant reduces its neutralizing ability**. J. Phys. Chem. B. **2022**, *126*(15), 2812-2823.

My contribution consisted of performing coarse-grained simulations, analyzing the results, preparing figures, and writing the manuscript.

Ho Chi Minh, July 2024

Pham Dang Lan

Daniel A. Nissley
665 NE 25th Street, Unit 2505
Miami, FL 33137
United States of America

STATEMENT

I declare that I am the co-author of the publication:

- Nguyen, H.; Pham, D. L.; Nissley, D. A.; O'Brien, E. P.; Li, M. S. **Cocktail of REGN antibodies binds more strongly to SARS-CoV-2 than its components, but the Omicron variant reduces its neutralizing ability**. J. Phys. Chem. B. **2022**, *126*(15), 2812-2823.

My contribution consisted of interpreting the results and helping to write the manuscript.

Miami FL, July 2024

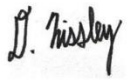

Daniel A. Nissley

Prof. Edward P. O'Brien, PhD
Department of Chemistry
The Pennsylvania State University
University Park PA, 16802
E-mail: epo2@psu.edu

PENNSTATE
1855

STATEMENT

I declare that I am the co-author of the publication:

- Nguyen, H.; Pham, D. L.; Nissley, D. A.; O'Brien, E. P.; Li, M. S. **Cocktail of REGN antibodies binds more strongly to SARS-CoV-2 than its components, but the Omicron variant reduces its neutralizing ability**. J. Phys. Chem. B. **2022**, *126*(15), 2812-2823.

My contribution consists of interpreting the results and assisting in writing the manuscript.

PA USA, July 2024

Edward P. O'Brien

Prof. Mai Suan Li, PhD
Division of Theoretical Physics
Institute of Physics, Polish Academy of Sciences
Al. Lotnikow 32/46
02-668 Warsaw, Poland
E-mail: masli@ifpan.edu.pl

INSTYTUT FIZYKI
POLSKIEJ AKADEMII NAUK

STATEMENT

I declare that I am the co-author of the publication:

- Nguyen, H.; Pham, D. L.; Nissley, D. A.; O'Brien, E. P.; Li, M. S. **Cocktail of REGN antibodies binds more strongly to SARS-CoV-2 than its components, but the Omicron variant reduces its neutralizing ability**. J. Phys. Chem. B. **2022**, *126*(15), 2812-2823.

My contribution consisted of designing the research, interpreting the data, writing the manuscript, and supervising the overall project.

Warsaw, August 22 2024

Mai Suan Li

c) Publication for this section:

Cocktail of REGN antibodies binds more strongly to SARS-CoV-2 than its components, but the Omicron variant reduces its neutralizing ability

Hung Nguyen, Pham Dang Lan, Daniel A. Nissley, Edward P. O'Brien, and Mai Suan Li

J. Phys. Chem. B, 2022, 126, 2812-2823

THE JOURNAL OF PHYSICAL CHEMISTRY B
A JOURNAL OF THE AMERICAN CHEMICAL SOCIETY

pubs.acs.org/JPCB

Article

Cocktail of REGN Antibodies Binds More Strongly to SARS-CoV-2 Than Its Components, but the Omicron Variant Reduces Its Neutralizing Ability

Hung Nguyen,[○] Pham Dang Lan,[○] Daniel A. Nissley, Edward P. O'Brien, and Mai Suan Li*

Cite This: J. Phys. Chem. B 2022, 126, 2812−2823

Read Online

ACCESS | Metrics & More | Article Recommendations | Supporting Information

ABSTRACT: A promising approach to combat Covid-19 infections is the development of effective antiviral antibodies that target the SARS-CoV-2 spike protein. Understanding the structures and molecular mechanisms underlying the binding of antibodies to SARS-CoV-2 can contribute to quickly achieving this goal. Recently, a cocktail of REGN10987 and REGN10933 antibodies was shown to be an excellent candidate for the treatment of Covid-19. Here, using all-atom steered molecular dynamics and coarse-grained umbrella sampling, we examine the interactions of the receptor-binding domain (RBD) of the SARS-CoV-2 spike protein with REGN10987 and REGN10933 separately as well as together. Both computational methods show that REGN10933 binds to RBD more strongly than REGN10987. Importantly, the cocktail binds to RBD (simultaneous binding) more strongly than its components. The dissociation constants of REGN10987-RBD and REGN10933-RBD complexes calculated from the coarse-grained simulations are in good agreement with the experimental data. Thus, REGN10933 is probably a better candidate for treating Covid-19 than REGN10987, although the cocktail appears to neutralize the virus more efficiently than REGN10933 or REGN10987 alone. The association of REGN10987 with RBD is driven by van der Waals interactions, while electrostatic interactions dominate in the case of REGN10933 and the cocktail. We also studied the effectiveness of these antibodies on the two most dangerous variants Delta and Omicron. Consistent with recent experimental reports, our results confirmed that the Omicron variant reduces the neutralizing activity of REGN10933, REGN10987, and REGN10933+REGN10987 with the K417N, N440K, L484A, and Q498R mutations playing a decisive role, while the Delta variant slightly changes their activity.

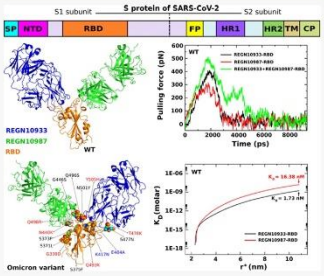

1. INTRODUCTION

Severe acute respiratory syndrome coronavirus 2 (SARS-CoV-2), is a member of the Coronaviridae family and the causative agent of the ongoing coronavirus disease 2019 (Covid-19) pandemic.[1] Currently, over 245 million cases have been officially diagnosed since its first emergence, and more than 5 million people have died from Covid-19.[2] Public health measures, along with rapid vaccine development, have helped slow the pandemic in some countries. Moreover, small-molecule inhibitors, antibody-based therapeutics, and convalescent plasma from recovered Covid-19 patients have received emergency use approvals.[3]

Monoclonal antibody (mAb) therapies for the treatment of SARS-CoV-2 have proven to be an excellent solution to reduce virus loads and alleviate symptoms when given shortly after diagnosis.[4,5] mAbs bind to the virus through the spike protein (S), which consists of the S1 and S2 subunits (Figure 1A), blocking the binding of SARS-CoV-2 to human angiotensin-converting enzyme 2 (ACE2) (Figure 1B), in turn preventing infection.[6] mAbs often target the S1 subunit,[7] which contains the receptor-binding domain (RBD) and N-terminal domain (NTD). RBD-specific mAbs fall into four main classes, while NTD-specific mAbs target the patch remote from RBD.[8,9] The discovery of mAbs that target S2 is another area of active research.[8]

Antibody cocktails, defined as mixtures of more than one unique antibody, have shown promise in preventing viruses from escaping neutralization *in vitro*.[10,11] Recently, a double antibody cocktail (REGN-COV2) for SARS-CoV-2, including REGN10933 and REGN10987, has entered phase 2/3 clinical trials. This can be seen as the REGN-COV2 therapy developed by Regeneron Pharmaceuticals in which both monoclonal antibodies bind to RBD (Figure 1C).[12,13] REGN10933 tethers at the top of RBD, significantly overlapping the binding site of ACE2 (dissociation constant K_D = 3.37 nM), while REGN10987 is located lateral to RBD, away from the REGN10933 epitope and has little to no overlap with the

Received: January 28, 2022
Revised: March 25, 2022
Published: April 11, 2022

The Journal of Physical Chemistry B pubs.acs.org/JPCB Article

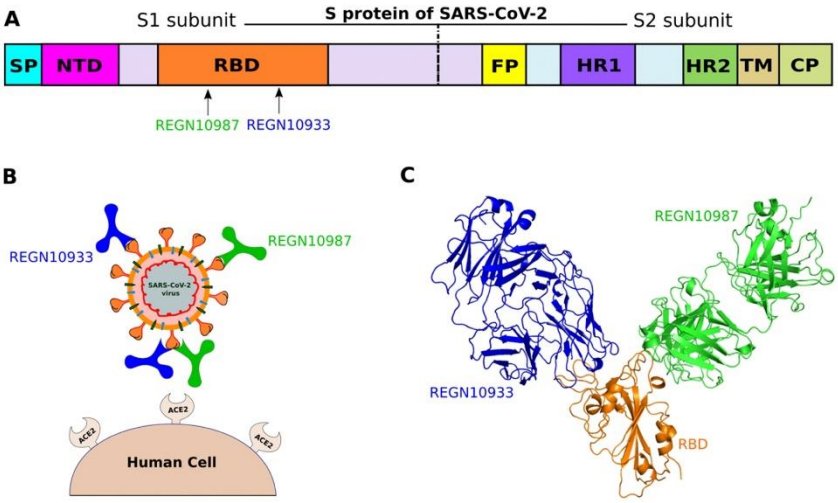

Figure 1. (A) Schematic description of the S protein of SARS-CoV-2, which consists of S1 and S2 subunits. (B) REGN10933 and REGN10987 bind to S protein, preventing the virus from entering cells. (C) Three-dimensional (3D) structures of REGN10933 and REGN10987 bound to RBD are shown in all-atom representation.

ACE2 binding site (K_D = 45.2 nM) (Table 1).[12] *In vitro* studies showed that combining two noncompeting antibodies protects against the rapid escape seen with individual antibody components.[13] This combination-based approach has been supported by subsequent studies showing that REGN-COV2 retains neutralization potency against SARS-CoV-2.[12,13]

Table 1. K_D (nM) of REGN-COV2 Antibodies Bound to RBD for the WT Case Estimated from the Experimental and Computational Results

	WT		
		K_D (simulation)	
	K_D (experiment)	REX-US	PRODIGY
REGN10933	3.37	1.73	31 ± 8.96
REGN10987	45.2	16.38	69 ± 25.33
REGN10933+REGN10987			0.056 ± 0.027

Despite reports of the important role of REGN-COV2 in the treatment of Covid-19, the structure and mechanism of binding of REGN-COV2 antibodies to RBD at the atomic level have not been studied. In this work, we use steered molecular dynamics (SMD) and coarse-grained simulations with umbrella sampling to evaluate the binding affinities of REGN10933, REGN10987 and both REGN10933+REGN10987 to RBD. Our theoretical estimation of the dissociation constant agrees with the experiment, according to which K_D of REGN10933-RBD is less than that of REGN10987-RBD (Table 1). Both SMD and PRODIGY (PROtein binDIng enerGY prediction) show that REGN10933+REGN10987 binds to RBD more tightly than its components.

More recently, many experimental studies on SARS-CoV-2 variants such as α, β, γ, Delta, Lambda, Omicron, etc. have shown that these variants can promote the ability to infect host cells and evade host immunity, which means that they will increase binding to ACE2 and weaken the neutralizing capacity of most SARS-CoV-2 antibodies.[14−24] However, there are some antibodies that recognize and bind to the S protein of these variants, blocking the virus from infecting human cells. For example, a cocktail of antibodies REGN10933 and REGN10987 can neutralize most variants of SARS-CoV-2 including α, γ, Delta, and so on.[25,26] The Omicron variant reported in November 2021 could reduce the effectiveness of a monoclonal antibody cocktail in treating Covid-19.[20,21] Therefore, understanding the molecular mechanism underlying the activity of SARS-CoV-2 variants is essential to find an appropriate and timely therapy for Covid-19.

Since the Delta and Omicron variants play a major role in viral infection, we investigated their interaction with REGN-COV2. We found that the binding affinities of REGN10933, REGN10987, and REGN10933+REGN10987 to the Delta variant remain almost the same as those of the wild type (WT). However, the Omicron variant significantly decreases the interaction with REGN-COV2, which is consistent with the experiment.[20,21] Our comprehensive study provides important mechanistic insights into the stability of the respective complexes, which can be useful for the development of antibody cocktail therapy for Covid-19.

2. MATERIALS AND METHODS

2.1. Preparing the Structures. The structure of the REGN-COV2 antibody cocktail with two components REGN10933 and REGN10987 bound to RBD (Figure 1C) was obtained from the Protein Data Bank, PDB ID: 6XDG.[12] Missing residues were added using the Modeler package.[27] In this work, we considered the Delta (B.1.617.2) and Omicron (B.1.1.529) variants. All mutations of these variants were generated using the mutagenesis tool in PyMOL package.[28]

https://doi.org/10.1021/acs.jpcb.2c00708
J. Phys. Chem. B 2022, 126, 2812−2823

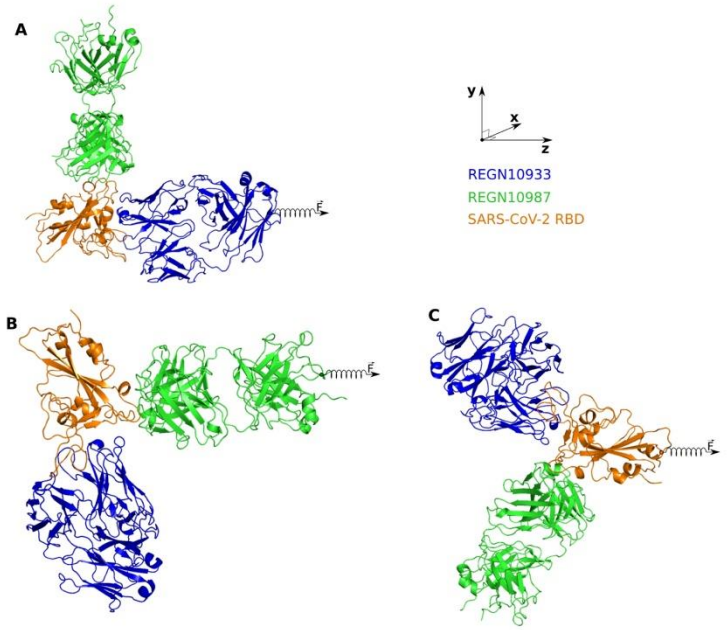

Figure 2. Structure of the REGN10933+REGN10987-RBD complex, retrieved from PDB with ID 6XDG. RBD is shown in orange, while green and blue describe REGN10987 and REGN10933. The external force is applied to (A) REGN10933, (B) REGN10987, and (C) RBD (REGN10933+REGN10987). The pulling direction in SMD simulations is shown with a spring along the *z*-axis.

2.2. All-Atom Simulation. Simulations were carried out with the CHARMM36 force field[29] in the GROMACS 2016 package[30] at a temperature of 310 K and a pressure of 1 bar, which were maintained using the v-rescale and Parrinello–Rahman algorithms.[31,32] The TIP3P water model[33] was used to solvate all structures. All bonds within proteins were constrained by the Linear Constraint Solver (LINCS) algorithm.[34] Electrostatic and van der Waals interactions were used to depict nonbonded interactions and their pair list is updated every 10 fs with a cutoff of 1.4 nm. The Particle Mesh Ewald algorithm[35] was used to calculate the long-range electrostatic interaction. The equations of motion were solved using the leap-frog algorithm[36] with an integration time step set to 2 fs. Periodic boundary conditions were applied in all directions. The energy of these systems was minimized using the steepest-descent algorithm and then equilibrated with a short 2 ns simulation performed in the NVT ensemble, followed by 3 ns NPT simulation. Finally, a 100 ns production simulation was performed to generate initial conformations for SMD simulation and for the estimation of the binding free energy using structure-based PRODIGY. Five statistically independent trajectories were run for each system.

2.2.1. Steered Molecular Dynamics. A rectangular box of $10 \times 16 \times 25$ nm^3 was used to allow enough space to pull the targets from their binding regions. The center of three-dimensional coordinates was at $5 \times 8 \times 6$ nm^3 for these complexes. K^+ and Cl^- ions were added to a concentration of 0.15 M. In the case of REGN10933-RBD and REGN10987-RBD, an external force is applied to a dummy atom, which is linked to the Cα atom closest to the antibody center of mass (CoM). The pulling direction is parallel to the vector connecting CoMs of the RBD and antibody (Figure 2A,B). In the case of REGN10933+REGN10987-RBD, the pulling direction is the line connecting RBD's CoM in perpendicular to the line connecting the CoMs of REGN10933 and REGN10987 (Figure 2C). These complexes were then rotated so that the REGN10933-RBD or REGN10987-RBD or REGN10933+REGN10987-RBD unbinding pathway is along the *z*-axis (Figure 2), which was displayed using the PyMOL 2.0 package.[28] The force experienced by the pulled atom is measured according to the following equation

$$F = k(\Delta z - vt) \tag{1}$$

where k is the force constant, v is the pulling velocity at time t, and Δz is the displacement of the chain's atom connected to the spring in the direction of pulling, respectively. The spring constant k value was set to 600 kJ/(mol nm^2) (~1020 pN/nm), which is a typical value used in atomic force microscopy (AFM) experiments.[37] The complete dissociation of REGN10933 or REGN10987 or RBD from the binding region was reached during simulations of duration ~10,000 ps at pulling speed v = 0.5 nm/ns.

Using the force–displacement profile gained in the SMD simulation, nonequilibrium work (W) was estimated using the trapezoidal rule

$$W = \int F\mathrm{d}z = \sum_{i=1}^{N} \frac{F_{i+1} + F_i}{2}(z_{i+1} - z_i) \tag{2}$$

https://doi.org/10.1021/acs.jpcb.2c00708
J. Phys. Chem. B 2022, 126, 2812−2823

where N is the number of simulation steps, and F_i and z_i are the force experienced by the target and position at step i, respectively. To estimate the binding free energy (ΔG) from the SMD simulation, we used Jarzynski's equality[38] in the presence of external force with constant pulling speed v. The ΔG was defined by[39]

$$\exp\left(\frac{-\Delta G}{k_B T}\right) = \left\langle \exp\left(\frac{W(t) - \frac{1}{2}k(z_t - vt)^2}{k_B T}\right)\right\rangle_N \quad (3)$$

here, $\langle ... \rangle_N$ is the average over N trajectories, z_t is the time-dependent displacement, and $W(t)$ is the nonequilibrium work at time t defined as eq 2.

Equation 3 means that we can extract an equilibrium quantity by assembling the external work of an infinite number of nonequilibrium processes.[40] In this study, while the transformation is not slow enough and the number of SMD runs is finite, we are able to estimate the nonequilibrium binding and unbinding energy barriers of the complexes based on the transition state (TS), the bound state (at t_0), and the unbound state (at t_{end}).

2.2.2. Measures Used in Data Analysis. A hydrogen bond (HB) defined by the distance between donor D and acceptor A is less than 0.35 nm, the H−A distance is less than 0.27 nm, and the D−H−A angle is larger than 135°. A nonbonded contact (NBC) between two residues of a protein was made considered to be present when the distance between their heavy atoms is 0.39 nm or less. The two-dimensional (2D) contact networks of HBs and NBCs of REGN10933-RBD and REGN10987-RBD were analyzed using the LIGPLOT package.[41]

2.3. Coarse-Grained Simulations. *2.3.1. Coarse-Grained Model for Proteins.* Protein was described using the Go-like model. Each amino acid is represented by a single interaction site positioning at the corresponding C_α coordinates. The configuration energy is calculated as below

$$\begin{aligned} E = & \sum_i k_b(r_i - r_0)^2 \\ & + \sum_i \frac{-1}{\gamma}\ln\{\exp[-\gamma(k_\alpha(\theta_i - \theta_\alpha)^2 + \varepsilon_\alpha)] \\ & + \exp[-\gamma k_\beta(\theta_i - \theta_\beta)^2]\} \\ & + \sum_{ij} k_{\varphi,ij}[1 + \cos(j\varphi_i - \delta_{ij})] + \sum_{ij} \frac{q_i q_j e^2}{4\pi\varepsilon_0\varepsilon_r r_{ij}}\exp[\frac{-r_{ij}}{l_D}] \\ & + \sum_{ij\in\{NC\}} \eta\varepsilon_{ij}^{NC}\left[13\left(\frac{\sigma_{ij}}{r_{ij}}\right)^{12} - 18\left(\frac{\sigma_{ij}}{r_{ij}}\right)^{10} + 4\left(\frac{\sigma_{ij}}{r_{ij}}\right)^{6}\right] \\ & + \sum_{ij\notin\{NC\}} \varepsilon_{ij}^{NN}\left[13\left(\frac{\sigma_{ij}}{r_{ij}}\right)^{12} - 18\left(\frac{\sigma_{ij}}{r_{ij}}\right)^{10} + 4\left(\frac{\sigma_{ij}}{r_{ij}}\right)^{6}\right] \end{aligned} \quad (4)$$

These terms represent, respectively, the energy contributions of C_α−C_α bonds, bond angles, dihedral angles, electrostatics, and Lennard-Jones (LJ)-like attractive and repulsive interactions of native and nonnative contacts. Details of parameters employed for these terms can be found elsewhere.[42] Lennard-Jones (LJ) well depths for native contact interactions were set by a scaling factor η to reproduce realistic protein stabilities. η values for intraprotein interactions of antibodies and RBD domain were defined through the procedure described previously based on a published training set.[43] An additional η is set for the inter-interactions between the antibody and RBD to reproduce the dissociation constant K_D at the nanomolar level reported by experiments. η values are listed in Table S1.

2.3.2. Replica Exchange Umbrella Sampling (REX-US) Simulations. Here, we employed Chemistry at Harvard Macromolecular Mechanics (CHARMM) version c35b5 to perform Replica Exchange Umbrella Sampling (REX-US) coarse-grained simulations to explore the binding of two antibodies REGN10933 and REGN10987 to RBD. In total, 200 umbrella windows were generated by translating the antibody in 0.05 nm increments away from RBD along the vector connecting their two interface centers of mass. A harmonic restraint with a force constant of 700 kcal/(mol nm^2) was applied to restrain the antibody and virus domain at target distances. Langevin dynamics simulations were then run at 310 K using a frictional coefficient of 0.050 ps^{-1}, an integration time step of 0.015 ps, and the SHAKE algorithm[44] applied to virtual bonds. Exchanges between neighboring windows were attempted every 5000 integration time steps (75 ps). In total, 10,000 exchanges (750 ns of simulation time) were run with the acceptance ratios between neighboring umbrellas falling in the range of 0.46−0.79. The first 1000 attempted exchanges were discarded to allow for equilibration, and the remaining 9000 exchanges used for analysis.

2.3.3. Method for Estimating the Dissociation Constant (K_D) from REX-US Simulations. The dissociation constant K_D is calculated as below[45,46]

$$K_D = \frac{P_u}{P_b}[A] \quad (5)$$

where [A] represents the concentration of the free antibody or free RBD in their unbound state. P_u is the probability of the system being in the unbound state, $P_u = 1 - P_b$. The bound-state probability P_b is calculated from the numerical integration of the one-dimensional potential of mean force (1D-PMF) $G_{1D}(r)$ as below

$$P_b = \frac{\int_0^{r_b} 4\pi r^2 \, e^{-\beta G_{1D}(r)} dr}{\int_0^{r^*} 4\pi r^2 \, e^{-\beta G_{1D}(r)} dr} \quad (6)$$

where $G_{1D}(r)$ was constructed from REX simulations using WHAM equations.[47]

2.4. Structure-Based Method to Predict the Binding Affinity of Antibodies. MD-based exact methods, such as free energy perturbation or thermodynamics integration, can provide highly accurate results, but due to high computational costs, their application is restricted to study the small compound binding or effect of mutations, which requires high precision. Docking methods based on the knowledge of the three-dimensional (3D) structure of associated molecular complexes are more commonly used due to their wide range of applicability, although the accuracy depends on structural characteristics. The result is obtained mainly from the contribution of surface interactions. Recently, more research has been conducted to improve the structure-based prediction for the protein−protein binding affinity. Taking into account the contribution of characteristics of the noninteracting

https://doi.org/10.1021/acs.jpcb.2c00708
J. Phys. Chem. B 2022, 126, 2812−2823

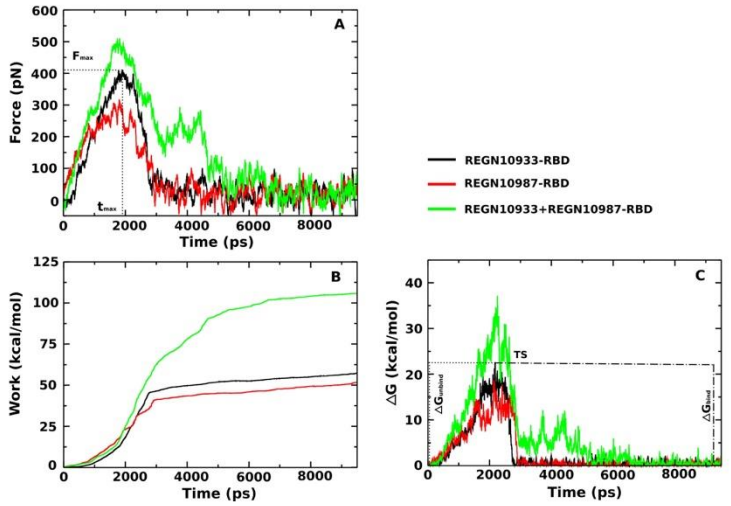

Figure 3. Time dependence of (A) force, (B) pulling work, and (C) nonequilibrium free energy of the REGN10933-RBD, REGN10987-RBD, and REGN10933+REGN10987-RBD complexes. The results were averaged over five independent SMD runs.

surface, Vangone and Bovine[48] described the binding affinity of two interacting proteins by an analytically linear equation. The combination of polar−nonpolar charge residues is sorted by the contribution of interresidue contacts. The buried surface area and the noninteracting surface effect are computed separately for polar−nonpolar residues. The corresponding weights are obtained by training different combinations of proteins whose binding affinities have been experimentally measured. This method is currently implemented as a web server tool PRODIGY (PROtein binDIng enerGY prediction) with a software version deposited on GitHub repository.[49] Here, we used PRODIGY to predict the binding affinity of the systems under study for comparison with the results obtained from our coarse-grained simulations and experiments.

3. RESULTS AND DISCUSSION

3.1. Hydrogen Bonded and Nonbonded Contact Networks. We analyzed the HB and NBC networks of REGN10933-RBD and REGN10987-RBD of the initial structure to gain some insight into the binding affinity between REGN-COV2 antibodies and RBD (Figure S1). There were 15 and 8 residues of REGN10933 and REGN10987, respectively, that have formed HB or NBC contacts with RBD. While seven HBs are formed between REGN10933 and RBD, no HBs are formed between REGN10987 and RBD. A total of 15 NCBs formed between REGN10933 and RBD as well as between REGN10987 and RBD. The difference in the number of HBs suggests that the binding affinity of REGN10933 to RBD may be stronger than that of REGN10987 to RBD.

3.2. Steered Molecular Dynamics Simulation Results. *3.2.1. Ranking of Binding Affinities of REGN-COV2 Antibodies to RBD: REGN10987 < REGN10933 < REGN10933+REGN10987.* The force, pulling work, and free energy barrier profiles of REGN10933-RBD, REGN10987-RBD, and REGN10933+REGN10987-RBD are shown in Figure 3. Averaging over five independent runs, for REGN10933-RBD and REGN10987-RBD, we obtained F_{max} ≈ 411.0 and 318.3 pN, respectively (Figure 3A and Table 2), which are lower than that of REGN10933+REGN10987-RBD (511.3 pN).

The nonequilibrium work W increased until the antibodies detached from RBD and then saturated. Therefore, W is defined as the saturated value at the end of the simulation. In detail, W = 57.3 ± 1.5, 51.6 ± 1.4, and 105.8 ± 2.7 kcal/mol for REGN10933-RBD, REGN10987-RBD, and REGN10933+REGN10987-RBD, respectively (Figure 3B and Table 2).

The nonequilibrium binding free energy (ΔG) for three complexes is estimated from eq 3. Clearly, we have $\Delta G_{bound} = \Delta G(t_0) \approx 0$ kcal/mol at the beginning of the bound state, while the unbound state occurs at the end of the simulation, $\Delta G_{unbound} = \Delta G(t_{end}) \approx 0$ kcal/mol. The binding and unbinding free energy barriers are defined by $\Delta\Delta G_{bind} = \Delta G_{TS} - \Delta G_{unbound}$ and $\Delta\Delta G_{unbind} = \Delta G_{TS} - \Delta G_{bound}$, where ΔG_{TS} is the maximum free energy corresponding to the transition state. Then, from Figure 3C, we have $\Delta\Delta G_{unbind}$ = 22.7 ± 1.7, 18.7 ± 0.5, and 37.1 ± 1.5 kcal/mol and $\Delta\Delta G_{bind}$ = 22.1 ± 1.3, 18.4 ± 0.7, and 37.0 ± 1.7 kcal/mol for REGN10933-RBD, REGN10987-RBD, and REGN10933+REGN10987-RBD, respectively (see also Table 2).

Thus, the data obtained for F_{max}, W, $\Delta\Delta G_{bind}$, and $\Delta\Delta G_{unbind}$ (Table 2) indicate that REGN10933 binds to RBD more strongly than REGN10987. Moreover, the REGN10933+REGN10987 cocktail associates with the spike protein more closely than the individual components, resulting in a ranking of REGN10987 < REGN10933 < REGN10933+REGN10987. It can be expected that after binding to the S protein, two antibodies will physically occupy the ACE2 interaction interface (see Figure S2) and completely block the ACE2-S interaction, which will lead to the fact that the virus neutralization process will be faster than the neutralization process of one of them separately.

https://doi.org/10.1021/acs.jpcb.2c00708
J. Phys. Chem. B 2022, 126, 2812−2823

Table 2. Rupture Force (F_{max}), Time Rupture (t_{max}), Nonequilibrium Work (W), and Nonequilibrium Binding Energy Barriers ($\Delta\Delta G_{bind}$ and $\Delta\Delta G_{unbind}$) Obtained from Five Independent SMD Trajectories of REGN10933-RBD, REGN10987-RBD, and REGN10933+REGN10987-RBD for the WT and the Variants[a]

	REGN10933-RBD			REGN10987-RBD		REGN10933+REGN10987-RBD		
	WT	Delta	Omicron	WT	Omicron	WT	Delta	Omicron
F_{max} (pN)	411.0 ± 21.3	424.0 ± 25.6	326.2 ± 21.1	318.3 ± 19.5	279.3 ± 14.3	511.3 ± 20.2	529.2 ± 22.5	436.4 ± 21.7
t_{max} (ps)	1915.3 ± 117.0	2007.5 ± 120.3	1557.0 ± 109.8	1800.9 ± 111.2	1684.3 ± 104.8	1739.6 ± 108.5	1638.2 ± 101.6	2426.7 ± 126.7
W (kcal/mol)	57.3 ± 1.5	56.9 ± 1.8	45.2 ± 1.7	51.6 ± 1.4	41.8 ± 1.0	105.8 ± 2.7	111.2 ± 2.2	65.5 ± 1.9
$\Delta\Delta G_{unbind}$ (kcal/mol)	22.7 ± 1.7	22.0 ± 1.1	12.8 ± 1.0	18.7 ± 0.5	11.2 ± 0.2	37.1 ± 1.5	37.2 ± 1.3	30.1 ± 0.4
$\Delta\Delta G_{bind}$ (kcal/mol)	22.1 ± 1.3	21.6 ± 1.4	12.7 ± 1.4	18.4 ± 0.7	11.1 ± 0.3	37.0 ± 1.7	37.1 ± 1.5	30.0 ± 0.9

[a]Here, the errors represent standard deviations.

3.2.2. Stabilities of REGN10933-RBD and REGN10933+REGN10987-RBD are Driven by Electrostatic Interactions, While the Stability of REGN10987-RBD is Controlled by vdW Interaction. The time dependence of the energy of electrostatic (E_{elec}), van der Waals (E_{vdW}), and total (E_{total}, the sum of electrostatic and vdW) interactions is illustrated in Figure 4A−C. The results are averaged over five SMD trajectories. In the bound state, E_{elec} of REGN10933-RBD and REGN10933+REGN10987-RBD started with a negative value, while for REGN10987-RBD, it fluctuated at a positive value. However, for the last complex, E_{vdW} was negative (Figure 4A), resulting in $E_{total} < 0$ (Figure 4C). In the unbound state, due to the long-range character, E_{elec} reached a positive value for all three systems. On the other hand, their E_{vdW} was negative in the bound state, and then eventually reached 0 in the unbound state.

Since the complex has been in the bound state before the rupture occurs, the interaction energy of this state can be obtained by averaging over the time window $[0, t_{max}]$. This gives us $E_{elec} = -65.7 \pm 4.3$, 44.2 ± 3.4, and -155.9 ± 4.4 kcal/mol, $E_{vdW} = -51.1 \pm 1.8$, -50.8 ± 2.4, and -107.2 ± 3.2 kcal/mol for REGN10933-RBD, REGN10987-RBD, and REGN10933+REGN10987-RBD, respectively (Table 3). Then, $E_{total} = -116.8 \pm 6.1$, -6.6 ± 5.8, and -263.1 ± 7.6 kcal/mol for REGN10933-RBD, REGN10987-RBD, and REGN10933+REGN10987-RBD, respectively. It is obvious that REGN10987-RBD is marginally stable in terms of the interaction energy without regard to entropy and is less stable than the other two complexes. In addition, the electrostatic interaction makes an important contribution to REGN10933-RBD and REGN10933+REGN10987-RBD, while the vdW interaction plays a key role in REGN10987-RBD binding.

3.2.3. Role of Specific Residues in the Binding Regions of REGN10933-RBD and REGN109387-RBD. To calculate the per-residue interaction energy in the bound state, we took into account the images collected in the window $[0, t_{max}]$ and averaged over all SMD trajectories. The results obtained for the residues from the REGN10933-RBD and REGN10987-RBD binding regions are shown in Figure 4D,E.

Assuming that important residues must have an interaction energy, the absolute value of which exceeds 20 kcal/mol, then for REGN10933-RBD residues Asp92(B), Asp31(C), and Arg100(C) of REGN10933 and Lys417(A), Glu484(A), and Phe486(A) of RBD make a major contribution. The letters in the brackets refer to the chains. With an interaction energy of about −71.1 kcal/mol, Lys417(A) of the spike protein is much more significant than Glu484(A) (−25.7 kcal/mol) and Phe486(A) (−21.6 kcal/mol) (Figure 4D). Negatively charged residues Asp92(B) and Asp31(C) from REGN10933 stabilize the complex, while positively charged Arg100(C) destabilize it with a positive energy.

In the REGN10987-RBD case, the interaction energy is much lower compared to the REGN10933-RBD complex, and only the Asp101(D) residue of REGN10987 has an energy below −20 kcal/mol (Figure 4E). However, the greatest influence on REGN10933 binding is exerted by Arg346(A), Lys444(a), and Val445(A) of RBD.

Since the total charge of SARS-CoV-2-RBD is +2e, the negatively charged residues of both REGN10933 (Asp92(B) and Asp31(C)) and REGN10987 (Asp101(D)) substantially increase their binding affinity with RBD. This means that an antibody that contains many negatively charged residues at the

https://doi.org/10.1021/acs.jpcb.2c00708
J. Phys. Chem. B 2022, 126, 2812−2823

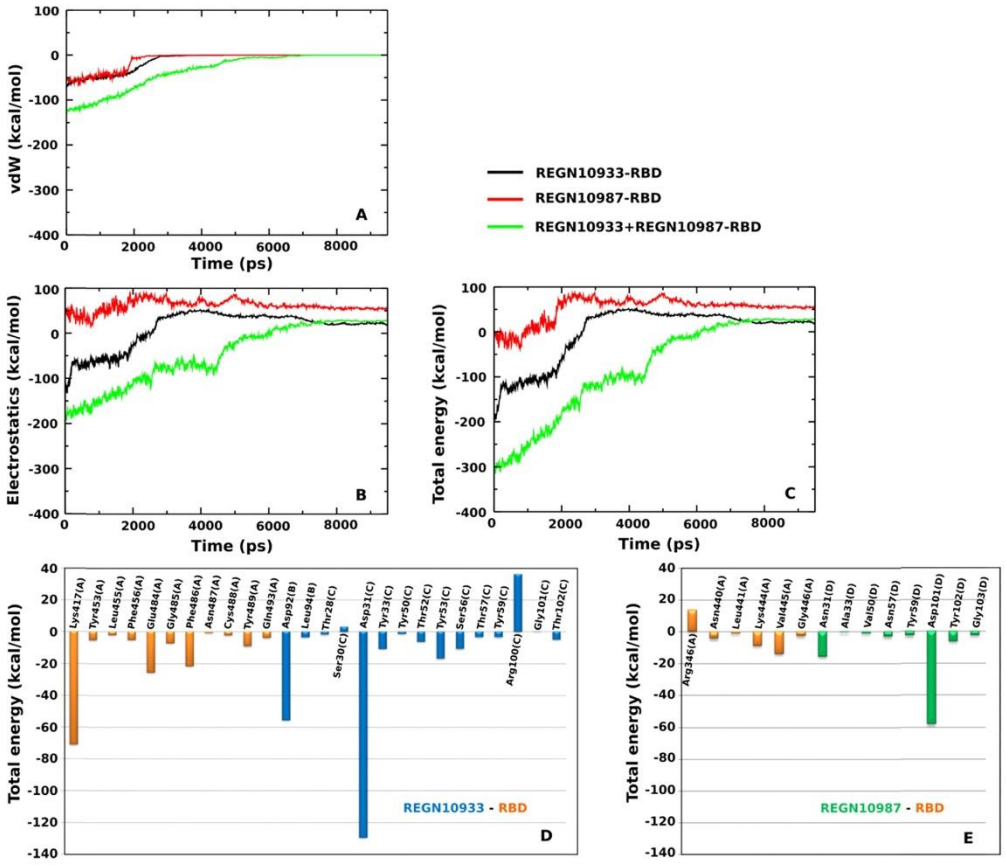

Figure 4. Time dependence of (A) vdW interaction energy, (B) electrostatic interaction energy, and (C) total interaction energy (sum of electrostatic and vdW interactions) of the REGN10933-RBD, REGN10987-RBD, and REGN10933+REGN10987-RBD complexes. (D, E) Total interaction energies of the residues at the binding regions of REGN10933 and REGN10987 with RBD (Figure S1). Results were obtained in the time window $[0, t_{max}]$ and averaged over five independent SMD runs.

Table 3. Nonbonded Interaction Energies (kcal/mol) of REGN10933-RBD, REGN10987-RBD, and REGN10933+REGN10987-RBD Complexes for the WT[a]

	REGN10933-RBD	REGN10987-RBD	REGN10933+REGN10987-RBD
E_{elec}	−65.7 ± 4.3	44.2 ± 3.4	−155.9 ± 4.4
E_{vdW}	−51.1 ± 1.8	−50.8 ± 2.4	−107.2 ± 3.2
E_{total}	−116.8 ± 6.1	−6.6 ± 5.8	−263.1 ± 7.6

[a]The results were obtained for a $[0-t_{max}]$ time window and averaged from five SMD trajectories.

interface with the spike protein is powerful in blocking a viral infection.

3.2.4. Delta Variant has a Little Effect on the Binding Affinities of REGN10933, REGN10987, and REGN10933+REGN10987 with RBD. Recent studies have indicated that mutated residues in RBD directly affected the neutralizing activity of most antibodies against Covid-19 variants.[15−26,50] In this work, we conducted SMD simulations for the most dangerous Delta and Omicron variants (Table S2) to shed light on the molecular mechanisms underlying the influence of mutated residues on the neutralizing ability of the REGN-COV2 cocktail.

As can be seen from Figure 5A, only REGN10933 has contact with RDB at L452 and T478 residues, where the mutation was made for the Delta variant. Therefore, SMD simulation was carried out for REGN10933-RBD and REGN10933+REGN10987-RBD, but not for REGN10987-RBD. Upon mutation, the RBD charge increases from +2e to

https://doi.org/10.1021/acs.jpcb.2c00708
J. Phys. Chem. B 2022, 126, 2812−2823

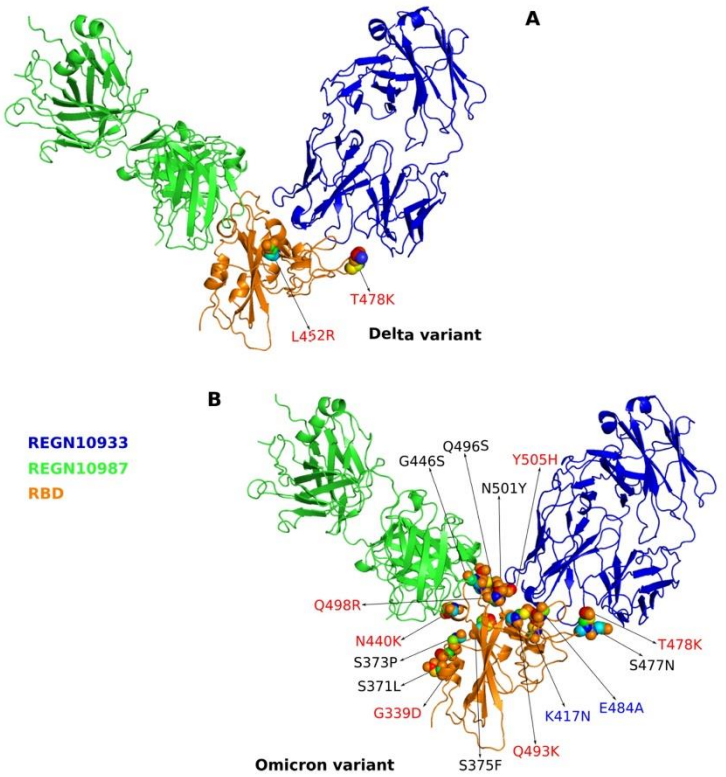

Figure 5. Mutations of (A) Delta and (B) Omicron variants in RBD. The mutations of the Omicron variant in RBD are at the binding regions for both constituents of the REGN-COV2 cocktail, while the mutations of the Delta variant in RBD influence only the REGN10933 binding site. Blue refers to residues that have charge in RBD-WT, while red denotes residues that have charge after mutation.

+4e (Table S3), but these mutations have a little effect on the interaction between antibodies and the spike protein. In particular, F_{max}, W, ΔG_{bind}, and ΔG_{unbind} of the Delta variant are close to those of WT (Figure 6 and Table 2), implying that, as for WT, REGN10933 and REGN10933+REGN10987 are also effective for this variant. This is because the L452R and T478K mutations do not significantly contribute to the REGN10933-RBD stability, as their total interaction energy varies from −0.5 and −3.4 kcal/mol (WT) to 0.4 and −3.5 kcal/mol (Delta) (Table 4).

As can be seen from Table 2 (columns 7 and 8), when two mAbs are combined, they show no difference in the binding affinity between the reference strain and the Delta strain, but they are known not to offer the same level of protection clinically. To clarify this issue from a biophysical point of view, we docked ACE2 to the complex of REGN10933, REGN10987, and RBD using the HDOCK software (Figure S2).[51,52] Since the distance between the centers of mass of RBD and ACE2 for the WT case (2.37 nm) is greater than for Delta (2.19 nm), two antibodies can prevent ACE2 from binding to the WT RBD to a greater extent than to the Delta RBD, which can lead to different protection activities. This effect is understandable if we take into account the ACE2-RBD attractive electrostatic interaction, which is stronger for Delta than for WT because ACE2 has a charge of −26e, while the charges of Delta RBD and WT RDB are +4e and +2e, respectively (Figure S2).

3.2.5. Omicron Variant Attenuates the Binding Affinities of REGN10933, REGN10987, and REGN10933+REGN10987 with RBD. For the Omicron variant, all 15 mutated residues in RBD interact with both REGN10933 and REGN10987 (Figure 5B). Therefore, we performed SMD simulations for all three complexes REGN10933-RBD, REGN10987-RBD, and REGN10933+REGN10987-RBD. After mutation, the RBD charge increases from +2e (WT) to +5e (Omicron) (Table S3), which enhances the repulsive interaction with positively charged REGN10933 (+3e) and REGN10987 (+6e) (Table S3), resulting in reduced binding affinity of the Omicron variant. This prediction has been confirmed by the SMD results obtained for three complexes (Figure 6 and Table 2). F_{max}, W, ΔG_{bind}, and ΔG_{unbind} of Omicron are clearly lower than those of WT, suggesting that REGN10933, REGN10987, and REGN10933+REGN10987 are less effective against this variant. To better understand this problem, we calculated the interaction energy of each mutated residue in RBD. The decrease in the interactions of REGN10933 and REGN10987

https://doi.org/10.1021/acs.jpcb.2c00708
J. Phys. Chem. B 2022, 126, 2812−2823

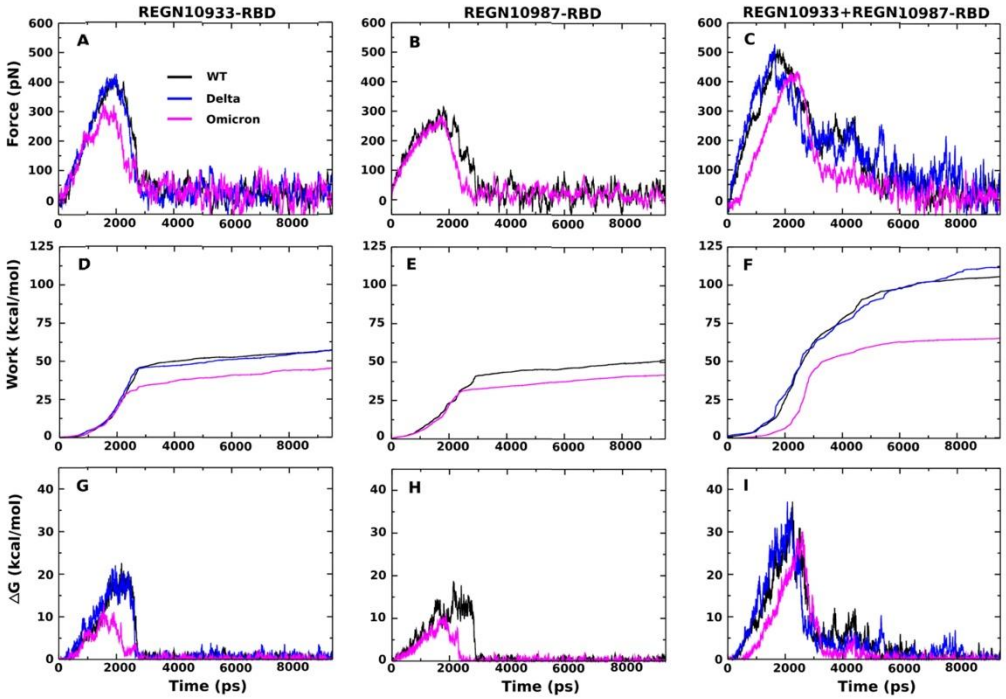

Figure 6. Time dependence of (A−C) pulling force, (D−F) pulling work, and (G−I) nonequilibrium free energy of the complexes. These results averaged over five independent SMD runs for WT and the variants.

Table 4. Total Interaction Energies (kcal/mol) of the Important Residues of RBD to REGN10933 and REGN10987 for the WT and the Variants[a]

mutation points on RBD		
WT	Delta	Omicron
G339: −0.1		D339: −2.5
S371: 0.03		L371: 0.1
S373: −0.2		P373: −0.1
S375: −0.03		F375: −0.04
K417: −71.1		N417: −5.0
N440: 0.1		K440: 6.4
G446: 0.02		S446: −0.8
L452: −0.5	R452: 0.4	
S477: −9.9		N477: −8.8
T478: −3.4	K478: −3.5	K478: −5.5
E484: −25.7		A484: −1.9
Q493: −3.9		K493: −8.5
G496: −0.3		S496: −2.1
Q498: 1.6		R498: 16.7
N501: −2.1		Y501: −1.2
Y505: −0.02		H505: 1.3

[a]The results were obtained in a $[0, t_{max}]$ time window averaged from five SMD trajectories.

with RBD is mainly due to the K417N, N440K, E484A, and Q498R mutations, which increases the interaction energy at these positions from −71.1, 0.1, −25.7, and 1.6 kcal/mol (WT) up to − 5.0, 6.4, −1.9, and 16.7 kcal/mol (Omicron) (Table 4). Although the total interaction energy of Q493K decreased from −3.9 kcal/mol (WT) to −8.5 kcal/mol (Omicron), this contribution is not enough to change the overall behavior of REGN-COV2 toward RBD in the Omicron variant. Thus, among the 15 mutations, K417N, N440K, E484A, and Q498R play a key role in reducing the effectiveness of REGN-COV2 antibodies against the Omicron variant.

3.3. Coarse-Grained Simulation Results. *3.3.1. REGN10933 Binds to RBD More Strongly than REGN10987.* Figure 7A represents the 1D-PMF constructed from REX-US simulations. A barrier separating the bound and unbound regimes occurs at ≈2.3 nm for both complexes. Hence, we decided to choose r_b = 2.3 nm to numerically compute the probability P_b in eq 6. To evaluate the binding affinity of antibodies to the RBD domain, we calculate the dissociation constant K_D from eq 5. To solve eq 6, we need to determine a cutoff r^* corresponding to a total volume limit to compute the probability of finding the system in the free monomer state and the free monomer concentration [A]. We select r^* at around 11 nm as there is no longer an interaction between antibody and RBD beyond this threshold. K_D as a function of the distance r^* tends to converge at large r^* as expected (Figure 7B), and the approximately converged value was reported as K_D in our calculations. The results of K_D values for REGN10933 and REGN10987 binding to the RBD domain

https://doi.org/10.1021/acs.jpcb.2c00708
J. Phys. Chem. B 2022, 126, 2812−2823

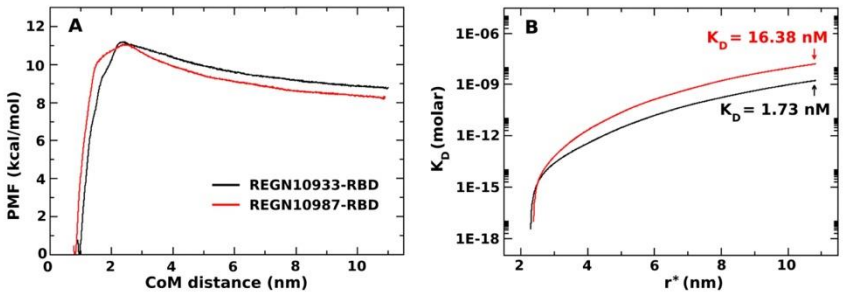

Figure 7. (Left) one-dimensional potential of mean force of REGN10933-RBD (black curve) and REGN10987-RBD (red curve). (Right) K_D curves as a function of r^* corresponding to the change in the total free monomer concentration.

are listed in Table 1. As seen, the binding affinity of REGN10933 is stronger than that of RENG10987, and the difference is about 9−10 times. Our calculation is consistent with the experimental results of these monoclonal antibodies where the K_D were measured using surface plasmon resonance technology.[12] From the experimental results, the K_D values of REGN10933 and REGN10987 are 3.37 and 45.2 nM, respectively, which means REGN10933 binds to RBD on the order of 13−14 times stronger than REGN10987.

3.4. PRODIGY Results. The free binding energy ΔG_{bind} calculated using PRODIGY is −10.7 ± 0.4 kcal/mol (K_D = 31 ± 8.96 nM) for REGN10933 and −10.2 ± 0.8 kcal/mol (K_D = 69 ± 25.33 nM) (Table 1) for REGN10987, implying that within the margin of error, this structure-based method cannot distinguish the binding affinity of REGN10933 from that of REGN10987. Therefore, PRODIGY is less accurate compared to our all-atom SMD and coarse-grained simulations, which show that, according to the experiment, REGN10933 binds to RBD more strongly than REGN10987. Applying PRODIGY to REGN10933+RENG10987-RBD, we obtained a binding free energy of −14.6 ± 1.0 kcal/mol (K_D = 0.056 ± 0.027 nM), which means that the cocktail can bind more tightly to the spike protein compared to its components. This result is consistent with the SMD result.

4. CONCLUSIONS

We studied the association of REGN10933 or REGN10987 or both REGN10933+REGN10987 with RBD of the SARS-COV-2 spike protein. The SMD results show that REGN10933 binds to RBD more strongly than REGN10987, which is consistent with the result calculated from coarse-grained REX-US. These computational results are in good agreement with the experimental results of Hansen et al.[12] Moreover, SMD modeling and PRODIGY-based evaluation demonstrated that the REGN10933+REGN10987 cocktail tethers to RBD with higher affinity than either REGN10933 or REGN10987 alone, suggesting that this cocktail is more capable of preventing viral activity than its components.

The stabilities of REGN10933-RBD and REGN10933+REGN10987-RBD are mainly contributed by electrostatics interactions, while the stability of REGN10987-RBD is decided by vdW interactions. Lys417(A), Glu484(A), and Phe486(A) residues of the spike protein were found to play a crucial role in the binding affinity for the REGN10933 antibody, which may contribute to its neutralizing ability.

We show that REGN10933 and REGN10933+REGN10987 seem to have a similar activity for the Delta variant and WT. However, they are not effective against the Omicron variant, which is consistent with recent experiments.[20−22,45]

■ ASSOCIATED CONTENT

Supporting Information

The Supporting Information is available free of charge at https://pubs.acs.org/doi/10.1021/acs.jpcb.2c00708.

Hydrogen bonded and nonbonded contact networks of (A) REGN10933-RBD and (B) REGN10987-RBD complexes (Figure S1); structures obtained by molecular docking for ACE2 in combination with REGN10987, REGN10933, and RBD of WT and Delta (Figure S2); η values determined for stabilities of protein domains and interfaces, as well as for interactions between antibodies and RBD in CG simulations (Table S1); mutations in RBD of Delta and Omicron variants; the name of the lineage is also displayed; and total charge of RBD for WT, Delta, and Omicron as well as antibodies REGN10933 and REGN10987 (Table S3) (PDF)

■ AUTHOR INFORMATION

Corresponding Author

Mai Suan Li − *Institute of Physics, Polish Academy of Sciences, 02-668 Warsaw, Poland*; orcid.org/0000-0001-7021-7916; Email: masli@ifpan.edu.pl

Authors

Hung Nguyen − *Institute of Physics, Polish Academy of Sciences, 02-668 Warsaw, Poland*

Pham Dang Lan − *Life Science Lab, Institute for Computational Science and Technology, Quang Trung Software City, 729110 Ho Chi Minh City, Vietnam; Faculty of Physics and Engineering Physics, VNUHCM-University of Science, 749000 Ho Chi Minh City, Vietnam*

Daniel A. Nissley − *Department of Statistics, University of Oxford, Oxford Protein Bioinformatics Group, OX1 2JD Oxford, United Kingdom*

Edward P. O'Brien − *Department of Chemistry, Penn State University, University Park, Pennsylvania 16802, United States; Bioinformatics and Genomics Graduate Program, The Huck Institutes of the Life Sciences and Institute for Computational and Data Sciences, Penn State University, University Park, Pennsylvania 16802, United States;* orcid.org/0000-0001-9809-3273

https://doi.org/10.1021/acs.jpcb.2c00708
J. Phys. Chem. B 2022, 126, 2812−2823

Complete contact information is available at:
https://pubs.acs.org/10.1021/acs.jpcb.2c00708

Author Contributions

○H.N. and P.D.L. contributed equally to this work.

Notes

The authors declare no competing financial interest.

■ ACKNOWLEDGMENTS

This work was supported by the Narodowe Centrum Nauki in Poland (Grant 2019/35/B/ST4/02086), and the Department of Science and Technology at Ho Chi Minh city (Grant 07/2020/HĐ-KHCNTT). E.P.O. acknowledges funding support from the National Science Foundation (MCB-1553291) and the National Institutes of Health (R35-GM124818). This research was supported by the supercomputer centre TASK in Gdansk, PLGrid infrastructure, Poland, and the computer cluster at ICST, Vietnam.

■ REFERENCES

(1) Wu, F.; Zhao, S.; Yu, B.; Chen, Y.-M.; Wang, W.; Song, Z.-G.; Hu, Y.; Tao, Z.-W.; Tian, J.-H.; Pei, Y.-Y.; et al. A new coronavirus associated with human respiratory disease in China. *Nature* **2020**, *579*, 265−269.

(2) Dong, E.; Du, H.; Gardner, L. An interactive web-based dashboard to track COVID-19 in real-time. *Lancet Infect. Dis.* **2020**, *20*, 533−534.

(3) Siemieniuk, R. A.; Bartoszko, J. J.; Ge, L.; Zeraatkar, D.; Izcovich, A.; Kum, E.; Pardo-Hernandez, H.; Qasim, A.; Martinez, J. P. D.; Rochwerg, B.; et al. Drug treatments for covid-19: living systematic review and network meta-analysis. *Br. Med. J.* **2020**, *45*, No. m2980.

(4) Weinreich, D. M.; Sivapalasingam, S.; Norton, T.; Ali, S.; Gao, H.; Bhore, R.; Musser, B. J.; Soo, Y.; Rofail, D.; Im, J.; et al. REGN-COV2, a neutralizing antibody cocktail, in outpatients with Covid-19. *N. Engl. J. Med.* **2021**, *384*, 238−251.

(5) Chen, P.; Nirula, A.; Heller, B.; Gottlieb, R. L.; Boscia, J.; Morris, J.; Huhn, G.; Cardona, J.; Mocherla, B.; Stosor, V.; et al. SARS-CoV-2 neutralizing antibody LY-CoV555 in outpatients with Covid-19. *N. Engl. J. Med.* **2021**, *384*, 229−237.

(6) Wrapp, D.; Wang, N.; Corbett, K. S.; Goldsmith, J. A.; Hsieh, C.-L.; Abiona, O.; Graham, B. S.; McLellan, J. S. Cryo-EM structure of the 2019-nCoV spike in thes prefusion conformation. *Science* **2020**, *367*, 1260−1263.

(7) Wang, C.; Li, W.; Drabek, D.; Okba, N. M. A.; Haperen van, R.; Osterhaus, A. D. M. E.; van Kuppeveld, F. J. M.; Haagmans, B. L.; Grosveld, F.; Bosch, B.-J. A human monoclonal antibody blocking SARS-CoV-2 infection. *Nat. Commun.* **2020**, *11*, No. 2251.

(8) Liu, L.; Wang, P.; Nair, M. S.; Yu, J.; Rapp, M.; Wang, Q.; Luo, Y.; Chan, J. F.-W.; Sahi, V.; Figueroa, A.; et al. Potent neutralizing antibodies against multiple epitopes on SARS-CoV-2 spike. *Nature* **2020**, *584*, 450−456.

(9) Chi, X.; Yan, R.; Zhang, J.; Zhang, G.; Zhang, Y.; Hao, M.; Zhang, Z.; Fan, P.; Dong, Y.; Yang, Y.; et al. A neutralizing human antibody binds to the N-terminal domain of the Spike protein of SARS-CoV-2. *Science* **2020**, *369*, 650−655.

(10) Wang, L.; Shi, W.; Chappell, J. D.; Joyce, M. G.; Zhang, Y.; Kanekiyo, M.; Becker, M. M.; Doremalen van, N.; Fischer, R.; Wang, N.; et al. Importance of neutralizing monoclonal antibodies targeting multiple antigenic sites on the middle east respiratory syndrome coronavirus spike glycoprotein to avoid neutralization escape. *J. Virol.* **2018**, *92*, No. e02002-17.

(11) ter Meulen, J.; Van Den Brink, E. N.; Poon, L. L. M.; Marissen, W. E.; Leung, C. S. W.; Cox, F.; Cheung, C. Y.; Bakker, A. Q.; Bogaards, J. A.; van Deventer, E.; et al. Human monoclonal antibody combination against SARS coronavirus: synergy and coverage of escape mutants. *PLoS Med.* **2006**, *3*, No. e237.

(12) Hansen, J.; Baum, A.; Pascal, K. E.; Russo, V.; Giordano, S.; Wloga, E.; Fulton, B. O.; Yan, Y.; Koon, K.; Patel, K.; et al. Studies in humanized mice and convalescent humans yield a SARS-CoV-2 antibody cocktail. *Science* **2020**, *369*, 1010−1014.

(13) Baum, A.; Fulton, B. O.; Wloga, E.; Copin, R.; Pascal, K. E.; Russo, V.; Giordano, S.; Lanza, K.; Negron, N.; Ni, M.; et al. Antibody cocktail to SARS-CoV-2 spike protein prevents rapid mutational escape seen with individual antibodies. *Science* **2020**, *369*, 1014−1018.

(14) Davies, N. G.; Abbott, S.; Barnard, R. C.; Jarvis, C. I.; Kucharski, A. J.; Munday, J. D.; Pearson, C. A. B.; Russell, T. W.; Tully, D. C.; Washburne, A. D.; et al. Estimated transmissibility and impact of SARS-CoV-2 lineage B.1.1.7 in England. *Science* **2021**, *372*, No. eabg3055.

(15) Abdool Karim, S. S.; Oliveira, T. de. New SARS-CoV-2 variants—Clinical, public, health, and vaccine implications. *N. Engl. J. Med.* **2021**, *384*, 1866−1868.

(16) Faria, N. R.; Mellan, T. A.; Whittaker, C.; Claro, I. M.; Candido, D.; da, S.; Mishra, S.; Crispim, M. A. E.; Sales, F. C. S.; Hawryluk, I.; McCrone, J. T.; et al. Genomics and epidemiology of the P.1 SARS-CoV-2 lineage in Manaus, Brazil. *Science* **2021**, *372*, 815−821.

(17) Mlcochova, P.; Kemp, S. A.; Dhar, M. S.; Papa, G.; Meng, B.; Ferreira, I. A. T. M.; Datir, R.; Collier, D. A.; Albecka, A.; Singh, S.; et al. SARS-CoV-2 B.1.617.2 Delta variant replication and immune evasion. *Nature* **2021**, *599*, 114−119.

(18) Kimura, I.; Kosugi, Y.; Wu, J.; Zahradnik, J.; Yamasoba, D.; Butlertanaka, E. P.; Tanaka, Y. L.; Uriu, K.; Liu, Y.; Morizako, N.; et al. The SARS-CoV-2 Lambda variant exhibits enhanced infectivity and immune resistance. *Cell Rep.* **2022**, *38*, No. 110218.

(19) Planas, D.; Veyer, D.; Baidaliuk, A.; Staropoli, I.; Guivel-Benhassine, F.; Rajah, M. M.; Planchais, C.; Porrot, F.; Robillard, N.; Puech, J.; et al. Reduced sensitivity of SARS-CoV-2 variant Delta to antibody neutralization. *Nature* **2021**, *596*, 276−280.

(20) Cao, Y.; Wang, J.; Jian, F.; Xiao, T.; Song, W.; Yisimayi, A.; Huang, W.; Li, Q.; Wang, P.; An, R.; et al. Omicron escapes the majority of existing SARS-CoV-2 neutralizing antibodies. *Nature* **2022**, *602*, 657−663.

(21) VanBlargan, L. A.; Errico, J. M.; Halfmann, P. J.; Zost, S. J.; Crowe, J. E., Jr.; Purcell, L. A.; Kawaoka, Y.; Corti, D.; Fremont, D. H.; Diamond, M. S. An infectious SARS-CoV-2 B.1.1.529 Omicron virus escapes neutralization by several therapeutic monoclonal antibodies. *Nat. Med.* **2022**, *28*, 490−495.

(22) Du, S.; Cao, Y.; Zhu, Q.; Yu, P.; Qi, F.; Wang, G.; Du, X.; Bao, L.; Deng, W.; Zhu, H.; et al. Structurally resolved SARS-CoV-2 antibody shows high efficacy in severely infected hamsters and provides a potent a cocktail pairing strategy. *Cell* **2020**, *183*, 1013−1023.e13.

(23) Ferraz, M. V. F.; Moreira, E. G.; Coêlho, D. F.; Wallau, G. L.; Lins, R. D. Immune evasion of SARS-CoV-2 variants of concern is driven by low affinity to neutralizing antibodies. *Chem. Commun.* **2021**, *57*, 6094−6097.

(24) Naveca, F. G.; Nascimento, V.; Souza, V.; Corado, A.; de, L.; Nascimento, F.; Silva, G.; Mejía, M. C.; Brandão, M. J.; Costa, Á.; Duarte, D.; et al. Spread of Gamma (P.1) sub-lineages carrying spike mutations close to the furin cleavage site and deletions in the N-terminal domain drives ongoing transmission of SARS-CoV-2 in Amazonas, Brazil. *Microbiol. Spectrum* **2022**, *10*, No. e0236621.

(25) Takashita, E.; Kinoshita, N.; Yamayoshi, S.; Sakai-Tagawa, Y.; Fujisaki, S.; Ito, M.; Iwatsuki-Horimoto, K.; Chiba, S.; Halfmann, P.; Nagai, H.; et al. Efficacy of antibodies and antiviral drug against Covid-19 Omicron variant. *N. Engl. J. Med.* **2022**, *386*, 995−998.

(26) Tada, T.; Zhou, H.; Dcosta, B. M.; Samanovic, M. I.; Mulligan, M. J.; Landau, N. R. Partial resistance of SARS-CoV-2 Delta variants to vaccine-elicited antibodies and convalescent sera. *iScience* **2021**, *24*, No. 103341.

(27) Webb, B.; Sali, A. Comparative protein structure modeling using MODELLER. *Curr. Protoc. Bioinf.* **2016**, *54*, 5.6.1−5.6.37.

(28) *The PyMOL Molecular Graphics System*, version 2.0; Schrödinger, LLC, 2017.
(29) Huang, J.; MacKerell, A. D., Jr. CHARMM36 all-atom additive protein force field: Validation based on comparison to NMR data. *J. Comput. Chem.* **2013**, *34*, 2135−2145.
(30) Abraham, M. J.; Murtola, T.; Schulz, R.; Páll, S.; Smith, J. C.; Hess, B.; Lindahl, E. GROMACS: High performance molecular simulations through multi-level parallelism from laptops to supercomputers. *SoftwareX* **2015**, *1*−*2*, 19−25.
(31) Bussi, G.; Donadio, D.; Parrinello, M. Canonical sampling through velocity rescaling. *J. Chem. Phys.* **2007**, *126*, No. 014101.
(32) Parrinello, M. Polymorphic transitions in single crystals: A new molecular dynamics method. *J. Appl. Phys.* **1981**, *52*, 7182−7190.
(33) Jorgensen, W. L.; Jenson, C. Temperature dependence of TIP3P, SPC, and TIP4P water from NPT Monte Carlo simulations: Seeking temperatures of maximum density. *J. Comput. Chem.* **1998**, *19*, 1179−1186.
(34) Hess, B.; Bekker, H.; Berendsen, H. J. C.; Fraaije, J. G. E. M. LINCS: A linear constraint solver for molecular simulations. *J. Comput. Chem.* **1998**, *18*, 1463−1472.
(35) Darden, T.; York, D.; Pedersen, L. Particle mesh Ewald: An Nlog(N) method for Ewald sums in large systems. *J. Chem. Phys.* **1993**, *98*, 10089−10092.
(36) Hockney, R. W.; Goel, S. P.; Eastwood, J. W. Quiet high-resolution computer models of a plasma. *J. Comput. Phys.* **1974**, *14*, 148−158.
(37) Binnig, G.; Quate, C. F.; Gerber, C. Atomic force microscope. *Phys. Rev. Lett.* **1986**, *56*, No. 930.
(38) Jarzynski, C. Nonequilibrium equality for free energy differences. *Phys. Rev. Lett.* **1997**, *78*, No. 2690.
(39) Hummer, G.; Szabo, A. Free energy reconstruction from nonequilibirium single-molecule pulling experiments. *Proc. Natl. Acad. Sci. U.S.A.* **2001**, *98*, 3658−3661.
(40) Truong, D. T.; Li, M. S. Probing the binding affinity by Jarzynski's nonequilibrium binding free energy and rupture time. *J. Phys. Chem. B* **2018**, *122*, 4693−4699.
(41) Wallace, A. C.; Laskowski, R. A.; Thornton, J. M. LIGPLOT: A program to generate schematic diagrams of protein-ligand interactions. *Protein Eng.* **1995**, *8*, 127−134.
(42) Nissley, D. A.; Vu, Q. V.; Trovato, F.; Ahmed, N.; Jiang, Y.; Li, M. S.; O'Brien, E. P. Electrostatic interactions govern extreme nascent protein ejection times from ribosomes and can delay ribosome recycling. *J. Am. Chem. Soc.* **2020**, *142*, 6103−6110.
(43) Leininger, S. E.; Trovato, F.; Nissley, D. A.; O'Brien, E. P. Domain topology, stability, and translation speed determine mechanical force generation on the ribosome. *Proc. Natl. Acad. Sci. U.S.A.* **2019**, *116*, 5523−5532.
(44) Elber, R.; Ruymgaart, A. P.; Hess, B. SHAKE parallelization. *Eur. Phys. J.: Spec. Top.* **2011**, *200*, 211−223.
(45) Nguyen, H. L.; Lan, P. D.; Thai, N. Q.; Nissley, D. A.; O'Brien, E. P.; Li, M. S. Does SARS-CoV-2 bind to human ACE2 more strongly than does SARS-CoV? *J. Phys. Chem. B* **2020**, *124*, 7336−7347.
(46) Nguyen, H.; Lan, P. D.; Nissley, D. A.; O'Brien, E. P.; Li, M. S. Electrostatic interactions explain the higher binding affinity of the CR3022 antibody for SARS-CoV-2 than the 4A8 antibody. *J. Phys. Chem. B* **2021**, *125*, 7368−7379.
(47) Kumar, S.; Rosenberg, J. M.; Bouzida, D.; Swendsen, R. H.; Kollman, P. A. THE weighted histogram analysis method for free-energy calculations on biomolecules. I. The method. *J. Comput. Chem.* **1992**, *13*, 1011−1021.
(48) Vangone, A.; Bonvin, A. M. Contacts-based prediction of binding affinity in protein-protein complexes. *eLife* **2015**, *4*, No. e07454.
(49) Xue, L. C.; Rodrigues, J. P.; Kastritis, P. L.; Bonvin, A. M.; Vangone, A. PRODIGY: a web server for predicting the binding affinity of protein-protein complexes. *Bioinformatics* **2016**, *35*, 3676−3678.
(50) Baum, A.; Ajithdoss, D.; Copin, R.; Zhou, A.; Lanza, K.; Negron, N.; Ni, M.; Wei, Y.; Mohammadi, K.; Musser, B.; et al. REGN-COV2 antibodies prevent and treat SARS-CoV-2 infection in rhesus macaques and hamsters. *Science* **2020**, *370*, 1110−1115.
(51) Yan, Y.; Zhang, D.; Zhou, P.; Li, B.; Huang, S.-Y. HDOCK: a web server for protein-protein and protein-DNA/RNA docking based on hybrid strategy. *Nucleic Acids Res.* **2017**, *45*, W365−W373.
(52) Yan, Y.; Tao, H.; He, J.; Huang, S.-Y. The HDOCK server for integrated protein-protein docking. *Nat. Protoc.* **2020**, *15*, 1829−1852.

https://doi.org/10.1021/acs.jpcb.2c00708
J. Phys. Chem. B 2022, 126, 2812−2823

3.2 Antibody-nanobody combination increases their neutralizing activity against SARS-CoV-2 and nanobody H11-H4 is effective against Alpha, Kappa and Delta variants

3.2.1 Introduction

mAb has emerged as a highly promising therapeutic class against SARS-CoV-2 infection [148]. Numerous studies have provided evidence that convalescent plasma obtained from individuals who have recovered from SARS-CoV-2 infection, containing neutralizing Ab generated as part of the adaptive immune response, can significantly enhance patient survival rates [284-286]. However, plasma-based therapies based on plasma encounter significant limitations, primarily related to scalability. Therefore, the pursuit of potent Ab-based therapies on an industrial scale is increasingly recognized as one of the most viable strategies in the fight against SARS-CoV-2. As discussed in the previous chapter, the S protein plays a pivotal role in viral infection. This multifunctional molecular machine interacts with the ACE2 receptor in human cells and serves as a prime target to neutralize Ab. Consequently, it has become the focal point of therapeutic and vaccine development efforts [287]. Within the S protein, RBD and NTD located in the S1 subunit, along with FP in the S2 subunit, are considered particularly significant targets for combating SARS-CoV-2 infection.

Ab can neutralize SARS-CoV-2 by binding to various regions, such as RBD, or NTD, or FP. However, the majority of Ab has been found to primarily target RBD [288-289], rendering it a pivotal focus. Unfortunately, varying experimental methods, conditions, and calibrations across different studies have yielded biased results concerning the binding affinity of Ab. This discrepancy has posed challenges in the development of Ab-based therapies for SARS-CoV-2 [288]. For example, CR3022, an Ab, that originates from a convalescent patient with SARS-CoV-2, has shown potential due to its robust binding to RBD, with K_D = 6.3 nM, as reported by Tian *et al.* [290], however, contrasting results have been reported in another study, indicating a much higher K_D = 115 nM, as documented by Yuan *et al.* [291]. This disparity underscores the need for a comprehensive understanding of Ab interactions with components of SARS-CoV-2 to facilitate the development of effective therapies.

Nb offers an alternative to conventional Ab for applications in diagnostics and structural biology [292]. Recently, they have gained prominence as therapeutic agents against SARS-CoV-2 [293-294]. Notably, H11-H4, an Nb derived from llamas, demonstrates binding to RBD with K_D = 11.8 nM [176]. This K_D value is higher than that reported by Tian *et al.* [290] for CR3022, suggesting that H11-H4 exhibits weaker binding to RBD compared to CR3022. However, in comparison to the K_D value reported by Yuan *et al.* [291], it becomes evident that H11-H4 binds to RBD more strongly than CR3022. In addition, it is important to note that Nb can be used either alone or in combination with Ab for the treatment of severely ill COVID-19 patients (Figure 3.2A) [176]. Although the binding affinity of Ab to SARS-CoV-2 has been computationally studied [165-166], the binding free energy of Nb has not been calculated, despite molecular modeling studies exploring its interaction with RBD. Furthermore, no theoretical investigation of how the combination of Ab and Nb affects their neutralizing ability has been conducted.

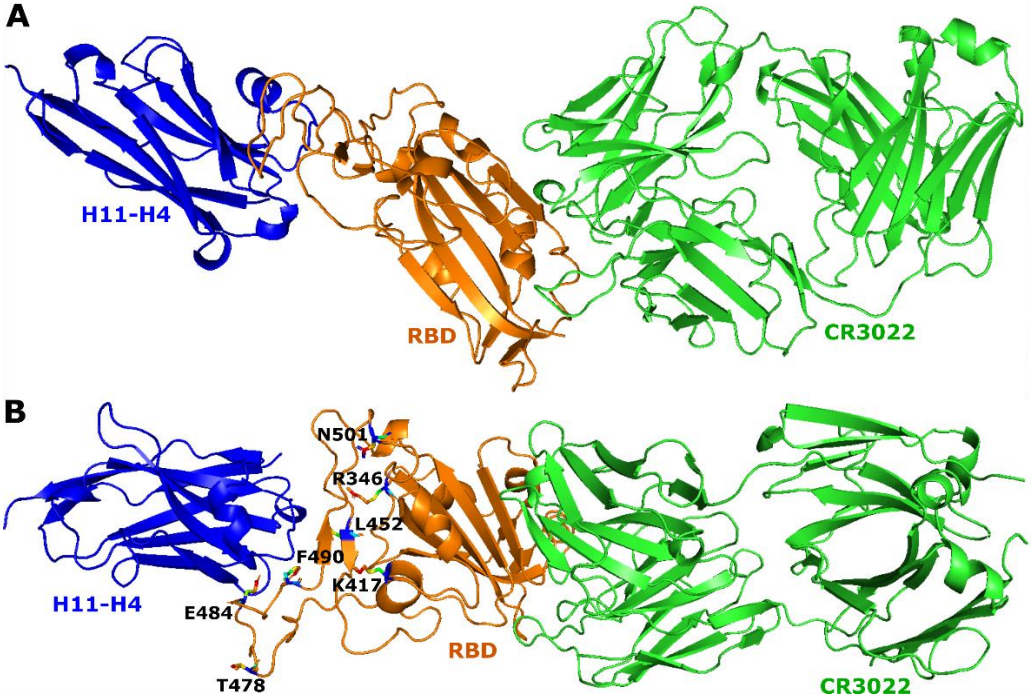

Figure 3.2: 3D structures of A) H11-H4 Nb and CR3022 Ab bound to RBD, and B) RBD mutations of variants Alpha, Beta, Gamma, Kappa, Delta, Lambda and Mu. They have contact with H11-H4, but not with CR3022.

Numerous experimental studies have been conducted on SARS-CoV-2 variants, including Alpha, Beta, Gamma, Kappa, Delta, Lambda, Omicrons, and others (Figure 3.2B) [114, 275-278, 295-296]. These studies have shown that many Abs and Nbs lose their neutralizing ability against SARS-CoV-2 due to these variants [279, 297]. However, recent studies showed that certain Ab and Nb can effectively neutralize most of these variants. For example, REGN10933 and REGN10987 Abs have demonstrated the ability to neutralize the Lambda variant, or Nbs derived from llamas have shown promise in combating the Delta variant [298-299].

In this study, we utilized all-atom SMD and Martini coarse-grained US simulations to estimate the binding affinity of CR3022 and H11-H4 with RBD, both individually and together.

For all-atom SMD simulations, the direction of H11-H4 or CR3022 pullout from the RBD binding region, as well as the direction of RBD pullout from the H11-H4 and CR3022 binding region, were determined. H11-H4–RBD and CR3022–RBD cases, an external force is applied to a dummy atom, which is linked to the C_α atom closest to the CoM of H11-H4 or CR3022. The pulling direction is aligned with the vector connecting the CoMs of RBD and Nb or Ab. For the H11-H4 + CR3022–RBD case, the pulling direction is selected differently due to the involvement of three molecules. An external force is applied to a dummy atom that is bonded to the C_α atom closest to RBD CoM, and the pulling direction is along the line connecting RBD CoM perpendicular to the line connecting CoMs of H11-H4 and CR3022

[192]. At v = 0.5 nm/ns, the force-time profiles for the three complexes show that CR3022 (F_{max} = 1214.2±21.2 pN) binds to RBD more strongly than H11-H4 (F_{max} = 925.6±15.2 pN). When RBD is extracted simultaneously from both CR3022 and H11-H4, F_{max} = 2034.9±27.7 pN, which is approximately twice as much as for CR3022–RBD and H11-H4–RBD individually. Note that although the rupture force F_{max} appears quite high due to fast pulling, the relative binding affinities of the complexes do not change with different pulling speeds [165]. This combination of CR3022 and H11-H4 is expected to enhance the binding affinity of RBD, thus increasing its neutralizing activity. The SMD results agree with the experimental results presented by Tian *et al.* [290] and Huo *et al.* [176] for H11-H4 and CR3022 that interact with SARS-CoV-2. Still, for CR3022–RBD complex, they contradict Yuan *et al.* [291]. The variation in binding affinity is attributed to differences in the experimental conditions of the two groups, as discussed by Yuan *et al.* [291]. Our all-atom SMD results also showed that the binding of H11-H4 to RBD is mediated by vdW interactions, while the binding of CR3022 and H11-H4+CR3022 to RBD is driven by electrostatic interactions.

Martini coarse-grained US was used to estimate the binding free energy between CR3022 and H11-H4 to RBD. Binding free energy was obtained at -19.8 and -21.4 kcal/mol for H11-H4–RBD and CR3022–RBD, respectively. The lower binding free energy of CR3022 indicates that this Ab binds more tightly to RBD, which is consistent with previous computational studies [165]. For H11-H4 + CR3022–RBD, we obtained a binding free energy of -23.9 kcal/mol, consistent with the SMD results, indicating that the combination of H11-H4 and CR3022 enhances binding affinity and improves their ability to neutralize SARS-CoV-2.

Additionally, all-atom SMD was also employed to assess the binding affinity between H11-H4 and various SARS-CoV-2 variants, including Alpha, Beta, Gamma, Kappa, Delta, Lambda, and Mu. We found that H11-H4 exhibits effective neutralization of Alpha, Kappa and Delta variants, positioning it as a highly promising therapeutic for COVID-19.

3.2.2 Publication

a) Abstract: The global spread of COVID-19 is devastating health systems and economies worldwide. While the use of vaccines has yielded encouraging results, the emergence of new variants of SARS-CoV-2 shows that combating COVID-19 remains a big challenge. One of the most promising treatments is the use of not only antibodies, but also nanobodies. Recent experimental studies revealed that the combination of antibody and nanobody can significantly improve their neutralizing ability through binding to the SARS-CoV-2 spike protein, but the molecular mechanisms underlying this observation remain largely unknown. In this work, we investigated the binding affinity of the CR3022 antibody and H11-H4 nanobody to the SARS-CoV-2 receptor binding domain (RBD) using molecular modeling. Both all-atom steered molecular dynamics simulations and coarse-grained umbrella sampling showed that, consistent with the experiment, CR3022 associates with RBD more strongly than H11-H4. We predict that the combination of CR3022 and H11-H4 considerably increases their binding affinity to the spike protein. The electrostatic interaction was found to control the association strength of CR3022, but the van der Waals interaction dominates in the case of H11-H4. However, our study for a larger set of nanobodies and antibodies showed

that the relative role of these interactions depends on the specific complex. Importantly, we showed Beta, Gamma, Lambda, and Mu variants reduce the H11-H4 activity while Alpha, Kappa, and Delta variants increase its neutralizing ability, which is in line with experiment reporting that the nanobody elicited from the llama is very promising for fighting against the Delta variant.

- DOI: 10.1038/s41598-022-14263-1
- Publication source: https://www.nature.com/articles/s41598-022-14263-1

b) Author contribution statements:

Hung Van Nguyen
Division of Theoretical Physics
Institute of Physics, Polish Academy of Sciences
Al. Lotnikow 32/46
02-668 Warsaw, Poland

INSTYTUT FIZYKI
POLSKIEJ AKADEMII NAUK

STATEMENT

I declare that I am the co-author of the publication:

- Nguyen, H.; Li, M. S. **Antibody-nanobody combination increases their neutralizing activity against SARS-CoV-2 and nanobody H11-H4 is effective against Alpha, Kappa and Delta variants**. Sci. Rep. **2022**, *12* (9701).

My contributions consisted of designing the research, performing simulations, analyzing the results, preparing figures, and writing the manuscript.

Warsaw, August 2024

Hung Van Nguyen

Prof. Mai Suan Li, PhD
Division of Theoretical Physics
Institute of Physics, Polish Academy of Sciences
Al. Lotnikow 32/46
02-668 Warsaw, Poland
E-mail: masli@ifpan.edu.pl

INSTYTUT FIZYKI
POLSKIEJ AKADEMII NAUK

STATEMENT

I declare that I am the co-author of the publication:

- Nguyen, H.; Li, M. S. **Antibody-nanobody combination increases their neutralizing activity against SARS-CoV-2 and nanobody H11-H4 is effective against Alpha, Kappa and Delta variants**. Sci. Rep. **2022**, *12* (9701).

My contribution consisted of designing the research, interpreting the data, writing the manuscript, and supervising the overall project.

Warsaw, August 22 2024

Mai Suan Li

c) Publication for this section:

Antibody-nanobody combination increases their neutralizing activity against SARS-CoV-2 and nanobody H11-H4 is effective against Alpha, Kappa and Delta variants

Hung Nguyen, Mai Suan Li

Sci. Rep. 2022, 12:9701

www.nature.com/scientificreports

scientific reports

Check for updates

OPEN

Antibody–nanobody combination increases their neutralizing activity against SARS-CoV-2 and nanobody H11-H4 is effective against Alpha, Kappa and Delta variants

Hung Nguyen[1] & Mai Suan Li[1,2]✉

The global spread of COVID-19 is devastating health systems and economies worldwide. While the use of vaccines has yielded encouraging results, the emergence of new variants of SARS-CoV-2 shows that combating COVID-19 remains a big challenge. One of the most promising treatments is the use of not only antibodies, but also nanobodies. Recent experimental studies revealed that the combination of antibody and nanobody can significantly improve their neutralizing ability through binding to the SARS-CoV-2 spike protein, but the molecular mechanisms underlying this observation remain largely unknown. In this work, we investigated the binding affinity of the CR3022 antibody and H11-H4 nanobody to the SARS-CoV-2 receptor binding domain (RBD) using molecular modeling. Both all-atom steered molecular dynamics simulations and coarse-grained umbrella sampling showed that, consistent with the experiment, CR3022 associates with RBD more strongly than H11-H4. We predict that the combination of CR3022 and H11-H4 considerably increases their binding affinity to the spike protein. The electrostatic interaction was found to control the association strength of CR3022, but the van der Waals interaction dominates in the case of H11-H4. However, our study for a larger set of nanobodies and antibodies showed that the relative role of these interactions depends on the specific complex. Importantly, we showed Beta, Gamma, Lambda, and Mu variants reduce the H11-H4 activity while Alpha, Kappa and Delta variants increase its neutralizing ability, which is in line with experiment reporting that the nanobody elicited from the llama is very promising for fighting against the Delta variant.

Fully human monoclonal antibodies (mAbs) have recently been demonstrated to be a promising class of therapeutics against severe acute respiratory syndrome coronavirus 2 (SARS-CoV-2) infection[1]. Several studies have shown that convalescent plasma from recovered SARS-CoV-2 patients, which contains neutralizing antibodies generated by an adaptive immune response, can effectively improve patient survival rate[2–4]. However, plasma-based therapies cannot be produced on a large scale. Thus, the search for potent antibody therapies on an industrial-scale is becoming one of the most feasible strategies for combating SARS-CoV-2. Spike (S) protein of SARS-CoV-2 (Fig. 1A), a multi-functional molecular machine that binds to angiotensin-converting enzyme 2 (ACE2) of the human cell (Fig. 1B), is a target of neutralizing antibodies and is the focus of therapeutic and vaccine development efforts[5].

S protein consists of N-terminal S1 and C-terminal S2 subunits[6,7] (Fig. 1A) that have a function to mediate receptor binding and membrane fusion[6,8]. Especially, both the receptor-binding domain (RBD) and the N-terminal domain (NTD) in the S1 subunit are important for determining host ranges and tissue nutrition[9,10]. NTD is able to recognize specific sugar components during the initial association of the virus and host cells[11,12] and is critical in the transition of the S protein from pre-fusion to post-fusion[13,14].

RBD binding to human cells is a critical step, allowing coronaviruses to enter cells and cause infection[15,16]. The S2 subunit contains heptad repeat region 1 (HR1) and 2 (HR2), both of which interact to form a six-helix

[1]Institute of Physics, Polish Academy of Sciences, Al. Lotnikow 32/46, 02-668 Warsaw, Poland. [2]Life Science Lab, Institute for Computational Science and Technology, Quang Trung Software City, Tan Chanh Hiep Ward, District 12, Ho Chi Minh City, Vietnam. ✉email: masli@ifpan.edu.pl

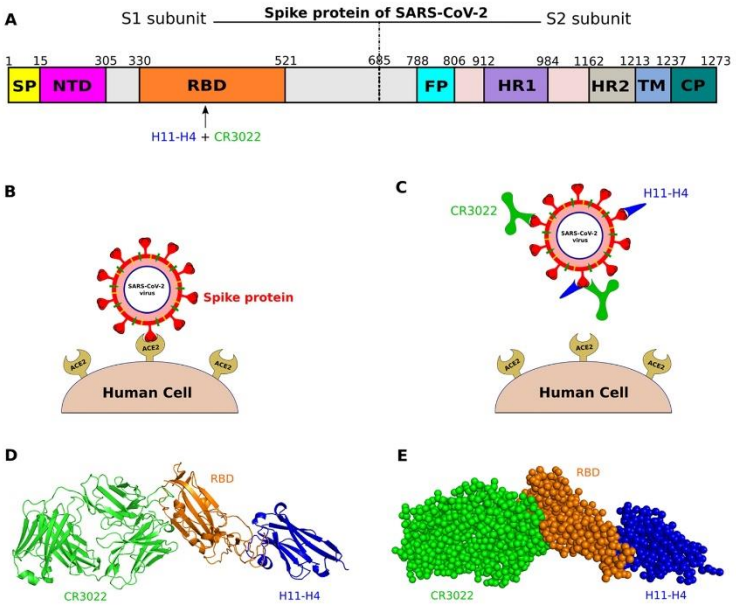

Figure 1. (**A**) Schematic description of the S protein of SARS-CoV-2, which consists of the S1 and S2 subunits. (**B**) SARS-CoV-2 S protein binds to human ACE2 before entering cells. (**C**) H11-H4 and CR3022 bind to S protein, preventing the virus from entering cells. The 3D structures of H11-H4 and CR3022 bound to RBD are shown in all-atom (**D**) and coarse-grained (**E**) models.

	K_d, ΔG_{exp} (experiment)	ΔG_{bind} (our simulation)
H11-H4–RBD	$K_d = 11.8 \pm 1.5$ nM (Huo et al.[25]) $\Delta G_{exp} = -10.9 \pm 0.1$ kcal/mol	− 19.8
CR3022–RBD	$K_d = 6.3$ nM (Tian et al.[20]) $\Delta G_{exp} = -11.3$ kcal/mol OR $K_d = 115 \pm 3.0$ nM (Yuan et al.[21]) $\Delta G_{exp} = -9.5 \pm 0.02$ kcal/mol	− 21.4
H11-H4 + CR3022–RBD	N/A	− 23.9

Table 1. Dissociation constant K_d (nM) obtained by in vitro experiment. The experimental binding free energy ΔG_{exp} was converted from K_d using $\Delta G_{exp} = RTlnK_d$. Binding free energy ΔG_{bind} (kcal/mol) was obtained using coarse-grained umbrella sampling and Eq. (4) for the H11-H4–RBD, CR3022–RBD, and H11-H4 + CR3022–RBD complexes. Shown is the WT case .

bundle (6-HB) fusion core structure that brings the viral and cell target membranes into close proximity for fusion. Peptide fusion (FP) targeting the HR1 and HR2 regions is considered as a key factor for developing broad-spectrum viral fusion to inhibit t6-HB formation and virus-cell membrane fusion[17]. Therefore, RBD and NTD from the S1 subunit and FP from the S2 subunit of protein S may serve as important therapeutic targets against SARS-CoV-2 infection.

Antibodies that can neutralize SARS-CoV-2 can bind to RBD, NTD or FP, but most of them have been found to bind with RBD[18,19], making RBD a key target. Due to different experimental methods, conditions and calibrations, recent studies have provided biased results regarding the binding affinity of antibodies, which has hampered the development of antibody-based therapy for SARS-CoV-2[18]. For instance, according to Tian et al.[20], antibody CR3022, derived from a convalescent SARS-CoV-2 patient may be active due to its strong binding to RBD with a dissociation constant $K_d = 6.3$ nM, but another study reported that this is not the case, since the corresponding K_d is much higher ($K_d = 115$ nM) (Table 1)[21].

Nanobodies are small, but stable and straightforward to manufacture. They serve as an alternative to conventional antibodies as diagnostic and structural biology tools[22], and have recently been developed as therapeutic agents against SARS-CoV-2[23,24]. H11-H4, a llama-derived nanobody binds to RBD with $K_d = 11.8$ nM[25] (Table 1),

which is greater than K_d obtained by Tian et al.[20] for CR3022, suggesting that H11-H4 binds to RBD weaker than the CR3022 antibody. However, when comparing with K_d reported by Yuan et al.[21] (Table 1), we see that H11-H4 binds to RBD more strongly than CR3022. To solve this dispute we will calculate binding affinity using molecular simulation.

It is important to note that nanobodies can be used alone or in combination with antibodies in the treatment of severely ill patients with Covid-19 (Fig. 1C)[25]. The binding affinity of antibodies to SARS-CoV-2 was computationally studied[26,27], but the binding free energy of nanobodies has not been calculated although their interaction with RBD was explored using molecular modeling. Moreover, the effect of the combination of antibodies and nanobodies on their neutralizing ability has not been theoretically investigated. Therefore, in this paper, using the coarse grained model and umbrella sampling, we will calculate the binding free energy of the H11-H4 nanobody with RBD and study how the combination of the CR3022 antibody and the H11-H4 nanobody changes their ability to neutralize SARS-CoV-2.

There have been many experimental studies of SARS-CoV-2 variants such as Alpha, Beta, Gamma, Kappa, Delta, Lambda, Mu, etc.[28–36], which reduce the neutralizing ability of most antibodies and nanobodies against SARS-CoV-2[37–39]. The Beta variant reduces the neutralizing potential of antibodies REGN10933, C105, BD23 and H11-H4 nanobodies, etc[38]. However, recent studies have identified some potential antibodies and nanobodies that can effectively neutralize most of these variants[40,41]. For instance, cocktails of antibodies REGN10933 and REGN10987 can neutralize the Lambda variant[40], while nanobodies obtained from the llama are good agents against the Delta variant[41]. In this study, we use steered molecular dynamics (SMD) to access the binding affinity between H11-H4 and the SARS-CoV-2 variants, including Alpha, Beta, Gamma, Kappa, Delta, Lambda and Mu variants. We show that H11-H4 can effectively neutralize Alpha and Delta variants, which makes it a very promising therapy for Covid-19.

Material and methods

PDB structures of the three studied systems. The structures of H11-H4–RBD, CR3022–RBD, and H11-H4 + CR3022–RBD complexes were extracted from the Protein Data Bank with PDB ID: 6ZH9[25]. Modeler package[42] was used to add the missing residues. The structure of H11-H4 + CR3022–RBD complex is shown in Fig. 1D (all-atom) and Fig. 1E (coarse-grained) prepared by using the PyMOL package[43]. All mutations including variants Alpha, Beta, Gamma, Kappa, Delta, Lambda and Mu were generated by using the mutagenesis tool in PyMOL package.

All-atom molecular dynamics simulations. All-atom molecular dynamics (MD) simulations were performed using the CHARMM36M force field[44] implemented in the GROMACS 2016 package[45] at 310 K and isotropic pressure of 1 bar, which was obtained using the v-rescale[46] and Parrinello-Rahman[47] algorithms, respectively. The water model TIP3P[48] was used for all systems. Bond lengths were constrained by the linear constraint solver (LINCS) algorithm[49], allowing a time step of 2 fs.

Electrostatic and van der Waals interactions were calculated with a cutoff of 1.4 nm, and the non-bonded interaction pair-list was updated every 10 fs. The Particle Mesh Ewald algorithm[50] was used to treat long-range electrostatic interactions. Periodic boundary conditions were applied in all directions. The energy of the system was first minimized by using the steepest-descent algorithm, then a short 3 ns MD simulation was performed in the NVT and NPT ensembles. Production MD simulation of 100 ns was performed with the help of the leap-frog algorithm[51]. For each complex, using the "gmx_mpi cluster" tool available in GROMACS, we grouped the snapshots collected from the 100 ns of conventional MD simulation into clusters. We then selected 5 representative structures from the five most populated clusters and used them as the initial configuration for running 5 trajectories of steered molecular dynamics (SMD) simulations[52–55].

Steered molecular dynamics. We carried out SMD simulations to pull H11-H4 or CR3022 from the binding region of RBD as well as pulling RBD from the binding region of H11-H4 and CR3022 (Fig. 2). In the case of H11-H4–RBD and CR3022–RBD, an external force is applied to a dummy atom, which is linked to the Cα atom closest to the center of mass (COM) of H11-H4 or CR3022. The pulling direction is parallel to the vector connecting COMs of RBD and nanobody or antibody (Fig. 2A,B). In order to prevent RBD from drifting under the action of an external force, its backbone was restrained, but the side chain could fluctuate. The choice of pulling direction is different in the case of H11-H4 + CR3022–RBD due to the presence of three molecules. In this case an external force is applied to a dummy atom that is bonded to the Cα atom closest to the COM of RBD, and the pulling direction is along the line connecting The RBD COM in perpendicular to the line connecting the COMs of H11-H4 and CR3022 (Fig. 2C). During the SMD simulation the backbone of H11-H4 and CR3022 was restrained. For convenience, three complexes H11-H4–RBD, CR3022–RBD and H11-H4 + CR3022–RBD were rotated so that the pulling direction was always along the z-axis (Fig. 2).

One of the limitations of unidirectional pulling is that not all rotational states of proteins can be sampled. However, as shown in previous works[26,55], this approach provides reasonable results on the relative binding affinity of protein–protein complexes.

The pulling force experienced by a stretched molecule is calculated as follows:

$$F = k(\Delta z - vt) \tag{1}$$

where k is the stiffness of the spring, v is the pulling velocity, Δz is the displacement of a real atom connected to the spring in the direction of pulling, respectively. The spring constant k was set to 600 kJ/(mol nm^2) (≈ 1020 pN/nm), which is a typical value used in atomic force microscopy (AFM) experiments[56].

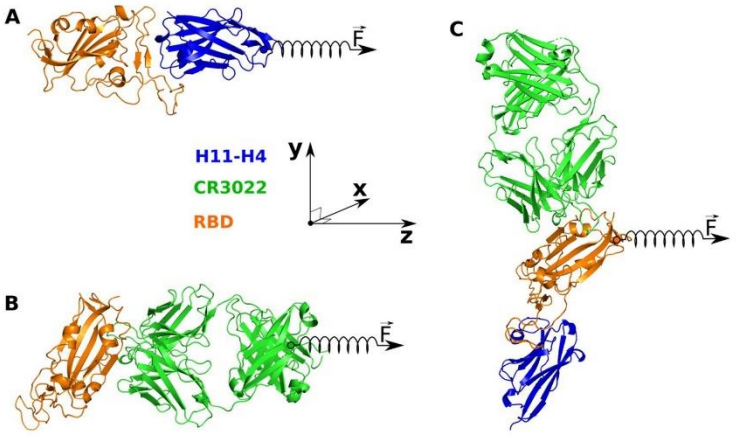

Figure 2. Structure of H11-H4 + CR3022–RBD retrieved from PDB with ID 6ZH9. RBD is shown in orange, while green and blue describe CR3022 and H11-H4. (**A**) H11-H4–RBD complex, external force $\vec{F}$ is applied to the H11-H4 nanobody through a dummy atom connected to a spring. (**B**) CR3022–RBD complex, $\vec{F}$ is applied to the CR3022 antibody. (**C**) H11-H4 + CR3022–RBD complex, $\vec{F}$ is applied to RBD. The pulling direction in SMD simulations is shown with a spring along the z-axis.

Using the force–displacement profile obtained from SMD simulations, the non-equilibrium work (W) performed by the pulled chain (H11-H4, CR3022 or H11-H4 + CR3022) was estimated using the trapezoidal rule:

$$W = \int F dz = \sum_{i=1}^{N} \frac{F_{i+1} + F_i}{2}(z_{i+1} - z_i) \tag{2}$$

where N is the number of simulation steps, F_i and z_i are the force determined by Eq. (1) and the position at step i, respectively.

To estimate the binding free energy (ΔG), we can use Jarzynski's equality[57] extended to the case when the applied external force grows at a constant speed v[58]:

$$exp\left(\frac{-\Delta G}{k_B T}\right) = \left\langle exp\left(\frac{W_t - \frac{1}{2}k(z_t - vt)^2}{k_B T}\right)\right\rangle_N \tag{3}$$

here $\langle \ldots \rangle_N$ is the average over N trajectories, z_t is the time-dependent displacement, and W_t is the non-equilibrium work at time t determined by Eq. (2).

From Eq. (3), we can extract the equilibrium free energy if the number of SMD trajectories is large enough and the pulling is sufficiently slow. Therefore, this approach is practical for small systems[59] but not for large systems such as those studied in this work. However, we can estimate the non-equilibrium binding and unbinding barriers separating the transition state (TS) from the bound state at $t = 0$ and the unbound state at t_{end}[60], which allows us to discern weak binding from strong binding.

Rectangular boxes with dimension of $10 \times 9 \times 25$ nm^3, $10 \times 11 \times 25$ nm^3 and $10 \times 18 \times 25$ nm^3 were used for H11-H4–RBD, CR3022–RBD and H11-H4 + CR3022–RBD, respectively. The complexes were immersed in a 0.15 M sodium chloride salt solution and counter ions were added to neutralize the system. In order to show that our results on the relative binding affinity is independent of the pulling speed, for each system, 5 different trajectories were run at $v = 0.5$ and 1 nm/ns.

Coarse-grained simulation. Since the combination of SMD with Jarzynski's equality does not allow us to calculate the equilibrium binding free energy, we will use umbrella sampling (US). However, this approach is very time consuming if we use all-atom models, because in our case the proteins and antibodies are large. Therefore, we used the MARTINI 2.2 force field developed for coarse-grained (CG) modeling of biological systems such as biological membrane, protein, nucleotide, and etc[61–63]. This force field is accurate enough for extracting the interaction energy for a pair of proteins in an aqueous environment from constraint force profiles. The standard MARTINI water model was used with a minimum distance between water beads of 1.0 nm[64]. The system was neutralized by adding sodium chloride salt solution. The temperature was set at T = 300 K with a Berendsen thermostat, and pressure was set at p = 1.0 bar with a Berendsen barostat[65,66]. Bond lengths in the aromatic amino acid side chains and the bonds between the backbone and side chains were constrained by the LINCS algorithm[49].

To perform coarse-grained umbrella sampling[67] (CG-US) simulations, we made a series of configurations along the z-axis involving 81 windows each of 0.1 nm (Fig. S1). Here z is the reaction coordinate (RC). The choice of the z-axis has been already described in the SMD method. Namely, for CR3022-RBD and H11-H4-RBD this axis connects two COMs (Fig. S1A,B), while for H11-H4 + CR3022-RBD it is parallel to the line connecting COMs of H11-H and CR3022 (Fig. S1C).

To create an initial configuration for the first window, energy minimization was performed and the neutralized and solvated structure was simulated for 1 ns with position restraints throughout the structure to allow the solvent to equilibrate around the solute. Temperature and pressure were relaxed for 10 ns. The resulting conformation was then used as the initial conformation in a subsequent 100 ns run without position restraints. The last snapshot obtained in this run will be used as the initial configuration for the first window in CG-US simulations.

To generate the initial configuration for other windows, we pulled antibody, nanobody or RBD to the corresponding window. Then we performed energy minimization and equilibration using a 5 ns MD simulation restraining the distance between COMs of subsystems. The last snapshot obtained in this simulation will be used as an initial conformation for the production run.

To hold one chain (H11-H4, CR3022 or RBD) around the center of each window, we applied a bias harmonic potential with a spring constant of 600 kJ/mol/nm^2 to make sure that the interacting surface of both targets is not change. To get a good sampling, for each window, we performed a conventional MD production run of 1000 ns. The WHAM procedure[68] is then used to determine a one-dimensional potential of mean force (1D PMF) as a function of the reaction coordinate z.

The binding free energy (ΔG_{bind}) is defined as the difference between the free energies in the bound and unbound states[69]:

$$\Delta G_{bind} = \left(-k_B T ln \int^{bound} e^{\frac{-G_{1D}(z)}{k_B T}}\right) - \left(-k_B T ln \int^{unbound} e^{\frac{-G_{1D}(z)}{k_B T}}\right) \quad (4)$$

here $G_{1D}(z)$ is the 1D PMF as a function of z, k_B is the Boltzmann constant, and T is the absolute temperature. Symbols $\int^{bound}$ and $\int^{unbound}$ refer to summation over bound and unbound regions, respectively. To determine the cut-off distance between the bound and unbound states we calculated the number interchain contacts as a function of the distance between pulled and nonpulled chains in CG-US simulations. Then the cutoff distance is the distance above which interchain contacts disappear (Fig. S2).

Measures used in data analysis. A hydrogen bond (HB) is formed if the distance between donor D and acceptor A is less than 0.35 nm, the H-A distance is less than 0.27 nm, and the D-H-A angle is greater than 135 degrees. A non-bonded contact (NBC) between two residues is formed if the shortest distance between their atoms is within 0.39 nm. 2D contact networks of HBs and NBCs of CR3022–RBD and H11-H4–RBD were displayed using the LIGPLOT package[70]. The standard deviation (Er) are approximately expressed as follows:

$$E_r = \sqrt{\frac{\sum_{i=1}^{N} (x_i - \langle x \rangle)^2}{N-1}} \quad (5)$$

where N is the total number of data points in the data set, x_i is the individual value of the *ith* in the data set, and $\langle x \rangle$ is the mean value of the data set.

Results and discussion

Hydrogen bond and non-bonded contact networks of CR3022-RBD and H11-H4-RBD complexes: analysis based on the PDB structure. Using the 6ZH9 PDB structure, we build networks of hydrogen bonds (HBs) and non-bonded contacts (NBCs) of H11-H4 and CR3022 with RBD (Fig. S3A–D). The numbers of H11-H4 and CR3022 residues that form HB and NBC with RBD are 11 and 19, respectively. There are 9 and 10 HBs for H11-H4-RBD and CR3022-RBD, respectively, while the numbers of NBCs of H11-H4-RBD and CR3022-RBD correspond to 14 and 20. The number of HBs and NBCs in the crystal structure cannot determine the binding affinity, since other factors also matter. However, more HBs and NBCs may indicate higher binding affinity, which suggests that CR3022 has a higher binding affinity for RBD than H11-H4. To verify this we will carry out SMD and coarse-grained umbrella simulations.

Binding affinity of H11-H4 and CR3022 to RBD: SMD results. *CR3022 binds to RBD more strongly than H11-H4 and combination of antibody and nanobody enhances their neutralizing activity.* Force–time profiles obtained at $v = 0.5$ nm/ns for the three complexes (Fig. 3A, Table 2) show that CR3022 ($F_{max} = 1214.2 \pm 21.2$ kcal/mol) binds to RBD more strongly than H11-H4 ($F_{max} = 925.6 \pm 15.2$ kcal/mol) to RBD. It should be noted that the rupture force F_{max} appears to be quite high due to the fast pulling. In the so-called Bell approximation, where the transition state separating the bound state from the unbound state is independent of external force, $F_{max} \sim \ln(v)$[71], where v is the puling speed. Beyond the Bell approximation, the dependence of F_{max} on v is more complex[72].

As expected, F_{max} increases with increasing of pulling speed (Tables 2 and S1, Figs. 3A and S4A). The unbinding time t_{max} of CR3022–RBD is also longer than H11-H4–RBD, and this time decreases with increasing v. It is important to note that if RBD is simultaneously extracted from the CR3022 antibody and H11-H4 nanobody, then at $v = 0.5$ nm/ns, $F_{max} = 2034.9 \pm 27.7$ kcal/mol is required, which is approximately twice as much as in CR3022–RBD and H11-H4–RBD. Therefore, the combination of nanobody and antibody is expected to increase the binding affinity for RBD, which increases their neutralizing activity.

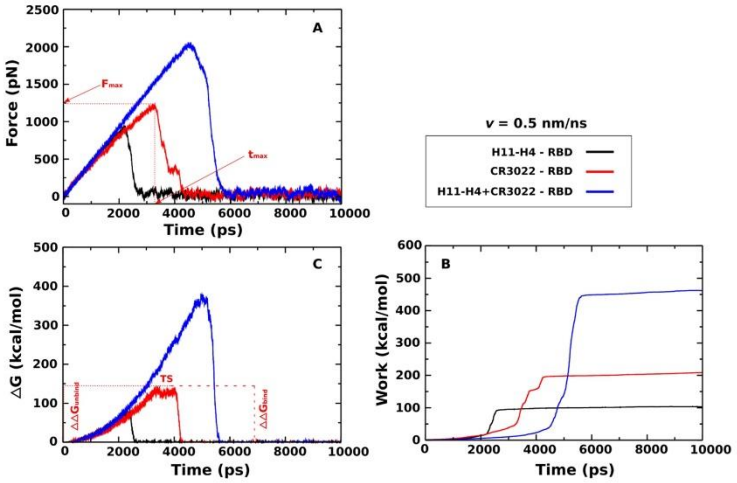

Figure 3. Time dependence of the pulling force (**A**), work (**B**), and (non-equilibrium energy profiles (**C**) of the H11-H4-RBD, CR3022-RBD, and H11-H4 + CR3022-RBD. The results were obtained at $v = 0.5$ nm/ns and averaged from five independent SMD runs.

	$v = 0.5$ nm/ns		
	H11-H4	CR3022	H11-H4 + CR3022
F_{max} (pN)	925.6 ± 15.2	1214.2 ± 21.2	2034.9 ± 27.7
t_{max} (ps)	2219.3 ± 38.5	3203.4 ± 36.9	4539.8 ± 47.2
W (kcal/mol)	101.6 ± 3.4	208.6 ± 5.3	461.3 ± 5.7
$\Delta\Delta G_{unbind}$ (kcal/mol)	82.5 ± 2.1	140.2 ± 2.9	379.0 ± 4.2
$\Delta\Delta G_{bind}$ (kcal/mol)	82.1 ± 2.5	137.9 ± 3.7	378.5 ± 4.4

Table 2. Rupture force (F_{max}), rupture time (t_{max}), work of the external force (W), and non-equilibrium binding free energy ΔG_{bind} and ΔG_{unbind} for the H11-H4–RBD, CR3022–RBD, and H11-H4 + CR3022–RBD complexes. The results were obtained from five independent SMD trajectories for the WT case at a pulling speed of $v = 0.5$ nm/ns. The errors represent standard deviations.

Since the non-equilibrium work (W) is better than F_{max} for characterizing the relative binding affinity[73], we will look at it in detail. W increased rapidly until the pulled molecule (H11-H4, CR3022 or RBD) left the binding region, reaching a stable value when two subsystems ceased to interact (Fig. 3B), and also increases with v[74]. For $v = 0.5$ nm/ns, we obtained $W = 101.6 \pm 3.4$, 208.6 ± 5.3 and 461.3 ± 5.7 kcal/mol for H11-H4–RBD, CR3022–RBD, and H11-H4 + CR3022–RBD, respectively (Table 2). Therefore, similar to F_{max}, our results obtained for W further support the fact that CR3022 is more active than H11-H4 and their combination increases their binding strength to RBD.

Figure 3C displays the time dependence of the non-equilibrium binding free energy (ΔG) estimated from Eq. (3) for the three complexes at $v = 0.5$ nm/ns. The maximum corresponds to the transition state (TS) with $\Delta G = \Delta G_{TS}$. We have $\Delta G_{bound} = \Delta G(t_0 = 0) \approx 0$ kcal/mol at the beginning of the bound state, while the unbound state occurs at the end of simulation $\Delta G_{unbound} = \Delta G(t_{end}) \approx 0$ kcal/mol. Thus, the binding and unbinding free energy energies (barriers), defined as $\Delta\Delta G_{bind} = \Delta G_{TS} - \Delta G_{unbound}$ and $\Delta\Delta G_{unbind} = \Delta G_{TS} - \Delta G_{bound}$, are roughly equal. $\Delta\Delta G_{unbind} = 82.5 \pm 2.1$, 140.2 ± 2.9, and 379.0 ± 4.2 kcal/mol for H11-H4–RBD, CR3022–RBD, and H11-H4 + CR3022–RBD, respectively, and $\Delta\Delta G_{bind} = 82.1 \pm 2.5$, 137.9 ± 3.7 and 378.5 ± 4.4 kcal/mol (Table 2). This provides further evidence that CR3022 binds to RBD more tightly than H11-H4, and the binding affinity is higher if both H11-H4 and CR3022 are combined.

To ensure that our result does not depend on the pulling speed, we also conducted SMD simulations for $v = 1$ nm/ns. Although F_{max}, W, and the non-equilibrium binding free energy increase with increasing v, the main conclusion about the relative binding affinities of the three complexes remains the same (Fig. S4, Table S1).

Therefore, our SMD data indicate that CR3022 binds more strongly to RBD than H11-H4, which is consistent with the experiment of Tian et al.[20] and Huo et al.[25] (Table 1). Measuring K_d, Yuan et al.[21] reported that the binding affinity of CR3022 for RBD is lower than that reported by Huo et al.[25] for H11-H4. From this point of view our

result is in conflict with Yuan et al.[21] and Huo et al.[25] The discrepancy may be caused by different techniques used by the two groups. Namely, Yuan et al.[21] used biolayer interferometry binding assays, while isothermal titration calorimetry was employed by Huo et al.[25] The advantage of our computational study is that we used the same model to compare the relative binding affinity, giving us confidence that CR3022 is a better binder than H11-H4.

Binding of H11-H4 to RBD is driven by vdW interaction, but binding of CR3022 and H11-H4 + CR3022 is driven by electrostatic interactions. A cutoff of 1.0 and 1.2 nm for van der Waals and electrostatic energies was applied to investigate the interaction of H11-H4–RBD, CR3022–RBD and H11-H4 + CR3022–RBD complexes. Fig. 4A1,A2 display the time dependence of the total non-bonded interaction energy E_{total}, which is the sum of electrostatic (E_{elec}) and van der Waals (E_{vdW}) energies of H11-H4, CR3022, and H11-H4 + CR3022 interacting with RBD. These results were averaged over five SMD trajectories.

At $v = 0.5$ nm/ns, when bound, the E_{elec} of H11-H4–RBD, CR3022–RBD and H11-H4 + CR3022–RBD starts at a negative value, but in all three cases E_{elec} eventually reaches ≈ 50 kcal/mol in the unbound state. E_{vdW} of three complexes is also negative in the bound state reaching 0 kcal/mol in the unbound state (Fig. 4A2). Neglecting the contribution of entropy, the results shown in Fig. 4A1,A2 reaffirm the ordering of stability H11-H4 + CR3022 > CR3022 > H11-H4.

We calculated the mean interaction energy in the bound state by averaging over the time window $[0, t_{\max}]$, where $t_{\max}$ is shown in Table 3. At $v = 0.5$ nm/ns, for CR3022–RDB, we obtained $E_{\text{elec}} = -252.8 \pm 3.7$ kcal/mol, which is clearly lower than $E_{\text{vdW}} = -77.1 \pm 1.3$ kcal/mol, implying that binding of CR3022 to RBD is driven by electrostatic interactions. This observation was also obtained previously[26]. The opposite occurs for the case of H11-H4, where the vdW interaction ($E_{vdW} = -61.8 \pm 1.2$ kcal/mol) is lower than the electrostatic interaction ($E_{elec} = -8.9 \pm 0.7$ kcal/mol), indicating that the vdW interaction dominates, but not the electrostatic interaction. Thus, the nature of binding of the H11-H4 nanobody is very different from CR3022 and the question of whether this remains true for other nanobodies is left for future research.

If H11-H4 and CR3022 simultaneously bind to RBD, we obtained $E_{\text{elec}} = -355.5 \pm 2.3$ kcal/mol and $E_{\text{vdW}} = -146.1 \pm 1.1$ kcal/mol, which means that as in the single CR3022 case, the electrostatic interaction is more important than the vdW interaction in stabilizing the complex with RBD. The role of electrostatic and vdW interactions revealed in SMD simulations with $v = 0.5$ nm/ns remains unchanged for other pulling speed ($v = 1$ nm/ns) (Fig. S5, Table S2).

Role of specific residues in binding of H11-H4 and CR3022 to RBD. To understand the role of each residue at the interface (Fig. 4B1,B2) in stabilization of the three complexes, we calculated its interaction energy in the $[0, t_{\max}]$ time window for pulling speed $v = 0.5$ nm/ns. For CR3022–RBD, residues Lys378(C), Lys386(C) and Asp428(C) of RBD, and residues Asp56(A) and Glu58(A) of CR3022 have the total non-bonded interactions smaller than − 20 kcal/mol (Fig. 4B1). For H11-H4–RBD, residues Glu484(C) and Gln493(C) of RBD and residue Arg52(D) of H11-H4 have the interaction energy smaller than − 20 kcal/mol (Fig. 4B2). Having a very low interaction energy of about − 156.3 kcal/mol, the Glu484(C) residue plays a very important role in the binding of the H11-H4 nanobody with the spike protein. Since the residue at position 484 is related to variants Beta (South Africa, lineage B.1.351, K417N, E484K, N501Y mutations), Gamma (Brazil, P.1 lineage, K417T, E484K, N501Y mutations), Kappa (India, B.1.617.1 lineages, L452R and E484Q mutations), and Mu (Colombia, B.1.621, R346K, E484K and N501Y), it is very interesting to consider these variants in more detail (see below).

The role of electrostatic and vdW interactions in the binding of nanobodies and antibodies to RBD depends on the specific system. Our previous work[26] showed that the electrostatic interaction governs the binding of CR3022 to RBD, while in the present work the vdW interaction is found to be more important for H11-H4 nanobody. An interesting question emerges is if this conclusion is valid for other systems. To answer this question, we calculated the interaction energy for the ten antibody-RBD complexes and ten nanobody-RBD complexes using their PDB structures and the CHARMM36M force field with the TIP3P water model.

For antibodies, electrostatic interaction dominates over vdW interaction for the five antibodies, while vdW interaction takes over electrostatic interaction for the other five antibodies (Table S3). For nanobodies, the vdW interaction is more important than the Coulomb interaction in five cases, while the opposite occurs in the other four complexes. In the case of WNb 10-RBD, their role is almost the same (Table S4). Consequently, which interaction is dominant in the association of the antibodies and nanobodies with the spike protein depends on the specific system.

Effects of mutations on binding affinity of H11-H4 to RBD: SMD results. As mentioned in the previous section, for the WT case, residue 484 makes an important contribution to the stability of the H11-H4–RBD complex. It has recently been demonstrated that this residue decreases the neutralizing activity of antibodies and nanobodies against the Covid-19 variants[37,41] (see Table S5 for mutation points in some variants). To shed light on the molecular mechanisms underlying this interesting phenomenon we performed a series of SMD simulations at a pulling speed $v = 0.5$ nm/ns for the Alpha (United Kingdom, lineage B.1.1.7, N501Y), Beta, Gamma, Kappa, Delta (India, lineage B.1.617.2, L452R, T478K), Lambda (Peru, lineage C37, L452Q, F490S) and Mu variants (Table S5). Note that CR3022 does not have contact with all R346, K417, L452, T478, E484, F490 and N501 residues of RBD, where the mutation is made for the aforementioned SARS-CoV-2 variants (Fig. S6). Therefore, we carried out SMD simulation only for H11-H4–RBD.

Beta, Gamma, Lambda and Mu variants reduce the binding affinity of H11-H4 to RBD. As seen from Fig. 5A1–A3 and Table 4, $F_{\max}$, W, $\Delta\Delta G_{\text{bind}}$ and $\Delta\Delta G_{\text{unbind}}$ of Beta, Gamma, Lambda and Mu variants are lower than those

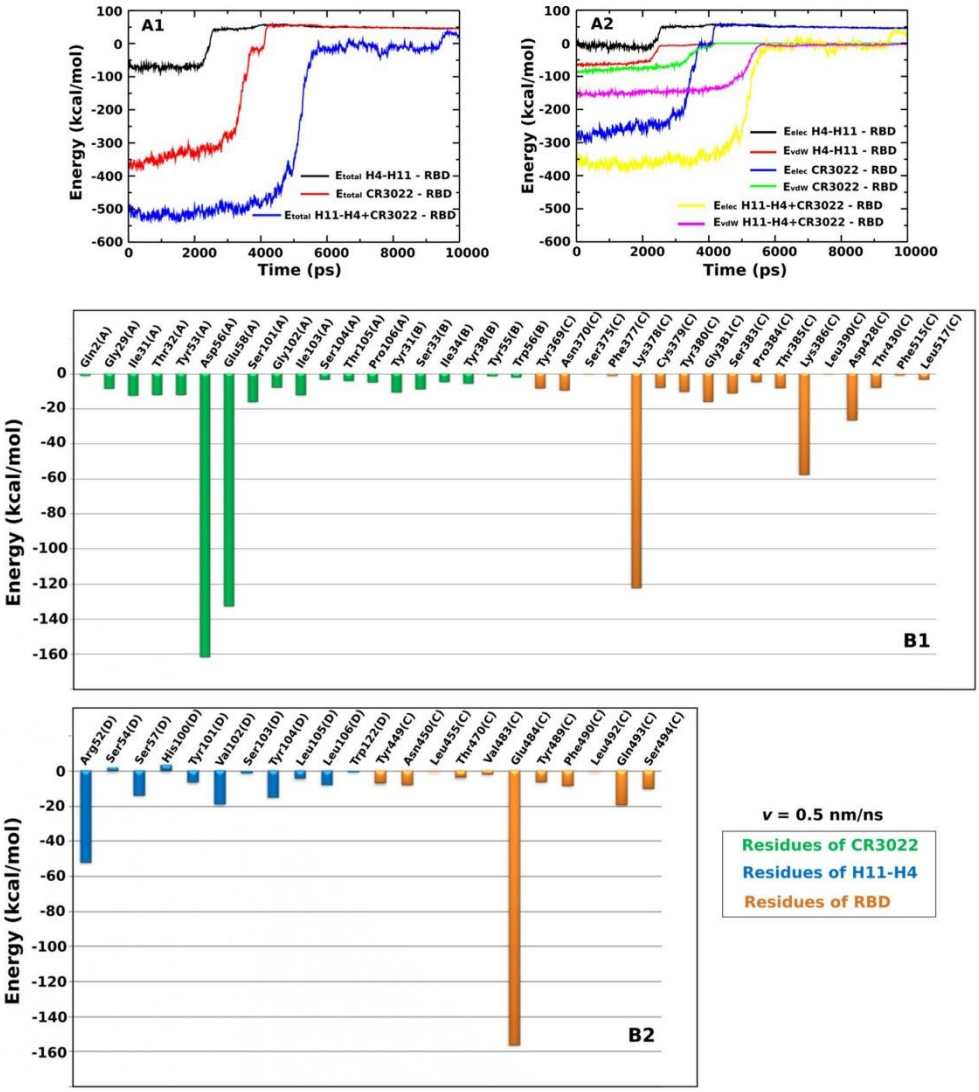

Figure 4. Time dependence of the total non-bonded interaction energy (sum of electrostatic and vdW) (**A1**) , and electrostatic and vdW interaction energies (**A2**) of the H11-H4-RBD, CR3022-RBD and H11-H4 + CR3022-RBD complexes. Total non-bonded interaction energy of residues located at the binding region of H11-H4-RBD (**B1**) and CR3022-RBD (**B2**). The results were obtained for a time window [0, t_{max}] and averaged from five independent SMD runs at pulling speed $v = 0.5$ nm/ns.

of WT, suggesting that H11-H4 is less active against these variants. The decrease in the interaction between H11-H4 and RBD caused by the Beta, Gamma and Mu variants is mainly due to the E484K mutation, which increases the total non-bonded interaction energy at this position from − 156.3 kcal/mol (WT) to 62.9, 72.2 and 79.2 kcal/mol for Beta, Gamma and Mu variants, respectively (Table 5). The strong attractive interaction becomes even repulsive after E484K mutation.

Meanwhile, the decrease in the interaction of H11-H4 with the Lambda variant occurs predominantly due to L452Q and F490S, which change the total non-bonded interaction energy from − 0.2 to − 8.4 kcal/mol (WT)

	$v = 0.5$ nm/ns		
	H11-H4–RBD	CR3022–RBD	H11-H4 + CR3022–RBD
E_{vdW}	− 61.8 ± 1.2	− 77.1 ± 1.3	− 146.1 ± 1.1
E_{elec}	− 8.9 ± 0.7	− 252.8 ± 3.7	− 355.5 ± 2.3
E_{Total}	− 70.7 ± 1.9	− 329.9 ± 5.0	− 501.6 ± 3.4

Table 3. Non-bonded interaction energies (kcal/mol) of the H11-H4–RBD, CR3022–RBD, and H11-H4 + CR3022–RBD complexes. The results were obtained for a $[0\text{-}t_{max}]$ time window and averaged from five SMD trajectories performed at a pulling speed of $v = 0.5$ nm/ns. The errors represent standard deviations.

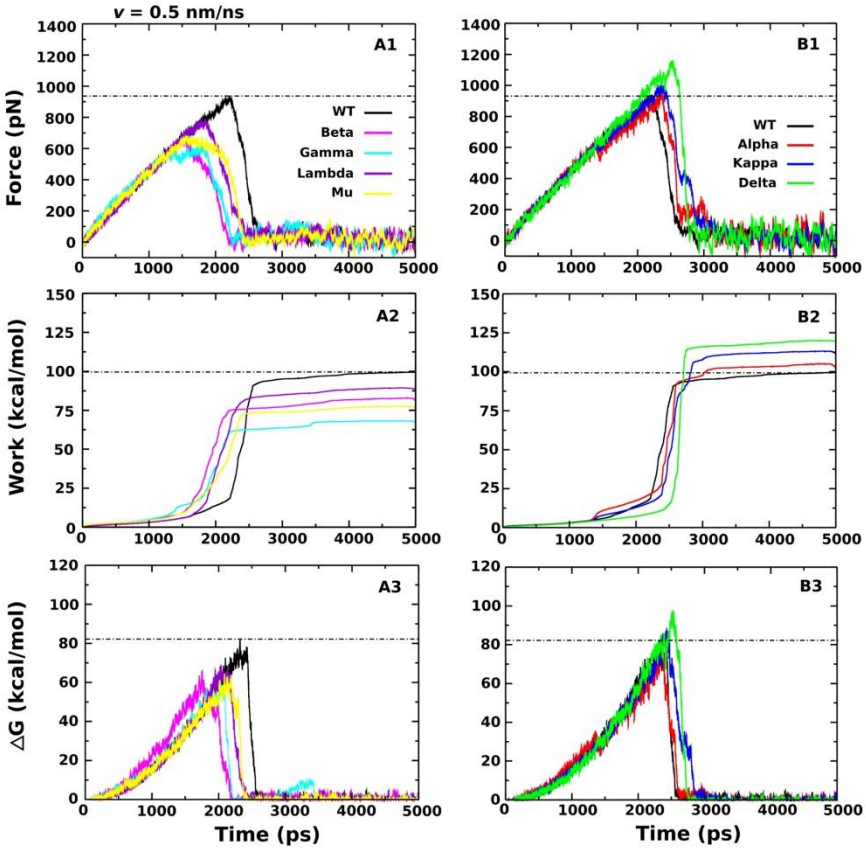

Figure 5. Time dependence of the force (**A1** and **B1**), work (**A2** and **B2**), and non-equilibrium free energy (**A3** and **B3**) of H11-H4-RBD. The results were obtained for WT and different variants at $v = 0.5$ nm/ns and averaged from five independent SMD runs.

to − 0.7 and − 0.1 kcal/mol (Lambda variant) (Table 5). The residues K417N-T and N501Y belong to the Beta, Gamma and Mu (only N501Y) variants, but do not interact with H11-H4. The R346K mutation reduced the total non-bonded interaction energy at this point from 71.5 (WT) to 62.8 kcal/mol (Mu variant) (Table 5), but this gain is not enough to compensate for the loss due to the E484K mutation for the Mu variant.

Alpha, Kappa and Delta variants increase the binding affinity of H11-H4 to RBD. In addition to the Beta, Gamma, Lambda and Mu variants, we also examined the binding affinity of H11-H4 to Alpha, Kappa and Delta

	WT	Beta (B.1.351)	Gamma (P.1)	Lambda (C37)	Mu (B.1.621)	Alpha (B.1.1.7)	Kappa (B.1.617.1)	Delta (B.1.617.2)
F_{max} (pN)	925.6 ± 42.2	714.5 ± 36.1	621.3 ± 38.7	776.2 ± 41.3	670.5 ± 33.1	982.6 ± 47.7	1018 ± 57.9	1162.1 ± 52.3
W (kcal/mol)	101.6 ± 3.3	80.8 ± 4.5	67.1 ± 4.9	87.4 ± 5.1	76.6 ± 6.0	105.8 ± 5.8	111.3 ± 9.3	119.5 ± 7.7
$\Delta\Delta G_{unbind}$ (kcal/mol)	82.5 ± 2.1	66.4 ± 3.6	61.3 ± 4.1	68.1 ± 4.4	64.6 ± 3.3	83.8 ± 3.1	87.5 ± 7.0	97.6 ± 6.2
$\Delta\Delta G_{bind}$ (kcal/mol)	82.1 ± 2.9	65.9 ± 4.1	58.7 ± 3.7	67.8 ± 4.8	64.2 ± 3.4	82.7 ± 3.6	85.8 ± 7.3	97.3 ± 5.4

Table 4. Rupture force (F_{max}), pulling work (W), and non-equilibrium binding (ΔG_{bind}) and unbinding (ΔG_{unbind}) free energies obtained from five independent SMD trajectories with $v = 0.5$ nm/ns for H11-H4–RBD. Results are shown for WT and variants Alpha, Beta, Gamma, Kappa, Delta, Lambda and Mu. The errors represent standard deviations.

WT	Beta (B.1.351)	Gamma (P.1)	Lambda (C37)	Mu (B.1.621)	Alpha (B.1.1.7)	Kappa (B.1.617.1)	Delta (B.1.617.2)
R346: 71.5				K346: 62.8			
K417: 0	N417: 0	T417: 0					
L452: − 0.2			Q452: − 0.7			R452: 58.6	R452: 56.5
T478: 0							K478: 0
E484: − 156.3	K484: 62.9	K484: 72.2		K484: 79.2		Q484: − 20.1	
F490: − 8.4			S490: − 0.1				
N501: 0	Y501: 0	Y501: 0		Y501: 0	Y501: − 0.1		

Table 5. The interaction energy (kcal/mol), which is the sum of the electrostatic and vdW interaction energy, between the important residues of RBD and H11-H4 in WT and different variants. The results were obtained in a [0, t_{max}] time window and averaged from five SMD trajectories performed at a pulling speed of $v = 0.5$ nm/ns. Black and red refer to WT and mutations, respectively.

variants. Unlike Beta, Gamma, Lambda and Mu variants, the F_{max}, W, $\Delta\Delta G_{bind}$ and $\Delta\Delta G_{unbind}$ of Alpha, Kappa and Delta variants increase (Fig. 5B1–B3; Table 4), implying that H11-H4 can neutralize these variants better than WT.

For the Alpha variant, although the mutation point N501Y does not significantly contribute to the stability of H11-H4–RBD (Table 5), the binding affinity is insignificantly stronger than that of WT (Fig. 5B1–B3; Table 4). The total non-bonded interaction energy of N501Y slightly drops from 0 (WT) to − 0.1 kcal/mol. For the Kappa variant, the E484Q mutation destabilizes the H11-H4–RBD complex, as the corresponding total non-bonded interaction energy increases from − 156.3 (WT) to − 20.1 kcal/mol (Table 5). The L452R mutation also weakens the interaction with H11-H4 due to an increase in total non-bonded interaction energy from − 0.2 (WT) to 58.6 kcal/mol (Table 5). Based on the total non-bonded interaction energy obtained at mutation positions 484 and 452, we cannot explain why the Kappa variant enhances the stability of H11-H4–RBD complex. Same as the Kappa variant, the L452R mutation of the Delta variant has an increase in the total non-bonded interaction energy from − 0.2 (WT) to 56.5 kcal/mol (Table 5), but the binding affinity is still much higher than WT. So what is the reason for the increased binding affinity between H11-H4 and RBD in the Kappa and Delta variants?

To solve these issues, we calculated the total interaction energy not only for the residues related to the mutation points, but also for all important residues (Fig. 6A,B). For WT, the total energy is − 89.3 kcal/mol, which is higher than Alpha (− 99.1 kcal/mol), Kappa (− 118.4 kcal/mol) and Delta (− 129.3 kcal/mol). For Gamma, Mu, Beta and Lambda we obtained 368.2, 335.1, 320.9 and − 49.3 kcal/mol, respectively, which is clearly higher than for WT. Therefore, the order of stability is as follows: Gamma < Mu < Beta < Lambda < WT < Alpha < Kappa < Delta. This finding is consistent with a report that nanobodies elicited from a llama could neutralize the Delta variant[41]. In addition, we also predict that H11-H4 maybe an excellent candidate to treat Alpha and Kappa variants.

Binding free energy of H11-H4 and CR3022 to RBD: coarse-grained umbrella sampling results. The SMD, known as a method used to investigate the unbinding process of a small molecule to other molecules, is capable of predicting relative binding affinity but cannot be used to calculate the binding free energy. Overall, although the SMD method has provided a good correlation with experimental results[26,52,55,75], their predictions are not always perfect. Therefore, we also used coarse-grained umbrella sampling to determine the binding free energies in an effort to elucidate the interactions of H11-H4–RBD, CR3022–RBD and H11-H4 + CR3022–RBD complexes.

The MARTINI CG-US was used to estimate the binding free energy (ΔG_{bind}). To show that the equilibrium phase has been reached, we calculated the 1D PMF for three time intervals of 500, 800 and 1000 ns. Since the

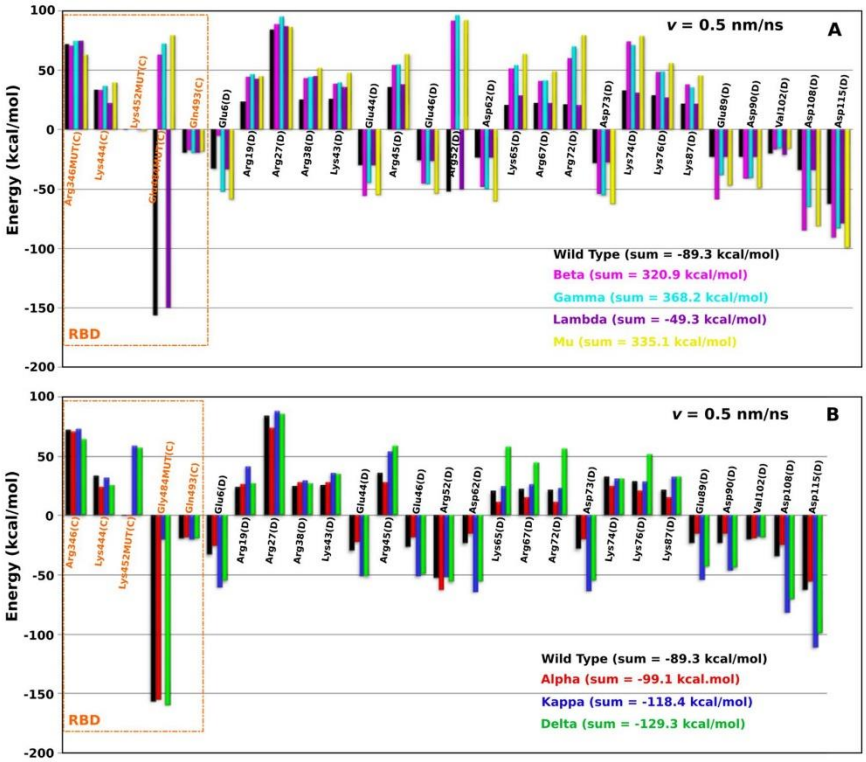

Figure 6. Total non-bonded interactions of the important residues of (**A**) H11-H4-RBD of WT and variants Beta, Gamma, Lambda and Mu, and (**B**) H11-H4-RBD of WT and variants Alpha, Kappa and Delta. The results were obtained in the time window [0, t_{max}] and averaged from five independent SMD runs at a pulling speed of $v = 0.5$ nm/ns.

1D PMF profiles for these windows are essentially the same (Fig. S7) our data was equilibrated. Therefore, the profile obtained from the largest window (Fig. 7) was used for estimating the binding free energy.

In order to use Eq. (4) to extract the binding free energy from the 1D PMF profiles we must estimate the cutoff distance between bound and unbound states, which was defined in "Material and methods". From the distance dependence of the number of interchain contacts (Fig. S2) we obtained the cutoff distance of 4.9, 2.8 and 3.0 nm for H11-H4 + CR3022-RBD, H11-H4–RBD and CR3022–RBD, respectively. Using these cutoff distances, Eq. (4) and the 1D PMF profiles shown in Fig. 7, we obtained $\Delta G_{bind} = -19.8$ kcal/mol for H11-H4–RBD and − 21.4 kcal/mol for CR3022-RBD (Table 1). The low value of ΔG_{bind} of CR3022 indicates that this antibody tightly binds to the S protein which is consistent with previous computational studies[26]. Moreover, in agreement with the SMD results shown above and the in vitro results reported by Huo et al.[25] ($K_d = 11.8$ nM, $\Delta G_{bind} = -10.9$ kcal/mol for H11-H4) and Tian et al.[20] ($K_d = 6.3$ nM, $\Delta G_{bind} = -11.3$ kcal/mol for CR3022), H11-H4 binds to RBD weaker than CR3022. Obviously, the ΔG_{bind} value obtained with the MARTINI CG-US is much lower than the experimental data, which may be related to the force field we used and the complexity of the studied systems.

According to our CG-US results, the relative binding affinity of CR3022 and H11-H4 is ΔG_{bind}(H11-H4)/ΔG_{bind}(CR3022) = − 19.8/− 21.4 = 0.93, which is not too far from experimental value ΔG_{exp}(H11-H4)/ΔG_{exp}(CR3022) = − 10.9/− 11.3 = 0.97. Thus, although the difference between simulation and experiment in absolute binding free energy is quite large, agreement on the relative binding affinity is satisfactory. In addition, bearing in mind that it is very challenging to obtain the absolute binding free energy even for small ligands using different MD based methods, our results are reasonable.

For H11-H4 + CR3022–RBD we obtained $\Delta G_{bind} = -23.9$ kcal/mol, which shows that, consistent with the SMD results, the combination of antibody and nanobody enhances their binding affinity. Since ΔG_{bind} (H11-H4 + CR3022)-ΔG_{bind}(CR3022) = − 23.9 − (− 21.4) = − 2.5 kcal/mol, we predict that in combination with H11-H4 the dissociation constant K_D of CR3022 is decreased by about 66 times (exp(2.5 kcal/mol/RT) ≈ 66). On the other hand, ΔG_{bind} (H11-H4 + CR3022)-ΔG_{bind}(H11-H4) = − 23.9 − (− 19.8) = − 4.1 kcal/mol, which results in a

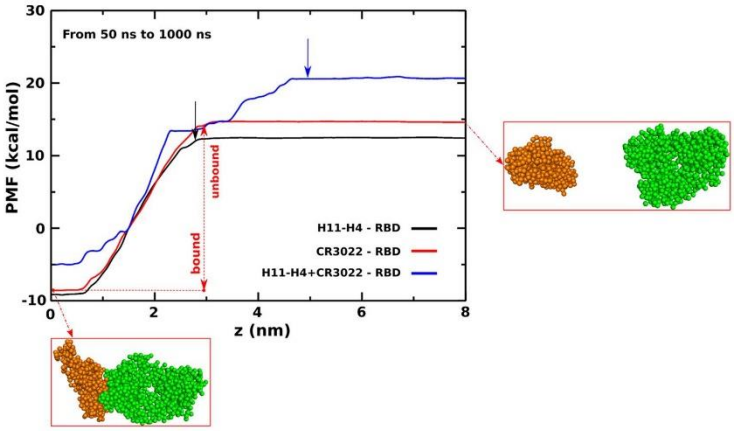

Figure 7. One-dimensional potential of mean force (1D PMF) of complexes H11-H4–RBD, CR3022–RBD and H11-H4 + CR3022-RBD as a function of the reaction coordinate. The result was obtained for a [50, 1000 ns] time window using CG-US simulations with the MARTINI force field. The left and right snapshots refer to the bound and unbound state of CR3022–RBD. The arrow indicates the position of the cutoff distance between bound and unbound states.

decrease of K_D of H11-H4 by 960 times (exp(4.1 kcal/mol/RT) ≈ 960). Although these theoretical estimates are approximate, they show that the combination of antibody and nanobody significantly improves the neutralization of SARS-CoV-2 activity.

Discussion and conclusion

Combining various computational methods, we studied the association of H11-H4, CR3022, and both H11-H4 and CR3022 with RBD. A number of interesting results have been obtained. SMD simulation showed that the H11-H4 nanobody binds to RBD weaker than CR3022, which is consistent with the binding free energy ΔG_{bind} computed from the coarse-grained US. Our theoretical estimates of the binding affinity are in good agreement with the experimental results presented by Tian et al.[20] and Huo et al.[25] for H11-H4 and CR3022 interacting with SARS-CoV-2, but for the CR3022–RBD complex they contradict Yuan et al.[21] (Table 1). To clarify the contradiction, recall that Tian et al.[20] reported a K_d of 6.3 nM for CR3022–RBD, which is lower than Kd = 115 nM of Yuan et al.[21] (Table 1). The difference in binding affinity may be due to differences in experimental conditions of these two groups, as discussed by Yuan et al.[21]. Namely, CR3022 was expressed as an Fab in Yuan et al.[21], but single-chain fragment variable (scFv) in Tian et al.[20]; CR3022 was expressed in mammalian cells in Yuan et al.[21], but in *E. coli* in Tian et al.[20]. SARS-CoV-2 RBD was expressed in insect 150 cells in Yuan et al.[21], but in mammalian cells in Tian et al.[20]. Since the result of Yuan et al.[21] does not agree with our simulations, we assume that their experimental conditions do not match our modeling. However, we cannot confirm this with molecular simulations because none of the existing models is able to capture differences in the behavior of proteins in different cells.

We predict that the concurrent binding of H11-H4 and CR3022 to RBD results in a higher binding affinity than when they are individually associated with RBD. Thus, the combination of H11-H4 and CR3022 enhances the neutralization of SARS-CoV-2, and this could open up a new treatment strategy for Covid-19. Whether this conclusion holds for the other antibody–nanobody pairs is a matter of further clarification.

Stability of the H11-H4–RBD complex is mainly contributed by the vdW interaction, while electrostatic interaction is more important for the CR3022–RBD and H11-H4 + CR3022–RBD complexes. In general, the role of vdW and electrostatic interaction in the binding of antibodies and nanobodies to SARS-CoV-2 depends on the specific case.

Our computational study found CR3022 to be a better candidate for treating Covid-19 than H11-H4, but only for WT. It is important to note that H11-H4 shows a high ability to neutralize the Alpha, Kappa and the highly dangerous Delta variants, and this fact is consistent with recent experiment.

In our work, the advantage of SMD is that it can provide all-atom description, but the disadvantage is that it does not allow the calculation of the free energy at equilibrium. In contrast, the equilibrium binding free energy can be obtained by coarse-grained umbrella sampling, but only at the coarse level. Nevertheless, these two approach complement each other, leading to a satisfactory description of the experiment.

For protein–ligand systems, SMD has been shown to be as efficient as the MM-PBSA method but computationally faster due to fast pull[76]. Although a similar analysis has not been carried out for protein–protein interactions, in conjunction with previous woks[26,55,75], the present study shows that this method is useful for characterizing the relative binding affinity of protein–protein complexes. It would be useful to compare the SMD

method with the MM-PBSA and other MD-based methods for estimating the absolute binding free energy of these complexes.

In the reaction coordinate space, PMF shown in Fig. 7 is one-dimensional (1D), and mapping the multidimensional free energy landscape to the 1D profile is an approximation. However, Z in Fig. 7 is the radial distance in real 3D space, which can reflect the 3D nature of the problem. This may be one of the reasons why umbrella sampling is one of the best methods for calculating free energy[77]. In other words, 1D PMF is adequate for our problem.

Data availability

The data files are available in the "SciRep_data.zip" file, which includes: *SMD simulation data:* They are located in the "SMD_data" folder. The "WT" subfolder contains binding affinity and interaction energy data obtained from SMD simulation for the wild type. The "MUTATION" subfolder contains data on Covid-19 variants. *Coarse-grained simulation data*: The data obtained from umbrella sampling coarse-grained simulations are presented in the "US-CG" folder.

Received: 2 March 2022; Accepted: 3 June 2022
Published online: 11 June 2022

References

1. Cohen, J. Antibodies may curb pandemic before vaccines. *Science* **369**, 752–753 (2020).
2. Cao, X. COVID-19: Immunopathology and its implications for therapy. *Nat. Rev. Immunol.* **20**, 269–270 (2020).
3. Chen, L. *et al.* Convalescent plasma as a potential therapy for COVID-19. *Lancet Infect. Dis.* **20**, 398–400 (2020).
4. Shen, C. *et al.* Treatment of 5 critically ill patients with COVID-19 with convalescent plasma. *JAMA* **323**, 1582–1589 (2020).
5. Tortorici, M. A. & Veesler, D. Structural insights into coronavirus entry. *Adv. Virus Res.* **105**, 93–116 (2019).
6. Simmons, G. *et al.* Proteolytic activation of the SARS-coronavirus Spike protein: Cutting enzymes at the cutting edge of antiviral research. *Antiviral Res.* **100**, 605–614 (2013).
7. Gallagher, T. M. & Buchmeier, M. J. Coronavirus Spike proteins in viral entry and pathogenesis. *Virology* **279**, 371–374 (2001).
8. Belouzard, S. *et al.* Activation of the SARS coronavirus Spike protein via sequential proteolytic cleavage at two distinct sites. *Proc. Natl. Acad. Sci. USA* **106**, 5871–5876 (2009).
9. Wrapp, D. *et al.* Cryo-EM structure of the 2019-nCoV Spike in the prefusion conformation. *Science* **367**, 1260–1263 (2020).
10. Walls, A. C. *et al.* Structure, function, and antigenicity of the SARS-CoV-2 Spike glycoprotein. *Cell* **180**, 281–292 (2020).
11. Krempl, C. *et al.* Point mutations in the S protein connect the sialic acid binding activity with the enteropathogenicity of transmissible gastroenteritis coronavirus. *J. Virol.* **71**, 3285–3287 (1997).
12. Kunkel, F. & Herrler, G. Structural and functional analysis of the S proteins of two human coronavirus OC43 strains adapted to growth in different cells. *Arch. Virol.* **141**, 1123–1131 (1996).
13. Lu, G. *et al.* Bat-to-human: Spike features determining 'host jump' of coronaviruses SARS-CoV, MERS-CoV, and beyond. *Trends Microbiol.* **23**, 468–478 (2015).
14. Zhou, H. *et al.* Structural definition of a neutralization epitope on the N-terminal domain of MERS-CoV Spike glycoprotein. *Nat. Commun.* **10**, 3068 (2019).
15. Tai, W. *et al.* Characterization of the receptor-binding domain (RBD) of 2019 novel coronavirus: Implication for development of RBD protein as a viral attachment inhibitor and vaccine. *Cell. Mol. Immunol.* **17**, 613–620 (2020).
16. Lan, J. *et al.* Structure of the SARS-CoV-2 Spike receptor-binding domain bound to the ACE2 receptor. *Nature* **581**, 215–220 (2020).
17. Jiang, S. *et al.* Therapeutic antibodies and fusion inhibitors targeting the spike protein of SARS-CoV-2. *Expert Opin. Ther. Targets.* **25**, 415–421 (2021).
18. Chen, J. *et al.* Review of Covid 19 antibody therapies. *Annu. Rev. Biophys.* **50**, 1–30 (2021).
19. Lu, M. *et al.* Real-time conformational dynamics of SARS-CoV-2 Spikes on virus particles. *Cel Host Microbe* **28**, P880-891.E8 (2020).
20. Tian, X. *et al.* Potent binding of 2019 novel coronavirus Spike protein by a SARS coronavirus-specific human monoclonal antibody. *Emerg. Microbes Infect.* **9**, 382–385 (2020).
21. Yuan, M. *et al.* A highly conserved cryptic epitope in the receptor binding domains of SARS-CoV-2 and SARS-CoV. *Science* **368**, 630–633 (2020).
22. Jovčevska, I. & Muyldermans, S. The therapeutic potential of nanobodies. *BioDrugs* **34**, 11–26 (2020).
23. Zhou, P. *et al.* A pneumonia outbreak associated with a new coronavirus of probable bat origin. *Nature* **579**, 270–273 (2020).
24. Wrapp, D. *et al.* Structural basis for potent neutralization of Beta coronaviruses by single-domain camelid antibodies. *Cell* **181**, 1436–1441 (2020).
25. Huo, J. *et al.* Neutralizing nanobodies bind SARS-CoV-2 spike RBD and block interaction with ACE2. *Nat. Struct. Mol. Biol.* **27**, 846–854 (2020).
26. Nguyen, H. *et al.* Electrostatic interactions explain the higher binding affinity of the CR3022 antibody for SARS-CoV-2 than the 4A8 antibody. *J. Phys. Chem. B.* **125**, 7368–7379 (2021).
27. Carolina, C. G. *et al.* On the interaction of the receptor-binding domain of SARS-CoV-1 and SARS-CoV-2 spike proteins with monoclonal antibodies and the receptor ACE2. *Virus Res.* **285**, 198021 (2020).
28. Davies, N. G. *et al.* Estimated transmissibility and impact of SARS-CoV-2 lineage B.1.1.7 in England. *Science* **372**, eabg3055 (2021).
29. Karim, S. S. A. *et al.* New SARS-CoV-2 variants—Clinical, public, health, and vaccine implications. *N. Engl. J. Med.* **384**, 1866–1868 (2021).
30. Faria, N. R. *et al.* Genomics and epidemiology of the P.1 SARS-CoV-2 lineage in Manaus, Brazil. *Science* **372**, 815–821 (2021).
31. Singh, J. *et al.* SARS-CoV-2 variants of concern are emerging in India. *Nat. Med.* **27**, 1131–1133 (2021).
32. Mlcochova, P. *et al.* SARS-CoV-2 B.1.617.2 Delta variant replication and immune evasion. *Nature* **599**, 114–119 (2021).
33. Kimura, I. *et al.* SARS-CoV-2 Lambda variant exhibits higher infectivity and immune resistance. *Cell Rep.* **38**, 110218 (2022).
34. Laiton-Donato, K. *et al.* Characterization of the emerging B.1.621 variant of interest of SARS-CoV-2. *Infect. Genet. Evol.* **95**, 105038 (2021).
35. Salvatore, M. *et al.* Resurgence of SARS-CoV-2 in India: Potential role of the B.1.617.2 (Delta) variant and delayed interventions. *medRxiv* (2021).
36. Bai, C. *et al.* Predicting mutational effects on receptor binding of the Spike protein of SARS-CoV-2 variants. *J. Am. Chem. Soc.* **143**, 17646–17654 (2021).
37. Jangra, S. *et al.* SARS-CoV-2 skipe E484K mutation reduces antibody neutralisation. *Lancet Microbe* **2**, e283–e284 (2021).

38. Cheng, M. H. *et al.* Impact of South African 501.V2 variant on SARS-Cov-2 spike infectivity and neutralization: A structure-based computational assessment. *BioRxiv* (2021).
39. Planas, D. *et al.* Reduced sensitivity of SARS-CoV-2 variant Delta to antibody neutralization. *Nature* **596**, 276–280 (2021).
40. Tada, T. *et al.* SARS-CoV-2 Lambda variant remains susceptible to neutralization by mRNA vaccine-elicited antibodies and convalescent serum. *BioRxiv* (2021).
41. Xu, J. *et al.* Nanobodies from camelid mice and llamas neutrlize SARS-CoV-2 variants. *Nature* **595**, 278–282 (2021).
42. Webb, B. & Sali, A. Comparative protein structure modeling using MODELLER. *Curr. Protoc. Bioinform.* **54**, 5.6.1-5.6.37 (2016).
43. The PyMOL molecular graphics system, version 2.0 Schrödinger, LLC.
44. Robustelli, P. *et al.* Developing a molecular dynamics force field for both folded and disordered protein states. *Proc. Natl. Acad. Sci. USA* **115**, E4758–E4766 (2018).
45. Abraham, M. J. *et al.* GROMACS: High performance molecular simulations through multi-level parallelism from laptops to supercomputers. *SoftwareX* **1–2**, 19–25 (2015).
46. Bussi, G. *et al.* Canonical sampling through velocity rescaling. *J. Chem. Phys.* **126**, 014101 (2007).
47. Parrinello, M. Polymorphic transitions in single crystals: A new molecular dynamics method. *J. Appl. Phys.* **52**, 7182 (1981).
48. Jorgensen, W. L. & Jenson, C. Temperature dependence of TIP3P, SPC, and TIP4P water from NPT Monte Carlo simulations: Seeking temperatures of maximum density. *J. Comput. Chem.* **19**, 1179–1186 (1998).
49. Hess, B. *et al.* LINCS: A linear constraint solver for molecular simulations. *J. Comput. Chem.* **18**, 1463–1472 (1997).
50. Darden, T. *et al.* Particle mesh Ewald: An Nlog(N) method for Ewald sums in large systems. *J. Chem. Phys.* **98**, 10089 (1993).
51. Hockney, R. W. *et al.* Quiet high-resolution computer models of a plasma. *J. Comput. Phys.* **14**, 148–158 (1974).
52. Nguyen, H. *et al.* Steered molecular dynamics for investigating the interactions between Insulin Receptor Tyrosine Kinase (IRK) and variants pf Protein Tyrosine Phosphatase 1B (PTP1B). *Appl. Biochem. Biotechnol.* **184**, 401–413 (2018).
53. Nguyen, H. *et al.* Binding affinity of the L-742,001 inhibitor to the endonuclease domain of A/H1N1/PA influenza virus variants: Molecular simulation approaches. *Chem. Phys.* **500**, 26–36 (2018).
54. Pham, T. *et al.* Investigation of binding affinity between potential antiviral agents and PB2 protein of influenza A: Non-equilibrium molecular dynamics simulation approach. *Int. J. Med. Sci.* **17**, 2031–2039 (2020).
55. Nguyen, H. L. *et al.* Does SARS-CoV-2 bind to human ACE2 more strongly than does SARS-CoV?. *J. Phys. Chem. B.* **124**, 7336–7347 (2020).
56. Binnig, G. & Quate, C. F. Atomic force microscope. *Phys. Rev. Lett.* **56**, 930 (1986).
57. Jarzynski, C. Nonequilibrium equality for free energy differences. *Phys. Rev. Lett.* **78**, 2690 (1997).
58. Hummer, G. & Szabo, A. Free energy reconstruction from nonequilibrium single-molecule pulling experiments. *Proc. Natl. Acad. Sci. USA* **98**, 3658–3661 (2001).
59. Park, S. *et al.* Free energy calculation from steered molecular dynamics simulations using Jarzynski's equality. *J. Chem. Phys.* **119**, 3559 (2003).
60. Truong, D. T. & Li, M. S. Probing the binding affinity by Jarzynski's nonequilibrium binding free energy and rupture time. *J. Phys. Chem. B* **122**, 4693–4699 (2018).
61. Arnarez, C. *et al.* Dry Martini, a coarse-grained force field for lipid membrane simulations with implicit solvent. *J. Chem. Theory Comput.* **11**, 260–275 (2015).
62. Monticelli, L. *et al.* The MARTINI coarse-grained force field: Extension to proteins. *J. Chem. Theory Comput.* **4**, 819–834 (2008).
63. Uusitalo, J. J. *et al.* Martini coarse-grained force field: Extension to RNA. *Biophys. J.* **113**, 246–256 (2017).
64. Yesylevskyy, S. O. *et al.* Polarizable water model for coarse-grained Martini force field. *PLoS Comput. Biol.* **6**, e1000810 (2010).
65. Berendsen, H. J. C. *et al.* Molecular dynamics with coupling to an external bath. *J. Chem. Phys.* **81**, 3684–3690 (1984).
66. Thomas, D. P. *et al.* Automated coarse-grained mapping algorithm for the Martini force field and benchmarks for membrane-water partitioning. *J. Chem. Theory Comput.* **17**, 5777–5791 (2021).
67. Torrie, G. M. & Valleau, J. P. Nonphysical sampling distributions in Monte Carlo free-energy estimation: Umbrella sampling. *J. Comput. Phys.* **23**, 187–199 (1977).
68. Kumar, S. *et al.* The weighted histogram analysis method for free-energy calculations on biomolecules. 1. The method. *J. Comput. Chem.* **13**, 1011–1021 (1992).
69. Patel, J. S. & Ytreberg, F. M. Fast calculation of protein-protein binding free energies using umbrella sampling with a coarse-grained model. *J. Chem. Theory Comput.* **14**, 991–997 (2018).
70. Wallace, A. C. *et al.* LIGPLOT: A program to generate schematic diagrams of protein-ligand interactions. *Protein Eng.* **8**, 127–134 (1995).
71. Evans, E. & Ritchie, K. Dynamic strength of molecular adhesion bonds. *Biophys. J.* **72**, 1541–1555 (1997).
72. Dudko, O. K. *et al.* Intrinsic rates and activation free energies from single-molecule pulling experiments. *Phys. Rev. Lett.* **96**, 108101 (2006).
73. Vuong, V. Q. *et al.* A new method for navigating optimal direction for pulling ligand from binding pocket: Application to ranking binding affinity by steered molecular dynamics. *J. Chem. Inf. Model.* **55**, 2731–2738 (2015).
74. Pham, H. A. *et al.* Dependence of work on the pulling speed in mechaical ligand unbinding. *J. Phys. Chem. B.* **125**, 8325–8330 (2021).
75. Nguyen, H. *et al.* Cocktail of REGN antibodies binds more strongly to SARS-CoV-2 than its components, but the Omicron variant reduces its neutralizing ability. *J. Phys. Chem. B.* **126**, 2812–2823 (2022).
76. Mai, B. K. *et al.* Top leads for swine influenza A/H1N1 virus revealed by steered molecular dynamics approach. *J. Chem. Inf. Model.* **50**, 2236–2247 (2010).
77. Kästner, J. Umbrella sampling. *WIREs Comput. Mol. Sci.* **1**, 932–942 (2011).

Acknowledgements

This work was supported by Narodowe Centrum Nauki in Poland (Grant 2019/35/B/ST4/02086), and the Department of Science and Technology at Ho Chi Minh city (Grant 13/2020/HĐ-QPTKHCN). This research was supported by the supercomputer centre TASK in Gdansk, PLGrid infrastructure, Poland, and the computer cluster at ICST, Vietnam.

Author contributions

H.N. and M.S.L. designed the research. M.S.L. supervised the study. H.N. performed simulations. H.N. and M.S.L. analyzed the data and wrote the manuscript.

Competing interests

The authors declare no competing interests.

Additional information

Supplementary Information The online version contains supplementary material available at https://doi.org/10.1038/s41598-022-14263-1.

Correspondence and requests for materials should be addressed to M.S.L.

Reprints and permissions information is available at www.nature.com/reprints.

Publisher's note Springer Nature remains neutral with regard to jurisdictional claims in published maps and institutional affiliations.

Chapter 4: Effect of SARS-CoV-2 non-structural protein 1 on protein synthesis

4.1 Binding of SARS-CoV-2 non-structural protein 1 to 40S ribosome inhibits mRNA translation

4.1.1 Introduction

SARS-CoV-2 is an enveloped, positive-sense, single-stranded RNA virus closely related to species known to infect a wide range of vertebrates [300-301]. Its genome, approximately 30 kb in length, is a 5'-capped and 3'-polyadenylated RNA component of coronavirus particles. This genome encodes two large overlapping open reading frames in gene 1 (ORF1a and ORF1b) and includes various structural and NSPs at the 3′ end [293, 302]. After entering host cells, the viral genomic RNA is translated by the cellular protein synthesis machinery to produce NSPs that create favorable conditions for viral infection and mRNA synthesis [193, 303]. Among these proteins, NSP1 is particularly enigmatic [201]. NSP1, produced from the N-terminus of ORF1a, acts as a host shutoff factor, suppressing host gene expression and immune response, and playing a crucial role in the viral life cycle [304].

All viruses rely on cellular ribosomes for protein synthesis and compete with endogenous mRNA to access this translation machinery, which serves as the focal point of control [305]. A common viral strategy to limit host gene expression is by redirecting translational resources toward viral mRNA. This phenomenon, known as host shutoff, enhances the access of viral transcripts to ribosomes and promotes evasion of the innate immune system [306-307]. Host shutoff is a hallmark of coronavirus infections, significantly contributing to the suppression of innate immune responses in several pathogenic coronaviruses, including SARS-CoV, MERS-CoV, and pandemic SARS-CoV-2 [308-310]. SARS-CoV-2-induced host shutoff is multifaceted, involving the inhibition of host mRNA splicing by NSP16, restriction of cellular cytoplasmic mRNA accumulation and translation by NSP1, and disruption of protein secretion by NSP8 and NSP9 [311-314].

NSP1 does not interact with the 60S ribosomal subunit, it exclusively binds to the 40S ribosomal subunit and stalls canonical mRNA translation at various stages during initiation [199, 315]. NSP1 is composed of 180 amino acids, organized into three distinct domains: the N-terminal domain, the linker domain, and the C-terminal domain [54]. An early model of NSP1 lacked the C-terminal domain because it remains disordered in solution, forming an ordered helix-loop-helix structure only upon binding to the small ribosomal subunit [54, 316]. In contrast, the N-terminal and linker regions do not directly bind to the 40S mRNA entry channel but instead stabilize NSP1's association with the ribosome and mRNA [55, 316].

Schubert *et al.* [198] demonstrated that the C-terminal domain interacts specifically with the 40S subunit of the human ribosome, inhibiting mRNA translation. The C-terminal domain binds to the mRNA entry channel, folds into two helices, and interacts with h18 of 18S rRNA, as well as with the 40S ribosomal proteins uS3, uS5, and eS30. These interactions cause NSP1 to partially overlap with the fully accommodated mRNA. NSP1 suppresses all cellular antiviral defense processes that depend on the expression of host factor expression,

including the interferon response, acting as a ribosome gatekeeper to stop translation and inhibit host cell protein synthesis. This shutdown of key parts of the innate immune system facilitates efficient viral replication and immune evasion [317-318]. Due to its crucial role in dampening the antiviral immune response, NSP1 is considered a potential therapeutic target [57, 198, 319]. However, the precise atomistic mechanism by which NSP1 interactions with a conserved region in the 5′ untranslated region of viral mRNA suppress viral protein expression remains unclear [198].

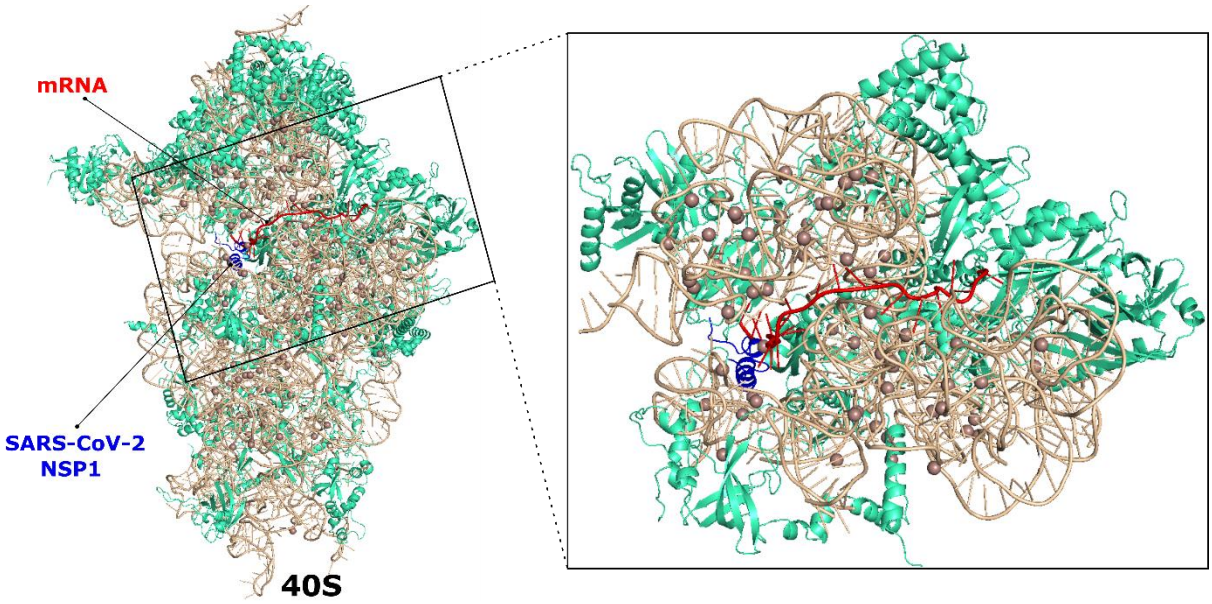

Figure 4.1: The 3D structure of the mRNA-40S-NSP1 complex, including 40S ribosome (ribosomal proteins: green-cyan, ribosomal RNA: wheat), mRNA (red), NSP1 (blue), and Mg^{2+} and Zn^{2+} ions (dark-salmon).

In this study, we used all-atom SMD and coarse-grained alchemical simulations (for the full 40S and truncated 40S ribosome (Figure 4.1)) to examine the impact of NSP1 binding on the 40S ribosome and its inhibition of the mRNA translation process [204].

To calculate the binding affinity of mRNA to the ribosome in the presence and absence of NSP1, SMD simulations were conducted by pulling mRNA along its entry channel for both full 40S and truncated 40S complexes. An external force was applied to a dummy atom connected to the 5′-mRNA (O5′ atom) via a spring with stiffness k. The pulling direction was along the mRNA entry channel. The complexes were rotated so that the exit direction was parallel to the z-axis [204]. We applied a pulling speed of v = 0.5 nm/ns, which is about 10 orders of magnitude greater than in experiments; however, previous work has shown that this choice does not affect the relative binding affinity, allowing us to distinguish strong binders from weak ones [165]. The force-time profile shows that mRNA binds to 40S-NSP1 (F_{max} = 5023.3±232.1 and 4501.3±227.5 pN for the full 40S and truncated 40S ribosome, respectively) more strongly than to the 40S ribosome (F_{max} = 1832.9±127.4 and 1763.6±103.3 pN for the full 40S and truncated 40S ribosome). Here, the mRNA translation

process is primarily driven by the electrostatic interactions between mRNA and the 40S ribosome.

We also applied coarse-grained alchemical simulations with the Martini model to calculate the binding free energy of mRNA to the 40S ribosome with and without NSP1. For alchemical transformations, an optimal set of λ-values ranging from $\lambda = 0$ to $\lambda = 1$ was used, where $\lambda = 0$ and $\lambda = 1$ correspond to a system with and without full interaction, respectively. The optimal set of 30, 30, and 20 windows of λ-values was selected for the mRNA-40S, mRNA-40S-NSP1, and mRNA, respectively. The free energy of mRNA-40S binding is -13.1±1.1 and -8.6±1.2 kcal/mol for the full 40S and the truncated 40S ribosome, respectively, which is very close to the experimental value of -10.7±0.1 kcal/mol [320]. In the presence of NSP1, the binding free energy of mRNA-40S-NSP1 is reduced to -37.1±2.2 and -28.2±2.6 kcal/mol for the full 40S and truncated 40S ribosome, respectively. This indicates that NSP1 significantly increases the binding affinity of mRNA to the 40S ribosome, suggesting that its attachment to the mRNA entry channel obstructs translation. This observation is consistent with the findings from all-atom SMD simulations, and our calculated results closely match the experimental data of earlier studies [198, 316].

4.1.2 Publication

a) Abstract: Experimental evidence has established that SARS-CoV-2 NSP1 acts as a factor that restricts cellular gene expression and impedes mRNA translation within the ribosome's 40S subunit. However, the precise molecular mechanisms underlying this phenomenon have remained elusive. To elucidate this issue, we employed a combination of all-atom steered molecular dynamics and coarse-grained alchemical simulations to explore the binding affinity of mRNA to the 40S ribosome, both in the presence and absence of SARS-CoV-2 NSP1. Our investigations revealed that the binding of SARS-CoV-2 NSP1 to the 40S ribosome leads to a significant enhancement in the binding affinity of mRNA. This observation, which aligns with experimental findings, strongly suggests that SARS-CoV-2 NSP1 has the capability to inhibit mRNA translation. Furthermore, we identified electrostatic interactions between mRNA and the 40S ribosome as the primary driving force behind mRNA translation. Notably, water molecules were found to play a pivotal role in stabilizing the mRNA-40S ribosome complex, underscoring their significance in this process. We successfully pinpointed the specific SARS-CoV-2 NSP1 residues that play a critical role in triggering the translation arrest.

- DOI: 10.1021/acs.jpcb.4c01391
- Publication source: https://pubs.acs.org/doi/full/10.1021/acs.jpcb.4c01391

b) Author contribution statements:

Hung Van Nguyen
Division of Theoretical Physics
Institute of Physics, Polish Academy of Sciences
Al. Lotnikow 32/46
02-668 Warsaw, Poland

INSTYTUT FIZYKI
POLSKIEJ AKADEMII NAUK

STATEMENT

I declare that I am the co-author of the publication:

- Nguyen, H.; Nguyen, H. L.; Li, M. S. **Binding of SARS-CoV-2 non-structural protein 1 to 40S ribosome inhibits mRNA translation**. J. Phys. Chem. B. **2024**, *128*(29), 7033-7042.

My contribution consisted of designing the research, performing MD simulations, analyzing the results, preparing figures, and writing the manuscript.

Warsaw, August 2024

Hung Van Nguyen

Hoang Linh Nguyen
Institute of Fundamental and Applied Sciences, Duy Tan University, Ho Chi Minh City 700000, Vietnam

STATEMENT

I declare that I am the co-author of the publication:

- Nguyen, H.; Nguyen, H. L.; Li, M. S. **Binding of SARS-CoV-2 non-structural protein 1 to 40S ribosome inhibits mRNA translation**. J. Phys. Chem. B. **2024**, *128*(29), 7033-7042.

My contribution consisted of designing the research, and analyzing the results.

Ho Chi Minh, July 2024

Hoang Linh Nguyen

Prof. Mai Suan Li, PhD
Division of Theoretical Physics
Institute of Physics, Polish Academy of Sciences
Al. Lotnikow 32/46
02-668 Warsaw, Poland
E-mail: masli@ifpan.edu.pl

INSTYTUT FIZYKI
POLSKIEJ AKADEMII NAUK

STATEMENT

I declare that I am the co-author of the publication:

- Nguyen, H.; Nguyen, H. L.; Li, M. S. **Binding of SARS-CoV-2 non-structural protein 1 to 40S ribosome inhibits mRNA translation**. J. Phys. Chem. B. **2024**, *128*(29), 7033-7042.

My contribution consisted of designing the research, writing the manuscript, and supervising the overall project.

Warsaw, August 22 2024

Mai Suan Li

c) Publication for this section:

Binding of SARS-CoV-2 non-structural protein 1 to 40S ribosome inhibits mRNA translation

Hung Nguyen, Hoang Linh Nguyen, and Mai Suan Li

J. Phys. Chem. B, 2024, 128, 7033-7042

THE JOURNAL OF PHYSICAL CHEMISTRY B
A JOURNAL OF THE AMERICAN CHEMICAL SOCIETY

pubs.acs.org/JPCB
Article

Binding of SARS-CoV-2 Nonstructural Protein 1 to 40S Ribosome Inhibits mRNA Translation

Hung Nguyen, Hoang Linh Nguyen, and Mai Suan Li*

Cite This: J. Phys. Chem. B 2024, 128, 7033−7042
Read Online

ABSTRACT: Experimental evidence has established that SARS-CoV-2 NSP1 acts as a factor that restricts cellular gene expression and impedes mRNA translation within the ribosome's 40S subunit. However, the precise molecular mechanisms underlying this phenomenon have remained elusive. To elucidate this issue, we employed a combination of all-atom steered molecular dynamics and coarse-grained alchemical simulations to explore the binding affinity of mRNA to the 40S ribosome, both in the presence and absence of SARS-CoV-2 NSP1. Our investigations revealed that the binding of SARS-CoV-2 NSP1 to the 40S ribosome leads to a significant enhancement in the binding affinity of mRNA. This observation, which aligns with experimental findings, strongly suggests that SARS-CoV-2 NSP1 has the capability to inhibit mRNA translation. Furthermore, we identified electrostatic interactions between mRNA and the 40S ribosome as the primary driving force behind mRNA translation. Notably, water molecules were found to play a pivotal role in stabilizing the mRNA-40S ribosome complex, underscoring their significance in this process. We successfully pinpointed the specific SARS-CoV-2 NSP1 residues that play a critical role in triggering the translation arrest.

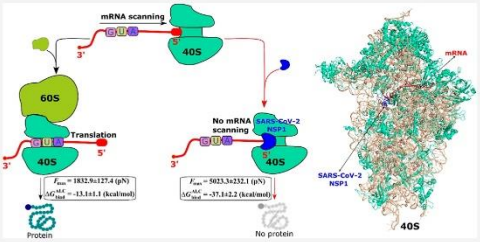

1. INTRODUCTION

Severe acute respiratory syndrome coronavirus 2 (SARS-CoV-2) caused the 2019 coronavirus disease (COVID-19) worldwide pandemic, which affected millions of people.[1] Like other coronaviruses, SARS-CoV-2 is an enveloped, positive-sense, single-stranded RNA virus, and its closely related phylogenetic species are known to infect a large number of vertebrate species.[2] The SARS-CoV-2 genome consists of about 30 kb linear, one of the 5′-capped and 3′-polyadenylated RNA genomic components that make up coronavirus particles, encoding two large overlapping open reading frames in gene 1 (ORF1a and ORF1b), and includes various structural and nonstructural proteins at the 3′ end.[3] After entering host cells, the viral genomic RNA is translated by the cellular protein synthesis machinery to produce a set of nonstructural proteins that render cellular conditions favorable for viral infection and viral mRNA synthesis.[4] In cells infected with SARS-CoV-2, one of the most enigmatic viral proteins is a host shutoff factor called nonstructural protein 1 (SARS-CoV-2 NSP1).[5] SARS-CoV-2 NSP1 is the product of the N-terminus of the first open reading frame ORF1a and serves to suppress host gene expression and host immune response. Generally, SARS-CoV-2 NSP1 plays an important role in the viral life cycle.[6]

All viruses rely on cellular ribosomes for their protein synthesis and compete with endogenous mRNA for access to a translation machinery known as protein synthesis, which acts as a focal point of control.[7] Host gene expression is limited by the common viral strategy of shifting translational resources toward viral mRNA.[8] This phenotype termed host shutoff, increases the access of viral transcripts to ribosomes and promotes innate immune evasion.[8a] Host shutoff is a hallmark of coronavirus infection and has significantly contributed to the suppression of innate immune responses in multiple pathogenic coronaviruses, including SARS-CoV, Middle East respiratory syndrome coronavirus, and pandemic SARS-CoV-2.[9] SARS-CoV-2 induced host shutoff, which is multifaceted and involves inhibition of host mRNA splicing by SARS-CoV-2 NSP16, restriction of cellular cytoplasmic mRNA accumulation and translation by SARS-CoV-2 NSP1, and disruption of protein secretion by SARS-CoV-2 NSP8 and SARS-CoV-2 NSP9.[10]

NSP1 of SARS-CoV (SARS-CoV NSP1) and SARS-CoV-2 NSP1 do not interact with 60S ribosomal subunit, they bind to only 40S ribosomal subunit and stall canonical mRNA translation at various stages during initiation.[11] Although in vitro binding and translation assays revealed that both SARS-CoV NSP1 and SARS-CoV-2 NSP1 exert similar efficacy in the host translational shutdown mechanism,[12] SARS-CoV-2 was

Received: March 3, 2024
Revised: June 26, 2024
Accepted: July 1, 2024
Published: July 15, 2024

https://doi.org/10.1021/acs.jpcb.4c01391
J. Phys. Chem. B 2024, 128, 7033−7042

The Journal of Physical Chemistry B pubs.acs.org/JPCB Article

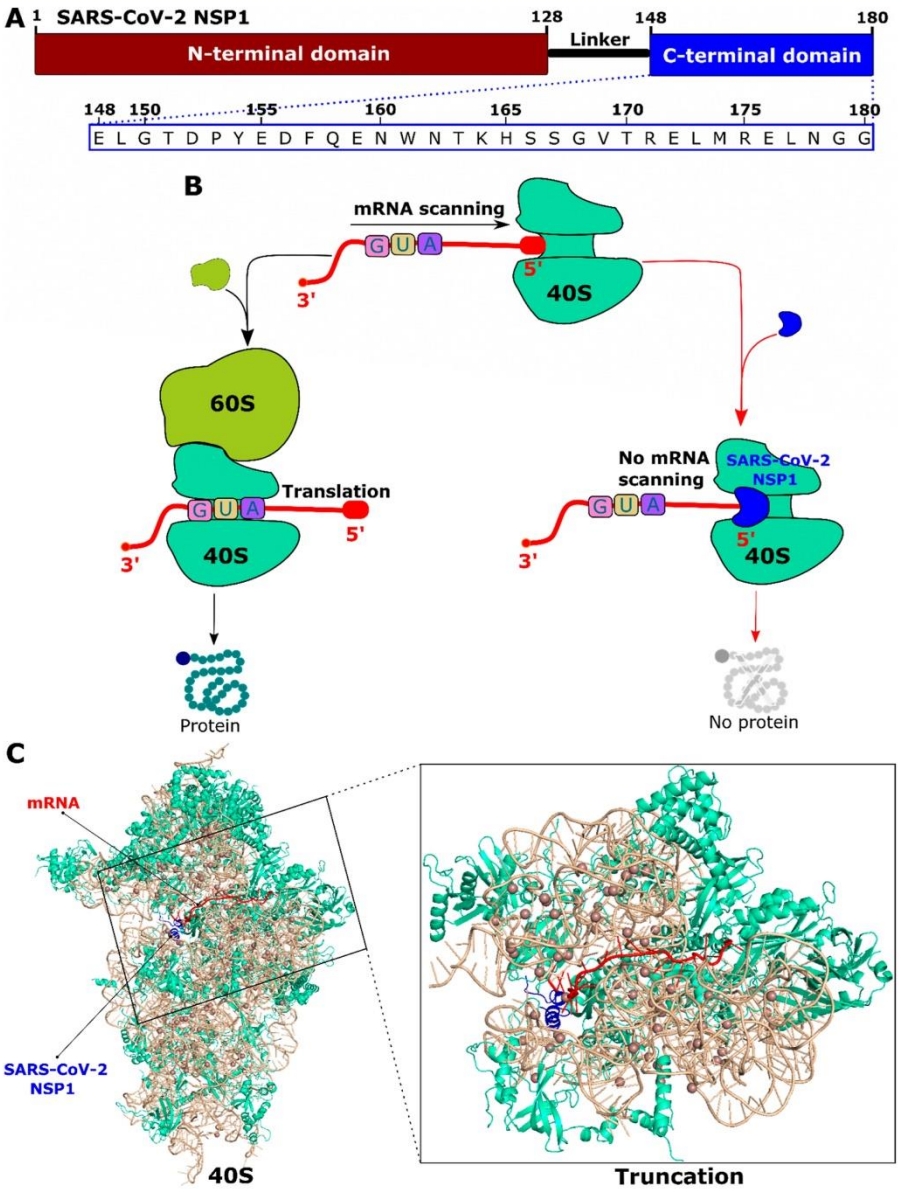

Figure 1. (A) Scheme of SARS-CoV-2 NSP1 structure; the C-terminal domain includes 32 residues from E148 to G180. (B) Scheme of SARS-CoV-2 NSP1 action to suppress mRNA translation (the mRNA sequence used in our simulations is C A G A C A C C A U G G U G C A C C U G A C). (C) 3D structure of the mRNA-40S-NSP1 complex constructed from a superposition of two different PDB structures 6ZOJ and 6HCJ and the truncation of the mRNA-40S-NSP1 complex. This structure includes rRNA (wheat), SARS-CoV-2 NSP1 (blue), mRNA (red), rproteins (green-cyan), and Mg^{2+} and Zn^{2+} ions (dark-salmon). The rectangle depicts a truncated ribosome used for the second set of simulation.

shown to be more infectious and triggers more comorbid conditions than SARS-CoV.[13] Here, SARS-CoV-2 NSP1 consists of 180 amino acids, which are organized into three distinct domains: the N-terminal domain, the linker domain,

https://doi.org/10.1021/acs.jpcb.4c01391
J. Phys. Chem. B 2024, 128, 7033−7042

and the C-terminal domain (Figure 1A).[14] An early model of SARS-CoV-2 NSP1 model lacks the C-terminal domain, as it remains disordered in solution and the ordered helix−loop−helix is formed only upon binding to the small ribosomal subunit.[12,14] In contrast, the N-terminal and linker regions of SARS-CoV-2 NSP1 do not engage in direct binding to the 40S mRNA entry channel, but rather they are involved in stabilizing its association with the ribosome and mRNA.[12,15] Schubert et al.[16] recently showed that the C-terminal domain specifically interacts with the 40S subunit of the human ribosome, thereby causing inhibition of mRNA translation. It binds to the mRNA entry channel, folds into two helices, and interacts with h18 of the 18S rRNA (rRNA) as well as with the 40S ribosomal protein (rprotein) uS3 in the head and uS5 and eS30 in the body, where SARS-CoV-2 NSP1 would partially overlap with the fully accommodated mRNA. In short, SARS-CoV-2 NSP1 suppresses all cellular antiviral defense processes that depend on expression of host factors, including the interferon response. It acts as a ribosome gatekeeper to halt translation and inhibit host cell protein synthesis. This shutdown of key parts of the innate immune system may facilitate efficient viral replication[17] and immune evasion. Its important role in dampening the antiviral immune response makes SARS-CoV-2 NSP1 a potential therapeutic target.[16,18] However, the atomistic mechanism of how interactions between SARS-CoV-2 NSP1 and a conserved region in the 5′ untranslated region of viral mRNA suppress viral protein expression remains (Figure 1B).[16]

In computational work, Borišek et al.[19] used all-atom simulation to investigate the interaction of SARS-CoV NSP1 and SARS-CoV-2 NSP1 to the 40S subunit of the ribosome. They found that upon SARS-CoV-2 NSP1/SARS-CoV NSP1 binding to 40S, the critical switch of Gln158/Glu158 and Glu159/Gln159 residues remodels the interaction pattern between SARS-CoV-2 NSP1/SARS-CoV NSP1 and neighboring proteins (uS3 and uS5) and rRNA (h18) lining the exit tunnel. This finding provides a clear picture of how SARS-CoV-2 invades human cells. However, the effect of SARS-CoV-2 NSP1 binding to 40S ribosome on mRNA translation has not been theoretically studied.

In this work, we applied steered molecular dynamics (SMD) and alchemical simulations to observe the effect of SARS-CoV-2 NSP1 binding to the 40S ribosome and inhibiting the mRNA translation process. Our results demonstrated that the presence of SARS-CoV-2 NSP1 significantly increased the binding affinity of mRNA to 40S ribosome, which means that SARS-CoV-2 NSP1 binding to the mRNA entry channel inhibits its translation in the ribosome. In addition, electrostatic mRNA-ribosome interactions have been found to play a key role in mRNA translation.

2. MATERIALS AND METHODS

2.1. Building Two Complexes. To study the effect of SARS-CoV-2 NSP1 on the binding affinity of mRNA to the 40S ribosome, two complexes will be considered. One of them includes mRNA bound to the 40S ribosome and some additional components in the absence of SARS-CoV-2 NSP1, and this complex will be called mRNA-40S. The second complex, which will be referred to as mRNA-40S-NSP1, is similar to mRNA-40S, but in the presence of SARS-CoV-2 NSP1.

In detail, the cryo-EM structure of SARS-CoV-2 NSP1 in complex with the 40S ribosome and additional components including 18S rRNA, 60S rprotein L41, receptor of activated protein C kinase 1, and 165 Mg^{2+} and 2 Zn^{2+}ions, was retrieved from the Protein Data Bank (PDB) with PDB identifier 6ZOJ.[16] This structure is called 40S-NSP1 and was used as the basic for building the mRNA-40S and mRNA-40S-NSP1 complexes. The 3D structure of mRNA-40S-NSP1 was constructed by superimposing two PDB structures, 6ZOJ and 6HCJ,[16,20] which means that the mRNA structure extracted from 6HCJ 20 was inserted into the 6ZOJ structure. The mRNA-40S was then obtained from the mRNA-40S-NSP1 by removing SARS-CoV-2 NSP1. The mRNA-40S-NSP1 complex is displayed by using the PYMOL package[21] (Figure 1C). The divalent cations Mg^{2+} and Zn^{2+} stabilize rRNA, mRNA, and hence the ribosome complexes.

2.2. MD Simulations. Because the mRNA has been mechanically inserted into the complexes, they should be allowed to relax before running the SMD simulation. Since the systems are large they may not be equilibrated using only all-atom simulations forcing us to combine coarse-grained (CG) and all-atom simulations (see Supporting Information). First, we performed energy minimization, followed by a short 5 ns simulation in *NVT* and *NPT* ensembles, and a 1000 ns of conventional CG molecular dynamics (CGMD) simulation for mRNA-40S and mRNA-40S-NSP1 complexes using the MARTINI force field[22] and CG water model.[23] It should be noted that, due to the elastic network model implemented in the MARTINI force field, secondary structures are preserved during the simulation. However, using this MARTINI force field in the first step is acceptable because after mRNA insertion or NSP1 removal, the space around the entrance channel is needed to relax to accommodate molecules in this area, but does not care much about secondary structures. These structures are subject to change during the following all-atom conventional molecular dynamics (CMD) simulations.

The last snapshot of the CGMD simulation was converted to the all-atom structure and its energy was minimized by using the steepest-descent algorithm, followed by a short simulation of 3 ns in *NVT* and *NPT* ensembles, and then was a 500 ns production CMDs simulation for full 40S ribosome. By utilizing the clustering analysis on the snapshots obtained from a 500 ns all-atom CMD run, we were able to acquire10 representative structures. These structures were served as the starting point for conducting 10 independent SMD simulations. The most prevalent structure derived from clustering the snapshots obtained from the 500 ns CMD simulations of the mRNA-40S and mRNA-40S-NSP1 complexes was selected to carry out the MARTINI CG alchemical simulations. All steps of energy minimization and MD runs are described in Figure S1.

Additionally, to ensure that the full ribosome complexes are equilibrated we performed simulations for truncated mRNA-40S and mRNA-40S-NSP1. The structure of the most abundant snapshot obtained from the 500 ns CMD simulations of complete ribosomes was used for truncation. Truncated mRNA-40S and mRNA-40S-NSP1 are rectangular boxes with dimensions of 22 nm $\leq x \leq$ 30 nm, 18 nm $\leq y \leq$ 30 nm, and 7 nm $\leq z \leq$ 19 nm (Figure 1C). The energy of these truncated complexes was then minimized, followed by short 5 ns simulations in both the *NVT* and *NPT* ensembles. A production all-atom CMD simulation of 1000 ns was carried out and the computational procedure was repeated as in the case of full ribosomes. Namely, from this run, 10 representative snapshots obtained by the clustering analysis were selected and

https://doi.org/10.1021/acs.jpcb.4c01391
J. Phys. Chem. B 2024, 128, 7033−7042

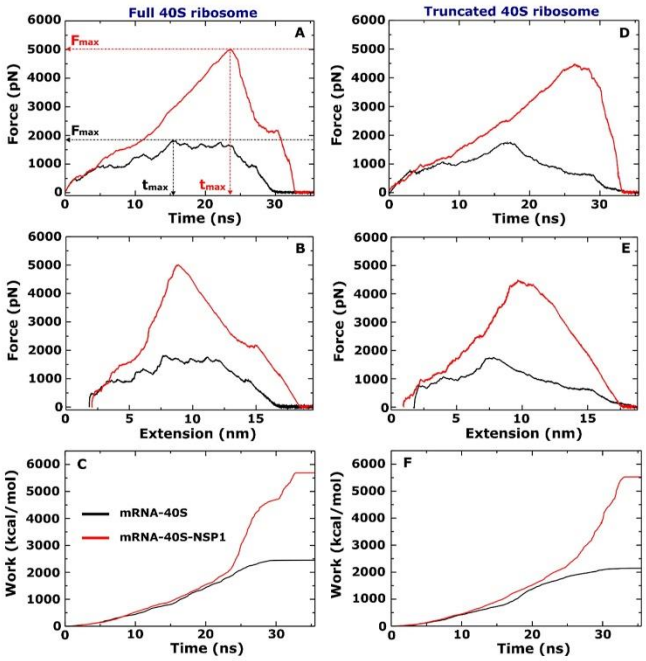

Figure 2. (A,D) Time-dependent behavior of force, (B,E) extension-dependent behavior of force, and (C,F) time-dependent behavior of work profiles of the mRNA-40S (black) and mRNA-40S-NSP1 (red) complexes for the cases of the full 40S ribosome and the truncated version of the 40S ribosome. The results were averaged over 10 independent SMD runs.

used as initial structures for conducting 10 independent SMD simulations, while the most representative structure was used for MARTINI CG alchemical simulations. The purpose of this step was to compare the results obtained from the full 40S ribosome and the truncated 40S ribosome for mRNA-40S and mRNA-40S-NSP1. More details are shown in Figure S1. The AMBER99SB force field[24] and the water model TIP3P[25] were used for all-atom CMD runs for both full and truncated systems.

As shown in Figure S2, the root-mean-square deviation (rmsd) of both complexes exhibits fluctuations. The rmsd consistently remains below 0.35 nm in the CGMD simulations (Figure S2A). In the case of CMD simulations of the full ribosome, the rmsd reaches equilibrium after approximately 200 ns, displaying fluctuations around 1.15 nm (Figure S2B). Moreover, Figure S2B shows that NSP1 has little effect on the rest of the ribosomal complex structure. This is reasonable because our model only considers the C-terminal domain of NSP1, and this small fragment (32 residues), especially compared to the ribosome, may significantly affect the region near the mRNA entry tunnel, but not other parts of the ribosome. For CMD simulations of truncated complexes, equilibrium is also attained after 200 ns, with the rmsd fluctuating below 0.3 nm (Figure S2C). Thus, our results suggest that equilibrium was achieved in both the full and truncated models. Another reason to believe that these systems have already reached equilibrium in our simulations is that the PDB structure of the ribosome with NSP1 was used (PDB ID 6ZOJ). Addition of a short mRNA (and removal of the relatively short C-terminus of NSP1 to create the mRNA-40S complex) should not affect much the system. Of course, it is impossible to equilibrate ribosomal complexes starting from random conformations.

2.3. SMD Simulations. In order to probe the binding affinity of mRNA to the ribosome in the presence and absence of NSP1 SMD simulations[26] were conducted by pulling it along its entry channel for full 40S and truncated 40S complexes. An external force is applied to the dummy atom connected to the 5′-mRNA (O5′ atom) through a spring with a stiffness k. In general, the direction of pulling is along the mRNA entry channel. The spring constant k was set to 600 kJ/(mol.nm^2) (≈1020 pN/nm), which is a typical value used in atomic force microscopy experiments.[27] The complexes were rotated so that the exit direction was parallel to the z-axis (Figure S3). A pulling speed of v = 0.5 nm/ns was used, and this value is about 10 orders of magnitude greater than in the experiment, but, as shown in previous works,[28] this choice does not affect the relative binding affinity, i.e., it can be used to discern strong from weak binders. More details on SMD simulations can be found in Supporting Information.

2.4. Alchemical Molecular Dynamics Simulations. Since SMD at high pulling speeds only allows estimation of relative binding affinity, in order to evaluate the effect of SARS-CoV-2 NSP1 on the absolute binding affinity of mRNA to the 40S ribosome, alchemical free energy calculations were performed using the MARTINI CG model.

https://doi.org/10.1021/acs.jpcb.4c01391
J. Phys. Chem. B 2024, 128, 7033−7042

Table 1. Rupture Force (F_{max}), Rupture Time (T_{max}), and Non-Equilibrium Work (W) Were Averaged Over 10 Independent SMD Trajectories of mRNA-40S and mRNA-40S-NSP1 with the Full and Truncated 40S ribosomes[a]

	mRNA-40S (full 40S ribosome)	mRNA-40S-NSP1 (full 40S ribosome)	mRNA-40S (truncated 40S ribosome)	mRNA-40S-NSP1 (truncated 40S ribosome)
F_{max} (pN)	1832.9 ± 127.4	5023.3 ± 232.1	1763.6 ± 103.3	4501.3 ± 227.5
t_{max} (ps)	15625.1 ± 1170.5	23666.9 ± 1270.2	17302.7 ± 1208.9	26448.7 ± 1311.3
W (kcal/mol)	2401.4 ± 60.8	5688.5 ± 121.2	2147.4 ± 66.2	5526.4 ± 121.3

[a]The errors represent standard deviations.

The mRNA-40S and mRNA-40S-NSP1 complexes used for alchemical free energy calculations were taken from the most populated structure for each system of 500 ns CMD simulations for the full 40S ribosome, and of 1000 ns CMD simulations for the truncated 40S ribosome. Here, the standard CG MARTINI 2.2 force field, which was developed for modeling of biological systems such as biological membranes, proteins, nucleotides, etc.[22,29] was used to calculate the binding free energy of mRNA to the 40S and the 40S-NSP1. This force field is accurate enough to describe the ligand−protein, protein−protein, protein−DNA/RNA, and protein-liquid interaction in an aqueous medium.[22,29,30] The MARTINI water model[23] was used with a minimum distance between water beads of 1.0 nm. The system was neutralized by adding sodium chloride salt solution. The temperature was set to T = 300 K using a v-rescale thermostat,[31] and pressure was set to p = 1.0 bar with a Parrinello−Rahman barostat.[32] The LINCS algorithm[33] was used to constrain the length of all bonds.

To evaluate the free energy of mRNA binding to the 40S ribosome with and without SARS-CoV-2 NSP1, we created the thermodynamic cycle described in Figure S4. From the thermodynamic cycle, we have

$$\Delta G_{bind}^{ALC} - \Delta G = \Delta G_{complexation} - \Delta G_{solvation} \quad (1)$$

$\Delta G \equiv 0$ as it is related to noninteracting ($\lambda = 1$) mRNA being dummy and dummy-40S-NSP1. Then the binding free energy has the following form

$$\Delta G_{bind}^{ALC} = \Delta G_{complexation} - \Delta G_{solvation} \quad (2)$$

For alchemical transformations, we used an optimal set of λ-values ranging from $\lambda = 0$ to $\lambda = 1$, where $\lambda = 0$ and $\lambda = 1$ correspond to a system with and without full interaction, respectively. To obtain the optimal set of λ-values, we used the available script at https://gitlab.com/KomBioMol/converge_lambdas.[34] The optimal set of 30, 30, and 20 windows of λ-values were selected for the mRNA-40S, mRNA-40S-NSP1, and mRNA, respectively. Thus, a total of 80 windows were used for alchemical calculations of free energy. These windows are the same for the full and truncated models. For each window, simulations were run for 1000 ns to ensure that the complexes reached equilibrium. Free energy changes were estimated using the Bennett acceptance ratio.[35] The binding free energy was then calculated from the thermodynamics cycle (Figure S4).

The CG MARTINI force field allows long-term simulations of large systems by reducing the number of degrees of freedom compared to all-atom models. However, one limitation of the MARTINI model is that it uses an elastic network model, which may introduce artificial stiffness that could affect the free energy calculations. This is an important issue that requires further study, but despite the limitation mentioned here, the free energy estimates obtained with the CG MARTINI model agree reasonably well with experimental results obtained in several previous cases.[28c,36] From this point of view, our results should be considered as a rough estimate and carefully compared with the SMD and experimental results.

3. RESULTS AND DISCUSSIONS

3.1. Binding Affinity of mRNA to 40S Ribosome with and without SARS-CoV-2 NSP1: SMD Simulations. Details and setup of SMD simulations are described in SI (Figure S3). The ten most representative structures obtained by clustering snapshots collected during 500 and 1000 ns CMD for the full and truncated 40S ribosome, respectively, were used as starting conformations for the SMD trajectories for the mRNA-40S and mRNA-40S-NSP1 complexes. Figure 2 shows the force, and nonequilibrium work profiles of these complexes, where the result was averaged over 10 independent SMD simulations.

The unbinding pathways can be divided into two distinct parts: before and after reaching the maximum point. For simple systems, such as two interacting proteins without a ribosome, the force−extension profile exhibits linear behavior typical of a spring before rupture.[37] However, in our case, a nonlinear dependence occurs in all complexes (Figure 2). Beyond the peak, the behavior remains complex, especially in the case of the complete ribosome, where weak peaks appear over large time scales. The mRNA molecule is on the verge of leaving the binding region when the force begins to vanish. Overall, in the presence of NSP1, the complex becomes more rigid, reducing force fluctuations.

Although the first regime in the force-time/extension profile in not linear and several peaks occur in the second regime, the choice of t_{max} is not ambiguous, because the main peak (F_{max}) is clearly higher than other peaks and the dependence of force on time is a single-valued function (Figure 2). For full 40S ribosome, the force−time profile shows that mRNA binds to the 40S-NSP1 (F_{max} = 5023.3 ± 232.1 pN) more strongly than to the 40S ribosome (F_{max} = 1832.9 ± 127.4 pN). The time to reach the maximum force t_{max} increases with increasing F_{max} (Figure 2A,B and Table 1).

Since the nonequilibrium work W is determined for the entire process (eq S2) while F_{max} is determined at a single point, W characterizes the binding affinity better than F_{max}.[38] Therefore, we also present the results obtained for W. Initially, W showed an increase as the extended molecule moved out of the binding region, eventually reaching a stable value when the interaction of the mRNA with 40S or 40S-NSP1 disappeared (Figure 2C). In other words, the nonequilibrium work increased until the mRNA separated from the 40S ribosome entry tunnel and became saturated. By defining the work done by mRNA upon exiting the ribosome as the saturation value at the end of the simulation, we obtained W = 5688.5 ± 121.2 and 2401.4 ± 60.8 kcal/mol for mRNA-40S-NSP1 and mRNA-40S, respectively (Table 1). Thus the results obtained

https://doi.org/10.1021/acs.jpcb.4c01391
J. Phys. Chem. B 2024, 128, 7033−7042

The Journal of Physical Chemistry B pubs.acs.org/JPCB Article

Table 2. Non-Bonded Interaction Energies (kcal/mol) of the mRNA-40S and mRNA-40S-NSP1 with Both the Full and the Truncated 40S Ribosomes[a]

	mRNA-40S (full 40S ribosome)	mRNA-40S-NSP1 (full 40S ribosome)	mRNA-40S (truncated 40S ribosome)	mRNA-40S-NSP1 (truncated 40S ribosome)
ΔE_{elec}	125425.2 ± 313.7	105814.4 ± 301.7	71538.9 ± 225.4	57929.2 ± 216.5
ΔE_{vdW}	−177.6 ± 4.1	−308.2 ± 4.2	−269.6 ± 4.4	−305.3 ± 3.7
ΔE_{total}	125247.6 ± 317.8	105506.2 ± 305.9	71269.3 ± 229.8	57623.9 ± 220.2

[a]The results were obtained for a $[0\text{-}t_{max}]$ time window and averaged over 10 SMD trajectories. The errors represent standard deviations.

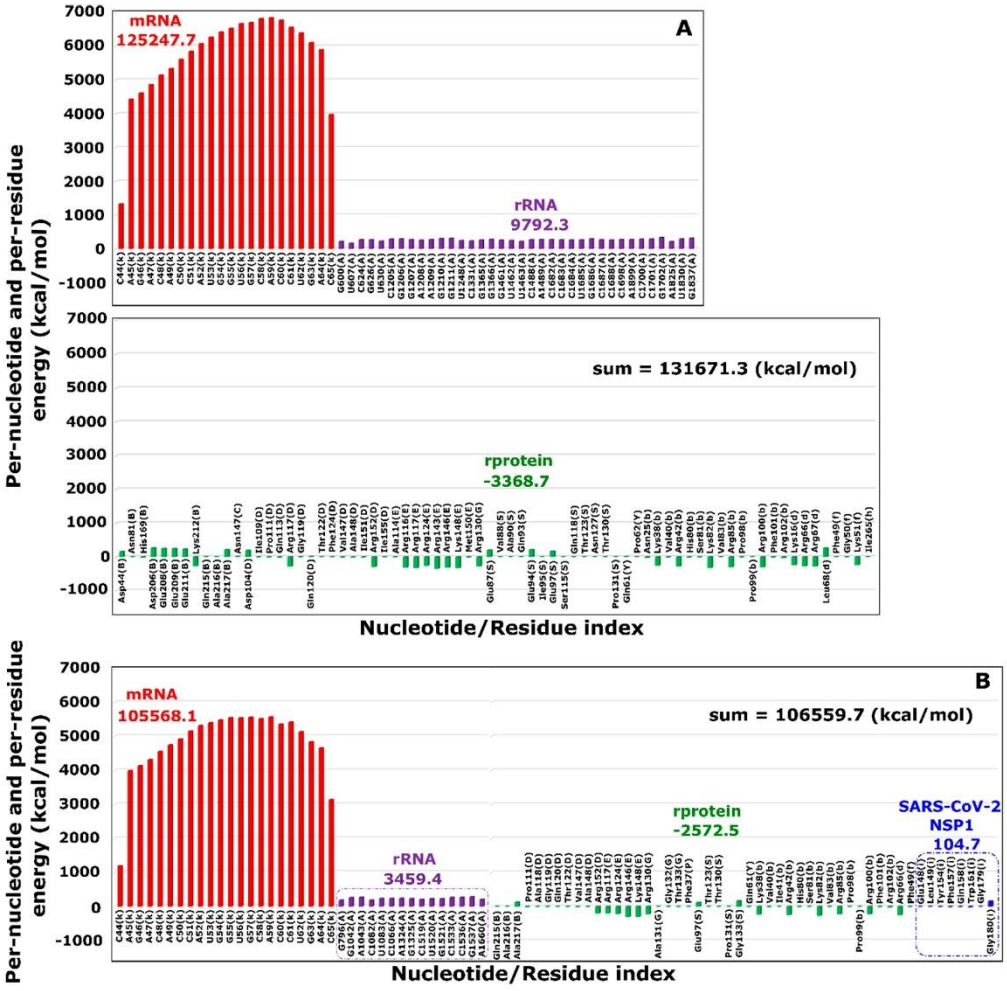

Figure 3. Interaction energy (electrostatic and vdW) per-nucleotide and per-residue at the binding regions of mRNA to (A) 40S ribosome and (B) 40S-NSP1. The numbers next to the profiles refer to the total energy (sum over all interacting residues or nucleotides) measured in kcal/mol. For example, for mRNA in (A) the sum over all nucleotides and residues in the binding site is 131671.3 kcal/mol, while in (B) it is only 106559.7 kcal/mol. The results were averaged over 10 independent SMD runs of the full 40S ribosome.

for both F_{max} and W indicate that NSP1 increases the binding affinity of mRNA to the ribosome, which interferes with the translation process.

For the truncated 40S ribosome, before rupture the force−extension relationship is not linear, as is the case for the full ribosome (Figure 2D,E), but the overall force−extension/time

https://doi.org/10.1021/acs.jpcb.4c01391
J. Phys. Chem. B 2024, 128, 7033−7042

Table 3. Binding Free Energies (kcal/mol) of the mRNA-40S and mRNA-40S-NSP1 Complexes with Both the Full 40S Ribosome and the Truncated 40S Ribosome[a]

		full 40S ribosome		truncated 40S ribosome	
		mRNA-40S	mRNA-40S-NSP1	mRNA-40S	mRNA-40S-NSP1
ΔG_{bind}, Experiment[39]	−10.7 ± 0.1	N/A	N/A	N/A	
ΔG^{ALC}_{bind}, Our simulation	200−800 ns	−12.7 ± 1.2	−35.8 ± 2.1	−8.3 ± 1.7	−27.9 ± 3.1
	200−1000 ns	−13.1 ± 1.1	−37.1 ± 2.2	−8.6 ± 1.2	−28.2 ± 2.6

[a]The results were obtained using alchemical free energy calculations and the MARTINI CG model.

profile is less complex, likely due to fewer residues interacting with the mRNA. To detach mRNA from the binding region of the 40S-NSP1 complex, a much higher force is required (F_{max} = 4501.3 ± 227.5 pN) compared to the case of 40S (F_{max} = 1763.6 ± 103.3 pN) (Table 1). For mRNA-40S, the full and truncated ribosome models provide the same F_{max}, while for mRNA-40S-NSP1 the truncated version gives a slightly lower value within the error bars. The nonequilibrium work shows a further difference in binding affinity caused by NSP1 (Figure 2F), for mRNA-40S-NSP1 W = 5526.4 ± 121.3 kcal/mol, and for mRNA-40S, W = 2147.4 ± 66.2 kcal/mol (Table 1). Interestingly, W is the same for full and truncated ribosomes, both for complexes with and without NSP1. Thus, along with the results obtained for F_{max}, this result suggests that the truncated ribosome model reasonably predicts relative binding affinities of mRNA, highlighting the increased stability of mRNA-40S-NSP1 compared to mRNA-40S, which is also in good agreement with the experiments on inhibition of mRNA translation by NSP1.[12,16] Since the relatively small truncated system is easy to equilibrate, this result can be seen as further confirmation of the fact that large complete ribosome models were equilibrated in our simulations.

3.2. SARS-CoV-2 NSP1 Binding to 40S Ribosome Reduces the Electrostatic and vdW Interaction Energies between mRNA and 40S Ribosome. van der Waals (ΔE_{vdW}), electrostatic (ΔE_{elec}), and total ($\Delta E_{total} = \Delta E_{elec} + \Delta E_{vdW}$) interaction energies averaged over 10 independent SMD runs are shown as a function of simulation time for both mRNA-40S and for mRNA- 40S-NSP1 complexes in full and truncated 40S ribosome models. ΔE_{vdW} is negative in the bound state, then reaches 0 kcal/mol in the unbound state for both complexes (Figure S5A,D). In contrast, ΔE_{elec} is positive in the bound and unbound states (Figure S5B,E). Clearly, ΔE_{elec} is much larger than ΔE_{vdW} for the mRNA-40S and mRNA-40S-NSP1 complexes, resulting in $\Delta E_{total} > 0$ (Figure S5C,F).

In the full 40S ribosome, the energy of the bound state ($t < t_{max}$) was determined by averaging over the time interval $[0, t_{max}]$. Then ΔE_{elec} = 105814.4 ± 301.7 and 125425.2 ± 313.7 kcal/mol, ΔE_{vdW} = −308.2 ± 4.2 and −177.6 ± 4.1 kcal/mol, and ΔE_{total} = 105506.2 ± 305.9 and 125247.6 ± 317.8 kcal/mol for the mRNA-40S-NSP1 and the mRNA-40S complexes, respectively (Table 2). For the truncated 40S ribosome model, the following energy values were obtained for the mRNA-40S-NSP1 and the mRNA-40S complexes: ΔE_{elec} = 57929.2 ± 216.5 and 71538.9 ± 225.4 kcal/mol, ΔE_{vdW} = −305.3 ± 3.7 and −269.6 ± 4.4 kcal/mol, and ΔE_{total} = 57623.9 ± 220.2 and 71269.3 ± 229.8 kcal/mol, respectively (Table 2). Although ΔE_{vdW}, ΔE_{elec}, and ΔE_{total} differ for full and truncated 40S ribosomes, these results indicate that the interaction between mRNA and 40S ribosome is reduced by SARS-CoV-2 NSP1 binding.

Thus, for both complexes, the electrostatic interaction predominates over the vdW interaction. The positive value of ΔE_{total} is due to repulsion between negatively charged 40S ribosome (−1215e), mRNA (−21e), and SARS-CoV-2 NSP1 (−3e) (Table S1). Our result also shows that SARS-CoV-2 NSP1 binding reduces the interaction between mRNA and 40S ribosome, making the mRNA-40S complex more stable.

Note that the AMBER99SB force field we use is a nonpolarizable force field that neglects charge regulation effects. This may lead to inaccurate predictions of electrostatic interactions of mRNA with surrounding molecules. Therefore, we should be cautious in concluding that Coulomb electrostatic interactions play a more important role than van der Waals interactions for mRNA stability.

3.3. Water Molecules Stabilize the Systems. Since the total interaction energy ΔE_{total} obtained in the previous section is positive for both complexes, an important question emerges is whether these complexes are stable? To answer this question we will take into account water molecules. Again, ΔE_{total} was calculated by averaging over 10 SMD trajectories in the time window $[0, t_{max}]$ for the full 40S ribosome. We obtained the total energy of −288942.4 ± 212.5, and −311478.3 ± 267.3 kcal/mol for the mRNA-40S and the mRNA-40S-NSP1, respectively (Table S2), which implies that these complexes are stabilized by water molecules.

3.4. Important SARS-CoV-2 NSP1 Residues. The energy per nucleotide of mRNA and rRNA, as well as the energy per residue of rprotein and SARS-CoV-2 NSP1 are shown in Figure 3 for mRNA-40S and mRNA-40S-NSP1 complexes. They were obtained by averaging over 10 SMD trajectories in the $[0, t_{max}]$ time window only for the full 40S ribosome case. This took into account the interaction of mRNA with all rproteins, rRNA and NSP1 of SARS-CoV-2 for the mRNA-40S and mRNA-40S-NSP1 complexes. Clearly, the energy of mRNA per nucleotide is much higher than that of rRNA per nucleotide, rprotein per residue, and SARS-CoV-2 NSP1 per residue. It is important to note that the total energy of nucleotides and residues of mRNA-40S-NSP1 (106559.7 kcal/mol) is significantly less than that of mRNA-40S (131671.3 kcal/mol) (Figure 3A,B). This result is consistent with the result obtained for the entire system, including the binding region, that SARS-CoV-2 NSP1 reduces the interaction between mRNA and the 40S ribosome upon binding to the mRNA channel.

Moreover, the contribution of each SARS-CoV-2 NSP1 residue at the binding region to the binding energy is Glu148 = −4.4, Leu149 = −3.9, Tyr154 = −7.5, Phe157 = −9.4, Gln158 = −8.4, Trp161 = −20.5, Gly179 = −1.6, and Gly180 = 160.6 kcal/mol (Figure 3B). Since the interaction energy of Glu148, Leu149, Tyr154, Phe157, Gln158, Trp161 and Gly179 is negative, these residues stabilize the system, whereas with positive interaction energy only Gly180 makes the complex less stable. Although the SARS-CoV-2 NSP1 total energy of

https://doi.org/10.1021/acs.jpcb.4c01391
J. Phys. Chem. B 2024, 128, 7033−7042

interaction with mRNA is positive (104.7 kcal/mol), its presence makes the complex more stable by reducing the interaction energy of mRNA with rRNA and rprotein. Taken together, mRNA translation at the 40S ribosome of the host immune system is controlled by electrostatic interactions and can be stalled by SARS-CoV-2 NSP1. SARS-CoV-2 NSP1 residues Glu148, Leu149, Tyr154, Phe157, Gln158, Trp161, Gly179, and Gly180 play a key role as they are at the interface with mRNA.

3.5. Binding Free Energy of mRNA to the 40S Ribosome with and without SARS-CoV-2 NSP1: Alchemical Simulations. Figure S6 displays the time dependence of rmsd of mRNA, mRNA-40S, and mRNA-40S-NSP1 at $\lambda = 0$ for both the full 40S ribosome and the truncated 40S ribosome cases. This plot shows that these systems achieved equilibrium after approximately 200 ns. As a result, we proceeded to calculate the binding free energy of mRNA to the 40S ribosome and 40S-NSP1 using two different time windows: [200−800 ns] and [200−1000 ns] (Table 3). It is worth noting that the results obtained in these two time windows are similar within the margin of error, indicating that the data were indeed equilibrated. Therefore, we decided to base our analysis on the results obtained from the [200−1000 ns] time window.

For the full 40S ribosome, the binding free energy of mRNA-40S, denoted as $\Delta G^{ALC}_{bind} = -13.1 \pm 1.1$ kcal/mol, which is very close to the experimental value of -10.7 ± 0.1 kcal/mol.[39] In contrast, in the presence of NSP1, the binding free energy of mRNA-40S-NSP1 is reduced to $\Delta G^{ALC}_{bind} = -37.1 \pm 2.2$ kcal/mol. The binding affinity increases approximately 3-fold at a ratio of $R = \Delta G^{ALC}_{bind}(\text{mRNA-40S-NSP1})/\Delta G^{ALC}_{bind}(\text{mRNA-40S}) = -37.1/-13.1 = 2.8$. Thus, consistent with the SMD results, NSP1 strongly increases the binding affinity of mRNA to the entry channel, stopping translation and hence the protein synthesis process.[12,16]

For the truncated 40S ribosome, the binding free energy of mRNA-40S the binding free energy ($\Delta G^{ALC}_{bind} = -8.6 \pm 1.2$ kcal/mol) is higher than that of mRNA-40S-NSP1 ($\Delta G^{ALC}_{bind} = -28.2 \pm 2.6$ kcal/mol) (Table 3). The fact that the absolute value of ΔG^{ALC}_{bind} of a truncated ribosome is lower than a full ribosome is reasonable since the smaller system must be less stable than larger one. Nevertheless our results obtained for the truncated complexes also support the main conclusion that NSP1 suppresses mRNA translation by increasing binding affinity ($R = \Delta G^{ALC}_{bind}(\text{mRNA-40S-NSP1}\Delta G^{ALC}_{bind})/(\text{mRNA-40S}) = -28.2/-8.6 = 3.3$). This R ratio is higher than in the case of a complete ribosome.

Since nonequilibrium work is a good measure of binding affinity, R can be defined as $R = W(\text{mRNA-40S-NSP1})/W(\text{mRNA-40S})$. Using the SMD data shown in Table 1, we obtain $R = 2.4$ and 2.6 for the full and truncated complexes, respectively. These values are not far from 2.8 obtained from the binding free energies of the full ribosome complexes. Moreover, both SMD and alchemical simulations yield R of full ribosome complexes lower than the truncated case.

4. CONCLUSION

In conclusion, our study employed a combination of SMD and alchemical simulations to investigate the association of mRNA with the 40S ribosome, both in the absence and presence of SARS-CoV-2 NSP1. Our all-atom SMD results clearly demonstrate that mRNA exhibits a much stronger binding affinity to the 40S-NSP1 complex than to the 40S ribosome alone. This observation aligns with the results obtained from the binding free energy calculations using CG alchemical simulations. Therefore, it can be inferred that the mRNA-40S complex is relatively less stable when compared to the mRNA-40S-NSP1 complex. Our findings are in excellent agreement with experimental data from previous studies.[12,16] It is shown that the mRNA translation process is primarily driven by the electrostatic interactions between mRNA and the 40S ribosome. Upon entering host cells, SARS-CoV-2 NSP1 has the potential to bind to the 40S ribosome, thereby inhibiting the translation process. Our analysis identified key SARS-CoV-2 NSP1 residues, including Glu148, Leu149, Tyr154, Phe157, Gln158, Trp161, Gly179, and Gly180, at the interface with mRNA, which play a crucial role in triggering translational arrest of the host immune system.

■ ASSOCIATED CONTENT

Supporting Information

The Supporting Information is available free of charge at https://pubs.acs.org/doi/10.1021/acs.jpcb.4c01391.

A brief overview of the methods used to estimate binding affinity using molecular dynamics simulations is provided, as well as a detailed description of conventional and SMDs simulations. Figure S1: the scheme describes all MD simulations in this work. Figure S2: rmsd as a function of simulation time of mRNA-40S, and mRNA-40S-NSP1 complexes with the full and truncated 40S ribosome. Figure S3: initial and final conformations from SMDs simulation of the extraction of mRNA from 40S ribosomal subunit and SARS-CoV-2 NSP1 for both full and truncated 40S ribosome. Figure S4: an example of a thermodynamics cycle to calculate binding free energy between mRNA and the 40S-NSP1 using alchemical simulation. Figure S5: time dependence of vdW, electrostatic, and total interaction energy of mRNA-40S and mRNA-40S-NSP1 for full and truncated 40S ribosomes. Figure S6: rmsd as a function of simulation time of only mRNA, mRNA-40S, mRNA-40S-NSP1 at $\lambda = 0$ in the alchemical free energy calculations using the MARTINI CG model. Table S1: Total charge of the 40S ribosome, SARS-CoV-2 NSP1 and mRNA. Table S2: total nonbonded energy of the mRNA-40S and mRNA-40S-NSP1 complexes with water and ions (PDF)

■ AUTHOR INFORMATION

Corresponding Author

Mai Suan Li − *Institute of Physics, Polish Academy of Sciences, 02-668 Warsaw, Poland; Quang Trung Software City, Life Science Lab, Institute for Computational Science and Technology, Ho Chi Minh City 729110, Vietnam;* orcid.org/0000-0001-7021-7916; Email: masli@ifpan.edu.pl

Authors

Hung Nguyen − *Institute of Physics, Polish Academy of Sciences, 02-668 Warsaw, Poland;* orcid.org/0000-0002-1282-319X

Hoang Linh Nguyen − *Institute of Fundamental and Applied Sciences, Duy Tan University, Ho Chi Minh City 700000, Vietnam; Faculty of Environmental and Natural Sciences,*

https://doi.org/10.1021/acs.jpcb.4c01391
J. Phys. Chem. B 2024, 128, 7033−7042

Duy Tan University, Da Nang City 550000, Vietnam;
orcid.org/0000-0003-4141-1642

Complete contact information is available at:
https://pubs.acs.org/10.1021/acs.jpcb.4c01391

Author Contributions

MSL, HN and HLN designed the research. MSL supervised the study. HN performed simulations. HN and HLN analyzed the data. HN and MSL wrote the manuscript.

Notes

The authors declare no competing financial interest.

■ ACKNOWLEDGMENTS

We thank Giovanni La Penna for useful discussions. This research was supported by Narodowe Centrum Nauki in Poland (grant 2019/35/B/ST4/02086) and in part by PLGrid Infrastructure and the supercomputer centre TASK in Gdansk, Poland.

■ REFERENCES

(1) Gorbalenya, A. E.; Baker, S. C.; Baric, R. S.; de Groot, R. J.; Drosten, C.; Gulyaeva, A. A.; Haagmans, B. L.; Lauber, C.; Leontovich, A. M.; Neuman, B. W.; et al. The species Severe acute respiratory syndrome-related coronavirus: classifying 2019-nCoV and naming it SARS-CoV-2. *Nat. Microbiol.* **2020**, *5* (4), 536−544.

(2) (a) Astuti, I.; Ysrafil. Severe Acute Respiratory Syndrome Coronavirus 2 (SARS-CoV-2): An Overview of Viral Structure and Host Response. *Diabetes, Metab. Syndrome* **2020**, *14* (4), 407−412. (b) Diaz, J. SARS-CoV-2 Molecular Network Structure. *Front. Physiol.* **2020**, *11*, 870.

(3) (a) Lim, Y. X.; Ng, Y. L.; Tam, J. P.; Liu, D. X. Human Coronaviruses: A Review of Virus-host Interactions. *Diseases* **2016**, *4* (3), 26. (b) Zhou, P.; Yang, X. L.; Wang, X. G.; Hu, B.; Zhang, L.; Zhang, W.; Si, H. R.; Zhu, Y.; Li, B.; Huang, C. L.; Chen, H. D.; Chen, J.; Luo, Y.; Guo, H.; Jiang, R. D.; Liu, M. Q.; Chen, Y.; Shen, X. R.; Wang, X.; Zheng, X. S.; Zhao, K.; Chen, Q. J.; Deng, F.; Liu, L. L.; Yan, B.; Zhan, F. X.; Wang, Y. Y.; Xiao, G. F.; Shi, Z. L. A Pneumonia Outbreak Associated with A New Coronavirus of Probable Bat Origin. *Nature* **2020**, *579* (7798), 270−273.

(4) (a) Masters, P. S. The Molecular Biology of Coronaviruses. *Adv. Virus Res.* **2006**, *66*, 193−292. (b) Prentice, E.; McAuliffe, J.; Lu, X.; Subbarao, K.; Denison, M. R. Identification and Characterization of Severe Acute Respiratory Syndrome Coronavirus Replicase Proteins. *J. Virol.* **2004**, *78* (18), 9977−9986.

(5) Lin, J. W.; Tang, C.; Wei, H. C.; Du, B.; Chen, C.; Wang, M.; Zhou, Y.; Yu, M. X.; Cheng, L.; Kuivanen, S.; Ogando, N. S.; Levanov, L.; Zhao, Y.; Li, C. L.; Zhou, R.; Li, Z.; Zhang, Y.; Sun, K.; Wang, C.; Chen, L.; Xiao, X.; Zheng, X.; Chen, S. S.; Zhou, Z.; Yang, R.; Zhang, D.; Xu, M.; Song, J.; Wang, D.; Li, Y.; Lei, S.; Zeng, W.; Yang, Q.; He, P.; Zhang, Y.; Zhou, L.; Cao, L.; Luo, F.; Liu, H.; Wang, L.; Ye, F.; Zhang, M.; Li, M.; Fan, W.; Li, X.; Li, K.; Ke, B.; Xu, J.; Yang, H.; He, S.; Pan, M.; Yan, Y.; Zha, Y.; Jiang, L.; Yu, C.; Liu, Y.; Xu, Z.; Li, Q.; Jiang, Y.; Sun, J.; Hong, W.; Wei, H.; Lu, G.; Vapalahti, O.; Luo, Y.; Wei, Y.; Connor, T.; Tan, W.; Snijder, E. J.; Smura, T.; Li, W.; Geng, J.; Ying, B.; Chen, L. Genomic Monitoring of SARS-CoV-2 Uncovers An Nsp1 Deletion Variant That Modulates Type I Interferon Response. *Cell Host Microbe* **2021**, *29* (3), 489.e8−502.e8.

(6) Yuan, S.; Balaji, S.; Lomakin, I. B.; Xiong, Y. Coronavirus Nsp1: Immune Response Suppression and Protein Expression Inhibition. *Front. Microbiol.* **2021**, *12*, 752214.

(7) de Breyne, S.; Vindry, C.; Guillin, O.; Conde, L.; Mure, F.; Gruffat, H.; Chavatte, L.; Ohlmann, T. Translational Control of Coronaviruses. *Nucleic Acids Res.* **2020**, *48* (22), 12502−12522.

(8) (a) Abernathy, E.; Glaunsinger, B. Emerging Roles for RNA Degradation in Viral Replication and Antiviral Defense. *Virology* **2015**, *479*−*480*, 600−608. (b) Stern-Ginossar, N.; Thompson, S. R.; Mathews, M. B.; Mohr, I. Translational Control in Virus-infected Cells. *Cold Spring Harbor Perspect. Biol.* **2019**, *11* (3), a033001.

(9) (a) Hartenian, E.; Nandakumar, D.; Lari, A.; Ly, M.; Tucker, J. M.; Glaunsinger, B. A. The Molecular Virology of Coronaviruses. *J. Biol. Chem.* **2020**, *295* (37), 12910−12934. (b) Nakagawa, K.; Makino, S. Mechanisms of Coronavirus Nsp1-mediated Control of Host and Viral Gene Expression. *Cells* **2021**, *10* (2), 300. (c) Narayanan, P.; Chatterton, P.; Ikeda, A.; Ikeda, S.; Corey, D. P.; Ervasti, J. M.; Perrin, B. J. Length Regulation of Mechanosensitive Stereocilia Depends on Very Slow Actin Dynamics and Filament-severing Proteins. *Nat. Commun.* **2015**, *6* (1), 6855.

(10) (a) Banerjee, A. K.; Blanco, M. R.; Bruce, E. A.; Honson, D. D.; Chen, L. M.; Chow, A.; Bhat, P.; Ollikainen, N.; Quinodoz, S. A.; Loney, C.; Thai, J.; Miller, Z. D.; Lin, A. E.; Schmidt, M. M.; Stewart, D. G.; Goldfarb, D.; De Lorenzo, G.; Rihn, S. J.; Voorhees, R. M.; Botten, J. W.; Majumdar, D.; Guttman, M. SARS-CoV-2 Disrupts Splicing, Translation, and Protein Trafficking to Suppress Host Defenses. *Cell* **2020**, *183* (5), 1325.e21−1339.e21. (b) Hillen, H. S.; Kokic, G.; Farnung, L.; Dienemann, C.; Tegunov, D.; Cramer, P. Structure of Replicating SARS-CoV-2 Polymerase. *Nature* **2020**, *584* (7819), 154−156. (c) Littler, D. R.; Gully, B. S.; Colson, R. N.; Rossjohn, J. Crystal Structure of the SARS-CoV-2 Non-structural Protein 9, Nsp9. *iScience* **2020**, *23* (7), 101258. (d) Zhang, L.; Richards, A.; Barrasa, M. I.; Hughes, S. H.; Young, R. A.; Jaenisch, R. Reverse-transcribed SARS-CoV-2 RNA Can Integrate into the Genome of Cultured Human Cells and Can Be Expressed in Patient-derived Tissues. *Proc. Natl. Acad. Sci. U. S. A.* **2021**, *118* (21), No. e2105968118.

(11) (a) Lokugamage, K. G.; Narayanan, K.; Huang, C.; Makino, S. Severe Acute Respiratory Syndrome Coronavirus Protein Nsp1 Is A Novel Eukaryotic Translation Inhibitor That Represses Multiple Steps of Translation Initiation. *J. Virol.* **2012**, *86* (24), 13598−13608. (b) Kamitani, W.; Huang, C.; Narayanan, K.; Lokugamage, K. G.; Makino, S. A Two-pronged Strategy to Suppress Host Protein Synthesis by SARS Coronavirus Nsp1 Protein. *Nat. Struct. Mol. Biol.* **2009**, *16* (11), 1134−1140.

(12) Thoms, M.; Buschauer, R.; Ameismeier, M.; Koepke, L.; Denk, T.; Hirschenberger, M.; Kratzat, H.; Hayn, M.; Mackens-Kiani, T.; Cheng, J.; Straub, J. H.; Sturzel, C. M.; Frohlich, T.; Berninghausen, O.; Becker, T.; Kirchhoff, F.; Sparrer, K. M. J.; Beckmann, R. Structural Basis for Translational Shutdown and Immune Evasion by the Nsp1 Protein of SARS-CoV-2. *Science* **2020**, *369* (6508), 1249−1255.

(13) (a) Paules, C. I.; Marston, H. D.; Fauci, A. S. Coronavirus Infections—More Than Just the Common Cold. *JAMA* **2020**, *323* (8), 707−708. (b) Shen, Z.; Zhang, G.; Yang, Y.; Li, M.; Yang, S.; Peng, G. Lysine 164 Is Critical for SARS-CoV-2 Nsp1 Inhibition of Host Gene Expression. *J. Gen. Virol.* **2021**, *102* (1), 001513.

(14) Clark, L. K.; Green, T. J.; Petit, C. M. Structure of Nonstructural Protein 1 from SARS-CoV-2. *J. Virol.* **2021**, *95* (4), 10.

(15) Mendez, A. S.; Ly, M.; González-Sánchez, A. M.; Hartenian, E.; Ingolia, N. T.; Cate, J. H.; Glaunsinger, B. A. The N-terminal Domain of SARS-CoV-2 Nsp1 Plays Key Roles in Suppression of Cellular Gene Expression and Preservation of Viral Gene Expression. *Cell Rep.* **2021**, *37* (3), 109841.

(16) Schubert, K.; Karousis, E. D.; Jomaa, A.; Scaiola, A.; Echeverria, B.; Gurzeler, L. A.; Leibundgut, M.; Thiel, V.; Muhlemann, O.; Ban, N. SARS-CoV-2 Nsp1 Binds the Ribosomal mRNA Channel to Inhibit Translation. *Nat. Struct. Mol. Biol.* **2020**, *27* (10), 959−966.

(17) (a) Narayanan, K.; Huang, C.; Lokugamage, K.; Kamitani, W.; Ikegami, T.; Tseng, C. T.; Makino, S. Severe Acute Respiratory Syndrome Coronavirus Nsp1 Suppresses Host Gene Expression, Including That of Type I Interferon, in Infected Cells. *J. Virol.* **2008**, *82* (9), 4471−4479. (b) Wathelet, M. G.; Orr, M.; Frieman, M. B.; Baric, R. S. Severe Acute Respiratory Syndrome Coronavirus Evades Antiviral Signaling: Role of Nsp1 and Rational Design of An Attenuated Strain. *J. Virol.* **2007**, *81* (21), 11620−11633.

(18) (a) Wu, C.; Liu, Y.; Yang, Y.; Zhang, P.; Zhong, W.; Wang, Y.; Wang, Q.; Xu, Y.; Li, M.; Li, X.; Zheng, M.; Chen, L.; Li, H. Analysis

of Therapeutic Targets for SARS-CoV-2 and Discovery of Potential Drugs by Computational Methods. *Acta Pharm. Sin. B* **2020**, *10* (5), 766−788. (b) Jauregui, A. R.; Savalia, D.; Lowry, V. K.; Farrell, C. M.; Wathelet, M. G. Identification of Residues of SARS-CoV Nsp1 That Differentially Affect Inhibition of Gene Expression and Antiviral Signaling. *PLoS One* **2013**, *8* (4), No. e62416.

(19) Borišek, J.; Spinello, A.; Magistrato, A. Molecular Basis of SARS-CoV-2 Nsp1-induced Immune Translational Shutdown as Revealed by All-atom Simulations. *J. Phys. Chem. Lett.* **2021**, *12*, 11745−11750.

(20) Juszkiewicz, S.; Chandrasekaran, V.; Lin, Z.; Kraatz, S.; Ramakrishnan, V.; Hegde, R. ZNF598 Is A Quality Control Sensor of Collided Ribosomes. *Mol. Cell* **2018**, *72*, 469−481.e7.

(21) The PyMOL Molecular Graphics System, Version 2.0 Schrödinger LLC.

(22) (a) Monticelli, L.; Kandasamy, S. K.; Periole, X.; Larson, R. G.; Tieleman, D. P.; Marrink, S. J. The MARTINI Coarse-Grained Force Field: Extension to Proteins. *J. Chem. Theory Comput.* **2008**, *4* (5), 819−834. (b) Uusitalo, J. J.; Ingolfsson, H. I.; Marrink, S. J.; Faustino, I. Martini Coarse-grained Force Field: Extension to RNA. *Biophys. J.* **2017**, *113* (2), 246−256.

(23) Yesylevskyy, S. O.; Schafer, L. V.; Sengupta, D.; Marrink, S. J. Polarizable Water Model for the Coarse-grained MARTINI Force Field. *PLoS Comput. Biol.* **2010**, *6* (6), No. e1000810.

(24) Hornak, V.; Abel, R.; Okur, A.; Strockbine, B.; Roitberg, A.; Simmerling, C. Comparison of Multiple Amber Force Fields and Development of Improved Protein Backbone Parameters. *Proteins* **2006**, *65* (3), 712−725.

(25) Jorgensen, W. L.; Jenson, C. Temperature Dependence of TIP3P, SPC, and TIP4P Water from NPT Monte Carlo Simulations: Seeking Temperatures of Maximum Density. *J. Comput. Chem.* **1998**, *19*, 1179−1186.

(26) (a) Nguyen, H.; Do, N.; Phan, T.; Pham, T. Steered Molecular Dynamics for Investigating the Interactions Between Insulin Receptor Tyrosine Kinase (IRK) and Variants of Protein Tyrosine Phosphatase 1B (PTP1B). *Appl. Biochem. Biotechnol.* **2018**, *184* (2), 401−413. (b) Lu, H.; Schulten, K. Steered Molecular Dynamics Simulations of Force-induced Protein Domain Unfolding. *Proteins* **1999**, *35* (4), 453−463. (c) Pham, T.; Nguyen, H. L.; Phan-Toai, T.; Nguyen, H. Investigation of Binding Affinity between Potential Antiviral Agents and PB2 Protein of Influenza A: Non-equilibrium Molecular Dynamics Simulation Approach. *Int. J. Med. Sci.* **2020**, *17* (13), 2031−2039.

(27) Binnig, G.; Quate, C. F.; Gerber, C. Atomic Force Microscope. *Phys. Rev. Lett.* **1986**, *56* (9), 930−933.

(28) (a) Nguyen, H.; Lan, P. D.; Nissley, D. A.; O'Brien, E. P.; Li, M. S. Electrostatic Interactions Explain the Higher Binding Affinity of the CR3022 Antibody for SARS-CoV-2 Than the 4A8 Antibody. *J. Phys. Chem. B* **2021**, *125* (27), 7368−7379. (b) Nguyen, H.; Lan, P. D.; Nissley, D. A.; O'Brien, E. P.; Li, M. S. Cocktail of REGN Antibodies Binds More Strongly to SARS-CoV-2 Than Its Components, but the Omicron Variant Reduces Its Neutralizing Ability. *J. Phys. Chem. B* **2022**, *126* (15), 2812−2823. (c) Nguyen, H.; Li, M. S. Antibody-nanobody Combination Increases Their Neutralizing Activity Against SARS-CoV-2 and Nanobody H11-H4 Is Effective Against Alpha, Kappa and Delta Variants. *Sci. Rep.* **2022**, *12* (1), 9701.

(29) Uusitalo, J. J.; Ingolfsson, H. I.; Akhshi, P.; Tieleman, D. P.; Marrink, S. J. Martini Coarse-grained Force Field: Extension to DNA. *J. Chem. Theory Comput.* **2015**, *11* (8), 3932−3945.

(30) (a) Arnarez, C.; Uusitalo, J. J.; Masman, M. F.; Ingolfsson, H. I.; de Jong, D. H.; Melo, M. N.; Periole, X.; de Vries, A. H.; Marrink, S. J. Dry Martini, A Coarse-grained Force Field for Lipid Membrane Simulations with Implicit Solvent. *J. Chem. Theory Comput.* **2015**, *11* (1), 260−275. (b) Souza, P. C. T.; Thallmair, S.; Conflitti, P.; Ramirez-Palacios, C.; Alessandri, R.; Raniolo, S.; Limongelli, V.; Marrink, S. J. Protein-ligand Binding with the Coarse-grained Martini Model. *Nat. Commun.* **2020**, *11* (1), 3714.

(31) Bussi, G.; Donadio, D.; Parrinello, M. Canonical Sampling Through Velocity Rescaling. *J. Chem. Phys.* **2007**, *126* (1), 014101.

(32) Parrinello, M.; Rahman, A. Polymorphic Transitions in Single Crystals: A New Molecular Dynamics Method. *J. Appl. Phys.* **1981**, *52*, 7182−7190.

(33) Hess, B.; Bekker, H.; Berendsen, H.; Fraaije, J. LINCS: A Linear Constraint Solver for Molecular Simulations. *J. Comput. Chem.* **1997**, *18*, 1463−1472.

(34) Wieczor, M.; Czub, J. Telomere Uncapping by Common Oxidative Guanine Lesions: Insights from Atomistic Models. *Free Radic. Biol. Med.* **2020**, *148*, 162−169.

(35) Bruckner, S.; Boresch, S. Efficiency of Alchemical Free Energy Simulations. I. A Practical Comparison of the Exponential Formula, Thermodynamic Integration, and Bennett's Acceptance Ratio Method. *J. Comput. Chem.* **2011**, *32* (7), 1303−1319.

(36) Patel, J. S.; Ytreberg, F. M. Fast Calculation of Protein-protein Binding Free Energies Using Umbrella Sampling with A Coarse-Grained Model. *J. Chem. Theory Comput.* **2018**, *14* (2), 991−997.

(37) Nguyen, H. L.; Lan, P. D.; Thai, N. Q.; Nissley, D. A.; O'Brien, E. P.; Li, M. S. Does SARS-CoV-2 Bind to Human ACE2More Strongly Than Does SARS-CoV? *J. Phys. Chem. B* **2020**, *124* (34), 7336−7347.

(38) Vuong, Q. V.; Nguyen, T. T.; Li, M. S. A New Method for Navigating Optimal Direction for Pulling Ligand from Binding Pocket: Application to Ranking Binding Affinity by Steered Molecular Dynamics. *J. Chem. Inf. Model.* **2015**, *55* (12), 2731−2738.

(39) Fraser, C. S.; Berry, K. E.; Hershey, J. W.; Doudna, J. A. eIF3j Is Located in the Decoding Center of the Human 40S Ribosomal Subunit. *Mol. Cell* **2007**, *26* (6), 811−819.

https://doi.org/10.1021/acs.jpcb.4c01391
J. Phys. Chem. B 2024, 128, 7033−7042

Chapter 5: Conclusions and future work

5.1 Conclusions

The results presented in this dissertation concern the mechanisms by which Ab and Nb bind to SARS-CoV-2 RBD, preventing the virus from entering human cells. They shed light on potential treatment strategies not only for wild-type SARS-CoV-2 but also for various variants of concern. In addition, we investigated how SARS-CoV-2 NSP1 interacts with the mRNA entry channel, which ultimately leads to the inhibition of the protein synthesis process. Our studies employ a range of theoretical and computational methods, including all-atom and coarse-grained models combined with MD methods. The main findings are as follows:

1) Using all-atom SMD and coarse-grained US simulations, we investigated the binding affinities between REGN10933 Ab, REGN10987 Ab, and the combination of REGN10933 and REGN10987 with RBD. Our results indicate that REGN10933 exhibits stronger binding affinity to RBD compared to REGN10987. Moreover, the combination of REGN10933 and REGN10987 demonstrates even greater binding strength to RBD. The stability of both REGN10933-RBD and REGN10933+REGN10987-RBD complexes is mainly governed by electrostatic interactions, whereas the stability of REGN10987-RBD complex relies on van der Waals interactions. In particular, REGN10933 and REGN10933+REGN10987 exhibit similar potency against both the Delta variant and the wild type. However, their effectiveness against the Omicron variant is reduced, which is in line with recent experimental findings.
2) We investigated the concurrent binding of H11-H4 Nb and CR3022 Ab to RBD using all-atom SMD and coarse-grained US simulations. Our results revealed significantly enhanced binding affinity compared to their individual associations with RBD. The combined action of H11-H4 and CR3022 resulted in increased neutralizing capacity against SARS-CoV-2. The stability of H11-H4-RBD complex is primarily governed by van der Waals interactions, while electrostatic interactions play a more significant role in the stability of CR3022-RBD and H11-H4+CR3022-RBD complexes. CR3022 has emerged as a promising candidate for COVID-19 treatment, especially against the wild-type strain. H11-H4 exhibits strong neutralizing abilities against Alpha, Kappa, and highly dangerous Delta variants, consistent with recent experimental results.
3) We investigated the interaction between mRNA and the 40S ribosome in the presence and absence of NSP1. Using full-atom SMD and coarse-grained alchemical simulations, our analysis revealed that mRNA exhibits significantly stronger binding affinity for the 40S-NSP1 complex compared to the 40S ribosome alone. This suggests that upon entry into host cells, NSP1 binds to the 40S ribosome, thereby hindering the translation process. These results are consistent with experimental observations. Our studies have shown that electrostatic interactions between mRNA and the 40S ribosome play a key role in driving the mRNA translation process.

5.2 Future work

Through a combination of all-atom and coarse-grained MD simulations, this dissertation has focused on two key problems: (1) the binding of Ab and Nb to SARS-CoV-2 RBD to prevent SARS-CoV-2 from entering the host cell, considering both the wild type and variants of concern and (2) How NSP1 binds to the mRNA exit tunnel to inhibit the mRNA translation process and disrupt protein synthesis in the human ribosome. In the near future we plan to work on the following issues:

1) Although our study has shown the importance of Ab-Ab or Ab-Nb combinations in the treatment of SARS-CoV-2 for both wild type and variants, it is important to note that the number of such pairs examined in our study was still limited. Further investigations are needed to determine whether these findings can be generalized to other Ab-Ab or Ab-Nb pairs.
2) Our study confirmed the inhibitory effect of NSP1 on the protein synthesis process when mRNA translation occurs in human cells. However, an important question remains about how NSP1 affects m7G-cap mRNA at the initiation stage of the translation process. Therefore, it should be considered to investigate the effect of NSP1 on m7G-cap mRNA in eukaryotic cells for confirmation through MD simulations.
3) NSP16 was experimentally shown to bind to U1/U2 small nuclear RNA upon SARS-CoV-2 entry into the host cell. It disrupts mRNA splicing, resulting in decreased host protein and mRNA levels, triggering nonsense decay of misspliced mRNAs. NSP16 binds to the 50-splice site recognition sequence of U1 and the branchpoint recognition site of U2. The disruption of mRNA splicing is consistent with the significant drop in steady state mRNA levels observed during SARS-CoV-2 infection. This effect reduces the host cell's innate immune response to virus recognition. However, the exact mechanism by which NSP16 binds to U1/U2 snRNAs and interferes with mRNA splicing remains unclear, necessitating further studies to fully understand this process.
4) NSP8 and NSP9 interfere with protein trafficking to the cell membrane by binding to signal recognition particle RNA (7SL RNA) in the signal recognition particles (SRPs). NSP8 binds to 7SL RNA in the region associated with SRP54 protein, while NSP9 binds to 7SL RNA in the region associated with SRP19 protein. This binding causes a failure in the translocation of nascent peptides into the ER lumen, leading to protein mislocalization, degradation in the cytoplasm, and ultimately protein secretion. The detailed mechanisms by which NSP8 and NSP9 impair protein trafficking by displacing SRP54 and SRP19 proteins from 7SL RNA are still unknown and require further investigation.

References

1. Hui, D. S.; E, I. A.; Madani, T. A.; Ntoumi, F.; Kock, R.; Dar, O.; Ippolito, G.; McHugh, T. D.; Memish, Z. A.; Drosten, C.; Zumla, A.; Petersen, E., The continuing 2019-nCoV epidemic threat of novel coronaviruses to global health - The latest 2019 novel coronavirus outbreak in Wuhan, China. *Int J Infect Dis* **2020,** *91*, 264-266.
2. Worobey, M.; Levy, J. I.; Malpica Serrano, L.; Crits-Christoph, A.; Pekar, J. E.; Goldstein, S. A.; Rasmussen, A. L.; Kraemer, M. U. G.; Newman, C.; Koopmans, M. P. G.; Suchard, M. A.; Wertheim, J. O.; Lemey, P.; Robertson, D. L.; Garry, R. F.; Holmes, E. C.; Rambaut, A.; Andersen, K. G., The Huanan Seafood Wholesale Market in Wuhan was the early epicenter of the COVID-19 pandemic. *Science* **2022,** *377* (6609), 951-959.
3. Wang, G.; Jin, X., The progress of 2019 novel coronavirus event in China. *J Med Virol* **2020,** *92* (5), 468-472.
4. The species severe acute respiratory syndrome-related coronavirus: classifying 2019-nCoV and naming it SARS-CoV-2. *Nat Microbiol* **2020,** *5* (4), 536-544.
5. Pekar, J. E.; Magee, A.; Parker, E.; Moshiri, N.; Izhikevich, K.; Havens, J. L.; Gangavarapu, K.; Malpica Serrano, L. M.; Crits-Christoph, A.; Matteson, N. L.; Zeller, M.; Levy, J. I.; Wang, J. C.; Hughes, S.; Lee, J.; Park, H.; Park, M. S.; Ching Zi Yan, K.; Lin, R. T. P.; Mat Isa, M. N.; Noor, Y. M.; Vasylyeva, T. I.; Garry, R. F.; Holmes, E. C.; Rambaut, A.; Suchard, M. A.; Andersen, K. G.; Worobey, M.; Wertheim, J. O., The molecular epidemiology of multiple zoonotic origins of SARS-CoV-2. *Science* **2022,** *377* (6609), 960-966.
6. Dong, E.; Du, H.; Gardner, L., An interactive web-based dashboard to track COVID-19 in real time. *Lancet Infect Dis* **2020,** *20* (5), 533-534.
7. Coccia, M., Meta-analysis to explain unknown causes of the origins of SARS-COV-2. *Environ Res* **2022,** *211*, 113062.
8. Frutos, R.; Pliez, O.; Gavotte, L.; Devaux, C. A., There is no "origin" to SARS-CoV-2. *Environ Res* **2022,** *207*, 112173.
9. Di Fusco, M.; Lin, J.; Vaghela, S.; Lingohr-Smith, M.; Nguyen, J. L.; Scassellati Sforzolini, T.; Judy, J.; Cane, A.; Moran, M. M., COVID-19 vaccine effectiveness among immunocompromised populations: a targeted literature review of real-world studies. *Expert Rev Vaccines* **2022,** *21* (4), 435-451.
10. Zheng, C.; Shao, W.; Chen, X.; Zhang, B.; Wang, G.; Zhang, W., Real-world effectiveness of COVID-19 vaccines: a literature review and meta-analysis. *Int J Infect Dis* **2022,** *114*, 252-260.
11. Naidoo, D. B.; Chuturgoon, A. A., The potential of nanobodies for COVID-19 diagnostics and therapeutics. *Mol Diagn Ther* **2023,** *27* (2), 193-226.
12. Kokic, G.; Hillen, H. S.; Tegunov, D.; Dienemann, C.; Seitz, F.; Schmitzova, J.; Farnung, L.; Siewert, A.; Höbartner, C.; Cramer, P., Mechanism of SARS-CoV-2 polymerase stalling by remdesivir. *Nat Commun* **2021,** *12* (1), 279.
13. Kabinger, F.; Stiller, C.; Schmitzová, J.; Dienemann, C.; Kokic, G.; Hillen, H. S.; Höbartner, C.; Cramer, P., Mechanism of molnupiravir-induced SARS-CoV-2 mutagenesis. *Nat Struct Mol Biol* **2021,** *28* (9), 740-746.
14. Wen, W.; Chen, C.; Tang, J.; Wang, C.; Zhou, M.; Cheng, Y.; Zhou, X.; Wu, Q.; Zhang, X.; Feng, Z.; Wang, M.; Mao, Q., Efficacy and safety of three new oral antiviral treatment (molnupiravir, fluvoxamine and Paxlovid) for COVID-19：a meta-analysis. *Ann Med* **2022,** *54* (1), 516-523.
15. Hashemian, S. M. R.; Sheida, A.; Taghizadieh, M.; Memar, M. Y.; Hamblin, M. R.; Bannazadeh Baghi, H.; Sadri Nahand, J.; Asemi, Z.; Mirzaei, H., Paxlovid (Nirmatrelvir/Ritonavir): A new approach to Covid-19 therapy? *Biomed Pharmacother* **2023,** *162*, 114367.
16. El-Shabasy, R. M.; Nayel, M. A.; Taher, M. M.; Abdelmonem, R.; Shoueir, K. R.; Kenawy, E. R., Three waves changes, new variant strains, and vaccination effect against COVID-19 pandemic. *Int J Biol Macromol* **2022,** *204*, 161-168.
17. Callaway, E., Are COVID surges becoming more predictable? New Omicron variants offer a hint. *Nature* **2022,** *605* (7909), 204-206.
18. Rajah, M. M.; Hubert, M.; Bishop, E.; Saunders, N.; Robinot, R.; Grzelak, L.; Planas, D.; Dufloo, J.; Gellenoncourt, S.; Bongers, A.; Zivaljic, M.; Planchais, C.; Guivel-Benhassine, F.; Porrot,

F.; Mouquet, H.; Chakrabarti, L. A.; Buchrieser, J.; Schwartz, O., SARS-CoV-2 Alpha, Beta, and Delta variants display enhanced Spike-mediated syncytia formation. *Embo j* **2021,** *40* (24), e108944.
19. Mostafavi, E.; Dubey, A. K.; Teodori, L.; Ramakrishna, S.; Kaushik, A., SARS-CoV-2 Omicron variant: A next phase of the COVID-19 pandemic and a call to arms for system sciences and precision medicine. *MedComm (2020)* **2022,** *3* (1), e119.
20. Xia, S.; Wang, L.; Zhu, Y.; Lu, L.; Jiang, S., Origin, virological features, immune evasion and intervention of SARS-CoV-2 Omicron sublineages. *Signal Transduct Target Ther* **2022,** *7* (1), 241.
21. Kurhade, C.; Zou, J.; Xia, H.; Liu, M.; Chang, H. C.; Ren, P.; Xie, X.; Shi, P. Y., Low neutralization of SARS-CoV-2 Omicron BA.2.75.2, BQ.1.1 and XBB.1 by parental mRNA vaccine or a BA.5 bivalent booster. *Nat Med* **2023,** *29* (2), 344-347.
22. Wang, Q.; Iketani, S.; Li, Z.; Liu, L.; Guo, Y.; Huang, Y.; Bowen, A. D.; Liu, M.; Wang, M.; Yu, J.; Valdez, R.; Lauring, A. S.; Sheng, Z.; Wang, H. H.; Gordon, A.; Liu, L.; Ho, D. D., Alarming antibody evasion properties of rising SARS-CoV-2 BQ and XBB subvariants. *Cell* **2023,** *186* (2), 279-286.e8.
23. Davis-Gardner, M. E.; Lai, L.; Wali, B.; Samaha, H.; Solis, D.; Lee, M.; Porter-Morrison, A.; Hentenaar, I. T.; Yamamoto, F.; Godbole, S.; Liu, Y.; Douek, D. C.; Lee, F. E.; Rouphael, N.; Moreno, A.; Pinsky, B. A.; Suthar, M. S., Neutralization against BA.2.75.2, BQ.1.1, and XBB from mRNA Bivalent Booster. *N Engl J Med* **2023,** *388* (2), 183-185.
24. Entzminger, K. C.; Fleming, J. K.; Entzminger, P. D.; Espinosa, L. Y.; Samadi, A.; Hiramoto, Y.; Okumura, S. C. J.; Maruyama, T., Rapid engineering of SARS-CoV-2 therapeutic antibodies to increase breadth of neutralization including BQ.1.1, CA.3.1, CH.1.1, XBB.1.16, and XBB.1.5. *Antib Ther* **2023,** *6* (2), 108-118.
25. Lu, R.; Zhao, X.; Li, J.; Niu, P.; Yang, B.; Wu, H.; Wang, W.; Song, H.; Huang, B.; Zhu, N.; Bi, Y.; Ma, X.; Zhan, F.; Wang, L.; Hu, T.; Zhou, H.; Hu, Z.; Zhou, W.; Zhao, L.; Chen, J.; Meng, Y.; Wang, J.; Lin, Y.; Yuan, J.; Xie, Z.; Ma, J.; Liu, W. J.; Wang, D.; Xu, W.; Holmes, E. C.; Gao, G. F.; Wu, G.; Chen, W.; Shi, W.; Tan, W., Genomic characterisation and epidemiology of 2019 novel coronavirus: implications for virus origins and receptor binding. *Lancet* **2020,** *395* (10224), 565-574.
26. Wang, Y.; Grunewald, M.; Perlman, S., Coronaviruses: An updated overview of their replication and pathogenesis. *Methods Mol Biol* **2020,** *2203*, 1-29.
27. Brian, D. A.; Baric, R. S., Coronavirus genome structure and replication. *Curr Top Microbiol Immunol* **2005,** *287*, 1-30.
28. Nelson, C. W.; Ardern, Z.; Goldberg, T. L.; Meng, C.; Kuo, C. H.; Ludwig, C.; Kolokotronis, S. O.; Wei, X., Dynamically evolving novel overlapping gene as a factor in the SARS-CoV-2 pandemic. *Elife* **2020,** *9*.
29. Chen, Y.; Liu, Q.; Guo, D., Emerging coronaviruses: Genome structure, replication, and pathogenesis. *J Med Virol* **2020,** *92* (4), 418-423.
30. Li, W.; Moore, M. J.; Vasilieva, N.; Sui, J.; Wong, S. K.; Berne, M. A.; Somasundaran, M.; Sullivan, J. L.; Luzuriaga, K.; Greenough, T. C.; Choe, H.; Farzan, M., Angiotensin-converting enzyme 2 is a functional receptor for the SARS coronavirus. *Nature* **2003,** *426* (6965), 450-4.
31. Li, F.; Li, W.; Farzan, M.; Harrison, S. C., Structure of SARS coronavirus spike receptor-binding domain complexed with receptor. *Science* **2005,** *309* (5742), 1864-8.
32. Li, F., Structure, function, and evolution of Coronavirus Spike proteins. *Annu Rev Virol* **2016,** *3* (1), 237-261.
33. Walls, A. C.; Park, Y. J.; Tortorici, M. A.; Wall, A.; McGuire, A. T.; Veesler, D., Structure, function, and antigenicity of the SARS-CoV-2 Spike Glycoprotein. *Cell* **2020,** *181* (2), 281-292.e6.
34. Wrapp, D.; Wang, N.; Corbett, K. S.; Goldsmith, J. A.; Hsieh, C. L.; Abiona, O.; Graham, B. S.; McLellan, J. S., Cryo-EM structure of the 2019-nCoV spike in the prefusion conformation. *Science* **2020,** *367* (6483), 1260-1263.
35. Liu, S.; Xiao, G.; Chen, Y.; He, Y.; Niu, J.; Escalante, C. R.; Xiong, H.; Farmar, J.; Debnath, A. K.; Tien, P.; Jiang, S., Interaction between heptad repeat 1 and 2 regions in spike protein of SARS-associated coronavirus: implications for virus fusogenic mechanism and identification of fusion inhibitors. *Lancet* **2004,** *363* (9413), 938-47.

36. Xia, S.; Zhu, Y.; Liu, M.; Lan, Q.; Xu, W.; Wu, Y.; Ying, T.; Liu, S.; Shi, Z.; Jiang, S.; Lu, L., Fusion mechanism of 2019-nCoV and fusion inhibitors targeting HR1 domain in spike protein. *Cell Mol Immunol* **2020,** *17* (7), 765-767.
37. Xia, S.; Liu, M.; Wang, C.; Xu, W.; Lan, Q.; Feng, S.; Qi, F.; Bao, L.; Du, L.; Liu, S.; Qin, C.; Sun, F.; Shi, Z.; Zhu, Y.; Jiang, S.; Lu, L., Inhibition of SARS-CoV-2 (previously 2019-nCoV) infection by a highly potent pan-coronavirus fusion inhibitor targeting its spike protein that harbors a high capacity to mediate membrane fusion. *Cell Res* **2020,** *30* (4), 343-355.
38. Letko, M.; Marzi, A.; Munster, V., Functional assessment of cell entry and receptor usage for SARS-CoV-2 and other lineage B betacoronaviruses. *Nat Microbiol* **2020,** *5* (4), 562-569.
39. Wang, Q.; Zhang, Y.; Wu, L.; Niu, S.; Song, C.; Zhang, Z.; Lu, G.; Qiao, C.; Hu, Y.; Yuen, K. Y.; Wang, Q.; Zhou, H.; Yan, J.; Qi, J., Structural and functional basis of SARS-CoV-2 entry by using human ACE2. *Cell* **2020,** *181* (4), 894-904.e9.
40. Nieto-Torres, J. L.; DeDiego, M. L.; Verdiá-Báguena, C.; Jimenez-Guardeño, J. M.; Regla-Nava, J. A.; Fernandez-Delgado, R.; Castaño-Rodriguez, C.; Alcaraz, A.; Torres, J.; Aguilella, V. M.; Enjuanes, L., Severe acute respiratory syndrome coronavirus envelope protein ion channel activity promotes virus fitness and pathogenesis. *PLoS Pathog* **2014,** *10* (5), e1004077.
41. Schoeman, D.; Fielding, B. C., Coronavirus envelope protein: current knowledge. *Virol J* **2019,** *16* (1), 69.
42. Sturman, L. S.; Holmes, K. V.; Behnke, J., Isolation of coronavirus envelope glycoproteins and interaction with the viral nucleocapsid. *J Virol* **1980,** *33* (1), 449-62.
43. Mahtarin, R.; Islam, S.; Islam, M. J.; Ullah, M. O.; Ali, M. A.; Halim, M. A., Structure and dynamics of membrane protein in SARS-CoV-2. *J Biomol Struct Dyn* **2022,** *40* (10), 4725-4738.
44. Hu, Y.; Wen, J.; Tang, L.; Zhang, H.; Zhang, X.; Li, Y.; Wang, J.; Han, Y.; Li, G.; Shi, J.; Tian, X.; Jiang, F.; Zhao, X.; Wang, J.; Liu, S.; Zeng, C.; Wang, J.; Yang, H., The M protein of SARS-CoV: basic structural and immunological properties. *Genomics Proteomics Bioinformatics* **2003,** *1* (2), 118-30.
45. Ujike, M.; Taguchi, F., Incorporation of spike and membrane glycoproteins into coronavirus virions. *Viruses* **2015,** *7* (4), 1700-25.
46. Neuman, B. W.; Kiss, G.; Kunding, A. H.; Bhella, D.; Baksh, M. F.; Connelly, S.; Droese, B.; Klaus, J. P.; Makino, S.; Sawicki, S. G.; Siddell, S. G.; Stamou, D. G.; Wilson, I. A.; Kuhn, P.; Buchmeier, M. J., A structural analysis of M protein in coronavirus assembly and morphology. *J Struct Biol* **2011,** *174* (1), 11-22.
47. Arndt, A. L.; Larson, B. J.; Hogue, B. G., A conserved domain in the coronavirus membrane protein tail is important for virus assembly. *J Virol* **2010,** *84* (21), 11418-28.
48. Jacobs, L.; van der Zeijst, B. A.; Horzinek, M. C., Characterization and translation of transmissible gastroenteritis virus mRNAs. *J Virol* **1986,** *57* (3), 1010-5.
49. de Haan, C. A.; Roestenberg, P.; de Wit, M.; de Vries, A. A.; Nilsson, T.; Vennema, H.; Rottier, P. J., Structural requirements for O-glycosylation of the mouse hepatitis virus membrane protein. *J Biol Chem* **1998,** *273* (45), 29905-14.
50. Laude, H.; Gelfi, J.; Lavenant, L.; Charley, B., Single amino acid changes in the viral glycoprotein M affect induction of alpha interferon by the coronavirus transmissible gastroenteritis virus. *J Virol* **1992,** *66* (2), 743-9.
51. McBride, R.; van Zyl, M.; Fielding, B. C., The coronavirus nucleocapsid is a multifunctional protein. *Viruses* **2014,** *6* (8), 2991-3018.
52. Chang, C. K.; Sue, S. C.; Yu, T. H.; Hsieh, C. M.; Tsai, C. K.; Chiang, Y. C.; Lee, S. J.; Hsiao, H. H.; Wu, W. J.; Chang, W. L.; Lin, C. H.; Huang, T. H., Modular organization of SARS coronavirus nucleocapsid protein. *J Biomed Sci* **2006,** *13* (1), 59-72.
53. Stohlman, S. A.; Lai, M. M., Phosphoproteins of murine hepatitis viruses. *J Virol* **1979,** *32* (2), 672-5.
54. Clark, L. K.; Green, T. J.; Petit, C. M., Structure of nonstructural protein 1 from SARS-CoV-2. *J Virol* **2021,** *95* (4).
55. Mendez, A. S.; Ly, M.; González-Sánchez, A. M.; Hartenian, E.; Ingolia, N. T.; Cate, J. H.; Glaunsinger, B. A., The N-terminal domain of SARS-CoV-2 nsp1 plays key roles in suppression of cellular gene expression and preservation of viral gene expression. *Cell Rep* **2021,** *37* (3), 109841.

56. Verba, K.; Gupta, M.; Azumaya, C.; Moritz, M.; Pourmal, S.; Diallo, A.; Merz, G.; Jang, G.; Bouhaddou, M.; Fossati, A.; Brilot, A.; Diwanji, D.; Hernandez, E.; Herrera, N.; Kratochvil, H.; Lam, V.; Li, F.; Li, Y.; Nguyen, H.; Nowotny, C.; Owens, T.; Peters, J.; Rizo, A.; Schulze-Gahmen, U.; Smith, A.; Young, I.; Yu, Z.; Asarnow, D.; Billesbølle, C.; Campbell, M.; Chen, J.; Chen, K. H.; Chio, U. S.; Dickinson, M.; Doan, L.; Jin, M.; Kim, K.; Li, J.; Li, Y. L.; Linossi, E.; Liu, Y.; Lo, M.; Lopez, J.; Lopez, K.; Mancino, A.; Iii, F. M.; Paul, M.; Pawar, K.; Pelin, A.; Pospiech, T.; Puchades, C.; Remesh, S.; Safari, M.; Schaefer, K.; Sun, M.; Tabios, M.; Thwin, A.; Titus, E.; Trenker, R.; Tse, E.; Tsui, T. K. M.; Feng, F.; Zhang, K.; Zhang, Y.; Zhao, J.; Zhou, F.; Zhou, Y.; Zuliani-Alvarez, L.; Agard, D.; Cheng, Y.; Fraser, J.; Jura, N.; Kortemme, T.; Manglik, A.; Southworth, D.; Stroud, R.; Swaney, D.; Krogan, N.; Frost, A.; Rosenberg, O., CryoEM and AI reveal a structure of SARS-CoV-2 Nsp2, a multifunctional protein involved in key host processes. *Res Sq* **2021**.
57. Wu, C.; Liu, Y.; Yang, Y.; Zhang, P.; Zhong, W.; Wang, Y.; Wang, Q.; Xu, Y.; Li, M.; Li, X.; Zheng, M.; Chen, L.; Li, H., Analysis of therapeutic targets for SARS-CoV-2 and discovery of potential drugs by computational methods. *Acta Pharm Sin B* **2020,** *10* (5), 766-788.
58. Angelini, M. M.; Akhlaghpour, M.; Neuman, B. W.; Buchmeier, M. J., Severe acute respiratory syndrome coronavirus nonstructural proteins 3, 4, and 6 induce double-membrane vesicles. *mBio* **2013,** *4* (4).
59. Bonilla, P. J.; Gorbalenya, A. E.; Weiss, S. R., Mouse hepatitis virus strain A59 RNA polymerase gene ORF 1a: heterogeneity among MHV strains. *Virology* **1994,** *198* (2), 736-40.
60. Manolaridis, I.; Wojdyla, J. A.; Panjikar, S.; Snijder, E. J.; Gorbalenya, A. E.; Berglind, H.; Nordlund, P.; Coutard, B.; Tucker, P. A., Structure of the C-terminal domain of nsp4 from feline coronavirus. *Acta Crystallogr D Biol Crystallogr* **2009,** *65* (Pt 8), 839-46.
61. Hagemeijer, M. C.; Monastyrska, I.; Griffith, J.; van der Sluijs, P.; Voortman, J.; van Bergen en Henegouwen, P. M.; Vonk, A. M.; Rottier, P. J.; Reggiori, F.; de Haan, C. A., Membrane rearrangements mediated by coronavirus nonstructural proteins 3 and 4. *Virology* **2014,** *458-459*, 125-35.
62. Zhang, L.; Lin, D.; Sun, X.; Curth, U.; Drosten, C.; Sauerhering, L.; Becker, S.; Rox, K.; Hilgenfeld, R., Crystal structure of SARS-CoV-2 main protease provides a basis for design of improved α-ketoamide inhibitors. *Science* **2020,** *368* (6489), 409-412.
63. Anand, K.; Ziebuhr, J.; Wadhwani, P.; Mesters, J. R.; Hilgenfeld, R., Coronavirus main proteinase (3CLpro) structure: basis for design of anti-SARS drugs. *Science* **2003,** *300* (5626), 1763-7.
64. Oostra, M.; Hagemeijer, M. C.; van Gent, M.; Bekker, C. P.; te Lintelo, E. G.; Rottier, P. J.; de Haan, C. A., Topology and membrane anchoring of the coronavirus replication complex: not all hydrophobic domains of nsp3 and nsp6 are membrane spanning. *J Virol* **2008,** *82* (24), 12392-405.
65. Benvenuto, D.; Angeletti, S.; Giovanetti, M.; Bianchi, M.; Pascarella, S.; Cauda, R.; Ciccozzi, M.; Cassone, A., Evolutionary analysis of SARS-CoV-2: how mutation of Non-Structural Protein 6 (NSP6) could affect viral autophagy. *J Infect* **2020,** *81* (1), e24-e27.
66. Cottam, E. M.; Whelband, M. C.; Wileman, T., Coronavirus NSP6 restricts autophagosome expansion. *Autophagy* **2014,** *10* (8), 1426-41.
67. Konkolova, E.; Klima, M.; Nencka, R.; Boura, E., Structural analysis of the putative SARS-CoV-2 primase complex. *J Struct Biol* **2020,** *211* (2), 107548.
68. Zhai, Y.; Sun, F.; Li, X.; Pang, H.; Xu, X.; Bartlam, M.; Rao, Z., Insights into SARS-CoV transcription and replication from the structure of the nsp7-nsp8 hexadecamer. *Nat Struct Mol Biol* **2005,** *12* (11), 980-6.
69. Krishna, T. S.; Kong, X. P.; Gary, S.; Burgers, P. M.; Kuriyan, J., Crystal structure of the eukaryotic DNA polymerase processivity factor PCNA. *Cell* **1994,** *79* (7), 1233-43.
70. van Hemert, M. J.; van den Worm, S. H.; Knoops, K.; Mommaas, A. M.; Gorbalenya, A. E.; Snijder, E. J., SARS-coronavirus replication/transcription complexes are membrane-protected and need a host factor for activity in vitro. *PLoS Pathog* **2008,** *4* (5), e1000054.
71. Yin, W.; Mao, C.; Luan, X.; Shen, D. D.; Shen, Q.; Su, H.; Wang, X.; Zhou, F.; Zhao, W.; Gao, M.; Chang, S.; Xie, Y. C.; Tian, G.; Jiang, H. W.; Tao, S. C.; Shen, J.; Jiang, Y.; Jiang, H.; Xu, Y.; Zhang, S.; Zhang, Y.; Xu, H. E., Structural basis for inhibition of the RNA-dependent RNA polymerase from SARS-CoV-2 by remdesivir. *Science* **2020,** *368* (6498), 1499-1504.

72. De Clercq, E., Potential antivirals and antiviral strategies against SARS coronavirus infections. *Expert Rev Anti Infect Ther* **2006,** *4* (2), 291-302.
73. Gao, Y.; Yan, L.; Huang, Y.; Liu, F.; Zhao, Y.; Cao, L.; Wang, T.; Sun, Q.; Ming, Z.; Zhang, L.; Ge, J.; Zheng, L.; Zhang, Y.; Wang, H.; Zhu, Y.; Zhu, C.; Hu, T.; Hua, T.; Zhang, B.; Yang, X.; Li, J.; Yang, H.; Liu, Z.; Xu, W.; Guddat, L. W.; Wang, Q.; Lou, Z.; Rao, Z., Structure of the RNA-dependent RNA polymerase from COVID-19 virus. *Science* **2020,** *368* (6492), 779-782.
74. Cheng, A.; Zhang, W.; Xie, Y.; Jiang, W.; Arnold, E.; Sarafianos, S. G.; Ding, J., Expression, purification, and characterization of SARS coronavirus RNA polymerase. *Virology* **2005,** *335* (2), 165-76.
75. Zumla, A.; Chan, J. F.; Azhar, E. I.; Hui, D. S.; Yuen, K. Y., Coronaviruses - drug discovery and therapeutic options. *Nat Rev Drug Discov* **2016,** *15* (5), 327-47.
76. Nguyen, H. L.; Thai, N. Q.; Truong, D. T.; Li, M. S., Remdesivir strongly binds to both RNA-dependent RNA polymerase and main protease of SARS-CoV-2: Evidence from molecular simulations. *J Phys Chem B* **2020,** *124* (50), 11337-11348.
77. Sutton, G.; Fry, E.; Carter, L.; Sainsbury, S.; Walter, T.; Nettleship, J.; Berrow, N.; Owens, R.; Gilbert, R.; Davidson, A.; Siddell, S.; Poon, L. L. M.; Diprose, J.; Alderton, D.; Walsh, M.; Grimes, J. M.; Stuart, D. I., The nsp9 replicase protein of SARS-coronavirus, structure and functional insights. *Structure* **2004,** *12* (2), 341-353.
78. Egloff, M. P.; Ferron, F.; Campanacci, V.; Longhi, S.; Rancurel, C.; Dutartre, H.; Snijder, E. J.; Gorbalenya, A. E.; Cambillau, C.; Canard, B., The severe acute respiratory syndrome-coronavirus replicative protein nsp9 is a single-stranded RNA-binding subunit unique in the RNA virus world. *Proc Natl Acad Sci U S A* **2004,** *101* (11), 3792-6.
79. Ferron, F.; Subissi, L.; Silveira De Morais, A. T.; Le, N. T. T.; Sevajol, M.; Gluais, L.; Decroly, E.; Vonrhein, C.; Bricogne, G.; Canard, B.; Imbert, I., Structural and molecular basis of mismatch correction and ribavirin excision from coronavirus RNA. *Proc Natl Acad Sci U S A* **2018,** *115* (2), E162-e171.
80. Bouvet, M.; Imbert, I.; Subissi, L.; Gluais, L.; Canard, B.; Decroly, E., RNA 3'-end mismatch excision by the severe acute respiratory syndrome coronavirus nonstructural protein nsp10/nsp14 exoribonuclease complex. *Proc Natl Acad Sci U S A* **2012,** *109* (24), 9372-7.
81. Romano, M.; Ruggiero, A.; Squeglia, F.; Maga, G.; Berisio, R., A Structural view of SARS-CoV-2 RNA replication machinery: RNA synthesis, proofreading and final capping. *Cells* **2020,** *9* (5).
82. Zhang, C.; Zheng, W.; Huang, X.; Bell, E. W.; Zhou, X.; Zhang, Y., Protein structure and sequence reanalysis of 2019-nCoV genome refutes snakes as its intermediate host and the unique similarity between its Spike protein insertions and HIV-1. *J Proteome Res* **2020,** *19* (4), 1351-1360.
83. Ogando, N. S.; Ferron, F.; Decroly, E.; Canard, B.; Posthuma, C. C.; Snijder, E. J., The curious case of the nidovirus exoribonuclease: Its role in RNA synthesis and replication fidelity. *Front Microbiol* **2019,** *10*, 1813.
84. Smith, E. C.; Denison, M. R., Implications of altered replication fidelity on the evolution and pathogenesis of coronaviruses. *Curr Opin Virol* **2012,** *2* (5), 519-524.
85. Chen, Y.; Cai, H.; Pan, J.; Xiang, N.; Tien, P.; Ahola, T.; Guo, D., Functional screen reveals SARS coronavirus nonstructural protein nsp14 as a novel cap N7 methyltransferase. *Proc Natl Acad Sci U S A* **2009,** *106* (9), 3484-9.
86. Chen, Y.; Su, C.; Ke, M.; Jin, X.; Xu, L.; Zhang, Z.; Wu, A.; Sun, Y.; Yang, Z.; Tien, P.; Ahola, T.; Liang, Y.; Liu, X.; Guo, D., Biochemical and structural insights into the mechanisms of SARS coronavirus RNA ribose 2'-O-methylation by nsp16/nsp10 protein complex. *PLoS Pathog* **2011,** *7* (10), e1002294.
87. Menachery, V. D.; Debbink, K.; Baric, R. S., Coronavirus non-structural protein 16: evasion, attenuation, and possible treatments. *Virus Res* **2014,** *194*, 191-9.
88. Daffis, S.; Szretter, K. J.; Schriewer, J.; Li, J.; Youn, S.; Errett, J.; Lin, T. Y.; Schneller, S.; Zust, R.; Dong, H.; Thiel, V.; Sen, G. C.; Fensterl, V.; Klimstra, W. B.; Pierson, T. C.; Buller, R. M.; Gale, M., Jr.; Shi, P. Y.; Diamond, M. S., 2'-O methylation of the viral mRNA cap evades host restriction by IFIT family members. *Nature* **2010,** *468* (7322), 452-6.

89. Decroly, E.; Imbert, I.; Coutard, B.; Bouvet, M.; Selisko, B.; Alvarez, K.; Gorbalenya, A. E.; Snijder, E. J.; Canard, B., Coronavirus nonstructural protein 16 is a cap-0 binding enzyme possessing (nucleoside-2'O)-methyltransferase activity. *J Virol* **2008,** *82* (16), 8071-84.
90. Naqvi, A. A. T.; Fatima, K.; Mohammad, T.; Fatima, U.; Singh, I. K.; Singh, A.; Atif, S. M.; Hariprasad, G.; Hasan, G. M.; Hassan, M. I., Insights into SARS-CoV-2 genome, structure, evolution, pathogenesis and therapies: Structural genomics approach. *Biochim Biophys Acta Mol Basis Dis* **2020,** *1866* (10), 165878.
91. Gadhave, K.; Kumar, P.; Kumar, A.; Bhardwaj, T.; Garg, N.; Giri, R., Conformational dynamics of 13 amino acids long NSP11 of SARS-CoV-2 under membrane mimetics and different solvent conditions. *Microb Pathog* **2021,** *158*, 105041.
92. Kakavandi, S.; Zare, I.; VaezJalali, M.; Dadashi, M.; Azarian, M.; Akbari, A.; Ramezani Farani, M.; Zalpoor, H.; Hajikhani, B., Structural and non-structural proteins in SARS-CoV-2: potential aspects to COVID-19 treatment or prevention of progression of related diseases. *Cell Commun Signal* **2023,** *21* (1), 110.
93. Mickolajczyk, K. J.; Shelton, P. M. M.; Grasso, M.; Cao, X.; Warrington, S. E.; Aher, A.; Liu, S.; Kapoor, T. M., Force-dependent stimulation of RNA unwinding by SARS-CoV-2 nsp13 helicase. *Biophys J* **2021,** *120* (6), 1020-1030.
94. White, M. A.; Lin, W.; Cheng, X., Discovery of COVID-19 inhibitors targeting the SARS-CoV-2 Nsp13 helicase. *J Phys Chem Lett* **2020,** *11* (21), 9144-9151.
95. Skalny, A. V.; Rink, L.; Ajsuvakova, O. P.; Aschner, M.; Gritsenko, V. A.; Alekseenko, S. I.; Svistunov, A. A.; Petrakis, D.; Spandidos, D. A.; Aaseth, J.; Tsatsakis, A.; Tinkov, A. A., Zinc and respiratory tract infections: Perspectives for COVID-19 (Review). *Int J Mol Med* **2020,** *46* (1), 17-26.
96. Shu, T.; Huang, M.; Wu, D.; Ren, Y.; Zhang, X.; Han, Y.; Mu, J.; Wang, R.; Qiu, Y.; Zhang, D. Y.; Zhou, X., SARS-coronavirus-2 Nsp13 possesses NTPase and RNA helicase activities that can be inhibited by bismuth salts. *Virol Sin* **2020,** *35* (3), 321-329.
97. Kim, Y.; Jedrzejczak, R.; Maltseva, N. I.; Wilamowski, M.; Endres, M.; Godzik, A.; Michalska, K.; Joachimiak, A., Crystal structure of Nsp15 endoribonuclease NendoU from SARS-CoV-2. *Protein Sci* **2020,** *29* (7), 1596-1605.
98. Liu, X.; Fang, P.; Fang, L.; Hong, Y.; Zhu, X.; Wang, D.; Peng, G.; Xiao, S., Porcine deltacoronavirus nsp15 antagonizes interferon-β production independently of its endoribonuclease activity. *Mol Immunol* **2019,** *114*, 100-107.
99. Kern, D. M.; Sorum, B.; Mali, S. S.; Hoel, C. M.; Sridharan, S.; Remis, J. P.; Toso, D. B.; Kotecha, A.; Bautista, D. M.; Brohawn, S. G., Cryo-EM structure of the SARS-CoV-2 3a ion channel in lipid nanodiscs. *bioRxiv* **2021**.
100. Ren, Y.; Shu, T.; Wu, D.; Mu, J.; Wang, C.; Huang, M.; Han, Y.; Zhang, X. Y.; Zhou, W.; Qiu, Y.; Zhou, X., The ORF3a protein of SARS-CoV-2 induces apoptosis in cells. *Cell Mol Immunol* **2020,** *17* (8), 881-883.
101. Gunalan, V.; Mirazimi, A.; Tan, Y. J., A putative diacidic motif in the SARS-CoV ORF6 protein influences its subcellular localization and suppression of expression of co-transfected expression constructs. *BMC Res Notes* **2011,** *4*, 446.
102. Morante, S.; La Penna, G.; Rossi, G.; Stellato, F., SARS-CoV-2 virion stabilization by Zn binding. *Front Mol Biosci* **2020,** *7*, 222.
103. Schaecher, S. R.; Mackenzie, J. M.; Pekosz, A., The ORF7b protein of severe acute respiratory syndrome coronavirus (SARS-CoV) is expressed in virus-infected cells and incorporated into SARS-CoV particles. *J Virol* **2007,** *81* (2), 718-31.
104. Zhang, Y.; Chen, Y.; Li, Y.; Huang, F.; Luo, B.; Yuan, Y.; Xia, B.; Ma, X.; Yang, T.; Yu, F.; Liu, J.; Liu, B.; Song, Z.; Chen, J.; Yan, S.; Wu, L.; Pan, T.; Zhang, X.; Li, R.; Huang, W.; He, X.; Xiao, F.; Zhang, J.; Zhang, H., The ORF8 protein of SARS-CoV-2 mediates immune evasion through down-regulating MHC-I. *Proc Natl Acad Sci U S A* **2021,** *118* (23).
105. Bojkova, D.; Klann, K.; Koch, B.; Widera, M.; Krause, D.; Ciesek, S.; Cinatl, J.; Münch, C., Proteomics of SARS-CoV-2-infected host cells reveals therapy targets. *Nature* **2020,** *583* (7816), 469-472.

106. Nguyen, H.; Nguyen, H. L.; Lan, P. D.; Thai, N. Q.; Sikora, M.; Li, M. S., Interaction of SARS-CoV-2 with host cells and antibodies: experiment and simulation. *Chem Soc Rev* **2023,** *52* (18), 6497-6553.
107. Hoffmann, M.; Kleine-Weber, H.; Schroeder, S.; Krüger, N.; Herrler, T.; Erichsen, S.; Schiergens, T. S.; Herrler, G.; Wu, N. H.; Nitsche, A.; Müller, M. A.; Drosten, C.; Pöhlmann, S., SARS-CoV-2 cell entry depends on ACE2 and TMPRSS2 and is blocked by a clinically proven protease inhibitor. *Cell* **2020,** *181* (2), 271-280.e8.
108. Eastman, R. T.; Roth, J. S.; Brimacombe, K. R.; Simeonov, A.; Shen, M.; Patnaik, S.; Hall, M. D., Remdesivir: A review of its discovery and development leading to emergency use authorization for treatment of COVID-19. *ACS Cent Sci* **2020,** *6* (5), 672-683.
109. Pluskota-Karwatka, D.; Hoffmann, M.; Barciszewski, J., Reducing SARS-CoV-2 pathological protein activity with small molecules. *J Pharm Anal* **2021,** *11* (4), 383-397.
110. Butnariu, A. B.; Look, A.; Grillo, M.; Tabish, T. A.; McGarvey, M. J.; Pranjol, M. Z. I., SARS-CoV-2-host cell surface interactions and potential antiviral therapies. *Interface Focus* **2022,** *12* (1), 20200081.
111. Parums, V., Editorial: Revised World Health Organization (WHO) terminology for variants of concern and variants of interest of SARS-CoV-2. *Med Sci Monit* **2021,** *27*, e933622.
112. Parums, D. V., Editorial: World Health Organization (WHO) variants of concern lineages under monitoring (VOC-LUM) in response to the global spread of lineages and sublineages of Omicron, or B.1.1.529, SARS-CoV-2. *Med Sci Monit* **2022,** *28*, e937676.
113. Liu, H.; Wei, P.; Kappler, J. W.; Marrack, P.; Zhang, G., SARS-CoV-2 variants of concern and variants of interest receptor binding domain mutations and virus infectivity. *Front Immunol* **2022,** *13*, 825256.
114. Abdool Karim, S. S.; de Oliveira, T., New SARS-CoV-2 variants - clinical, public health, and vaccine implications. *N Engl J Med* **2021,** *384* (19), 1866-1868.
115. Sanyaolu, A.; Marinkovic, A.; Prakash, S.; Haider, N.; Williams, M.; Okorie, C.; Badaru, O.; Smith, S., SARS-CoV-2 Omicron variant (B.1.1.529): A concern with immune escape. *World J Virol* **2022,** *11* (3), 137-143.
116. Uraki, R.; Halfmann, P. J.; Iida, S.; Yamayoshi, S.; Furusawa, Y.; Kiso, M.; Ito, M.; Iwatsuki-Horimoto, K.; Mine, S.; Kuroda, M.; Maemura, T.; Sakai-Tagawa, Y.; Ueki, H.; Li, R.; Liu, Y.; Larson, D.; Fukushi, S.; Watanabe, S.; Maeda, K.; Pekosz, A.; Kandeil, A.; Webby, R. J.; Wang, Z.; Imai, M.; Suzuki, T.; Kawaoka, Y., Characterization of SARS-CoV-2 Omicron BA.4 and BA.5 isolates in rodents. *Nature* **2022,** *612* (7940), 540-545.
117. Huai Luo, C.; Paul Morris, C.; Sachithanandham, J.; Amadi, A.; Gaston, D. C.; Li, M.; Swanson, N. J.; Schwartz, M.; Klein, E. Y.; Pekosz, A.; Mostafa, H. H., Infection with the Severe Acute Respiratory Syndrome Coronavirus 2 (SARS-CoV-2) Delta variant is associated with higher recovery of infectious virus compared to the Alpha variant in both unvaccinated and vaccinated individuals. *Clin Infect Dis* **2022,** *75* (1), e715-e725.
118. Tao, K.; Tzou, P. L.; Nouhin, J.; Gupta, R. K.; de Oliveira, T.; Kosakovsky Pond, S. L.; Fera, D.; Shafer, R. W., The biological and clinical significance of emerging SARS-CoV-2 variants. *Nat Rev Genet* **2021,** *22* (12), 757-773.
119. Volz, E.; Mishra, S.; Chand, M.; Barrett, J. C.; Johnson, R.; Geidelberg, L.; Hinsley, W. R.; Laydon, D. J.; Dabrera, G.; O'Toole, Á.; Amato, R.; Ragonnet-Cronin, M.; Harrison, I.; Jackson, B.; Ariani, C. V.; Boyd, O.; Loman, N. J.; McCrone, J. T.; Gonçalves, S.; Jorgensen, D.; Myers, R.; Hill, V.; Jackson, D. K.; Gaythorpe, K.; Groves, N.; Sillitoe, J.; Kwiatkowski, D. P.; Flaxman, S.; Ratmann, O.; Bhatt, S.; Hopkins, S.; Gandy, A.; Rambaut, A.; Ferguson, N. M., Assessing transmissibility of SARS-CoV-2 lineage B.1.1.7 in England. *Nature* **2021,** *593* (7858), 266-269.
120. Choi, J. Y.; Smith, D. M., SARS-CoV-2 variants of concern. *Yonsei Med J* **2021,** *62* (11), 961-968.
121. Cascella, M.; Rajnik, M.; Aleem, A.; Dulebohn, S. C.; Di Napoli, R., Features, evaluation, and treatment of Coronavirus (COVID-19). In *StatPearls*, 2023.
122. Ramesh, S.; Govindarajulu, M.; Parise, R. S.; Neel, L.; Shankar, T.; Patel, S.; Lowery, P.; Smith, F.; Dhanasekaran, M.; Moore, T., Emerging SARS-CoV-2 variants: A review of its mutations, its implications and vaccine efficacy. *Vaccines (Basel)* **2021,** *9* (10).

123. Shiehzadegan, S.; Alaghemand, N.; Fox, M.; Venketaraman, V., Analysis of the Delta variant B.1.617.2 COVID-19. *Clin Pract* **2021,** *11* (4), 778-784.
124. Mohammadi, M.; Shayestehpour, M.; Mirzaei, H., The impact of spike mutated variants of SARS-CoV2 [Alpha, Beta, Gamma, Delta, and Lambda] on the efficacy of subunit recombinant vaccines. *Braz J Infect Dis* **2021,** *25* (4), 101606.
125. Cao, Y.; Wang, J.; Jian, F.; Xiao, T.; Song, W.; Yisimayi, A.; Huang, W.; Li, Q.; Wang, P.; An, R.; Wang, J.; Wang, Y.; Niu, X.; Yang, S.; Liang, H.; Sun, H.; Li, T.; Yu, Y.; Cui, Q.; Liu, S.; Yang, X.; Du, S.; Zhang, Z.; Hao, X.; Shao, F.; Jin, R.; Wang, X.; Xiao, J.; Wang, Y.; Xie, X. S., Omicron escapes the majority of existing SARS-CoV-2 neutralizing antibodies. *Nature* **2022,** *602* (7898), 657-663.
126. Mallapaty, S., Where did Omicron come from? Three key theories. *Nature* **2022,** *602* (7895), 26-28.
127. Callaway, E., Heavily mutated Omicron variant puts scientists on alert. *Nature* **2021,** *600* (7887), 21.
128. Bhattacharyya, R. P.; Hanage, W. P., Challenges in inferring intrinsic severity of the SARS-CoV-2 Omicron variant. *N Engl J Med* **2022,** *386* (7), e14.
129. Parums, D. V., Editorial: The XBB.1.5 ('Kraken') subvariant of Omicron SARS-CoV-2 and its rapid global spread. *Med Sci Monit* **2023,** *29*, e939580.
130. Beigel, J. H.; Tomashek, K. M.; Dodd, L. E.; Mehta, A. K.; Zingman, B. S.; Kalil, A. C.; Hohmann, E.; Chu, H. Y.; Luetkemeyer, A.; Kline, S.; Lopez de Castilla, D.; Finberg, R. W.; Dierberg, K.; Tapson, V.; Hsieh, L.; Patterson, T. F.; Paredes, R.; Sweeney, D. A.; Short, W. R.; Touloumi, G.; Lye, D. C.; Ohmagari, N.; Oh, M. D.; Ruiz-Palacios, G. M.; Benfield, T.; Fätkenheuer, G.; Kortepeter, M. G.; Atmar, R. L.; Creech, C. B.; Lundgren, J.; Babiker, A. G.; Pett, S.; Neaton, J. D.; Burgess, T. H.; Bonnett, T.; Green, M.; Makowski, M.; Osinusi, A.; Nayak, S.; Lane, H. C., Remdesivir for the treatment of Covid-19 - final report. *N Engl J Med* **2020,** *383* (19), 1813-1826.
131. Jayk Bernal, A.; Gomes da Silva, M. M.; Musungaie, D. B.; Kovalchuk, E.; Gonzalez, A.; Delos Reyes, V.; Martín-Quirós, A.; Caraco, Y.; Williams-Diaz, A.; Brown, M. L.; Du, J.; Pedley, A.; Assaid, C.; Strizki, J.; Grobler, J. A.; Shamsuddin, H. H.; Tipping, R.; Wan, H.; Paschke, A.; Butterton, J. R.; Johnson, M. G.; De Anda, C., Molnupiravir for oral treatment of Covid-19 in nonhospitalized patients. *N Engl J Med* **2022,** *386* (6), 509-520.
132. Ravetch, J. V.; Bolland, S., IgG Fc receptors. *Annu Rev Immunol* **2001,** *19*, 275-90.
133. Putnam, F. W.; Liu, Y. S.; Low, T. L., Primary structure of a human IgA1 immunoglobulin. IV. Streptococcal IgA1 protease, digestion, Fab and Fc fragments, and the complete amino acid sequence of the alpha 1 heavy chain. *J Biol Chem* **1979,** *254* (8), 2865-2874.
134. Heyman, B., Complement and Fc-receptors in regulation of the antibody response. *Immunol Lett* **1996,** *54* (2), 195-199.
135. Breedveld, F. C., Therapeutic monoclonal antibodies. *Lancet* **2000,** *355* (9205), 735-40.
136. Köhler, G.; Milstein, C., Continuous cultures of fused cells secreting antibody of predefined specificity. *Nature* **1975,** *256* (5517), 495-7.
137. Misasi, J.; Gilman, M. S.; Kanekiyo, M.; Gui, M.; Cagigi, A.; Mulangu, S.; Corti, D.; Ledgerwood, J. E.; Lanzavecchia, A.; Cunningham, J.; Muyembe-Tamfun, J. J.; Baxa, U.; Graham, B. S.; Xiang, Y.; Sullivan, N. J.; McLellan, J. S., Structural and molecular basis for Ebola virus neutralization by protective human antibodies. *Science* **2016,** *351* (6279), 1343-6.
138. Wang, L.; Shi, W.; Chappell, J. D.; Joyce, M. G.; Zhang, Y.; Kanekiyo, M.; Becker, M. M.; van Doremalen, N.; Fischer, R.; Wang, N.; Corbett, K. S.; Choe, M.; Mason, R. D.; Van Galen, J. G.; Zhou, T.; Saunders, K. O.; Tatti, K. M.; Haynes, L. M.; Kwong, P. D.; Modjarrad, K.; Kong, W. P.; McLellan, J. S.; Denison, M. R.; Munster, V. J.; Mascola, J. R.; Graham, B. S., Importance of neutralizing monoclonal antibodies targeting multiple antigenic sites on the Middle East Respiratory Syndrome Coronavirus Spike Glycoprotein to avoid neutralization escape. *J Virol* **2018,** *92* (10).
139. Taylor, P. C.; Adams, A. C.; Hufford, M. M.; de la Torre, I.; Winthrop, K.; Gottlieb, R. L., Neutralizing monoclonal antibodies for treatment of COVID-19. *Nat Rev Immunol* **2021,** *21* (6), 382-393.
140. Montezuma-Rusca, J. M.; Moir, S.; Kardava, L.; Buckner, C. M.; Louie, A.; Kim, L. J.; Santich, B. H.; Wang, W.; Fankuchen, O. R.; Diaz, G.; Daub, J. R.; Rosenzweig, S. D.; Chun, T. W.;

Li, Y.; Braylan, R. C.; Calvo, K. R.; Fauci, A. S., Bone marrow plasma cells are a primary source of serum HIV-1-specific antibodies in chronically infected individuals. *J Immunol* **2015,** *194* (6), 2561-8.
141. Hansel, T. T.; Kropshofer, H.; Singer, T.; Mitchell, J. A.; George, A. J., The safety and side effects of monoclonal antibodies. *Nat Rev Drug Discov* **2010,** *9* (4), 325-38.
142. Tirado, S. M.; Yoon, K. J., Antibody-dependent enhancement of virus infection and disease. *Viral Immunol* **2003,** *16* (1), 69-86.
143. Clark, I. A., The advent of the cytokine storm. *Immunol Cell Biol* **2007,** *85* (4), 271-3.
144. Walls, A. C.; Tortorici, M. A.; Bosch, B. J.; Frenz, B.; Rottier, P. J. M.; DiMaio, F.; Rey, F. A.; Veesler, D., Cryo-electron microscopy structure of a coronavirus spike glycoprotein trimer. *Nature* **2016,** *531* (7592), 114-117.
145. Walls, A. C.; Tortorici, M. A.; Snijder, J.; Xiong, X.; Bosch, B. J.; Rey, F. A.; Veesler, D., Tectonic conformational changes of a coronavirus spike glycoprotein promote membrane fusion. *Proc Natl Acad Sci U S A* **2017,** *114* (42), 11157-11162.
146. Chi, X.; Yan, R.; Zhang, J.; Zhang, G.; Zhang, Y.; Hao, M.; Zhang, Z.; Fan, P.; Dong, Y.; Yang, Y.; Chen, Z.; Guo, Y.; Zhang, J.; Li, Y.; Song, X.; Chen, Y.; Xia, L.; Fu, L.; Hou, L.; Xu, J.; Yu, C.; Li, J.; Zhou, Q.; Chen, W., A neutralizing human antibody binds to the N-terminal domain of the Spike protein of SARS-CoV-2. *Science* **2020,** *369* (6504), 650-655.
147. Min, L.; Sun, Q., Antibodies and vaccines target RBD of SARS-CoV-2. *Front Mol Biosci* **2021,** *8*, 671633.
148. Cohen, J., Antibodies may curb pandemic before vaccines. *Science* **2020,** *369* (6505), 752-753.
149. Li, D.; Sempowski, G. D.; Saunders, K. O.; Acharya, P.; Haynes, B. F., SARS-CoV-2 neutralizing antibodies for COVID-19 prevention and treatment. *Annu Rev Med* **2022,** *73*, 1-16.
150. Focosi, D.; McConnell, S.; Casadevall, A.; Cappello, E.; Valdiserra, G.; Tuccori, M., Monoclonal antibody therapies against SARS-CoV-2. *Lancet Infect Dis* **2022,** *22* (11), e311-e326.
151. Deng, J.; Heybati, K.; Ramaraju, H. B.; Zhou, F.; Rayner, D.; Heybati, S., Differential efficacy and safety of anti-SARS-CoV-2 antibody therapies for the management of COVID-19: a systematic review and network meta-analysis. *Infection* **2023,** *51* (1), 21-35.
152. Qi, H.; Liu, B.; Wang, X.; Zhang, L., The humoral response and antibodies against SARS-CoV-2 infection. *Nat Immunol* **2022,** *23* (7), 1008-1020.
153. Iannizzi, C.; Chai, K. L.; Piechotta, V.; Valk, S. J.; Kimber, C.; Monsef, I.; Wood, E. M.; Lamikanra, A. A.; Roberts, D. J.; McQuilten, Z.; So-Osman, C.; Jindal, A.; Cryns, N.; Estcourt, L. J.; Kreuzberger, N.; Skoetz, N., Convalescent plasma for people with COVID-19: a living systematic review. *Cochrane Database Syst Rev* **2023,** *5* (5), Cd013600.
154. Sievers, B. L.; Chakraborty, S.; Xue, Y.; Gelbart, T.; Gonzalez, J. C.; Cassidy, A. G.; Golan, Y.; Prahl, M.; Gaw, S. L.; Arunachalam, P. S.; Blish, C. A.; Boyd, S. D.; Davis, M. M.; Jagannathan, P.; Nadeau, K. C.; Pulendran, B.; Singh, U.; Scheuermann, R. H.; Frieman, M. B.; Vashee, S.; Wang, T. T.; Tan, G. S., Antibodies elicited by SARS-CoV-2 infection or mRNA vaccines have reduced neutralizing activity against Beta and Omicron pseudoviruses. *Sci Transl Med* **2022,** *14* (634), eabn7842.
155. Loo, Y. M.; McTamney, P. M.; Arends, R. H.; Abram, M. E.; Aksyuk, A. A.; Diallo, S.; Flores, D. J.; Kelly, E. J.; Ren, K.; Roque, R.; Rosenthal, K.; Streicher, K.; Tuffy, K. M.; Bond, N. J.; Cornwell, O.; Bouquet, J.; Cheng, L. I.; Dunyak, J.; Huang, Y.; Rosenbaum, A. I.; Pilla Reddy, V.; Andersen, H.; Carnahan, R. H.; Crowe, J. E., Jr.; Kuehne, A. I.; Herbert, A. S.; Dye, J. M.; Bright, H.; Kallewaard, N. L.; Pangalos, M. N.; Esser, M. T., The SARS-CoV-2 monoclonal antibody combination, AZD7442, is protective in nonhuman primates and has an extended half-life in humans. *Sci Transl Med* **2022,** *14* (635), eabl8124.
156. Hansen, J.; Baum, A.; Pascal, K. E.; Russo, V.; Giordano, S.; Wloga, E.; Fulton, B. O.; Yan, Y.; Koon, K.; Patel, K.; Chung, K. M.; Hermann, A.; Ullman, E.; Cruz, J.; Rafique, A.; Huang, T.; Fairhurst, J.; Libertiny, C.; Malbec, M.; Lee, W. Y.; Welsh, R.; Farr, G.; Pennington, S.; Deshpande, D.; Cheng, J.; Watty, A.; Bouffard, P.; Babb, R.; Levenkova, N.; Chen, C.; Zhang, B.; Romero Hernandez, A.; Saotome, K.; Zhou, Y.; Franklin, M.; Sivapalasingam, S.; Lye, D. C.; Weston, S.; Logue, J.; Haupt, R.; Frieman, M.; Chen, G.; Olson, W.; Murphy, A. J.; Stahl, N.; Yancopoulos, G. D.;

Kyratsous, C. A., Studies in humanized mice and convalescent humans yield a SARS-CoV-2 antibody cocktail. *Science* **2020,** *369* (6506), 1010-1014.
157. Xiaojie, S.; Yu, L.; Lei, Y.; Guang, Y.; Min, Q., Neutralizing antibodies targeting SARS-CoV-2 spike protein. *Stem Cell Res* **2020,** *50*, 102125.
158. Baum, A.; Fulton, B. O.; Wloga, E.; Copin, R.; Pascal, K. E.; Russo, V.; Giordano, S.; Lanza, K.; Negron, N.; Ni, M.; Wei, Y.; Atwal, G. S.; Murphy, A. J.; Stahl, N.; Yancopoulos, G. D.; Kyratsous, C. A., Antibody cocktail to SARS-CoV-2 spike protein prevents rapid mutational escape seen with individual antibodies. *Science* **2020,** *369* (6506), 1014-1018.
159. Li, D.; Edwards, R. J.; Manne, K.; Martinez, D. R.; Schäfer, A.; Alam, S. M.; Wiehe, K.; Lu, X.; Parks, R.; Sutherland, L. L.; Oguin, T. H., 3rd; McDanal, C.; Perez, L. G.; Mansouri, K.; Gobeil, S. M. C.; Janowska, K.; Stalls, V.; Kopp, M.; Cai, F.; Lee, E.; Foulger, A.; Hernandez, G. E.; Sanzone, A.; Tilahun, K.; Jiang, C.; Tse, L. V.; Bock, K. W.; Minai, M.; Nagata, B. M.; Cronin, K.; Gee-Lai, V.; Deyton, M.; Barr, M.; Von Holle, T.; Macintyre, A. N.; Stover, E.; Feldman, J.; Hauser, B. M.; Caradonna, T. M.; Scobey, T. D.; Rountree, W.; Wang, Y.; Moody, M. A.; Cain, D. W.; DeMarco, C. T.; Denny, T. N.; Woods, C. W.; Petzold, E. W.; Schmidt, A. G.; Teng, I. T.; Zhou, T.; Kwong, P. D.; Mascola, J. R.; Graham, B. S.; Moore, I. N.; Seder, R.; Andersen, H.; Lewis, M. G.; Montefiori, D. C.; Sempowski, G. D.; Baric, R. S.; Acharya, P.; Haynes, B. F.; Saunders, K. O., In vitro and in vivo functions of SARS-CoV-2 infection-enhancing and neutralizing antibodies. *Cell* **2021,** *184* (16), 4203-4219.e32.
160. Voss, W. N.; Hou, Y. J.; Johnson, N. V.; Delidakis, G.; Kim, J. E.; Javanmardi, K.; Horton, A. P.; Bartzoka, F.; Paresi, C. J.; Tanno, Y.; Chou, C. W.; Abbasi, S. A.; Pickens, W.; George, K.; Boutz, D. R.; Towers, D. M.; McDaniel, J. R.; Billick, D.; Goike, J.; Rowe, L.; Batra, D.; Pohl, J.; Lee, J.; Gangappa, S.; Sambhara, S.; Gadush, M.; Wang, N.; Person, M. D.; Iverson, B. L.; Gollihar, J. D.; Dye, J. M.; Herbert, A. S.; Finkelstein, I. J.; Baric, R. S.; McLellan, J. S.; Georgiou, G.; Lavinder, J. J.; Ippolito, G. C., Prevalent, protective, and convergent IgG recognition of SARS-CoV-2 non-RBD spike epitopes. *Science* **2021,** *372* (6546), 1108-1112.
161. Cheng, Z. J.; Li, B.; Zhan, Z.; Zhao, Z.; Xue, M.; Zheng, P.; Lyu, J.; Hu, C.; He, J.; Chen, R.; Sun, B., Clinical application of antibody immunity against SARS-CoV-2: Comprehensive review on immunoassay and immunotherapy. *Clin Rev Allergy Immunol* **2023,** *64* (1), 17-32.
162. Dacon, C.; Tucker, C.; Peng, L.; Lee, C. D.; Lin, T. H.; Yuan, M.; Cong, Y.; Wang, L.; Purser, L.; Williams, J. K.; Pyo, C. W.; Kosik, I.; Hu, Z.; Zhao, M.; Mohan, D.; Cooper, A. J. R.; Peterson, M.; Skinner, J.; Dixit, S.; Kollins, E.; Huzella, L.; Perry, D.; Byrum, R.; Lembirik, S.; Drawbaugh, D.; Eaton, B.; Zhang, Y.; Yang, E. S.; Chen, M.; Leung, K.; Weinberg, R. S.; Pegu, A.; Geraghty, D. E.; Davidson, E.; Douagi, I.; Moir, S.; Yewdell, J. W.; Schmaljohn, C.; Crompton, P. D.; Holbrook, M. R.; Nemazee, D.; Mascola, J. R.; Wilson, I. A.; Tan, J., Broadly neutralizing antibodies target the coronavirus fusion peptide. *Science* **2022,** *377* (6607), 728-735.
163. Low, J. S.; Jerak, J.; Tortorici, M. A.; McCallum, M.; Pinto, D.; Cassotta, A.; Foglierini, M.; Mele, F.; Abdelnabi, R.; Weynand, B.; Noack, J.; Montiel-Ruiz, M.; Bianchi, S.; Benigni, F.; Sprugasci, N.; Joshi, A.; Bowen, J. E.; Stewart, C.; Rexhepaj, M.; Walls, A. C.; Jarrossay, D.; Morone, D.; Paparoditis, P.; Garzoni, C.; Ferrari, P.; Ceschi, A.; Neyts, J.; Purcell, L. A.; Snell, G.; Corti, D.; Lanzavecchia, A.; Veesler, D.; Sallusto, F., ACE2-binding exposes the SARS-CoV-2 fusion peptide to broadly neutralizing coronavirus antibodies. *Science* **2022,** *377* (6607), 735-742.
164. Ng, K. W.; Faulkner, N.; Wrobel, A. G.; Gamblin, S. J.; Kassiotis, G., Heterologous humoral immunity to human and zoonotic coronaviruses: Aiming for the achilles heel. *Semin Immunol* **2021,** *55*, 101507.
165. Nguyen, H.; Lan, P. D.; Nissley, D. A.; O'Brien, E. P.; Li, M. S., Electrostatic interactions explain the higher binding affinity of the CR3022 antibody for SARS-CoV-2 than the 4A8 antibody. *J Phys Chem B* **2021,** *125* (27), 7368-7379.
166. Corrêa Giron, C.; Laaksonen, A.; Barroso da Silva, F. L., On the interactions of the receptor-binding domain of SARS-CoV-1 and SARS-CoV-2 spike proteins with monoclonal antibodies and the receptor ACE2. *Virus Res* **2020,** *285*, 198021.
167. Beshnova, D.; Fang, Y.; Du, M.; Sun, Y.; Du, F.; Ye, J.; Chen, Z. J.; Li, B., Computational approach for binding prediction of SARS-CoV-2 with neutralizing antibodies. *Comput Struct Biotechnol J* **2022,** *20*, 2212-2222.

168. Copin, R.; Baum, A.; Wloga, E.; Pascal, K. E.; Giordano, S.; Fulton, B. O.; Zhou, A.; Negron, N.; Lanza, K.; Chan, N.; Coppola, A.; Chiu, J.; Ni, M.; Wei, Y.; Atwal, G. S.; Hernandez, A. R.; Saotome, K.; Zhou, Y.; Franklin, M. C.; Hooper, A. T.; McCarthy, S.; Hamon, S.; Hamilton, J. D.; Staples, H. M.; Alfson, K.; Carrion, R., Jr.; Ali, S.; Norton, T.; Somersan-Karakaya, S.; Sivapalasingam, S.; Herman, G. A.; Weinreich, D. M.; Lipsich, L.; Stahl, N.; Murphy, A. J.; Yancopoulos, G. D.; Kyratsous, C. A., The monoclonal antibody combination REGEN-COV protects against SARS-CoV-2 mutational escape in preclinical and human studies. *Cell* **2021,** *184* (15), 3949-3961.e11.
169. Nguyen, H.; Lan, P. D.; Nissley, D. A.; O'Brien, E. P.; Li, M. S., Cocktail of REGN antibodies binds more strongly to SARS-CoV-2 than its components, but the Omicron variant reduces its neutralizing ability. *J Phys Chem B* **2022,** *126* (15), 2812-2823.
170. Hamers-Casterman, C.; Atarhouch, T.; Muyldermans, S.; Robinson, G.; Hammers, C.; Songa, E. B.; Bendahman, N.; Hammers, R., Naturally occurring antibodies devoid of light chains. *Nature* **1993,** *363* (6428), 446-448.
171. Yang, E. Y.; Shah, K., Nanobodies: Next generation of cancer diagnostics and therapeutics. *Front Oncol* **2020,** *10*, 1182.
172. Hu, Y.; Liu, C.; Muyldermans, S., Nanobody-based delivery systems for diagnosis and targeted tumor therapy. *Front Immunol* **2017,** *8*, 1442.
173. Zare, H.; Aghamollaei, H.; Hosseindokht, M.; Heiat, M.; Razei, A.; Bakherad, H., Nanobodies, the potent agents to detect and treat the Coronavirus infections: A systematic review. *Mol Cell Probes* **2021,** *55*, 101692.
174. Yu, S.; Xiong, G.; Zhao, S.; Tang, Y.; Tang, H.; Wang, K.; Liu, H.; Lan, K.; Bi, X.; Duan, S., Nanobodies targeting immune checkpoint molecules for tumor immunotherapy and immunoimaging (Review). *Int J Mol Med* **2021,** *47* (2), 444-454.
175. Arbabi-Ghahroudi, M., Camelid single-domain antibodies: historical perspective and future outlook. *Front Immunol* **2017,** *8*, 1589.
176. Huo, J.; Le Bas, A.; Ruza, R. R.; Duyvesteyn, H. M. E.; Mikolajek, H.; Malinauskas, T.; Tan, T. K.; Rijal, P.; Dumoux, M.; Ward, P. N.; Ren, J.; Zhou, D.; Harrison, P. J.; Weckener, M.; Clare, D. K.; Vogirala, V. K.; Radecke, J.; Moynié, L.; Zhao, Y.; Gilbert-Jaramillo, J.; Knight, M. L.; Tree, J. A.; Buttigieg, K. R.; Coombes, N.; Elmore, M. J.; Carroll, M. W.; Carrique, L.; Shah, P. N. M.; James, W.; Townsend, A. R.; Stuart, D. I.; Owens, R. J.; Naismith, J. H., Neutralizing nanobodies bind SARS-CoV-2 spike RBD and block interaction with ACE2. *Nat Struct Mol Biol* **2020,** *27* (9), 846-854.
177. Chi, X.; Liu, X.; Wang, C.; Zhang, X.; Li, X.; Hou, J.; Ren, L.; Jin, Q.; Wang, J.; Yang, W., Humanized single domain antibodies neutralize SARS-CoV-2 by targeting the spike receptor binding domain. *Nat Commun* **2020,** *11* (1), 4528.
178. Zhao, G.; He, L.; Sun, S.; Qiu, H.; Tai, W.; Chen, J.; Li, J.; Chen, Y.; Guo, Y.; Wang, Y.; Shang, J.; Ji, K.; Fan, R.; Du, E.; Jiang, S.; Li, F.; Du, L.; Zhou, Y., A Novel nanobody targeting Middle East Respiratory Syndrome Coronavirus (MERS-CoV) receptor-binding domain has potent cross-neutralizing activity and protective efficacy against MERS-CoV. *J Virol* **2018,** *92* (18).
179. Shi, R.; Shan, C.; Duan, X.; Chen, Z.; Liu, P.; Song, J.; Song, T.; Bi, X.; Han, C.; Wu, L.; Gao, G.; Hu, X.; Zhang, Y.; Tong, Z.; Huang, W.; Liu, W. J.; Wu, G.; Zhang, B.; Wang, L.; Qi, J.; Feng, H.; Wang, F. S.; Wang, Q.; Gao, G. F.; Yuan, Z.; Yan, J., A human neutralizing antibody targets the receptor-binding site of SARS-CoV-2. *Nature* **2020,** *584* (7819), 120-124.
180. Lu, Q.; Zhang, Z.; Li, H.; Zhong, K.; Zhao, Q.; Wang, Z.; Wu, Z.; Yang, D.; Sun, S.; Yang, N.; Zheng, M.; Chen, Q.; Long, C.; Guo, W.; Yang, H.; Nie, C.; Tong, A., Development of multivalent nanobodies blocking SARS-CoV-2 infection by targeting RBD of spike protein. *J Nanobiotechnology* **2021,** *19* (1), 33.
181. Ma, H.; Zeng, W.; Meng, X.; Huang, X.; Yang, Y.; Zhao, D.; Zhou, P.; Wang, X.; Zhao, C.; Sun, Y.; Wang, P.; Ou, H.; Hu, X.; Xiang, Y.; Jin, T., Potent neutralization of SARS-CoV-2 by Hetero-bivalent Alpaca nanobodies targeting the Spike receptor-binding domain. *J Virol* **2021,** *95* (10).
182. Custódio, T. F.; Das, H.; Sheward, D. J.; Hanke, L.; Pazicky, S.; Pieprzyk, J.; Sorgenfrei, M.; Schroer, M. A.; Gruzinov, A. Y.; Jeffries, C. M.; Graewert, M. A.; Svergun, D. I.; Dobrev, N.; Remans, K.; Seeger, M. A.; McInerney, G. M.; Murrell, B.; Hällberg, B. M.; Löw, C., Selection, biophysical

and structural analysis of synthetic nanobodies that effectively neutralize SARS-CoV-2. *Nat Commun* **2020,** *11* (1), 5588.
183. Palomo, C.; Mas, V.; Detalle, L.; Depla, E.; Cano, O.; Vázquez, M.; Stortelers, C.; Melero, J. A., Trivalency of a nanobody specific for the human respiratory syncytial virus fusion glycoprotein drastically enhances virus neutralization and impacts escape mutant selection. *Antimicrob Agents Chemother* **2016,** *60* (11), 6498-6509.
184. Bracken, C. J.; Lim, S. A.; Solomon, P.; Rettko, N. J.; Nguyen, D. P.; Zha, B. S.; Schaefer, K.; Byrnes, J. R.; Zhou, J.; Lui, I.; Liu, J.; Pance, K.; Azumaya, C. M.; Braxton, J. R.; Brilot, A. F.; Gupta, M.; Li, F.; Lopez, K. E.; Melo, A.; Merz, G. E.; Moss, F.; Paulino, J.; Pospiech, T. H.; Pourmal, S.; Puchades, C.; Rizo, A. N.; Smith, A. M.; Sun, M.; Thomas, P. V.; Wang, F.; Yu, Z.; Asarnow, D.; Braxton, J. R.; Campbell, M. G.; Chio, C. M.; Chio, U. S.; Dickinson, M. S.; Diwanji, D.; Faust, B.; Gupta, M.; Hoppe, N.; Jin, M.; Li, F.; Li, J.; Liu, Y.; Merz, G. E.; Nguyen, H. C.; Paulino, J.; Pospiech, T. H.; Pourmal, S.; Sangwan, S.; Trenker, R.; Trinidad, D.; Tse, E.; Zhang, K.; Zhou, F.; Azumaya, C. M.; Billesboelle, C.; Bowen, A.; Campbell, M. G.; Diwanji, D.; Hoppe, N.; Li, Y.-L.; Nguyen, P.; Nowotny, C.; Puchades, C.; Safari, M.; Sangwan, S.; Schaefer, K.; Smith, A. M.; Trenker, R.; Tsui, T. K. M.; Whitis, N.; Zhao, J.; Asarnow, D.; Azumaya, C. M.; Chio, C. M.; Faust, B.; Gupta, M.; Kim, K.; Moritz, M.; Owens, T. W.; Paulino, J.; Peters, J. K.; Pourmal, S.; Schaefer, K.; Tsui, T. K. M.; Biel, J.; Deshpande, I.; Herrera, N.; Kratochvil, H. T.; Liu, X.; Schulze-Gahmen, U.; Young, I. D.; Chen, J.; Diallo, A.; Doan, L.; Flores, S.; Gupta, M.; Jin, M.; Kratochvil, H. T.; Lam, V. L.; Li, Y.; Lo, M.; Merz, G. E.; Paulino, J.; Thwin, A. C.; Titus, E. W.; Yu, Z.; Zhou, F.; Zhang, Y.; Bulkley, D.; Joves, A.; Joves, A.; McKay, L.; Tabios, M.; Tse, E.; Agard, D. A.; Cheng, Y.; Fraser, J. S.; Frost, A.; Jura, N.; Kortemme, T.; Krogan, N. J.; Manglik, A.; Rosenberg, O. S.; Southworth, D. R.; Stroud, R. M.; Verba, K. A.; Zhou, X. X.; Leung, K. K.; Wells, J. A.; Consortium, Q. S. B.; Cryo, E. M. g. f. c. t.; Cryo, E. M. d. p. t.; Mammalian cell expression, t.; Protein purification, t.; Crystallography, t.; Bacterial expression, t.; Infrastructure, t.; Leadership, t., Bi-paratopic and multivalent VH domains block ACE2 binding and neutralize SARS-CoV-2. *Nat Chem Biol* **2021,** *17* (1), 113-121.
185. Huo, J.; Mikolajek, H.; Le Bas, A.; Clark, J. J.; Sharma, P.; Kipar, A.; Dormon, J.; Norman, C.; Weckener, M.; Clare, D. K.; Harrison, P. J.; Tree, J. A.; Buttigieg, K. R.; Salguero, F. J.; Watson, R.; Knott, D.; Carnell, O.; Ngabo, D.; Elmore, M. J.; Fotheringham, S.; Harding, A.; Moynié, L.; Ward, P. N.; Dumoux, M.; Prince, T.; Hall, Y.; Hiscox, J. A.; Owen, A.; James, W.; Carroll, M. W.; Stewart, J. P.; Naismith, J. H.; Owens, R. J., A potent SARS-CoV-2 neutralising nanobody shows therapeutic efficacy in the Syrian golden hamster model of COVID-19. *Nat Commun* **2021,** *12* (1), 5469.
186. Güttler, T.; Aksu, M.; Dickmanns, A.; Stegmann, K. M.; Gregor, K.; Rees, R.; Taxer, W.; Rymarenko, O.; Schünemann, J.; Dienemann, C.; Gunkel, P.; Mussil, B.; Krull, J.; Teichmann, U.; Groß, U.; Cordes, V. C.; Dobbelstein, M.; Görlich, D., Neutralization of SARS-CoV-2 by highly potent, hyperthermostable, and mutation-tolerant nanobodies. *Embo j* **2021,** *40* (19), e107985.
187. Casasnovas, J. M.; Margolles, Y.; Noriega, M. A.; Guzmán, M.; Arranz, R.; Melero, R.; Casanova, M.; Corbera, J. A.; Jiménez-de-Oya, N.; Gastaminza, P.; Garaigorta, U.; Saiz, J. C.; Martín-Acebes, M.; Fernández, L., Nanobodies protecting From lethal SARS-CoV-2 infection target receptor binding epitopes preserved in virus variants other than Omicron. *Front Immunol* **2022,** *13*, 863831.
188. Hanke, L.; Vidakovics Perez, L.; Sheward, D. J.; Das, H.; Schulte, T.; Moliner-Morro, A.; Corcoran, M.; Achour, A.; Karlsson Hedestam, G. B.; Hällberg, B. M.; Murrell, B.; McInerney, G. M., An alpaca nanobody neutralizes SARS-CoV-2 by blocking receptor interaction. *Nat Commun* **2020,** *11* (1), 4420.
189. Golcuk, M.; Hacisuleyman, A.; Erman, B.; Yildiz, A.; Gur, M., Binding mechanism of neutralizing nanobodies targeting SARS-CoV-2 Spike glycoprotein. *J Chem Inf Model* **2021,** *61* (10), 5152-5160.
190. Xiang, Y.; Nambulli, S.; Xiao, Z.; Liu, H.; Sang, Z.; Duprex, W. P.; Schneidman-Duhovny, D.; Zhang, C.; Shi, Y., Versatile and multivalent nanobodies efficiently neutralize SARS-CoV-2. *Science* **2020,** *370* (6523), 1479-1484.
191. Sanaei, M.; Setayesh, N.; Sepehrizadeh, Z.; Mahdavi, M.; Yazdi, M. H., Nanobodies in human infections: Prevention, detection, and treatment. *Immunol Invest* **2020,** *49* (8), 875-896.

192. Nguyen, H.; Li, M. S., Antibody-nanobody combination increases their neutralizing activity against SARS-CoV-2 and nanobody H11-H4 is effective against Alpha, Kappa and Delta variants. *Sci Rep* **2022,** *12* (1), 9701.
193. Masters, P. S., The molecular biology of coronaviruses. *Adv Virus Res* **2006,** *66*, 193-292.
194. Peng, Q.; Peng, R.; Yuan, B.; Zhao, J.; Wang, M.; Wang, X.; Wang, Q.; Sun, Y.; Fan, Z.; Qi, J.; Gao, G. F.; Shi, Y., Structural and biochemical characterization of the nsp12-nsp7-nsp8 core polymerase complex from SARS-CoV-2. *Cell Rep* **2020,** *31* (11), 107774.
195. Chen, Y.; Guo, D., Molecular mechanisms of coronavirus RNA capping and methylation. *Virol Sin* **2016,** *31* (1), 3-11.
196. Steitz, T. A., A structural understanding of the dynamic ribosome machine. *Nat Rev Mol Cell Biol* **2008,** *9* (3), 242-53.
197. Borišek, J.; Spinello, A.; Magistrato, A., Molecular basis of SARS-CoV-2 Nsp1-induced immune translational shutdown as revealed by all-atom simulations. *J Phys Chem Lett* **2021,** *12* (48), 11745-11750.
198. Schubert, K.; Karousis, E. D.; Jomaa, A.; Scaiola, A.; Echeverria, B.; Gurzeler, L. A.; Leibundgut, M.; Thiel, V.; Mühlemann, O.; Ban, N., SARS-CoV-2 Nsp1 binds the ribosomal mRNA channel to inhibit translation. *Nat Struct Mol Biol* **2020,** *27* (10), 959-966.
199. Kamitani, W.; Huang, C.; Narayanan, K.; Lokugamage, K. G.; Makino, S., A two-pronged strategy to suppress host protein synthesis by SARS coronavirus Nsp1 protein. *Nat Struct Mol Biol* **2009,** *16* (11), 1134-40.
200. Benedetti, F.; Snyder, G. A.; Giovanetti, M.; Angeletti, S.; Gallo, R. C.; Ciccozzi, M.; Zella, D., Emerging of a SARS-CoV-2 viral strain with a deletion in nsp1. *J Transl Med* **2020,** *18* (1), 329.
201. Lin, J.-W.; Tang, C.; Wei, H.-C.; Du, B.; Chen, C.; Wang, M.; Zhou, Y.; Yu, M.-X.; Cheng, L.; Kuivanen, S.; Ogando, N. S.; Levanov, L.; Zhao, Y.; Li, C.-L.; Zhou, R.; Li, Z.; Zhang, Y.; Sun, K.; Wang, C.; Chen, L.; Xiao, X.; Zheng, X.; Chen, S.-S.; Zhou, Z.; Yang, R.; Zhang, D.; Xu, M.; Song, J.; Wang, D.; Li, Y.; Lei, S.; Zeng, W.; Yang, Q.; He, P.; Zhang, Y.; Zhou, L.; Cao, L.; Luo, F.; Liu, H.; Wang, L.; Ye, F.; Zhang, M.; Li, M.; Fan, W.; Li, X.; Li, K.; Ke, B.; Xu, J.; Yang, H.; He, S.; Pan, M.; Yan, Y.; Zha, Y.; Jiang, L.; Yu, C.; Liu, Y.; Xu, Z.; Li, Q.; Jiang, Y.; Sun, J.; Hong, W.; Wei, H.; Lu, G.; Vapalahti, O.; Luo, Y.; Wei, Y.; Connor, T.; Tan, W.; Snijder, E. J.; Smura, T.; Li, W.; Geng, J.; Ying, B.; Ying, B.; Chen, L., Genomic monitoring of SARS-CoV-2 uncovers an Nsp1 deletion variant that modulates type I interferon response. *Cell Host Microbe* **2021,** *29* (3), 489-502.e8.
202. Afsar, M.; Narayan, R.; Akhtar, M. N.; Das, D.; Rahil, H.; Nagaraj, S. K.; Eswarappa, S. M.; Tripathi, S.; Hussain, T., Drug targeting Nsp1-ribosomal complex shows antiviral activity against SARS-CoV-2. *Elife* **2022,** *11*.
203. Ma, S.; Damfo, S.; Lou, J.; Pinotsis, N.; Bowler, M. W.; Haider, S.; Kozielski, F., Two ligand-binding sites on SARS-CoV-2 non-structural protein 1 revealed by fragment-based X-ray screening. *Int J Mol Sci* **2022,** *23* (20).
204. Nguyen, H.; Nguyen, H. L.; Li, M. S., Binding of SARS-CoV-2 nonstructural protein 1 to 40S ribosome inhibits mRNA translation. *J Phys Chem B* **2024,** *128* (29), 7033-7042.
205. Khare, R.; Sundaravadivelu Devarajan, D., Molecular simulations of nanocolloids. *Curr Opin Chem Eng* **2017,** *16*, 86-91.
206. Hockney, R. W.; Goel, S.; Eastwood, J. W., Quiet high resolution computer models of a plasma. *J Comput Phys* **1974,** *14*, 148-158.
207. Grubmüller, H.; Heller, H.; Windemuth, A.; Schulten, K., Generalized Verlet algorithm for efficient molecular dynamics simulations with long-range interactions. *Mol Sim* **1991,** *6*, 121.
208. Spreiter, Q.; Walter, M., Classical molecular dynamics simulation with the velocity Verlet algorithm at strong external magnetic fields. *J Comput Phys* **1999,** *152* (1), 102-119.
209. Miyamoto, S.; Kollman, P. A., Settle: An analytical version of the SHAKE and RATTLE algorithm for rigid water models. *J Comput Chem* **1992,** *13*.
210. Elber, R.; Ruymgaart, A. P.; Hess, B., SHAKE parallelization. *Eur Phys J Spec Top* **2011,** *200* (1), 211-223.
211. Hess, B.; Bekker, H.; Berendsen, H.; Fraaije, J., LINCS: A Linear Constraint Solver for molecular simulations. *J Comput Chem* **1998,** *18*.

212. Wu, X.; Brooks, B., Self-guided Langevin dynamics simulation method. *Chem Phys Lett* **2003,** *381*, 512-518.
213. Darden, T.; Perera, L.; Li, L.; Pedersen, L., New tricks for modelers from the crystallography toolkit: the particle mesh Ewald algorithm and its use in nucleic acid simulations. *Structure* **1999,** *7* (3), R55-60.
214. Shi, X.; Tian, F., Multiscale modeling and simulation of nano-carriers delivery through biological barriers-a review. *Adv Theory Simul* **2018,** *2*, 1800105.
215. Rai, B.; Pradip, P., Modeling self-assembly of surfactants at interfaces. *Curr Opin Chem Eng* **2017,** *15*, 84-94.
216. Francl, M. M.; Carey, C.; Chirlian, L. E.; Gange, D. M., Charges fit to electrostatic potentials. II. Can atomic charges be unambiguously fit to electrostatic potentials? *J Comput Chem* **1996,** *17*.
217. Higuchi, Y., Fracture processes of crystalline polymers using coarse-grained molecular dynamics simulations. *Polym J* **2018,** *50*, 1.
218. Noid, W. G.; Chu, J. W.; Ayton, G. S.; Krishna, V.; Izvekov, S.; Voth, G. A.; Das, A.; Andersen, H. C., The multiscale coarse-graining method. I. A rigorous bridge between atomistic and coarse-grained models. *J Chem Phys* **2008,** *128* (24), 244114.
219. Izvekov, S.; Voth, G., A Multiscale coarse-graining method for biomolecular systems. *J Phys Chem B* **2005,** *109*, 2469-73.
220. Nissley, D. A.; Vu, Q. V.; Trovato, F.; Ahmed, N.; Jiang, Y.; Li, M. S.; O'Brien, E. P., Electrostatic interactions govern extreme nascent protein ejection times from ribosomes and can delay ribosome recycling. *J Am Chem Soc* **2020,** *142* (13), 6103-6110.
221. Jiang, Y.; Neti, S. S.; Sitarik, I.; Pradhan, P.; To, P.; Xia, Y.; Fried, S. D.; Booker, S. J.; O'Brien, E. P., How synonymous mutations alter enzyme structure and function over long timescales. *Nat Chem* **2023,** *15* (3), 308-318.
222. Souza, P. C. T.; Alessandri, R.; Barnoud, J.; Thallmair, S.; Faustino, I.; Grünewald, F.; Patmanidis, I.; Abdizadeh, H.; Bruininks, B. M. H.; Wassenaar, T. A.; Kroon, P. C.; Melcr, J.; Nieto, V.; Corradi, V.; Khan, H. M.; Domański, J.; Javanainen, M.; Martinez-Seara, H.; Reuter, N.; Best, R. B.; Vattulainen, I.; Monticelli, L.; Periole, X.; Tieleman, D. P.; de Vries, A. H.; Marrink, S. J., Martini 3: a general purpose force field for coarse-grained molecular dynamics. *Nat Methods* **2021,** *18* (4), 382-388.
223. Marrink, S. J.; Risselada, H. J.; Yefimov, S.; Tieleman, D. P.; de Vries, A. H., The MARTINI force field: coarse grained model for biomolecular simulations. *J Phys Chem B* **2007,** *111* (27), 7812-24.
224. Liwo, A.; Khalili, M.; Czaplewski, C.; Kalinowski, S.; Ołdziej, S.; Wachucik, K.; Scheraga, H. A., Modification and optimization of the united-residue (UNRES) potential energy function for canonical simulations. I. Temperature dependence of the effective energy function and tests of the optimization method with single training proteins. *J Phys Chem B* **2007,** *111* (1), 260-85.
225. Liwo, A.; Baranowski, M.; Czaplewski, C.; Gołaś, E.; He, Y.; Jagieła, D.; Krupa, P.; Maciejczyk, M.; Makowski, M.; Mozolewska, M. A.; Niadzvedtski, A.; Ołdziej, S.; Scheraga, H. A.; Sieradzan, A. K.; Ślusarz, R.; Wirecki, T.; Yin, Y.; Zaborowski, B., A unified coarse-grained model of biological macromolecules based on mean-field multipole–multipole interactions. *J Mol Model* **2014,** *20* (8), 2306.
226. Best, R. B.; Chen, Y.-G.; Hummer, G., Slow protein conformational dynamics from multiple experimental structures: The helix/sheet transition of arc repressor. *Structure* **2005,** *13* (12), 1755-1763.
227. O'Brien, E. P.; Christodoulou, J.; Vendruscolo, M.; Dobson, C. M., Trigger factor slows co-translational folding through kinetic trapping while sterically protecting the nascent chain from aberrant cytosolic interactions. *J Am Chem Soc* **2012,** *134* (26), 10920-32.
228. Karanicolas, J.; Brooks, C. L., 3rd, The origins of asymmetry in the folding transition states of protein L and protein G. *Protein Sci* **2002,** *11* (10), 2351-61.
229. Betancourt, M. R.; Thirumalai, D., Pair potentials for protein folding: choice of reference states and sensitivity of predicted native states to variations in the interaction schemes. *Protein Sci* **1999,** *8* (2), 361-9.

230. Leininger, S. E.; Trovato, F.; Nissley, D. A.; O'Brien, E. P., Domain topology, stability, and translation speed determine mechanical force generation on the ribosome. *Proc Natl Acad Sci U S A* **2019,** *116* (12), 5523-5532.
231. Monticelli, L.; Kandasamy, S. K.; Periole, X.; Larson, R. G.; Tieleman, D. P.; Marrink, S.-J., The MARTINI coarse-grained force field: extension to proteins. *J Chem Theory and Comput* **2008,** *4* (5), 819-834.
232. Uusitalo, J. J.; Ingólfsson, H. I.; Akhshi, P.; Tieleman, D. P.; Marrink, S. J., Martini coarse-grained force field: Extension to DNA. *J Chem Theory and Comput* **2015,** *11* (8), 3932-3945.
233. Uusitalo, J. J.; Ingólfsson, H. I.; Marrink, S. J.; Faustino, I., Martini Coarse-Grained Force Field: Extension to RNA. *Biophys J* **2017,** *113* (2), 246-256.
234. de Jong, D. H.; Singh, G.; Bennett, W. F. D.; Arnarez, C.; Wassenaar, T. A.; Schäfer, L. V.; Periole, X.; Tieleman, D. P.; Marrink, S. J., Improved parameters for the Martini coarse-grained protein force field. *J Chem Theory and Comput* **2013,** *9* (1), 687-697.
235. Souza, P. C. T.; Thallmair, S.; Conflitti, P.; Ramírez-Palacios, C.; Alessandri, R.; Raniolo, S.; Limongelli, V.; Marrink, S. J., Protein–ligand binding with the coarse-grained Martini model. *Nat Commun* **2020,** *11* (1), 3714.
236. Yu, W.; MacKerell, A. D., Jr., Computer-aided drug design methods. *Methods Mol Biol* **2017,** *1520*, 85-106.
237. Müller, D. J.; Dumitru, A. C.; Lo Giudice, C.; Gaub, H. E.; Hinterdorfer, P.; Hummer, G.; De Yoreo, J. J.; Dufrêne, Y. F.; Alsteens, D., Atomic Force Microscopy-Based Force Spectroscopy and Multiparametric Imaging of Biomolecular and Cellular Systems. *Chem Rev* **2021,** *121* (19), 11701-11725.
238. Stahelin, R. V., Surface plasmon resonance: a useful technique for cell biologists to characterize biomolecular interactions. *Mol Biol Cell* **2013,** *24* (7), 883-6.
239. Desai, M.; Di, R.; Fan, H., Application of Biolayer Interferometry (BLI) for Studying Protein-Protein Interactions in Transcription. *J Vis Exp* **2019,** (149).
240. Drescher, H.; Weiskirchen, S.; Weiskirchen, R., Flow Cytometry: A Blessing and a Curse. *Biomedicines* **2021,** *9* (11).
241. Anczykowski, B.; Krüger, D.; Babcock, K. L.; Fuchs, H., Basic properties of dynamic force spectroscopy with the scanning force microscope in experiment and simulation. *Ultramicroscopy* **1996,** *66* (3), 251-259.
242. Kirkwood, J. G., Statistical mechanics of fluid mixtures. *J Chem Phys* **1935,** *3*, 300-313.
243. Zwanzig, R. W., High-temperature equation of state by a perturbation method. I. Nonpolar gases. *J Chem Phys* **1954,** *22*, 1420-1426.
244. Srinivasan, J.; Miller, J.; Kollman, P. A.; Case, D. A., Continuum solvent studies of the stability of RNA hairpin loops and helices. *J Biomol Struct Dyn* **1998,** *16* (3), 671-82.
245. Aqvist, J.; Medina Llanos, C.; Samuelsson, J.-E., A new method for predicting binding affinity in computer-aided drug design. *Protein Eng* **1994,** *7*, 385-91.
246. Lorenzo, A. C.; Bisch, P. M., Analyzing different parameters of steered molecular dynamics for small membrane interacting molecules. *J Mol Graph Model* **2005,** *24* (1), 59-71.
247. Torrie, G. M.; Valleau, J. P., Nonphysical sampling distributions in Monte Carlo free-energy estimation: Umbrella sampling. *J Comput Phys* **1977,** *23* (2), 187-199.
248. Binnig, G.; Quate, C. F.; Gerber, C., Atomic force microscope. *Phys Rev Lett* **1986,** *56* (9), 930-933.
249. Bustamante, C. J.; Chemla, Y. R.; Liu, S.; Wang, M. D., Optical tweezers in single-molecule biophysics. *Nat Rev Methods Primers* **2021,** *1* (1), 25.
250. Neuman, K. C.; Nagy, A., Single-molecule force spectroscopy: optical tweezers, magnetic tweezers and atomic force microscopy. *Nat Methods* **2008,** *5* (6), 491-505.
251. Vuong, Q. V.; Nguyen, T. T.; Li, M. S., A new method for navigating optimal direction for pulling ligand from binding pocket: Application to ranking binding affinity by steered molecular dynamics. *J Chem Inf Model* **2015,** *55* (12), 2731-8.
252. Jarzynski, C., Nonequilibrium equality for free energy differences. *Phys Rev Lett* **1996,** *78*, 2690-2693.

253. Hummer, G.; Szabo, A., Free energy reconstruction from nonequilibrium single-molecule pulling experiments. *Proc Natl Acad Sci U S A* **2001,** *98* (7), 3658-61.
254. Khalili-Araghi, F.; Tajkhorshid, E.; Schulten, K., Free energy calculation from steered molecular dynamics simulations using Jarzynski's equality. *J Chem Phys* **2003,** *119*.
255. Truong, D. T.; Li, M. S., Probing the binding affinity by Jarzynski's nonequilibrium binding free energy and rupture Time. *J Phys Chem B* **2018,** *122* (17), 4693-4699.
256. Kumar, S.; Rosenberg, J. M.; Bouzida, D.; Swendsen, R. H.; Kollman, P. A., THE weighted histogram analysis method for free-energy calculations on biomolecules. I. The method. *J Comput Chem* **1992,** *13*.
257. Nguyen, H. L.; Lan, P. D.; Thai, N. Q.; Nissley, D. A.; O'Brien, E. P.; Li, M. S., Does SARS-CoV-2 bind to human ACE2 more strongly than does SARS-CoV? *J Phys Chem B* **2020,** *124* (34), 7336-7347.
258. Patel, J. S.; Ytreberg, F. M., Fast calculation of protein-protein binding free energies using umbrella sampling with a coarse-grained model. *J Chem Theory Comput* **2018,** *14* (2), 991-997.
259. Chipot, C., Frontiers in free-energy calculations of biological systems. *Wiley Interdiscip Rev Comput Mol Sci* **2014,** *4*.
260. Hansen, N.; van Gunsteren, W. F., Practical aspects of free-energy calculations: A review. *J Chem Theory Comput* **2014,** *10* (7), 2632-47.
261. Chodera, J.; Mobley, D.; Shirts, M.; Dixon, R.; Branson, K.; Pande, V., Alchemical free energy methods for drug discovery: Progress and challenges. *Curr Opin Struct Biol* **2011,** *21*, 150-60.
262. Klimovich, P. V.; Mobley, D. L., A Python tool to set up relative free energy calculations in GROMACS. *J Comput Aided Mol Des* **2015,** *29* (11), 1007-14.
263. Inkscape project. (2020). Inkscape. retrieved from https://inkscape.org.
264. Turner, P., XMGRACE, version 5.1. 19. *Center for Coastal and Land-Margin Research, Oregon Graduate Institute of Science and Technology, Beaverton, OR* **2005,** *2*.
265. The PyMOL molecular graphics system, Version 1.3, Schrödinger, LLC.
266. Humphrey, W.; Dalke, A.; Schulten, K., VMD: visual molecular dynamics. *J Mol Graph* **1996,** *14* (1), 33-8, 27-8.
267. Eswar, N.; Webb, B.; Marti-Renom, M. A.; Madhusudhan, M. S.; Eramian, D.; Shen, M. Y.; Pieper, U.; Sali, A., Comparative protein structure modeling using Modeller. *Curr Protoc Bioinformatics* **2006,** *Chapter 5*, Unit-5.6.
268. Guex, N.; Peitsch, M. C., SWISS-MODEL and the Swiss-PdbViewer: an environment for comparative protein modeling. *Electrophoresis* **1997,** *18* (15), 2714-23.
269. Magnus, M., rna-tools.online: a Swiss army knife for RNA 3D structure modeling workflow. *Nucleic Acids Res* **2022,** *50* (W1), W657-w662.
270. Chen, P.; Nirula, A.; Heller, B.; Gottlieb, R. L.; Boscia, J.; Morris, J.; Huhn, G.; Cardona, J.; Mocherla, B.; Stosor, V.; Shawa, I.; Adams, A. C.; Van Naarden, J.; Custer, K. L.; Shen, L.; Durante, M.; Oakley, G.; Schade, A. E.; Sabo, J.; Patel, D. R.; Klekotka, P.; Skovronsky, D. M., SARS-CoV-2 neutralizing antibody LY-CoV555 in outpatients with Covid-19. *N Engl J Med* **2021,** *384* (3), 229-237.
271. Weinreich, D. M.; Sivapalasingam, S.; Norton, T.; Ali, S.; Gao, H.; Bhore, R.; Musser, B. J.; Soo, Y.; Rofail, D.; Im, J.; Perry, C.; Pan, C.; Hosain, R.; Mahmood, A.; Davis, J. D.; Turner, K. C.; Hooper, A. T.; Hamilton, J. D.; Baum, A.; Kyratsous, C. A.; Kim, Y.; Cook, A.; Kampman, W.; Kohli, A.; Sachdeva, Y.; Graber, X.; Kowal, B.; DiCioccio, T.; Stahl, N.; Lipsich, L.; Braunstein, N.; Herman, G.; Yancopoulos, G. D., REGN-COV2, a neutralizing antibody cocktail, in outpatients with Covid-19. *N Engl J Med* **2021,** *384* (3), 238-251.
272. Wang, C.; Li, W.; Drabek, D.; Okba, N. M. A.; van Haperen, R.; Osterhaus, A.; van Kuppeveld, F. J. M.; Haagmans, B. L.; Grosveld, F.; Bosch, B. J., A human monoclonal antibody blocking SARS-CoV-2 infection. *Nat Commun* **2020,** *11* (1), 2251.
273. Liu, L.; Wang, P.; Nair, M. S.; Yu, J.; Rapp, M.; Wang, Q.; Luo, Y.; Chan, J. F.; Sahi, V.; Figueroa, A.; Guo, X. V.; Cerutti, G.; Bimela, J.; Gorman, J.; Zhou, T.; Chen, Z.; Yuen, K. Y.; Kwong, P. D.; Sodroski, J. G.; Yin, M. T.; Sheng, Z.; Huang, Y.; Shapiro, L.; Ho, D. D., Potent neutralizing antibodies against multiple epitopes on SARS-CoV-2 spike. *Nature* **2020,** *584* (7821), 450-456.

274. ter Meulen, J.; van den Brink, E. N.; Poon, L. L.; Marissen, W. E.; Leung, C. S.; Cox, F.; Cheung, C. Y.; Bakker, A. Q.; Bogaards, J. A.; van Deventer, E.; Preiser, W.; Doerr, H. W.; Chow, V. T.; de Kruif, J.; Peiris, J. S.; Goudsmit, J., Human monoclonal antibody combination against SARS coronavirus: synergy and coverage of escape mutants. *PLoS Med* **2006,** *3* (7), e237.
275. Davies, N. G.; Abbott, S.; Barnard, R. C.; Jarvis, C. I.; Kucharski, A. J.; Munday, J. D.; Pearson, C. A. B.; Russell, T. W.; Tully, D. C.; Washburne, A. D.; Wenseleers, T.; Gimma, A.; Waites, W.; Wong, K. L. M.; van Zandvoort, K.; Silverman, J. D.; Diaz-Ordaz, K.; Keogh, R.; Eggo, R. M.; Funk, S.; Jit, M.; Atkins, K. E.; Edmunds, W. J., Estimated transmissibility and impact of SARS-CoV-2 lineage B.1.1.7 in England. *Science* **2021,** *372* (6538).
276. Faria, N. R.; Mellan, T. A.; Whittaker, C.; Claro, I. M.; Candido, D. D. S.; Mishra, S.; Crispim, M. A. E.; Sales, F. C. S.; Hawryluk, I.; McCrone, J. T.; Hulswit, R. J. G.; Franco, L. A. M.; Ramundo, M. S.; de Jesus, J. G.; Andrade, P. S.; Coletti, T. M.; Ferreira, G. M.; Silva, C. A. M.; Manuli, E. R.; Pereira, R. H. M.; Peixoto, P. S.; Kraemer, M. U. G.; Gaburo, N., Jr.; Camilo, C. D. C.; Hoeltgebaum, H.; Souza, W. M.; Rocha, E. C.; de Souza, L. M.; de Pinho, M. C.; Araujo, L. J. T.; Malta, F. S. V.; de Lima, A. B.; Silva, J. D. P.; Zauli, D. A. G.; Ferreira, A. C. S.; Schnekenberg, R. P.; Laydon, D. J.; Walker, P. G. T.; Schlüter, H. M.; Dos Santos, A. L. P.; Vidal, M. S.; Del Caro, V. S.; Filho, R. M. F.; Dos Santos, H. M.; Aguiar, R. S.; Proença-Modena, J. L.; Nelson, B.; Hay, J. A.; Monod, M.; Miscouridou, X.; Coupland, H.; Sonabend, R.; Vollmer, M.; Gandy, A.; Prete, C. A., Jr.; Nascimento, V. H.; Suchard, M. A.; Bowden, T. A.; Pond, S. L. K.; Wu, C. H.; Ratmann, O.; Ferguson, N. M.; Dye, C.; Loman, N. J.; Lemey, P.; Rambaut, A.; Fraiji, N. A.; Carvalho, M.; Pybus, O. G.; Flaxman, S.; Bhatt, S.; Sabino, E. C., Genomics and epidemiology of the P.1 SARS-CoV-2 lineage in Manaus, Brazil. *Science* **2021,** *372* (6544), 815-821.
277. Mlcochova, P.; Kemp, S. A.; Dhar, M. S.; Papa, G.; Meng, B.; Ferreira, I.; Datir, R.; Collier, D. A.; Albecka, A.; Singh, S.; Pandey, R.; Brown, J.; Zhou, J.; Goonawardane, N.; Mishra, S.; Whittaker, C.; Mellan, T.; Marwal, R.; Datta, M.; Sengupta, S.; Ponnusamy, K.; Radhakrishnan, V. S.; Abdullahi, A.; Charles, O.; Chattopadhyay, P.; Devi, P.; Caputo, D.; Peacock, T.; Wattal, C.; Goel, N.; Satwik, A.; Vaishya, R.; Agarwal, M.; Mavousian, A.; Lee, J. H.; Bassi, J.; Silacci-Fegni, C.; Saliba, C.; Pinto, D.; Irie, T.; Yoshida, I.; Hamilton, W. L.; Sato, K.; Bhatt, S.; Flaxman, S.; James, L. C.; Corti, D.; Piccoli, L.; Barclay, W. S.; Rakshit, P.; Agrawal, A.; Gupta, R. K., SARS-CoV-2 B.1.617.2 Delta variant replication and immune evasion. *Nature* **2021,** *599* (7883), 114-119.
278. Kimura, I.; Kosugi, Y.; Wu, J.; Zahradnik, J.; Yamasoba, D.; Butlertanaka, E. P.; Tanaka, Y. L.; Uriu, K.; Liu, Y.; Morizako, N.; Shirakawa, K.; Kazuma, Y.; Nomura, R.; Horisawa, Y.; Tokunaga, K.; Ueno, T.; Takaori-Kondo, A.; Schreiber, G.; Arase, H.; Motozono, C.; Saito, A.; Nakagawa, S.; Sato, K., The SARS-CoV-2 Lambda variant exhibits enhanced infectivity and immune resistance. *Cell Rep* **2022,** *38* (2), 110218.
279. Planas, D.; Veyer, D.; Baidaliuk, A.; Staropoli, I.; Guivel-Benhassine, F.; Rajah, M. M.; Planchais, C.; Porrot, F.; Robillard, N.; Puech, J.; Prot, M.; Gallais, F.; Gantner, P.; Velay, A.; Le Guen, J.; Kassis-Chikhani, N.; Edriss, D.; Belec, L.; Seve, A.; Courtellemont, L.; Péré, H.; Hocqueloux, L.; Fafi-Kremer, S.; Prazuck, T.; Mouquet, H.; Bruel, T.; Simon-Lorière, E.; Rey, F. A.; Schwartz, O., Reduced sensitivity of SARS-CoV-2 variant Delta to antibody neutralization. *Nature* **2021,** *596* (7871), 276-280.
280. VanBlargan, L. A.; Errico, J. M.; Halfmann, P. J.; Zost, S. J.; Crowe, J. E., Jr.; Purcell, L. A.; Kawaoka, Y.; Corti, D.; Fremont, D. H.; Diamond, M. S., An infectious SARS-CoV-2 B.1.1.529 Omicron virus escapes neutralization by therapeutic monoclonal antibodies. *Nat Med* **2022,** *28* (3), 490-495.
281. Naveca, F. G.; Nascimento, V.; Souza, V.; Corado, A. L.; Nascimento, F.; Silva, G.; Mejía, M. C.; Brandão, M. J.; Costa, Á.; Duarte, D.; Pessoa, K.; Jesus, M.; Gonçalves, L.; Fernandes, C.; Mattos, T.; Abdalla, L.; Santos, J. H.; Martins, A.; Chui, F. M.; Val, F. F.; de Melo, G. C.; Xavier, M. S.; Sampaio, V. S.; Mourão, M. P.; Lacerda, M. V.; Batista É, L. R.; Magalhães, A.; Dábilla, N.; Pereira, L. C. G.; Vinhal, F.; Miyajima, F.; Dias, F. B. S.; Dos Santos, E. R.; Coêlho, D.; Ferraz, M.; Lins, R.; Wallau, G. L.; Delatorre, E.; Gräf, T.; Siqueira, M. M.; Resende, P. C.; Bello, G., Spread of Gamma (P.1) sub-lineages carrying Spike mutations close to the furin cleavage site and deletions in the N-Terminal domain drives ongoing transmission of SARS-CoV-2 in Amazonas, Brazil. *Microbiol Spectr* **2022,** *10* (1), e0236621.

282. Takashita, E.; Kinoshita, N.; Yamayoshi, S.; Sakai-Tagawa, Y.; Fujisaki, S.; Ito, M.; Iwatsuki-Horimoto, K.; Chiba, S.; Halfmann, P.; Nagai, H.; Saito, M.; Adachi, E.; Sullivan, D.; Pekosz, A.; Watanabe, S.; Maeda, K.; Imai, M.; Yotsuyanagi, H.; Mitsuya, H.; Ohmagari, N.; Takeda, M.; Hasegawa, H.; Kawaoka, Y., Efficacy of antibodies and antiviral drugs against Covid-19 Omicron variant. *N Engl J Med* **2022,** *386* (10), 995-998.
283. Tada, T.; Zhou, H.; Dcosta, B. M.; Samanovic, M. I.; Mulligan, M. J.; Landau, N. R., Partial resistance of SARS-CoV-2 Delta variants to vaccine-elicited antibodies and convalescent sera. *iScience* **2021,** *24* (11), 103341.
284. Shen, Q.; Li, J.; Zhang, Z.; Guo, S.; Wang, Q.; An, X.; Chang, H., COVID-19: systemic pathology and its implications for therapy. *Int J Biol Sci* **2022,** *18* (1), 386-408.
285. Chen, L.; Xiong, J.; Bao, L.; Shi, Y., Convalescent plasma as a potential therapy for COVID-19. *Lancet Infect Dis* **2020,** *20* (4), 398-400.
286. Shen, C.; Wang, Z.; Zhao, F.; Yang, Y.; Li, J.; Yuan, J.; Wang, F.; Li, D.; Yang, M.; Xing, L.; Wei, J.; Xiao, H.; Yang, Y.; Qu, J.; Qing, L.; Chen, L.; Xu, Z.; Peng, L.; Li, Y.; Zheng, H.; Chen, F.; Huang, K.; Jiang, Y.; Liu, D.; Zhang, Z.; Liu, Y.; Liu, L., Treatment of 5 critically Ill patients with COVID-19 with convalescent plasma. *Jama* **2020,** *323* (16), 1582-1589.
287. Tortorici, M. A.; Veesler, D., Structural insights into coronavirus entry. *Adv Virus Res* **2019,** *105*, 93-116.
288. Chen, J.; Gao, K.; Wang, R.; Nguyen, D. D.; Wei, G. W., Review of COVID-19 antibody therapies. *Annu Rev Biophys* **2021,** *50*, 1-30.
289. Lu, M.; Uchil, P. D.; Li, W.; Zheng, D.; Terry, D. S.; Gorman, J.; Shi, W.; Zhang, B.; Zhou, T.; Ding, S.; Gasser, R.; Prévost, J.; Beaudoin-Bussières, G.; Anand, S. P.; Laumaea, A.; Grover, J. R.; Liu, L.; Ho, D. D.; Mascola, J. R.; Finzi, A.; Kwong, P. D.; Blanchard, S. C.; Mothes, W., Real-time conformational dynamics of SARS-CoV-2 Spikes on virus particles. *Cell Host Microbe* **2020,** *28* (6), 880-891.e8.
290. Tian, X.; Li, C.; Huang, A.; Xia, S.; Lu, S.; Shi, Z.; Lu, L.; Jiang, S.; Yang, Z.; Wu, Y.; Ying, T., Potent binding of 2019 novel coronavirus spike protein by a SARS coronavirus-specific human monoclonal antibody. *Emerg Microbes Infect* **2020,** *9* (1), 382-385.
291. Yuan, M.; Wu, N. C.; Zhu, X.; Lee, C. D.; So, R. T. Y.; Lv, H.; Mok, C. K. P.; Wilson, I. A., A highly conserved cryptic epitope in the receptor binding domains of SARS-CoV-2 and SARS-CoV. *Science* **2020,** *368* (6491), 630-633.
292. Jovčevska, I.; Muyldermans, S., The therapeutic potential of nanobodies. *BioDrugs* **2020,** *34* (1), 11-26.
293. Zhou, P.; Yang, X. L.; Wang, X. G.; Hu, B.; Zhang, L.; Zhang, W.; Si, H. R.; Zhu, Y.; Li, B.; Huang, C. L.; Chen, H. D.; Chen, J.; Luo, Y.; Guo, H.; Jiang, R. D.; Liu, M. Q.; Chen, Y.; Shen, X. R.; Wang, X.; Zheng, X. S.; Zhao, K.; Chen, Q. J.; Deng, F.; Liu, L. L.; Yan, B.; Zhan, F. X.; Wang, Y. Y.; Xiao, G. F.; Shi, Z. L., A pneumonia outbreak associated with a new coronavirus of probable bat origin. *Nature* **2020,** *579* (7798), 270-273.
294. Wrapp, D.; De Vlieger, D.; Corbett, K. S.; Torres, G. M.; Wang, N.; Van Breedam, W.; Roose, K.; van Schie, L.; Hoffmann, M.; Pöhlmann, S.; Graham, B. S.; Callewaert, N.; Schepens, B.; Saelens, X.; McLellan, J. S., Structural basis for potent neutralization of betacoronaviruses by single-domain Camelid antibodies. *Cell* **2020,** *181* (5), 1004-1015.e15.
295. Singh, J.; Rahman, S. A.; Ehtesham, N. Z.; Hira, S.; Hasnain, S. E., SARS-CoV-2 variants of concern are emerging in India. *Nat Med* **2021,** *27* (7), 1131-1133.
296. Laiton-Donato, K.; Franco-Muñoz, C.; Álvarez-Díaz, D. A.; Ruiz-Moreno, H. A.; Usme-Ciro, J. A.; Prada, D. A.; Reales-González, J.; Corchuelo, S.; Herrera-Sepúlveda, M. T.; Naizaque, J.; Santamaría, G.; Rivera, J.; Rojas, P.; Ortiz, J. H.; Cardona, A.; Malo, D.; Prieto-Alvarado, F.; Gómez, F. R.; Wiesner, M.; Martínez, M. L. O.; Mercado-Reyes, M., Characterization of the emerging B.1.621 variant of interest of SARS-CoV-2. *Infect Genet Evol* **2021,** *95*, 105038.
297. Jangra, S.; Ye, C.; Rathnasinghe, R.; Stadlbauer, D.; Krammer, F.; Simon, V.; Martinez-Sobrido, L.; García-Sastre, A.; Schotsaert, M., SARS-CoV-2 spike E484K mutation reduces antibody neutralisation. *Lancet Microbe* **2021,** *2* (7), e283-e284.

298. Szarpak, L.; Savytskyi, I.; Pruc, M.; Gozhenko, A.; Filipiak, K. J.; Rafique, Z.; Peacock, F. W.; Ilesanmi, O. S.; Chirico, F., Variant lambda of the severe acute respiratory syndrome coronavirus 2: A serious threat or the beginning of further dangerous mutations. *Cardiol J* **2022,** *29* (1), 176-177.
299. Xu, J.; Xu, K.; Jung, S.; Conte, A.; Lieberman, J.; Muecksch, F.; Lorenzi, J. C. C.; Park, S.; Schmidt, F.; Wang, Z.; Huang, Y.; Luo, Y.; Nair, M. S.; Wang, P.; Schulz, J. E.; Tessarollo, L.; Bylund, T.; Chuang, G. Y.; Olia, A. S.; Stephens, T.; Teng, I. T.; Tsybovsky, Y.; Zhou, T.; Munster, V.; Ho, D. D.; Hatziioannou, T.; Bieniasz, P. D.; Nussenzweig, M. C.; Kwong, P. D.; Casellas, R., Nanobodies from camelid mice and llamas neutralize SARS-CoV-2 variants. *Nature* **2021,** *595* (7866), 278-282.
300. Astuti, I.; Ysrafil, Severe Acute Respiratory Syndrome Coronavirus 2 (SARS-CoV-2): An overview of viral structure and host response. *Diabetes Metab Syndr* **2020,** *14* (4), 407-412.
301. Díaz, J., SARS-CoV-2 molecular network structure. *Front Physiol* **2020,** *11*, 870.
302. Lim, Y. X.; Ng, Y. L.; Tam, J. P.; Liu, D. X., Human coronaviruses: A review of virus-host interactions. *Diseases* **2016,** *4* (3).
303. Prentice, E.; McAuliffe, J.; Lu, X.; Subbarao, K.; Denison, M. R., Identification and characterization of severe acute respiratory syndrome coronavirus replicase proteins. *J Virol* **2004,** *78* (18), 9977-86.
304. Yuan, S.; Balaji, S.; Lomakin, I. B.; Xiong, Y., Coronavirus Nsp1: Immune response suppression and protein expression inhibition. *Front Microbiol* **2021,** *12*, 752214.
305. de Breyne, S.; Vindry, C.; Guillin, O.; Condé, L.; Mure, F.; Gruffat, H.; Chavatte, L.; Ohlmann, T., Translational control of coronaviruses. *Nucleic Acids Res* **2020,** *48* (22), 12502-12522.
306. Abernathy, E.; Glaunsinger, B., Emerging roles for RNA degradation in viral replication and antiviral defense. *Virology* **2015,** *479-480*, 600-8.
307. Stern-Ginossar, N.; Thompson, S. R.; Mathews, M. B.; Mohr, I., Translational control in virus-infected cells. *Cold Spring Harb Perspect Biol* **2019,** *11* (3).
308. Hartenian, E.; Nandakumar, D.; Lari, A.; Ly, M.; Tucker, J. M.; Glaunsinger, B. A., The molecular virology of coronaviruses. *J Biol Chem* **2020,** *295* (37), 12910-12934.
309. Nakagawa, K.; Makino, S., Mechanisms of coronavirus Nsp1-mediated control of host and viral gene expression. *Cells* **2021,** *10* (2).
310. Narayanan, P.; Chatterton, P.; Ikeda, A.; Ikeda, S.; Corey, D. P.; Ervasti, J. M.; Perrin, B. J., Length regulation of mechanosensitive stereocilia depends on very slow actin dynamics and filament-severing proteins. *Nat Commun* **2015,** *6* (1), 6855.
311. Banerjee, A. K.; Blanco, M. R.; Bruce, E. A.; Honson, D. D.; Chen, L. M.; Chow, A.; Bhat, P.; Ollikainen, N.; Quinodoz, S. A.; Loney, C.; Thai, J.; Miller, Z. D.; Lin, A. E.; Schmidt, M. M.; Stewart, D. G.; Goldfarb, D.; De Lorenzo, G.; Rihn, S. J.; Voorhees, R. M.; Botten, J. W.; Majumdar, D.; Guttman, M., SARS-CoV-2 disrupts splicing, translation, and protein trafficking to suppress host defenses. *Cell* **2020,** *183* (5), 1325-1339.e21.
312. Hillen, H. S.; Kokic, G.; Farnung, L.; Dienemann, C.; Tegunov, D.; Cramer, P., Structure of replicating SARS-CoV-2 polymerase. *Nature* **2020,** *584* (7819), 154-156.
313. Littler, D. R.; Gully, B. S.; Colson, R. N.; Rossjohn, J., Crystal structure of the SARS-CoV-2 non-structural protein 9, Nsp9. *iScience* **2020,** *23* (7), 101258.
314. Zhang, L.; Richards, A.; Barrasa, M. I.; Hughes, S. H.; Young, R. A.; Jaenisch, R., Reverse-transcribed SARS-CoV-2 RNA can integrate into the genome of cultured human cells and can be expressed in patient-derived tissues. *Proc Natl Acad Sci U S A* **2021,** *118* (21).
315. Lokugamage, K. G.; Narayanan, K.; Huang, C.; Makino, S., Severe acute respiratory syndrome coronavirus protein nsp1 is a novel eukaryotic translation inhibitor that represses multiple steps of translation initiation. *J Virol* **2012,** *86* (24), 13598-608.
316. Thoms, M.; Buschauer, R.; Ameismeier, M.; Koepke, L.; Denk, T.; Hirschenberger, M.; Kratzat, H.; Hayn, M.; Mackens-Kiani, T.; Cheng, J.; Straub, J. H.; Stürzel, C. M.; Fröhlich, T.; Berninghausen, O.; Becker, T.; Kirchhoff, F.; Sparrer, K. M. J.; Beckmann, R., Structural basis for translational shutdown and immune evasion by the Nsp1 protein of SARS-CoV-2. *Science* **2020,** *369* (6508), 1249-1255.
317. Narayanan, K.; Huang, C.; Lokugamage, K.; Kamitani, W.; Ikegami, T.; Tseng, C. T.; Makino, S., Severe acute respiratory syndrome coronavirus nsp1 suppresses host gene expression, including that of type I interferon, in infected cells. *J Virol* **2008,** *82* (9), 4471-9.

318. Wathelet, M. G.; Orr, M.; Frieman, M. B.; Baric, R. S., Severe acute respiratory syndrome coronavirus evades antiviral signaling: role of nsp1 and rational design of an attenuated strain. *J Virol* **2007,** *81* (21), 11620-33.
319. Jauregui, A. R.; Savalia, D.; Lowry, V. K.; Farrell, C. M.; Wathelet, M. G., Identification of residues of SARS-CoV nsp1 that differentially affect inhibition of gene expression and antiviral signaling. *PLoS One* **2013,** *8* (4), e62416.
320. Fraser, C. S.; Berry, K. E.; Hershey, J. W.; Doudna, J. A., eIF3j is located in the decoding center of the human 40S ribosomal subunit. *Mol Cell* **2007,** *26* (6), 811-9.